



University  
of Glasgow

Perry, Joan M. (2001) *Erosion-corrosion of WC-Co-Cr cermet coatings*.  
PhD thesis.

<http://theses.gla.ac.uk/2845/>

Copyright and moral rights for this thesis are retained by the author

A copy can be downloaded for personal non-commercial research or  
study, without prior permission or charge

This thesis cannot be reproduced or quoted extensively from without first  
obtaining permission in writing from the Author

The content must not be changed in any way or sold commercially in any  
format or medium without the formal permission of the Author

When referring to this work, full bibliographic details including the  
author, title, awarding institution and date of the thesis must be given

# **Erosion-Corrosion of WC-Co-Cr Cermet Coatings**

**By**

**Joan M Perry ©**

A thesis submitted to  
The Department of Mechanical Engineering  
University of Glasgow



**UNIVERSITY**  
*of*  
**GLASGOW**

in fulfilment of the requirement for  
The Degree of Doctor of Philosophy

January 2001

**PAGE**

**NUMBERING**

**AS ORIGINAL**

## Abstract

The corrosion behaviour of WC-Co-Cr and WC-Co High Velocity-Oxy Fuel (HVOF) sprayed coatings has been examined in static saline conditions. The addition of chromium to the matrix has been found to greatly enhance the corrosion resistance of the coating. The electrochemical corrosion behaviour in static conditions is complex due to the composite ceramic/metal nature of the coating surface. The combination of in-situ electrochemical monitoring and observation in the changes of the microstructure using an Atomic Force Microscope has revealed differing corrosion mechanisms on the two coatings.

The erosion-corrosion characteristics of a WC-Co-Cr coating were assessed under an impinging jet of 3.5% NaCl solution at a velocity of  $12 \text{ ms}^{-1}$  both free from solids and containing solids up to 2500 mg/l at a range of impingement angles. The total weight loss increased with increasing solids in the liquid stream and maximum material loss occurred in the area directly under the jet where high impact angles occurred. The material loss tended to reduce as the impingement angle reduced.

The mechanism and contribution to the overall material loss in erosion-corrosion processes were studied. Surface profiling revealed the erosion mechanism to be that of solid particles causing craters on the surface of the coating, not associated with any specific microstructural aspect of the coating. The total contribution to overall material loss from corrosion processes was substantial (up to 30%). While the impinging jet increased the corrosion rate, in the absence and presence of solids, these corrosive effects could be inhibited, particularly in the presence of solids, by the application of cathodic protection which reduced overall material loss by up to 50%.

The synergistic component of material loss can be referred to as an indirect corrosion effect, and in this work, the synergistic effect was significant (up to 40%). However, more complex direct corrosion effects were found in the form of galvanic currents between the area directly under the impinging jet and the outer

area which significantly increase the corrosion rate on the impinged area. This study, which focuses on the interactions between corrosion and erosion, has improved the understanding of erosion-corrosion processes on complex composite materials.

# Contents

## Abstract

Contents.....	i
List of Figures.....	vi
List of Tables.....	xiv
Acknowledgements.....	xv
Nomenclature.....	xvi
Publication List.....	xvii

## Chapter 1 Introduction and Outline of Thesis..... 1

1.1 Introduction.....	1
1.2 Outline of Thesis.....	2

## Chapter 2 Basic Corrosion Principles ..... 4

2.1 Aqueous Corrosion.....	4
2.2 Electrochemical Polarisation.....	5
2.2.1 Activation Polarisation.....	5
2.2.2 Concentration Polarisation.....	6
2.3 Mixed Potential Theory.....	8
2.4 Potentiodynamic Polarisation.....	9
2.4.1 Cathodic and Anodic Polarisation.....	10
2.4.2 Linear Polarisation.....	12
2.4.3 AC Impedance.....	13
2.5 Forms of Aqueous Corrosion.....	14
2.5.1 General and Localised Corrosion.....	15
2.5.2 Pitting and Crevice Corrosion.....	15
2.5.3 Galvanic (Bimetallic) Corrosion.....	15
2.5.4 Intergranular Corrosion.....	15
2.5.5 Hydrogen Embrittlement and Hydrogen Damage.....	15
2.5.6 Dealloying and Dezincification.....	16

2.5.7 Stress and Corrosion Interaction.....	16
<b>Chapter 3 Literature Review .....</b>	<b>17</b>
3.1 Thermal Spray Technology .....	17
3.1.1 Introduction .....	17
3.1.2 Flame Spraying .....	17
3.1.3 Atmospheric Plasma Spraying (APS) .....	17
3.1.4 Arc Spraying (AS).....	17
3.1.5 Detonation Gun Spraying.....	17
3.1.6 Vacuum Plasma Spraying (VPS) .....	18
3.1.7 Controlled Atmosphere Plasma Spraying (CAPS).....	18
3.1.8 High Velocity Oxy-Fuel Spraying (HVOF).....	18
3.2 Powder Manufacture .....	21
3.3 WC-Cermet Coatings – Microstructure and Compositional Changes .....	22
3.4 Corrosion of Cermet Coatings.....	24
3.5 Erosion-Corrosion .....	30
3.5.1 The Hydrodynamics of a Turbulent Jet.....	31
3.5.2 ‘Flow Induced Corrosion’ .....	32
3.5.3 Effect of flow/impingement on metals.....	34
3.5.4 Dry Solid Erosion.....	35
3.5.5 Liquid-Solid Erosion .....	39
3.5.6 Slurry Erosion of Thermally Sprayed WC Coatings.....	42
3.5.7 Erosion-Corrosion-Synergy: Definitions and Mechanisms .....	42
3.5.8 Mapping of Erosion-Corrosion Regimes .....	48
3.6 Summary.....	50
<b>Chapter 4 Experimental Procedure and Analysis.....</b>	<b>52</b>
4.1 Introduction.....	52
4.2 Methodology.....	52
4.3 Specimen Preparation.....	53
4.4 Electrochemistry.....	54
4.5 Liquid Erosion Testing.....	55
4.6 Liquid-Solid Erosion-Corrosion.....	56
4.7 Tafel Extrapolation.....	57
4.8 Linear Polarisation.....	60

4.9 Post Test Analysis .....	61
4.9.1 Scanning Electron Microscopy (SEM) and Energy Dispersive X-Ray (EDX) .	61
4.9.2 X-Ray Diffraction (XRD) .....	62
4.9.3 Surface Profiling .....	62
4.9.4 Atomic Force Microscopy (AFM) .....	62
<b>Chapter 5 Coating Characterisation and Static Corrosion</b>	
<b>Behaviour.....</b>	<b>64</b>
5.1 Introduction .....	64
5.2 Coating I.....	64
5.2.1 Characterisation.....	64
5.2.2 Static Corrosion Behaviour .....	67
5.2.3 Cathodic Polarisation Tests.....	70
5.2.4 Long-term tests.....	70
5.3 Coating 2 .....	76
5.3.1 Characterisation.....	76
5.3.2 Static Corrosion Behaviour .....	77
5.3.3 Cathodic Polarisation Tests.....	83
5.4 Coating 3 .....	84
5.4.1 Coating Characterisation.....	84
5.4.2 Static Corrosion Behaviour .....	85
5.4.3 Cathodic Polarisation Tests.....	91
5.5 Summary and Comparison of Coatings .....	91
<b>Chapter 6 Erosion-Corrosion under Liquid Impingement and</b>	
<b>Liquid-Solid Impingement.....</b>	<b>96</b>
6.1 Introduction .....	96
6.2 Corrosion effects under liquid impingement at 18°C and 50°C .....	97
6.2.1 Anodic Polarisation .....	97
6.2.2 Cathodic Polarisation .....	98
6.2.3 Corrected Tafel Extrapolation.....	99
6.3 Corrosion Effects under Solid-Liquid Impingement.....	100
6.3.1 Anodic and Cathodic Polarisation.....	100
6.3.2 Corrected Tafel Extrapolation.....	105

6.4 Overall solid-liquid effects on material degradation.....	109
6.4.1 Weight losses under liquid-solid conditions .....	109
6.5 Material Degradation Quantification .....	115
6.5.1 Erosion, Corrosion and Synergy .....	115
6.6 Post Test Surface Analysis.....	120
6.6.1 Liquid Impingement.....	121
6.6.2 Liquid-Solid Impingement .....	122
<b>Chapter 7 An Investigation of Erosion-Corrosion Under a Liquid-Solid Jet Incorporating Effects from Varying Impact Angle and on Concentric Specimens .....</b>	<b>128</b>
7.1 Introduction .....	128
7.2 Weight Loss vs Solid Loading .....	128
7.3 Effect of Impingement Angle.....	133
7.3.1 Erosive Effects .....	133
7.3.2 Corrosive Effects with Differing Impact Angles .....	147
7.4 Concentric Specimens.....	150
7.4.1 Introduction .....	150
7.4.2 Galvanic Effects within Concentric Specimens.....	150
7.4.3 Linear Polarisation of Concentric Specimen.....	152
7.4.4 Anodic Polarisation of Concentric Specimens.....	154
7.4.5 Post Test Analysis of Concentric Specimens.....	155
7.5 Effects of Anodic Potentials Under Erosion-Corrosion Conditions .....	158
<b>Chapter 8 Discussion of Results .....</b>	<b>161</b>
8.1 Static Corrosion Behaviour.....	161
8.2 Liquid Impingement.....	166
8.3 Liquid-Solid Erosion.....	168
8.3.1 Corrosive Effects under Liquid-Solid Erosion.....	168
8.3.2 Pure Erosive Effects under Liquid-Solid Erosion.....	173
8.3.3 Erosion-Corrosion and Synergy.....	177
8.4 Practical Relevance of Work.....	178
<b>Chapter 9 Conclusions and Further Work.....</b>	<b>181</b>
9.1 Conclusions.....	181

9.2 Further Work.....	182
Appendix 1.....	184
References.....	196

## List of Figures

- Figure 2-1  $i_a/E$  plot for anodic reaction subject to activation polarisation
- Figure 2-2 Polarisation curve for cathodic reaction undergoing concentration polarisation
- Figure 2-3 Diagram of mixed potential
- Figure 2-4 Three-electrode cell
- Figure 2-5 Schematic diagram showing anodic and cathodic polarisation
- Figure 2-6 Schematic diagram showing cathodic overpotential of  $\epsilon_c$
- Figure 2-7 Schematic showing anodic overpotential
- Figure 2-8 Schematic Diagram of equivalent circuit
- Figure 2-9 Schematic diagram of Nyquist plot
- Figure 3-1 Schematic diagram of a HVOF gun
- Figure 3-2 Radial Wall jet produced by an impinging circular jet
- Figure 3-3 Classification of flow induced corrosion
- Figure 3-4 Typical erosion curves for ductile and brittle materials as a function of particle incidence,  $\beta_1$
- Figure 3-5 Calculated trajectories of sand particles of different diameters in a water jet 20mm wide and velocity 8 ms<sup>-1</sup> directed at a flat plate
- Figure 3-6 Co-ordinate system and particle motion in a slurry jet
- Figure 3-7 Variation in impact velocity  $V_p$ , impact angle  $\alpha$  and collision efficiency  $\eta$  for a water jet containing 176 $\mu$ m diameter glass beads for an average jet velocity of 11 ms<sup>-1</sup>
- Figure 3-8 Schematic diagram showing the profile of a wear scar of aluminium and glass at normal impingement from sand-water slurry<sup>72</sup>
- Figure 4-1 Specimen prepared for electrochemical monitoring
- Figure 4-2 Concentric specimen for electrochemical monitoring
- Figure 4-3 Three-electrode electrochemical cell
- Figure 4-4 Schematic diagram of liquid erosion rig
- Figure 4-5 Schematic diagram of liquid-solid apparatus
- Figure 4-6 Graph showing low anodic currents at -800mV
- Figure 4-7 Tafel Extrapolation from anodic polarisation curve

Figure 4-8 Schematic diagram showing the determination of  $i_{\text{corr}}$  in erosion-corrosion conditions

Figure 4-9 Schematic diagram showing calculation of polarisation resistances

Figure 4-10 Schematic diagram of AFM

Figure 5-1 Picture of WC-Co-Cr powder particles

Figure 5-2 SEM micrograph of sprayed coating

Figure 5-3 XRD trace for the constituent WC-Co-C powder

Figure 5-4 XRD trace for the sprayed WC-Co-Cr coating

Figure 5-5 Polished cross-section of WC-Co-Cr

Figure 5-6 Anodic polarisation curve on the WC-Co-Cr coating in static artificial seawater at 18°C

Figure 5-7 SEM image of the surface of the WC-Co-Cr HVOF coating after anodic polarisation at 18°C

Figure 5-8 Comparison of the anodic polarisation curves at 18°C and 50°C in static conditions

Figure 5-9 SEM micrograph of deep localised region of corrosion attack where extensive matrix dissolution has occurred

Figure 5-10 Cathodic Polarisation tests after 1 hour immersion

Figure 5-11 Anodic Polarisation after one month at 18°C

Figure 5-12 Corrosion attack on WC-Co-Cr coating after exposure to artificial seawater at 18°C for one month at the free corrosion potential

Figure 5-13 Crevice corrosion at coating/lacomit interface after one month immersion at 18°C

Figure 5-14 AC Impedance as a Nyquist after exposure to artificial seawater for one month at 18°C

Figure 5-15 Anodic Polarisation after one month immersion at 50°C

Figure 5-16 Unsupported carbide particles on the coating surface after exposure to artificial seawater at 50°C for one month at the free corrosion potential

Figure 5-17 AC Impedance as Nyquist plot for immersion in seawater at 50°C over a one month period

Figure 5-18 SEM micrograph of WC-Co-Cr as polished

Figure 5-19 XRD trace for the WC-Co-Cr coating II

Figure 5-20 Anodic polarisation of WC-Co-Cr in artificial seawater

Figure 5-21 SEM Micrograph of WC-Co-Cr after polarisation at 18°C

Figure 5-22 SEM micrograph of WC-Co-Cr after polarisation at 50°C

Figure 5-23 AFM Image of WC-CoCr coating at point A

Figure 5-24 AFM image of WC-CoCr coating a point B

Figure 5-25 AFM image of WC-CoCr coating at point C

Figure 5-26 AFM image of WC-CoCr coating at point D

Figure 5-27 AFM image of WC-CoCr coating at point E

Figure 5-28 Line scan of coating 2 after anodic polarisation at 18°C

Figure 5-29 Cathodic Polarisation of WC-Co-Cr after one hour immersion

Figure 5-30 Polished cross-section of WC-Co coating

Figure 5-31 XRD of WC-Co-Cr spray coating

Figure 5-32 Anodic polarisation of WC-Co coating

Figure 5-33 SEM micrograph after anodic polarisation at 18°C of WC-Co coating

Figure 5-34 SEM micrograph of WC-Co coating after anodic polarisation at 50°C

Figure 5-35 AFM Image of WC-Co coating at point A

Figure 5-36 AFM image of WC-Co coating at point A to B

Figure 5-37 AFM image of WC-Co Coating at point B to C

Figure 5-38 AFM image of WC-Co coating at point C to D

Figure 5-39 AFM image of WC-Co coating at point D to E

Figure 5-40 AFM Image WC-Co coating at point E

Figure 5-41 Cathodic polarisation tests of WC-Co after one hour immersion

Figure 5-42 Semi-log plots of anodic polarisation of all three coatings after one hour immersion at 18°C

Figure 5-43 Micrograph of WC-Co after anodic polarisation at 18°C

Figure 5-44 Micrograph of WC-CoCr coating after anodic polarisation at 18°C

Figure 5-45 Semi log plot of anodic polarisations of all three coatings after one hour immersion at 50°C

Figure 5-46 Micrograph of WC-Co coating after anodic polarisation at 50°C

Figure 5-47 Micrograph of WC-CoCr coating after anodic polarisation at 50°C

Figure 6-1 Example of corrected anodic currents incorporating residual cathodic currents at 4 hours impingement with 170 mg/l solids in 35% NaCl at 18°C

Figure 6-2 Anodic polarisation scans under liquid impinging jet at 12ms<sup>-1</sup> in 35% NaCl

Figure 6-3 Cathodic polarisation scan under a liquid impinging jet at  $12\text{ms}^{-1}$  in 35% NaCl

Figure 6-4 Corrected corrosion currents under liquid impingement conditions

Figure 6-5 Anodic polarisations scans under a liquid-solid impinging jet at  $18^\circ\text{C}$  at  $12\text{ms}^{-1}$

Figure 6-6 Anodic polarisation scans under a liquid-solid impinging jet of  $500\text{mg/l}$  solids at  $50^\circ\text{C}$  and  $12\text{ms}^{-1}$

Figure 6-7 Cathodic polarisation scans under a liquid-solid impinging jet containing  $500\text{mg/l}$  solids at  $50^\circ\text{C}$  and  $12\text{ms}^{-1}$

Figure 6-8 Anodic Polarisation curves under liquid-solid jet with  $650\text{mg/l}$  solids  $18^\circ\text{C}$ ,  $12\text{ms}^{-1}$

Figure 6-9 Anodic Polarisation curves under liquid-solid jet with  $1500\text{mg/l}$  solids  $18^\circ\text{C}$ ,  $12\text{ms}^{-1}$ , and  $90^\circ$  impingement

Figure 6-10 Anodic Polarisation curves under liquid-solid jet with  $1500\text{mg/l}$  solids  $18^\circ\text{C}$ ,  $12\text{ms}^{-1}$ ,  $45^\circ$  impingement

Figure 6-11 Corrected corrosion currents under liquid-solid conditions

Figure 6-12 Tafel Extrapolation for liquid-solid impingement with  $650\text{mg/l}$ ,  $12\text{ms}^{-1}$ ,  $18^\circ\text{C}$

Figure 6-13 Tafel Extrapolation for  $90^\circ$  liquid-solid jet impingement with  $1500\text{mg/l}$  solids  $12\text{ms}^{-1}$   $18^\circ\text{C}$

Figure 6-14 Tafel Extrapolation for  $45^\circ$  liquid-solid jet impingement with  $1500\text{mg/l}$  solids  $12\text{ms}^{-1}$   $18^\circ\text{C}$

Figure 6-15 Corrosion current densities measured in liquid and liquid-solid conditions

Figure 6-16 Currents measured during cathodic protection ( $-800\text{mV}$ ) at  $90^\circ$  solid-liquid impingement

Figure 6-17 Graph of average weight losses under solid-liquid impingement at  $90^\circ$

Figure 6-18 Graph of weight losses under solid-liquid impingement at  $45^\circ$

Figure 6-19 Comparison of effect of impingement angle on total weight losses under solid-liquid jet for four hours at  $18^\circ\text{C}$ ,  $12\text{ms}^{-1}$

Figure 6-20 Contributions to total weight loss from a  $500\text{mg/l}$  liquid-solid jet at  $90^\circ$  impingement

Figure 6-21 Contributions to total weight loss with a 650 mg/l liquid-solid jet at 90° impingement

Figure 6-22 Contributions to total weight loss with a 1500 mg/l liquid-solid jet at 90° impingement

Figure 6-23 Contributions to total weight loss from a 1500 mg/l liquid-solid jet at 45° impingement

Figure 6-24 Percentage contributions of E, C and S after 1 hour impingement

Figure 6-25 Percentage Contributions of E, C and S after 4 hours impingement

Figure 6-26 No wear scar after anodic polarisation under impinging jet for 4 hours at 18°C

Figure 6-27 Coating breaking up after anodic polarisation under impinging jet 1-hour 50°C

Figure 6-28 Macro holes after anodic polarisation under impinging jet for 4 hours at 50°C

Figure 6-29 Wear scar on surface of specimen after 4 hours impingement with 650 mg/l liquid-solid jet at 90° impingement

Figure 6-30 Magnified photograph of wear scar at 90° impingement

Figure 6-31 Surface profile after 4 hours impingement at free erosion-corrosion with 650 mg/l solids at 90°

Figure 6-32 Surface profile after 4 hours impingement with 650 mg/l solids at 90° with cathodic protection

Figure 6-33 Comparison of spike and hard phase particle size

Figure 6-34 Surface profile of after 4 hours impingement with 170 mg/l at free erosion-corrosion conditions

Figure 6-35 Surface profile after 4 hours impingement with 170 mg/l under cathodic protection

Figure 6-36 Photograph of wear scar at 45° impingement

Figure 6-37 Surface profile of wear scar at 45° impingement with 650 mg/l solids for 4 hours

Figure 7-1 Average Weight Losses and Scar Depths under Liquid-Solid Erosion-Corrosion after 4 Hours Impingement, 12 ms<sup>-1</sup> at 18°C

Figure 7-2 Surface profile of as-polished specimen

Figure 7-3 Surface profile after 4 hours impingement with 250 mg/l solids at 90° and 12 ms<sup>-1</sup>

Figure 7-4 Surface profile after 4 hours impingement with 1250 mg/l solids at 90° and 12 ms<sup>-1</sup>

Figure 7-5 Surface profile after 4 hours impingement with 2000 mg/l solids at 90° and 12 ms<sup>-1</sup>

Figure 7-6 Surface profile after 4 hours impingement with 2700 mg/l solids at 90° and 12 ms<sup>-1</sup>

Figure 7-7 Photograph of wear scar at 90° impingement

Figure 7-8 Photograph of wear scar at 30° impingement

Figure 7-9 Photograph of wear scar at 45° impingement

Figure 7-10 Photograph of wear scar at 60° impingement

Figure 7-11 Photograph of wear scar at 75° impingement

Figure 7-12 Graph of weight loss versus impact angle with 2000 mg/l solids

Figure 7-13 Photograph of sand impacts at 90° impingement

Figure 7-14 Craters in the middle of the 90° wear scar

Figure 7-15 Craters at the edge of the 90° wear scar

Figure 7-16 Diminishing craters at the edge of the 90° wear scar

Figure 7-17 Area just outside wear scar defining hard phase

Figure 7-18 Area outside wear scar showing discrete corroded areas

Figure 7-19 Wear scar when cathodic protection is applied at 90°, 2000 mg/l solids

Figure 7-20 Roughened surface at head of 30° wear scar

Figure 7-21 Middle of 30° wear scar

Figure 7-23 Tail of wear scar at 30°

Figure 7-24 Ploughing effects at 45° impingement angle

Figure 7-25 Middle of 45° impingement wear scar

Figure 7-26 Tail of 45° impingement wear scar

Figure 7-27 Inside wear scar at 60° impingement

Figure 7-28 Inside wear scar of 75° impingement

Figure 7-29 Corroded area at bottom of wear scar at 60° impingement

Figure 7-30 Uncorroded area above wear scar at 60° impingement

Figure 7-31 Anodic Polarisation curves at angles 90°, 75°, 60°, 45° and 30° with 2000 mg/l solids after 4 hours impingement at 12 ms<sup>-1</sup>

Figure 7-32 Anodic Polarisation curves at 90°, 45° and 30° after 1 hour impingement with 2000 mg/l solids at 12 ms<sup>-1</sup>

Figure 7-33 Linear Polarisation Results during 4 hours liquid-solid impingement at  $90^\circ$  at  $12 \text{ ms}^{-1}$  with  $2000 \text{ mg/l}$  solids

Figure 7-34 Erosion, corrosion and synergy components at  $30^\circ$ ,  $45^\circ$ ,  $60^\circ$ ,  $75^\circ$  and  $90^\circ$  impingements with  $2000 \text{ mg/l}$  solids at  $12 \text{ ms}^{-1}$

Figure 7-35 Linear polarisation curves of inner and outer concentric specimens at time zero with  $2000 \text{ mg/l}$  solids impinging at  $12 \text{ ms}^{-1}$

Figure 7-36 Linear polarisation curves of outer and inner concentric specimens after 1 hour with  $2000 \text{ mg/l}$  solids impinging at  $12 \text{ ms}^{-1}$

Figure 7-37 Linear polarisation of inner and outer concentric specimens after 2 hours with  $2000 \text{ mg/l}$  solids impinging at  $12 \text{ ms}^{-1}$

Figure 7-38 Linear polarisations on inner and outer specimens after 3 hours impingement with  $2000 \text{ mg/l}$  solids impinging at  $12 \text{ ms}^{-1}$

Figure 7-39 Anodic Polarisation curves for inner and outer concentric specimens after 4 hours impingement at  $12 \text{ ms}^{-1}$  with  $2000 \text{ mg/l}$  solids

Figure 7-40 Central specimen of concentric with eroded surface

Figure 7-41 Outer part of concentric specimen showing no erosion but more effect from corrosion

Figure 7-42 The outer ring where the matrix is effected by corrosion

Figure 7-43 Photograph of Specimen held at  $0\text{mV}$  under impingement with  $650 \text{ mg/l}$  solids for 4 hours

Figure 7-44 Photograph of central wear scar area of specimen held at  $0\text{mV}$  under impingement with  $650 \text{ mg/l}$  solids for 4 hours

Figure 7-45 Surface Profile of specimen held at  $0\text{mV}$  after 4 hours impingement with  $650 \text{ mg/l}$  solids at  $12 \text{ ms}^{-1}$

Figure 7-46 Surface profile of area outside wear scar of specimen held at  $0\text{mV}$  after 4 hours impingement with  $650 \text{ mg/l}$  solids at  $12 \text{ ms}^{-1}$

Figure 8-1 Schematic diagram of coating submerged in aqueous solution

Figure 8-2 Schematic diagram of corroding coating

Figure 8-3 Schematic diagram of the differing corrosion rates on a composite specimen

Figure 8-4 Comparison of experimental results with modelled results

Figure 8-5 Schematic diagram of erosion-corrosion mechanisms under a liquid-solid impinging jet I

Figure 8-6 Schematic diagram of erosion and corrosion mechanisms under a liquid-solid impinging jet II

Figure A-1 Anodic Polarisation curves of coating 1 after one hour immersion at 18°C

Figure A-2 Anodic Polarisation curves of coating 2 after one hour immersion at 50°C

Figure A-3 Anodic Polarisation of coating 2 after one hour immersion at 18°C

Figure A-4 Anodic polarisation curves of coating 3 after one hour immersion at 18°C

Figure A-5 Polarisation curves under liquid conditions after 1 and 4 hours at 18°C

Figure A-6 Anodic Polarisation under liquid conditions at 50°C

Figure A-7 Replicate polarisation curve after 4 hours impingement with 170 mg/l solids

Figure A-8 Anodic Polarisation after 4 hours impingement 500mg/l 18°C

Figure A-9 Replicate polarisation curves under liquid-solid impingement for 1 hour with 650 mg/l solids

Figure A-10 Replicate anodic polarisation curves for 4 hours impingement with 650 mg/l solids

Figure A-11 Replicate polarisation curves after 4 hours impingement with 1500 mg/l solids at 45°

Figure A-12 Replicate polarisation curves after 4 hours impingement with 1500 mg/l solids at 90°

## List of Tables

- Table 3-1 Comparison of some process parameters in thermal
- Table 4-1 Size distribution of sand
- Table 5-1 Parameters of coating 1
- Table 5-2 Chemical composition of the WC-Co-Cr coating 1 measured using the EDAX facility on the SEM
- Table 5-3 Table of duplicate Rp values over one month at 18°C
- Table 5-4 Table of duplicate Rp values over one month at 50°C
- Table 5-5 Parameters of Coating 2
- Table 5-6 Chemical composition of the WC-Co-Cr coating 2 measured using the EDAX facility on the SEM
- Table 5-7 Chemical composition of the WC-Co coating 3 measured using the EDAX facility on the SEM
- Table 5-8 Static corrosion rates for all three coatings
- Table 6-1 Corrosion currents under liquid-solid impingement conditions
- Table 6-2 Total Weight Losses in free erosion-corrosion conditions of a liquid-solid jet at 18°C, 90° impingement and 12ms<sup>-1</sup>
- Table 6-3 Weight losses under cathodic protection from a liquid-solid jet at 12ms<sup>-1</sup>, 90° impingement and 18°C
- Table 6-4 Weight losses from free erosion-corrosion under a liquid-solid jet at 45° impingement at 12ms<sup>-1</sup> and 18°C
- Table 6-5 Weight losses from cathodic protection under a liquid-solid jet at 45° impingement at 12 ms<sup>-1</sup> and 18°C
- Table 6-6 Corrosion rates and corresponding weight losses under a solid-liquid jet at 12ms<sup>-1</sup>
- Table 6-7 Scar Depths from Surface Profiles
- Table 7-1 Total weight loss of WC-CoCr coating under a solid-liquid jet at 12ms<sup>-1</sup> after 4 hours impingement at 18°C
- Table 7-2 Average wear scar depth and maximum spike depth on WC-CoCr coating under a solid- liquid jet at 12 ms<sup>-1</sup> after 4 hours impingement at 18°C
- Table 7-3 Weight loss on WC-CoCr coating after 4 hours impingement at 12 ms<sup>-1</sup> with 2000 mg/l solids at 18°C

Table 7-4 Corrosion rates found at angles 90°, 75°, 60°, 45° and 30° with 2000 mg/l solids after 4 hours impingement at 12 ms<sup>-1</sup>

Table 7-5 Polarisation resistance values from the linear polarisation curves after 4 hours impingement with 2000 mg/l solids

Table 7-6 Galvanic currents and E<sub>corr</sub> of concentric specimen

Table 7-7 Galvanic currents of concentric specimen

Table 7-8 R<sub>p</sub> values from linear polarisations on inner and outer concentric specimens

Table 7-9 Weight Losses and Currents under 4 hours impingement with 650 mg/l solids

Table 8-1 Average erosion rates under a solid-liquid impinging jet at 12 ms<sup>-1</sup>, 90° impingement and 18°C with the application of CP

## **Acknowledgements**

I would like to thank Dr. Trevor Hodgkiess for his supervision and for all the comments on my thesis. Also Dr. Anne Neville for consistent encouragement and guidance on this research. Thanks also to the technicians; Ian Russell and Gordon Hicks for maintaining the rigs, and Marian Millar at Heriot-Watt for assistance in the use of the AFM.

To the friends I made in the department: Lorna Smith and Kirsteen Lowe, lunchtimes just won't be the same without sharing your zest for fast cars and animals-stuffed or otherwise! Margaret Smith thanks for all your patient assistance in the lab and friendly advice. Thanks to my office mate, Shahid for all the tea breaks. To the troop at Heriot-Watt; Arnaud, Myrna, Vana and Rose for encouraging excursions instead of work! To Ruth, Kev, Mike and Rob for all the fun in the flat.

And last, but not least, my family for their support, especially my parents for their financial assistance during my student years.

## Nomenclature

$E_m$	Erosion rate
$T_m$	Target melting temperature
$n_c$	Strain hardening coefficient
$C_p$	Specific heat capacity
$E$	Electrochemical potential
$\mu_f$	Friction coefficient
$\mu_{f,c}$	Critical friction coefficient
$c$	Slurry concentration
$v$	Particle velocity
$\lambda$	Particle shape factor
$D_p$	Particle diameter
$H_s$	Static hardness
$e$	Coefficient of restitution
$D_z$	Diffusion coefficient
$C_B$	Concentration of $O_2$ in bulk solution
$\delta$	Diffusion layer thickness
$G$	Free Energy
$n$	Number of Electrons
$F$	Faraday's Constant
$\eta$	Over potential
$R$	Universal Gas Constant
$Re$	Reynolds Number
$Sh$	Sherwood Number
$Sc$	Schmidt Number
$\tau$	shear stress

## **List of Publications**

“Wrought and high-velocity oxy fuel sprayed Inconel 625-examination of corrosion aspects” A.Neville, J.M.Perry, T.Hodgkiess and H.P.Chua, Proc. Instn. Mechanical Engineers Vol. 214 Part 1 (2000) pp 41-48.

“Assessment of the corrosion and erosion-corrosion behaviour of a HVOF WC-CoCr coating” J.M.Perry, A.Neville and T.Hodgkiess, Proc. International Thermal Spray Conference, Montreal, Canada, May 2000, pp 1033-1038.

“Assessment of the corrosion rates and mechanisms of a WC-Co-Cr HVOF coating in static and liquid-solid impingement saline environments” J.M. Perry, A.Neville, V.A.Wilson and T.Hodgkiess, Surface and Coatings Technology Vol. 137 (2001) pp 43-51.

# Chapter 1

## Introduction and Outline of Thesis

### 1.1 Introduction

Corrosion when combined with erosion can lead to component failure in a variety of industrial environments including offshore oil and gas, mineral processing and mining. Corrosion on its own can be accentuated by temperature, velocity and salinity while erosion can be influenced by solid content, geometry, velocity and shape of erodent. Combining the two, corrosion and erosion, induces a third component, synergy which is corrosion-enhanced-synergy. Much work has been carried out on high-grade metallic materials identifying erosion-corrosion rates and mechanisms. While these materials have good corrosion resistance, in severe erosion-corrosion conditions their ability to resist deterioration reduces.

Consequently, alternative surface engineering options with superior resistance to wear in corrosive environments are constantly been sought. One possibility is the use of ceramics which have good wear resistance in dry erosion conditions. Cermets, which are metal/ceramic composites, in the form of thermally sprayed coatings, have been the subject of increasing interest as a means of protecting metallic substrates against erosion-corrosion. These coatings were initially developed for their high wear resistance in the aerospace industry. Their application as a barrier against erosion-corrosion in aqueous environments has, to an extent, preceded any understanding into their effectiveness and as such, has opened a door for a wealth of research.

These thermal sprayed coatings have been used in a variety of industrial applications to combat erosion-corrosion. One example is in offshore mineral extraction, where erosion-corrosion on the drill bit can lead to rapid failure when an internal jet emerges and impinges on the bit. Here thermally sprayed coatings have been implemented and shown to have a greater resistance to erosion-corrosion than hard steels and increase the life span of the bit. They have been

implemented on shipboard components i.e. pumps castings, shafts and valves, and extended the period between ship overhauls Thermal spray coatings have also been implemented in restoration of pressure vessels and pumps in the oil and gas production.

Of the family of thermal spray techniques available, the HVOF (High Velocity Oxy Fuel) process has been identified as having the most potential to produce good quality coatings in terms of low porosity and good adherence, without altering the mechanical properties of the substrate. One of the most seriously considered coatings sprayed by the HVOF process is the WC-based cermets. The work described in this thesis compares the corrosion rates and mechanisms in aqueous solutions of HVOF thermally sprayed WC-CoCr and WC-Co coatings. Focusing on the WC-Co-Cr coating, erosion-corrosion tests are reported in order to determine the degradation under aqueous liquid and liquid-solid impingement conditions.

## **1.2 Outline of Thesis**

The structure of this thesis is such that Chapter 2 contains all the relevant theory of corrosion subsequently used throughout the thesis.

Chapter 3 reviews the current literature on thermal sprayed coatings. It continues by summarising the processes in general and proceeds with a more detailed review of cermet coatings addressing their corrosion and erosion-corrosion resistance. A literature review on solid particle erosion and liquid-solid erosion-corrosion of materials other than coatings is also included.

Chapter 4 details the experimental equipment, procedures used in this thesis, and any post experiment analysis.

Chapter 5 introduces the three HVOF sprayed coatings studied in this research: two WC-CoCr coatings (from two different companies) and one WC-Co coating.

The results of all static corrosion tests carried out on each coating are presented here.

Chapters 6 and 7 continue with the two WC-CoCr coatings presenting results on erosion-corrosion tests.

Chapter 8 provides a discussion of all the results presented, drawing on major findings and comparing with those in the literature.

Chapter 9 lists the main conclusions from the work and suggests some topics where further work could be useful.

# Chapter 2

## Basic Corrosion Principles

### 2.1 Aqueous Corrosion

Metals corrode in an aqueous environment by an electrochemical mechanism. This comprises two simultaneous reactions, an anodic reaction which produces electrons and a cathodic reaction which consumes electrons. When a metal (M) is corroding (oxidising) in an aqueous environment, the metal goes into solution by the reaction below:



The corresponding cathodic (reduction) reaction predominantly comprises either the reduction of hydrogen ions, which occurs particularly in acidic environments, i.e.



or the reduction of dissolved oxygen (2.3) which is more favoured in neutral or alkaline solutions.



As with all chemical reactions, there is a change in free energy,  $\Delta G$ , when these reactions proceed. The free energy change may be associated with an equilibrium electrode potential,  $E_o$ , at equilibrium, by the fundamental relationship

$$\Delta G = -nFE_o \quad (2.4)$$

where n is the number of electrons and F is Faraday's constant, 96500 coulombs per

equivalent. The half-cell reactions (2.1) and (2.3) also have free-energy changes analogous to  $\Delta G$  and corresponding potentials  $e_a$  and  $e_c$  (the half cell potentials corresponding to the anodic and cathodic reactions respectively). The algebraic sum of these potentials  $e_a$  and  $e_c$  is equal to  $E_o$  in equation (2.4) i.e.

$$E_o = e_a + e_c \quad (2.5)$$

The potentials  $e_a$  and  $e_c$  have been called half-cell, single electrode or redox potentials for the corresponding half-cell reactions. It is impossible to measure the absolute value of any half-cell electrode potential. Only cell potentials consisting of two half-cell electrode potentials are measurable, and one must be selected as a primary reference.

## 2.2 Electrochemical Polarisation

Polarisation is the name given to potential change from a given “reference” potential associated with restricted charge transfer processes at electrodes. In relation to equilibrium electrode potential, polarisation ( $\eta$ ) is the potential change,  $E - E_o$ . For a cathodic polarisation,  $\eta_c$ , electrons are supplied to the surface, and a build-up in the metal due to the slow reaction rate causes the surface potential,  $E$ , to become negative to  $e_c$ . For anodic polarisation,  $\eta_a$ , electrons are removed from the metal, a deficiency results in a positive potential change due to the slow liberation from the metal by the surface reaction, hence  $\eta_a$  is positive. Polarisation can be classified into two types – activation polarisation and concentration polarisation.

### 2.2.1 Activation Polarisation

When the rate of charge flow is controlled by the activation energy required for a particular step, the reaction is said to be under activation or charge-transfer control, and activation polarisation results. The analysis of activation polarisation at the electrodes leads to a linear relationship between electrode potential and the log of the current density (Figure 2-1).

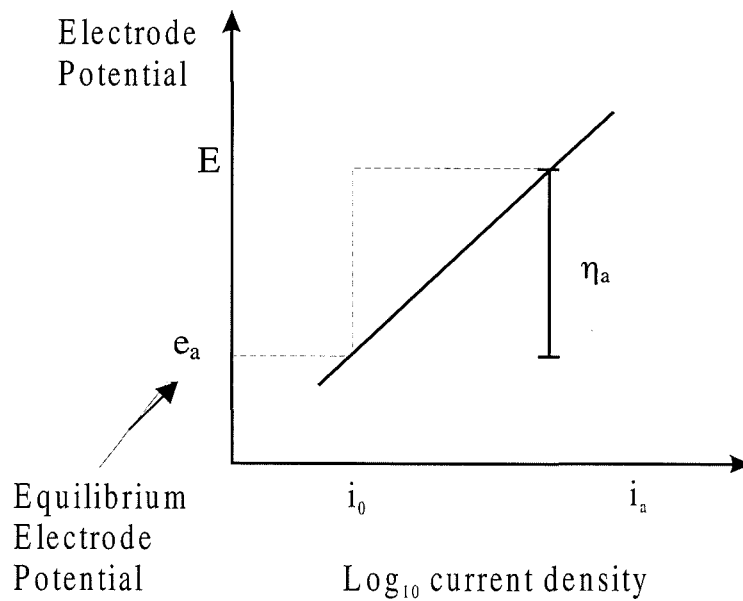


**Figure 2-1  $i_a/E$  plot for anodic reaction subject to activation polarisation**

The mathematical relationship corresponding to Figure 2-1 is:-

$$\eta_a = \beta_a \log_{10} (i_a/i_0) \quad (2.6)$$

where  $\beta_a$  (“Tafel constant”) is the gradient of the line and  $i_0$  is known as the “exchange current density” for the anodic reaction. Similarly for a cathodic reaction, the corresponding relationship is:-

$$\eta_c = \beta_c \log_{10} (i_c/i_0) \quad (2.7)$$

### 2.2.2 Concentration Polarisation

Concentration polarisation occurs where the progress of an electrode reaction is hindered by the rate of supply of reactants to or removal of products from a surface. For corrosion, concentration polarisation is significant mainly for the oxygen reduction reaction and it is usually negligible for anodic reactions because of the unlimited supply of metal atoms at the interface and relatively rapid diffusion of metal

ions away from the metal surface.

The potential change resulting from concentration polarisation can be expressed as:

$$\eta_{(\text{concentration})} = 2.3 \frac{RT}{nF} \log \frac{i_L - i}{i_L} \quad (2.8)$$

Where R is the universal gas constant, T is temperature, n is the number of electrons, F is Faraday's constant,  $i_L$  the limiting diffusion current density and i is the externally applied current density. This is shown graphically in Figure 2-2. The limiting current density,  $i_L$ , is a measure of the maximum reaction rate that cannot be exceeded because of a limited diffusion rate of ions or molecules through the bulk solution where:

$$i_L \equiv \frac{D_z n F C_B}{\delta} \quad (2.9)$$

$D_z$  is the diffusion coefficient of the reacting species, in this case oxygen;  $C_B$  is the concentration of oxygen in the bulk solution and  $\delta$  is the thickness of the diffusion layer.

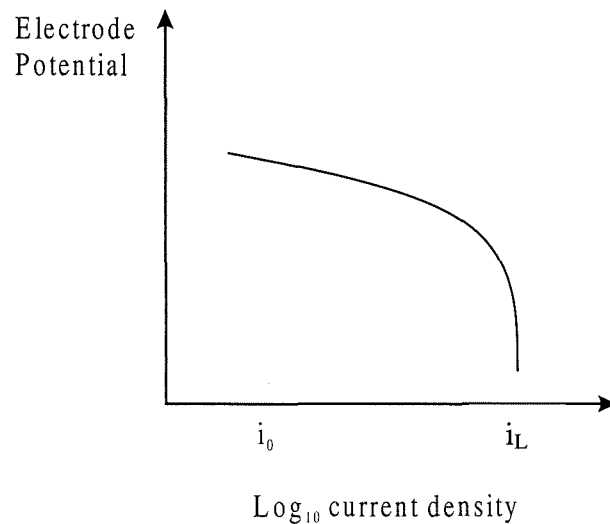


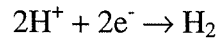
**Figure 2-2 Polarisation curve for cathodic reaction undergoing concentration polarisation.**

### 2.3 Mixed Potential Theory

When a metal is corroding in an aqueous solution, both the anodic



and the cathodic



half-cell reactions occur simultaneously on the surface. Each half-cell reaction has its own equilibrium electrode potential,  $E_o$ , and exchange current density,  $i_o$ , which represents a dynamic equilibrium corresponding to the balance of current caused by the forward and reverse reactions and which cannot exist separately on an electrically conductive surface. Each must polarise or change potential to a common intermediate value,  $E_{corr}$ , which is called the corrosion potential.

As the anodic and cathodic reactions polarise on the same surface, the half-cell electrode potentials (assuming activation polarisation dominates) change according to

$$\eta_a = \beta_a \log \frac{i_a}{i_o} \quad (2.10)$$

and

$$\eta_c = \beta_c \log \frac{i_c}{i_o} \quad (2.11)$$

until they become equal at  $E_{corr}$  as shown in. Also the rate of anodic dissolution,  $i_a$ , is identical to the corrosion rate,  $i_{corr}$ , in terms of current density, at  $E_{corr}$ , as indicated in Figure 2-3.

$$i_c = i_a = i_{corr} \quad (2.12)$$

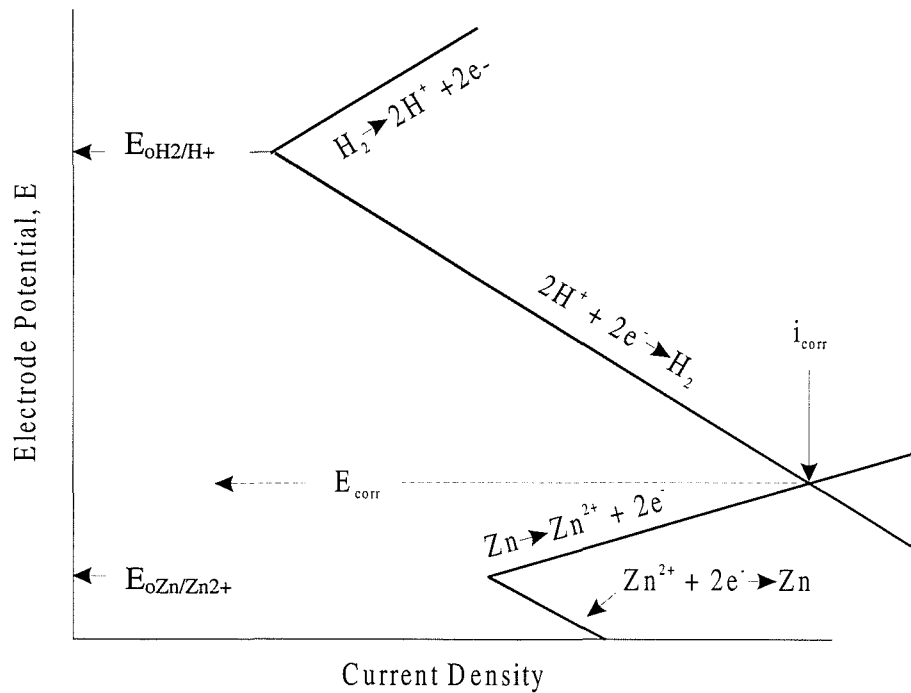


**Figure 2-3 Diagram of mixed potential referred to as the free corrosion potential  $E_{\text{corr}}$ .**

## 2.4 Potentiodynamic Polarisation

Polarisation tests involve the polarisation from the free corrosion potential,  $E_{\text{corr}}$ , by means of a potentiostat (Figure 2-4). A saturated calomel electrode (SCE), which is the reference electrode, provides a relative measure of the potential difference across the specimen. The inert counter electrode (normally platinum) acts as an electrical connection for current to flow between itself and the specimen when the potential is shifted from  $E_{\text{corr}}$ .

The potential shift can either be more positive than  $E_{\text{corr}}$ , in the anodic direction, or a negative shift from  $E_{\text{corr}}$ , in the cathodic direction and a potential current relationship can be plotted (Figure 2-5).

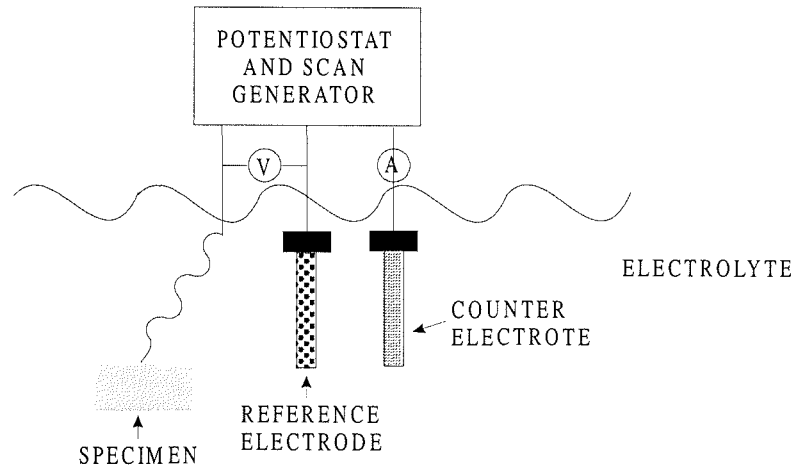


Figure 2-4 Three-electrode cell

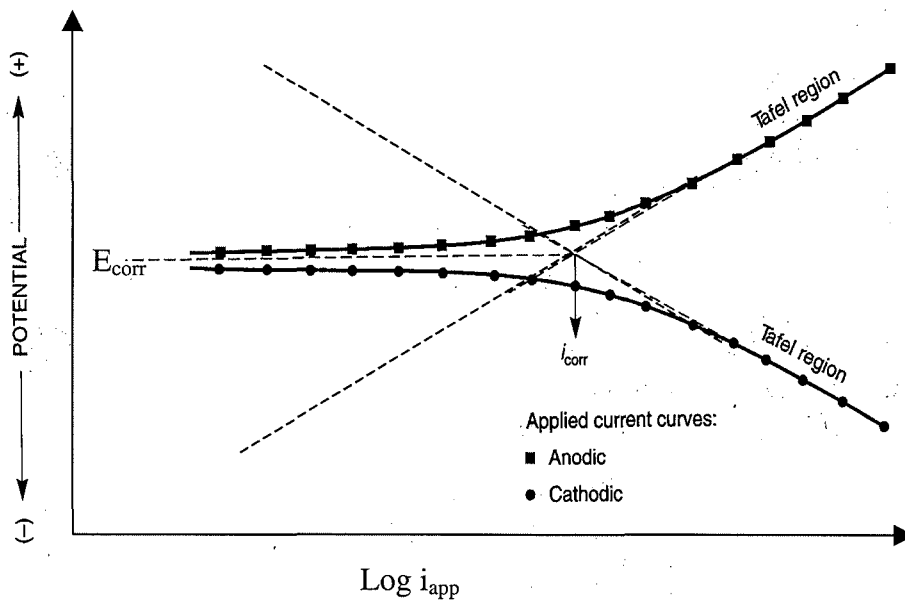


Figure 2-5 Schematic diagram showing anodic and cathodic polarisation

### 2.4.1 Cathodic and Anodic Polarisation

When an excess of electron flow (a current density  $i_{app}$ ) is applied to a corroding metal (Figure 2-6), it causes the electrode potential to shift negatively from  $E_{corr}$  to  $E$ . The negative potential shift,  $\epsilon_c = E - E_{corr}$ , is defined as cathodic overpotential. The excess of electrons suppresses the anodic reaction from  $i_{corr}$  to  $i_a$  and similarly increases the cathodic reduction reaction from  $i_{corr}$  to  $i_c$ . The difference in the increase in the cathodic reduction rate and the decrease in the anodic oxidation rate, is equal to the applied current:

$$i_{app} = i_c - i_a \quad (2.13)$$

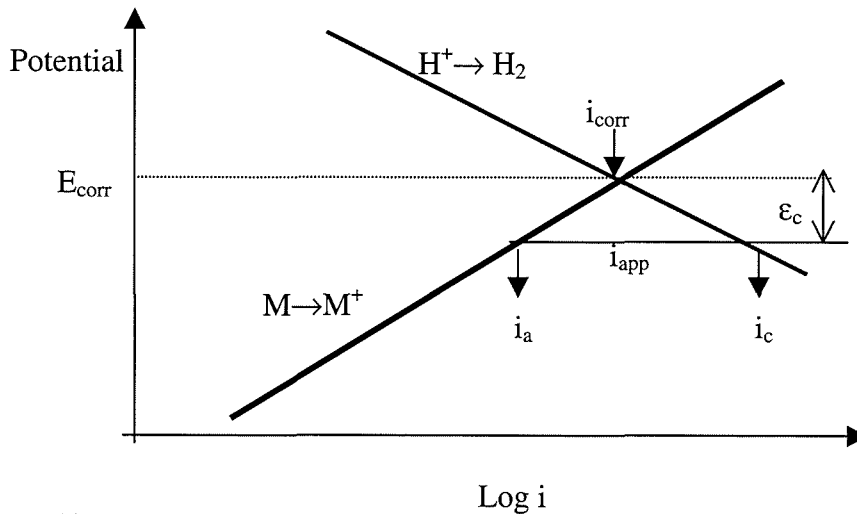


Figure 2-6 Schematic diagram showing cathodic overpotential of  $\epsilon_c$

Since the dissolution of metal is an anodic reaction, then suppressing this will reduce or prevent corrosion. This method of suppressing the current is the basis of impressed current cathodic protection. Lowering the potential to the reversible potential of the anodic reaction will stop the anodic dissolution. The surface of the cathodically protected object will provide sites for only cathodic corrosion reactions (either hydrogen evolution or oxygen reduction). Cathodic protection can be achieved by impressed current via a potentiostat or through a galvanic couple of a dissimilar metal of a more active metal i.e. sacrificial protection. The galvanic current cathodically protects the more noble metal and preferentially dissolves the more active metal. The electrons flow from the active sacrificial anode to the more noble cathode structure.

At low  $\epsilon_c$ ,  $i_c$  is only slightly higher than  $i_a$ , and  $i_{app}$  is very low. As  $\epsilon_c$  increases,  $i_c$  increases while  $i_a$  decreases until  $i_a$  becomes insignificant compared to  $i_c$ . Thus, the simulated cathodic polarisation curve of potential versus  $i_{app}$  is curved at low overpotential but becomes linear at higher overpotential (Figure 2-5). The linearity on a semilog plot is termed “Tafel behaviour” named after the German scientist who first discovered it.

Conversely (Figure 2-7), when electrons are drawn out of the metal, the deficiency causes the potential to change positively with respect to  $E_{\text{corr}}$ . The anodic reaction rate,  $i_a$ , is increased, while the cathodic reduction rate,  $i_c$ , is decreased, so that the applied current density is:

$$i_{\text{app}} = i_a - i_c \quad (2.14)$$

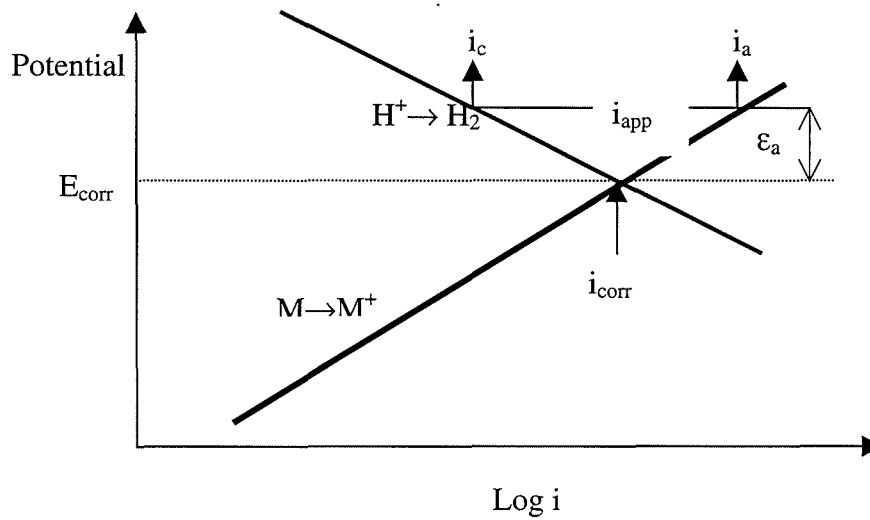


**Figure 2-7 Schematic showing anodic overpotential**

As the Tafel regions on the anodic and cathodic polarisation curves (Figure 2-5) are extrapolated back, the intersection of the two lines gives the corrosion current density,  $i_{\text{corr}}$ , from which corrosion rates can be determined.

#### 2.4.2 Linear Polarisation

Another method for determining the corrosion rate is linear polarisation. It involves manipulation of the Tafel equations to yield the following equation:

$$\frac{\Delta E}{\Delta I} \equiv \frac{B}{i_{\text{corr}}} \quad \text{and} \quad B \equiv \frac{\beta_a \beta_c}{2.3(\beta_a + \beta_c)} \quad (2.15)$$

where  $\Delta E/\Delta I$  is the slope of the polarisation plot within moderate shifts,  $\Delta E$ , of potential no more than about  $\pm 25\text{mV}$  from  $E_{\text{corr}}$  and  $\beta_a$  and  $\beta_c$  is the Tafel constant for the anodic and cathodic reactions respectively.

### 2.4.3 AC Impedance

Electrochemical Impedance Spectroscopy is employed to monitor electrochemical kinetics and has the advantage over classic DC methods that it involves only small electrochemical perturbations from  $E_{\text{corr}}$  and hence does not cause significant change in surface conditions of the specimen. The impedance  $Z(\omega)$  may be expressed in terms of real,  $Z'(\omega)$ , and imaginary,  $Z''(\omega)$ , components as in equation 2.16.

$$Z(\omega) = Z'(\omega) + Z''(\omega) \quad (2.16)$$

Where  $\omega = 2\pi f$  ( $f$  = frequency)

The impedance behaviour can be expressed in Nyquist plots of  $Z''(\omega)$  (on the real (Re) axis) as a function of  $Z'(\omega)$  (on the imaginary axis (Im)). The circuit for a simple parallel-connected resistance-capacitance circuit is shown schematically in (Figure 2-8). This circuit is often used to model a corroding surface. The solution adjacent to it has a varying concentration of ions, this is known as the double layer. The resistance due to the separation of charge across the solid metal interface and the outside edge of the double layer is known as the charge transfer resistance,  $R_p$  (this is the equivalent to the polarisation resistance). Therefore, determination of  $R_p$  enables quantification of the changes in the corrosion rate. There is also another resistance through the bulk solution,  $R_s$  and the double layer has a capacitance  $C_{dl}$ . This often an adequate representation of a simple corroding surface under activation control. The Nyquist plot (Figure 2-9) shows a semicircle, where (in the experiments conducted within this thesis) the frequency was decreased from 20000Hz to 0.2mHz and the resistance polarisation, which is inversely proportional to the corrosion rate, was determined.

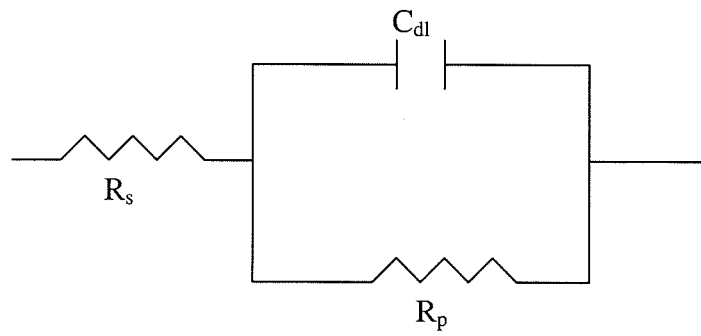


**Figure 2-8 Schematic Diagram of equivalent circuit**

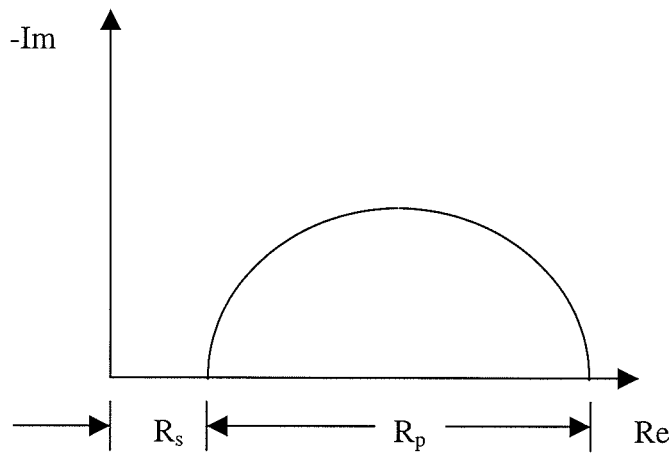


**Figure 2-9 Schematic diagram of Nyquist plot**

## 2.5 Forms of Aqueous Corrosion

Aqueous corrosion manifests itself as different forms depending on the environment, composition and the microstructure under attack

### 2.5.1 General and Localised Corrosion

General corrosion attack is more or less uniform over large areas of a component and is the most common form of corrosion. This happens when anodic and cathodic reactions are occurring simultaneously over the entire surface. Localised attack is when anodic and cathodic reactions occur at different parts of the surface due to surface inhomogenities or a variation in the availability of the cathodic reactants.

### **2.5.2 Pitting and Crevice Corrosion**

Pitting and crevice corrosion are localised forms of attack that result in relatively rapid penetration at small discrete areas. Pits may be initiated by a number of surface imperfections including sulphide inclusions, insufficient inhibitor coverage, and scratches in the coating or deposits of slag, scale, mud or sand. Stainless steels and nickel alloys with chromium are especially susceptible to pitting by breakdown of the passive film at isolated sites.

Crevice corrosion, as the name implies, occurs in the sheltered area of the crevice created by contact with another material e.g. where the other material may be a fastener (bolt, rivet, washer).

### **2.5.3 Galvanic (Bimetallic) Corrosion**

Bimetallic corrosion occurs when two dissimilar metals are coupled in a corrosive electrolyte. One metal suffers reduced corrosion while the other is preferentially corroded. The alloy with a more positive  $E_{\text{corr}}$  is the more noble metal which will suffer from less corrosion while the other with the less positive  $E_{\text{corr}}$  will preferentially corrode. Corrosion occurs at the junction of the two metals and decreases at points farther from the junction due to higher resistance through a longer electrolyte path.

### **2.5.4 Intergranular Corrosion**

As a result of segregation or depletion of passivating elements at grain boundaries, the grain boundaries or adjacent regions are often less corrosion resistant and preferential corrosion may occur. The corrosion may be severe enough so that the grains fall out of the surface.

### **2.5.5 Hydrogen Embrittlement and Hydrogen Damage**

Hydrogen entry into some metals and alloys can result in a significant reduction in ductility and load-bearing capacity, cause cracking and catastrophic brittle failure at stresses well below the yield stress of susceptible materials. There are many mechanisms whereby the above deleterious effects can occur including: hydrogen attack where, as the result of a reaction with carbon in steel to form methane results in decarburisation, voids and surface blisters. Voids are formed when atomic hydrogen migrates from the surface to internal defects and inclusions, where molecular hydrogen gas can nucleate generating sufficient internal pressure to deform and rupture the metal locally. Hydride formation can also cause embrittlement to metals; it increases the tensile strength and decreases ductility.

### **2.5.6 Dealloying and Dezincification**

In an alloy system the element which is more active (has a more negative  $E_{\text{corr}}$ ) compared to the major element will preferentially corrode by dealloying. The dealloying of brass, also known as dezincification, occurs when zinc, the more active metal, leaches out of brass leaving behind relatively pure porous copper with poor mechanical properties. Another example of dealloying, known as graphite corrosion or graphitisation, is the selective leaching of iron from grey cast iron, leaving behind a weak, porous network of inert graphite.

### **2.5.7 Stress and Corrosion Interaction**

Environmentally induced cracking (EIC) is a term used for the brittle mechanical failures as a result of the interaction of tensile stresses and a corrosive environment. EIC includes stress corrosion cracking (SCC), corrosion fatigue cracking (CFC) and hydrogen embrittlement, as explained above. SCC is the brittle failure at relatively low constant tensile stresses of a material exposed to a corrosive environment, while CFC is caused by fluctuating stresses. The result of these stresses is a crack within the microstructure of the material which can either be transgranular or intergranular.

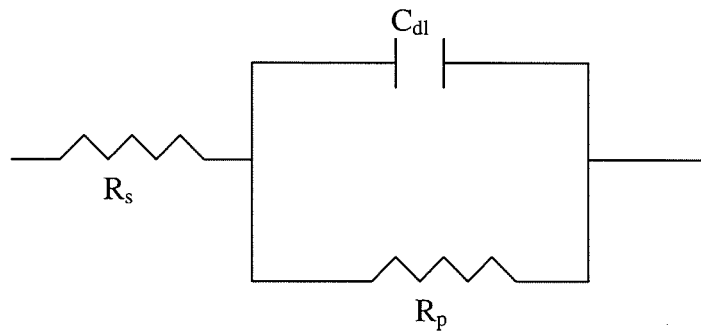


**Figure 2-8 Schematic Diagram of equivalent circuit**

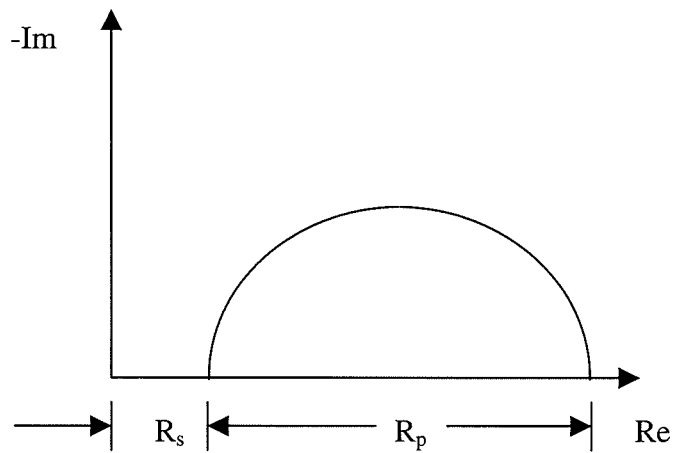


**Figure 2-9 Schematic diagram of Nyquist plot**

#### 2.4.4 General and Localised Corrosion

General corrosion attack is more or less uniform over large areas of a component and is the most common form of corrosion. This happens when anodic and cathodic reactions are occurring simultaneously over the entire surface. Localised attack is when anodic and cathodic reactions occur at different parts of the surface due to surface inhomogeneties or a variation in the availability of the cathodic reactants.

#### 2.4.5 Pitting and Crevice Corrosion

Pitting and crevice corrosion are localised forms of attack that result in relatively rapid penetration at small discrete areas. Pits may be initiated by a number of surface imperfections including sulphide inclusions, insufficient inhibitor coverage, and scratches in the coating or deposits of slag, scale, mud or sand. Stainless steels and nickel alloys with chromium are especially susceptible to pitting by breakdown of the passive film at isolated sites.

Crevice corrosion, as the name implies, occurs in the sheltered area of the crevice created by contact with another material e.g. where the other material may be a fastener (bolt, rivet, washer).

#### **2.4.6 Galvanic (Bimetallic) Corrosion**

Bimetallic corrosion occurs when two dissimilar metals are coupled in a corrosive electrolyte. One metal suffers reduced corrosion while the other is preferentially corroded. The alloy with a more positive  $E_{\text{corr}}$  is the more noble metal which will suffer from less corrosion while the other with the less positive  $E_{\text{corr}}$  will preferentially corrode. Corrosion occurs at the junction of the two metals and decreases at points farther from the junction due to higher resistance through a longer electrolyte path.

#### **2.4.7 Intergranular Corrosion**

As a result of segregation or depletion of passivating elements at grain boundaries, the grain boundaries or adjacent regions are often less corrosion resistant and preferential corrosion may occur. The corrosion may be severe enough so that the grains fall out of the surface.

#### **2.4.8 Hydrogen Embrittlement and Hydrogen Damage**

Hydrogen entry into some metals and alloys can result in a significant reduction in ductility and load-bearing capacity, cause cracking and catastrophic brittle failure at stresses well below the yield stress of susceptible materials. There are many

mechanisms whereby the above deleterious effects can occur including: hydrogen attack where, as the result of a reaction with carbon in steel to form methane results in decarburisation, voids and surface blisters. Voids are formed when atomic hydrogen migrates from the surface to internal defects and inclusions, where molecular hydrogen gas can nucleate generating sufficient internal pressure to deform and rupture the metal locally. Hydride formation can also cause embrittlement to metals; it increases the tensile strength and decreases ductility.

#### **2.4.9 Dealloying and Dezincification**

In an alloy system the element which is more active (has a more negative  $E_{\text{corr}}$ ) compared to the major element will preferentially corrode by dealloying. The dealloying of brass, also known as dezincification, occurs when zinc, the more active metal, leaches out of brass leaving behind relatively pure porous copper with poor mechanical properties. Another example of dealloying, known as graphite corrosion or graphitisation, is the selective leaching of iron from grey cast iron, leaving behind a weak, porous network of inert graphite.

#### **2.4.10 Stress and Corrosion Interaction**

Environmentally induced cracking (EIC) is a term used for the brittle mechanical failures as a result of the interaction of tensile stresses and a corrosive environment. EIC includes stress corrosion cracking (SCC), corrosion fatigue cracking (CFC) and hydrogen embrittlement, as explained above. SCC is the brittle failure at relatively low constant tensile stresses of a material exposed to a corrosive environment, while CFC is caused by fluctuating stresses. The result of these stresses is a crack within the microstructure of the material which can either be transgranular or intergranular.

## Chapter 3

### Literature Review

#### 3.1 Thermal Spray Technology

##### 3.1.1 Introduction

The current global economic value of the thermal spray market (\$1.35 billion<sup>1</sup>) reflects the popularity of thermally sprayed coatings within many industrial sectors to combat deterioration due to corrosion and other wear-related processes. These include the petroleum<sup>2</sup> industry where they are used to prevent corrosion cracking in liquid petroleum gas tanks. The paper and pulp industry<sup>3,4,5</sup> primarily use thermal spray coatings for their wear resistant properties to increase the lifespan of the blades, rolls and looms. The aerospace<sup>6</sup> industry relies extensively on coatings which can withstand wear and oxidation at temperatures in excess of 800°C. Their use is also expanding into biomedical applications<sup>7</sup> where the coating's purpose is to increase the compatibility and corrosion resistance of implants. The adverse effects from exposure to hexavalent chrome has promoted the increased use of HVOF thermal spray coatings where components were previously chrome plated, for example on aircraft landing gear<sup>8 9</sup>.

In thermal spraying there is a wide selection of processes and materials available which have a minimal amount of impact on the environment in comparison with conventional electrolytic plating. All thermal spray techniques involve similar processes; a material in the form of a powder, wire or rod is melted into a molten substance and accelerated onto a grit-blasted surface where it solidifies and binds to the surface.

In the following paragraphs some of the common processes are described and then a comparison is made with the process of most relevance in this work;

namely the HVOF process.

### **3.1.2 Flame Spraying**

Flame spraying can use either a powder feed or a wire feed. The velocity of the powder in the flame is in the range  $80\text{-}100\text{ms}^{-1}$  and reaches temperatures of up to  $3350\text{K}$ . It can deposit coatings up to  $2500\mu\text{m}$  thick but they can contain a large amount (10-20%) of porosity. A post spray fusion treatment of NiCr alloys with boron or silicon fluxing agents can be used to reduce the porosity and increase the bond strength of the coating.

### **3.1.3 Atmospheric Plasma Spraying (APS)**

Patented by Gage et al (1962)<sup>10</sup>, the plasma gun uses argon or argon and hydrogen, helium or nitrogen as a fuel to form the plasma that can reach temperatures of  $14,000\text{K}$  and velocities of  $800\text{ms}^{-1}$ . The molten powder can be sprayed to form a coating (typically  $50\text{-}500\mu\text{m}$  thick) with porosity levels in the range 1-7%.

### **3.1.4 Arc Spraying (AS)**

Consumable feed wires are also used as electrodes in the electric arc and are traditionally zinc and aluminium but wires cored with tungsten carbide are also used. The arc can generate temperatures of up to  $6100\text{K}$  and the molten particles can reach velocities of  $150\text{ms}^{-1}$ . A jet of gas atomises the melted particles and propels them to the substrate. The coating can be  $100\text{-}1500\mu\text{m}$  thick and porosity levels are in the range 10-20%.

### **3.1.5 Detonation Gun Spraying**

Detonation gun spraying, developed in the USA in the 1950s, is also known as flame shock spraying. The oxy-acetylene fuel is mixed with the powder and when ignited sends a detonation wave which accelerates the powder to  $750\text{ms}^{-1}$

at 4500K. The coatings are typically 300µm thick with a low porosity level: 0.5-2%.

### **3.1.6 Vacuum Plasma Spraying (VPS)**

Developed in the 1970s, the VPS consists of plasma torch with a vacuum nozzle where the powder is fed via a port. This enables the spraying of reactive material<sup>11</sup>. With a careful choice of spray parameters, the coatings can be pore-free but generally porosity is less than 2% within coatings of 150-500µm.

### **3.1.7 Controlled Atmosphere Plasma Spraying (CAPS)**

The CAPS technique can be applied to a spraying technique which is neither air nor a vacuum e.g. plasma spraying into a chamber of inert gas when the sprayed coating consists of reactive metals. It can also provide higher environmental pressures that will reduce porosity levels. Another variable which can be controlled is the substrate temperature.

### **3.1.8 High Velocity Oxy-Fuel Spraying (HVOF)**

The HVOF torch was developed in the early 1980s by James Browning<sup>12</sup> through Deloro Stellite with the Jet Kote process. The principles behind HVOF spraying (Figure 3-1) are that the fuel (propylene, propane, hydrogen or acetylene) is burnt with oxygen at high pressures. The product is ignited and combusts with the resulting flame, expanding supersonically through the nozzle. The powder is injected downstream of the combustion chamber and is melted and accelerated by the flame. The advantages of the HVOF system over other conventional methods of spraying are its higher exhaust velocities of 1380-2930ms<sup>-1</sup> and the lower temperatures, 1900-3000K, which give the added benefit of the sprayed carbides retaining their properties. The powder size distribution is quite important as very fine particles typically in the range 5-45µm can deposit on the walls of the nozzle. More importantly, the porosity level of these coatings can be

less than 1% within a coating of typical thickness 100-300 $\mu$ m.

There are many designs of HVOF guns. The Jet Kote II from Stellite<sup>12</sup> has a system whereby the fuel/oxygen mixture is burnt separately then powder is injected into a cylindrical chamber by a carrier gas stream. Metco's Diamond Jet has a stream of powder and carrier gas injected into an axial confined combustion zone. The Hobart Tofa system uses liquid fuel which creates higher combustion chamber pressures and the powder is fed in radially at the throat of the combustion chamber/nozzle.

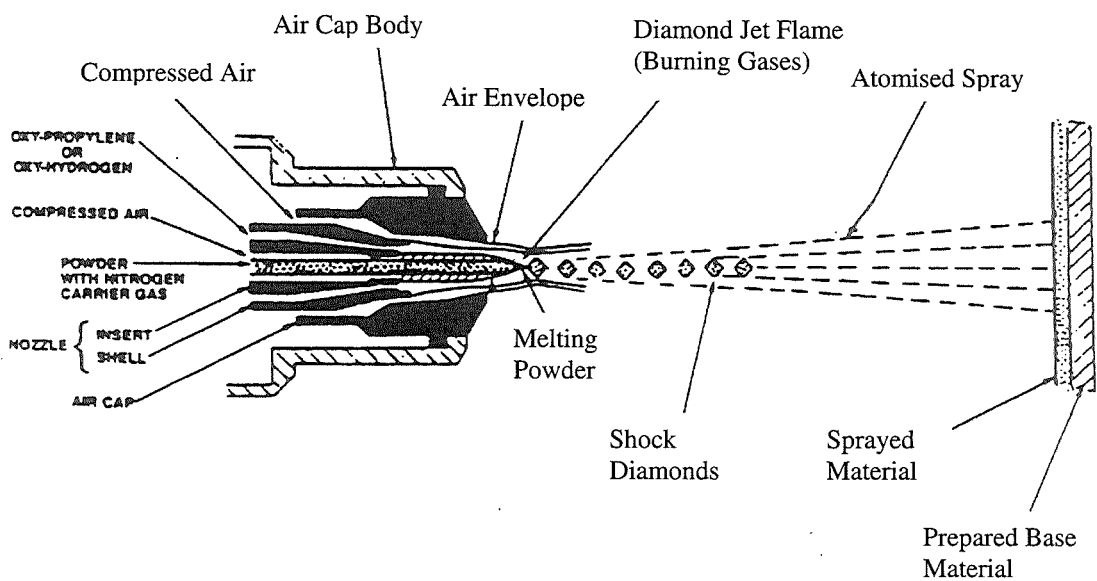


**Figure 3-1 Schematic diagram of a HVOF gun**

In summary, the HVOF spraying method results produces coatings with porosity levels less than 1% (Table 3-1) whereas other thermal spray techniques have much higher levels, up to 20%. These low porosity levels are associated with the combination of higher flame velocities and lower flame temperatures in comparison with flame spraying, APS, AS, D-Gun spraying and VPS. HVOF is a recent addition to the thermal spraying field<sup>13</sup>. It operates on a similar basis to the HVOF except that it uses air instead of oxygen. This results in the powder particles being exposed to lower temperatures and hence a low degree of phase transformation. Porosity levels in HVOF coatings have been measured at 4-16%.

Process	Flame Velocity	Flame Temperature	Coating Thickness	Porosity Level
Flame Spraying	80-100ms <sup>-1</sup>	3350K	2500μm	10-20%
APS	800ms <sup>-1</sup>	14000K	50-500μm	1-7%
AS	150ms <sup>-1</sup>	6100K	100-500μm	10-20%
Detonation Gun Spraying	750ms <sup>-1</sup>	4500K	300μm	1.5-2%
VPS	1500-3500ms <sup>-1</sup>	10000-15000K	150-500μm	<2%
HVOF	1370-2930ms <sup>-1</sup>	1900-3000K	100-300μm	<1%

**Table 3-1 Comparison of some process parameters in thermal spraying<sup>10</sup>**

### 3.2 Powder Manufacture

Powder manufacturing methods have an effect on the inherent coating properties<sup>14</sup>. There are four methods commonly used in the synthesis of thermal-sprayed powders<sup>10</sup>. The atomisation method is most commonly used for metals or alloys. A *gaseous atomising* medium produces more spherical particles whereas a water medium produces angular particles. A more versatile method of powder manufacture is the *agglomeration* method since it can produce ceramics, carbides and some metals. *Compositing or cladding* combines two dissimilar materials to form a single particle. The particle consists of a core material coated with either a dense or uniform outer layer e.g. an aluminium core coated with nickel. *Casting and crushing* is used to produce ceramics, carbides and brittle alloys.

Tungsten carbide can be prepared by a solid state reaction with fine powders of tungsten and carbon powders producing a fine powder, by the Thermit<sup>15</sup> process or from cast tungsten carbide produced by carbon resistance melting. These are then crushed to the desired grain size, mixed with an organic binder and cobalt and subsequently sintered or fused with cobalt and crushed to form a tungsten-

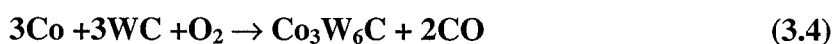
carbide-cobalt composite.

### 3.3 WC-Cermet Coatings – Microstructure and Compositional Changes

As with all cermet coatings, the structure on which WC-cermet coatings is based is that of cemented carbides. That is, a hard, fine carbide compound is encased within a metallic matrix. It has been well-documented<sup>16</sup> that the chemical composition of the sprayed coating alters somewhat from that of the feedstock powder. Nerz<sup>16</sup> et al. investigated two fused and crushed, tungsten-carbide coatings with 12% cobalt, one sprayed with a HVOF gun and one with a high energy plasma (HEP) gun. While the HVOF coating retained a larger percentage of tungsten mono-carbide crystals (WC) than the HEP coating, X-ray diffraction (XRD) showed that  $W_2C$  and elemental tungsten were present associated with the decarburisation of WC. No substantial amounts of sub-carbides i.e.  $Co_3W_3C$ ,  $Co_6W_6C$ ,  $Co_2W_4C$  were identified. The XRD trace showed a broad maximum in the 38 to 46 two-theta range in the XRD, from both the HVOF and HEP sprayed coatings, which is indicative of a microcrystalline or amorphous phase. Differential thermal analysis (DTA) was carried out on the coatings and subsequent XRD results concluded that the broad maxima indeed indicated the presence of an amorphous phase,  $Co_6W_6C$  and  $Co_2W_4C$ . These phases were created by diffusion of C and W into Co followed by rapid solidification. It was found that coatings produced by HEP contained more amorphous phases than the HVOF sprayed coatings and after DTA when these eta-phase carbides had precipitated out, the coatings showed an increase in wear resistance. However, in a study Li<sup>17</sup> et al found the presence of only one complex carbide,  $Co_6W_6C$ , and postulated that the second carbide found by Nerz<sup>16</sup> et al. was mistaken for the production of metallic cobalt, the complex carbide,  $Co_6W_6C$ , and a substantial amount of graphite.

In a comparison of air sprayed plasma (ASP) and an HVOF sprayed WC-Co coating, Provot<sup>18</sup> et al. also investigated XRD patterns of the powder and the sprayed coating and found new phases in the sprayed coatings at the expense of the metallic cobalt peaks from the powder and a broad maximum between the

main peaks of WC on the coating. Although the phases were not identified, they thought that the carbon can be diffused into the matrix as per the following reactions:



Evaluation of the two coatings' microstructure showed that the HVOF sprayed coating had a better quality than the ASP coating due to the finely distributed carbides and less porous structure.

Microstructure and phase transformations were studied on WC-17Co HVOF sprayed coatings sprayed with different fuels (diesel and oxygen, hydrogen, propylene, propane and acetylene) and with powders produced by sintering or spray drying<sup>19,20,21</sup>. All the coatings underwent phase transformation during spraying, detected by transmission electron microscopy (TEM) or XRD, forming  $W_2C$  and amorphous phases:  $Co_6W_6C$ ,  $Co_7W_6$  and  $Co_3W_3C$ . These amorphous phases were also detected by Guilemany<sup>22</sup> et al in a WC-Ni HVOF sprayed coating where WC particles decomposed and were taken into solution with the molten Ni. It was calculated<sup>19</sup> that up to 1.5 $\mu$ m of the WC particles become molten and go into solution with the matrix but that when powder is sintered more WC survives<sup>20</sup>. The coating sprayed with hydrogen had a very dense structure but retained little WC while the coating sprayed with acetylene had a porous structure and retained more WC i.e. the proportion of retained WC decreases as the gas power increases. Also more retained WC increased the wear resistance of the coatings when tested with a pin on disc or rubber wheel test.

In a comparison of HVOF and HVAF (sprayed with air and kerosene) WC-Co-Cr sprayed coatings, by Jacobs<sup>23</sup> et al, XRD analysis shows that only during

HVOF spraying does phase transformation occur i.e., the XRD patterns for the powder and the sprayed coating from the HVAF, are the same. In agreement with Coulson et al, they found that the outer edges of the WC particles are prone to dissolution reactions creating a “segregated” matrix microstructure i.e. areas which are rich in tungsten. In some areas the WC has completely dissolved leaving behind a tungsten rich binder phase and  $W_2C$  crystals. Subsequent wear tests, by pin-on-disc method, revealed that the HVAF coating was harder and more wear resistant than the HVOF coating.

In general, the favoured structure for a WC-Co HVOF sprayed coating, is one where there is minimal decarburisation of the WC particles to retain their good wear resistance and minimal W-Co-C amorphous phases which are detrimental to wear properties. The coating should have an even distribution of the hard phase particles and negligible porosity. To behave like an aggregate cermet<sup>24</sup>, and have higher hardness values, a finer distribution of WC particles is required. However, this tends to enhance amorphous phase formation<sup>16</sup>.

### **3.4 Corrosion of Cermet Coatings**

This section initially reviews the studies carried out on early thermally sprayed coatings where the quality, in terms of mainly its porosity, had not been optimised and hence the corrosion studies focused mainly on how effective the coating was at providing protection, or not, to the substrate. These initial coatings had high levels of porosity but developments in thermal spray technology have increased the quality of the coatings, so that provided good quality control is maintained, porosity is no longer a major issue in routinely sprayed HVOF coatings. The focus of corrosion studies has now moved onto the inherent corrosion properties of the coatings.

Initial electrochemical studies of  $Cr_2O_3$  plasma sprayed coatings<sup>25,26</sup> showed that interconnected porosity within the sprayed coating decreases the corrosion resistance of the system even although  $Cr_2O_3$  is generally unreactive. The pores allowed the aqueous solution to penetrate the coating, attacking the substrate,

(316L and Inconel 625) causing crevice corrosion at the coating/substrate interface. While no evidence of corrosion on the Cr<sub>2</sub>O<sub>3</sub> coating was observed, the corrosion behaviour was dominated by the corrosion characteristics of the substrate. Post spray sealing with an epoxy sealant was effective in closing the pores to the substrate, however there is potential for them to open up after the surface layer has worn away. In another study corrosion tests of plasma sprayed coatings<sup>27</sup>; Cr<sub>3</sub>C<sub>2</sub>+NiCr, Inconel 625 and Cr<sub>3</sub>C<sub>2</sub>+Inconel 625, showed that interconnected porosity still affected corrosion behaviour except on the Inconel 625 coating where it was effective in protecting the substrates from the corrosive media and the corrosion rate was therefore reduced. Post-test examination showed that the NiCr phase of the coating exhibited pitting and crevice corrosion and the Cr<sub>3</sub>C<sub>2</sub> phase in the coating remained unaffected.

Preliminary studies on plasma sprayed coatings referred to in the previous paragraph showed the potential for thermally sprayed coatings to offer corrosion protection to low grade alloy substrates but highlighted the need for a more homogeneous coating with lower porosity so that the corrosion characteristics of the system was not dependant on the ability of the fluid to penetrate to the substrate. With the development of HVOF spraying, coatings were of higher quality i.e. reduced porosity, and showed potential to provide a barrier against corrosion of the substrate.

A study by Hofman et al<sup>28</sup> investigated the corrosion resistance, which they determine by the number of oxide inclusions, of stainless steel coatings sprayed by HVOF and arc spraying. They mechanically removed the coating from the substrate and found that the electrochemical response from the removed coatings was similar to that when applied to a substrate when the coating was above a critical thickness. At lower thickness interconnected porosity facilitated a route for the fluid to penetrate. They found that arc sprayed coatings were less corrosion resistant than HVOF sprayed coatings, due to the higher porosity levels, but improved when sprayed within an inert (Argon) atmosphere.

Extensive studies by Neville and Hodgkiess<sup>29, 30, 31, 32</sup> on several high quality, i.e. low porosity, HVOF and oxy-acetylene thermally sprayed coatings were focused

on assessing the inherent corrosion behaviour of the coatings in a saline aqueous environment without interference from the substrate (stainless or carbon steel). The mechanisms of corrosive attack were identified in relation to the complex microstructures of the coatings and the effects of galvanic interactions within the coating system on a micro scale. The work also extended to include macro-galvanic interactions between the coating and different substrate materials by the study of cross-section specimens that exposed both coating and substrate simultaneously<sup>33</sup>.

The extent of galvanic interactions were assessed<sup>33 32</sup> between an HVOF Inconel 625 coating, oxy-acetylene vacuum fused W-C-Co-Cr and Ni-Cr-C-B coatings with carbon steel and stainless steel substrates. This study involved simulation of a coating/substrate couple by exposing a polished cross-section of a coated component and revealed that the carbon steel substrate acted as the anode and suffered accelerated galvanic corrosion while reducing the rate of corrosion of the coatings, however this varied for every coating/substrate combination. Near to the interface of the coating/substrate (stainless steel and carbon steel) on the WC-Co-Cr both the HVOF and oxy-acetylene sprayed coating, there was excessive “knifeline” attack tunnelling into the coating indicative of the vulnerability of the coating at the edge of a coated component. This was more extensive on the Ni-Cr-Co-Cr coating where the galvanic currents between it and the carbon steel were found to be higher than with the WC-Co-Cr coating. As well as these macro-galvanic interactions, although difficult to quantify, were found to occur between the hard phases and the metallic matrix within the coating. This resulted in localised attack at the interfaces and extensive removal of the hard phase as the attack progressed.

The corrosion behaviour, determined by anodic polarisation, of a HVOF WC-Co-Cr coating has been found<sup>31</sup> to be quite complex. Whereas the substrate (stainless steel) was passive over a large range of potentials, the coating had a rapid rise in current up to 100 $\mu$ A then a subsequent stabilisation and then a final breakdown. When similar experiments were conducted after two weeks and one month the stabilisation current increased and the breakdown potential decreased. The

mechanisms of attack were found to be crevice corrosion at a lacquer interface and general etching over the surface. SEM micrographs found material loss was due to the dislodgement of the hardphase. At 50°C, the anodic polarisation scan showed a much higher increase of current with potential and subsequently more severe general etching on the surface with some localised pitting attack. After immersing the WC-Co-Cr HVOF sprayed coating in seawater for one month, the interface of the matrix and the tungsten carbide hardphases exhibited signs of channelling attack. Some areas the hardphases were protruding and in others the hardphase was completely removed.

Numerous studies in the literature consider ways to further enhance the corrosion resistance of the coatings, by sealing pores, via post spray sealing through various methods. The following paragraphs report conflicting findings on whether sealing is beneficial or not.

The corrosion behaviour of HVOF WC-Co-Cr and WC-Ni-Cr-B-Si coatings was studied<sup>29</sup> in the as-sprayed state and after being sealed with a polymeric sealant in a saline environment. Both the sealed and unsealed coating displayed passive behaviour akin to that of stainless steel in seawater. However, the unsealed coating had a lower breakdown potential, where the current rises quickly, signifying anodic activity. No improvement in corrosion resistance was found from either coating when long term immersion tests were carried out.

In contrast with others, Lugscheider<sup>34</sup> et al found that post spray sealing with polycondensing phenolic resin, improved the corrosion resistance of a HVOF and APS sprayed WC-Co-Cr although the anodic polarisation tests were conducted in acidic and alkaline environments. However, the improvement is attributed to the decrease in the area when pores are sealed given that the corrosion current density is calculated from the nominal surface area. Additionally, it was found that the HVOF sprayed coating had better corrosion resistance, in comparable environments, than the APS sprayed coating, primarily due to the increased chromium content in the HVOF coating's matrix.

Oxy-acetylene sprayed coatings (Co-Cr-W-B and Ni-Cr-B), which were vacuum

fused in a furnace in an attempt to consolidate the coating, were investigated<sup>32</sup>. The microstructures of the two coatings were very different and this affected the way the two coatings corroded. Although they both had superior corrosion resistance compared with that of the active EN 8 carbon steel substrate, they both displayed some form of corrosive attack. While the cobalt-based coating displayed signs of crevice attack at the coating/lacquer interface after 6 weeks immersion in seawater, the nickel-based coating had crevice attack after only 3 weeks immersion. In addition, the cobalt coating showed evidence of pitting attack after 1 month to the extent that the microstructure could be seen clearly due to preferential attack of the matrix. It was found that the attack initiated at the Cr-rich grain edges and propagated into the Co-rich matrix. The Ni-based coating was not as prone to pitting attack, but more general attack as well as the crevice corrosion. This was found to be the result of intergranular corrosion attack where, at the crevice regions, the matrix had dissolved leaving a “skeletal structure” of hard phase particles.

A study of a HVOF sprayed Ni-Cr-Si-B coating<sup>35</sup> in the as sprayed condition, vacuum-sealed and vacuum-fused conditions was conducted and microstructure and corrosion resistance in seawater and 3.5% seawater solution was assessed. It was found, in agreement with the previous studies mentioned, that post spray sealing was neither detrimental nor beneficial to the corrosion behaviour nor did it alter the microstructure. However, vacuum fusion of the coating did have a big effect on the coating different microstructure. In addition to the hard phases,  $\text{Cr}_{23}\text{C}_6$ , present in the as-sprayed coating, there were additional hard phases of molybdenum borides in the vacuum fused coating. In general the hardphase particles were larger. The fusion process also eliminated the boundaries of the splat particle to give a more homogeneous coating. Despite the changes to the microstructure, the vacuum fused coating did not exhibit any significant improvement in corrosion resistance, although the mechanisms of attack differed. In the sprayed (and sealed) coating there was localised attack at the splat particle boundaries postulated to be micro-crevice corrosion. Some crevice corrosion was also apparent near the coating/lacomit sealant interface whereas in the vacuum fused coating there was micro pitting as a consequence of the hard phase loss.

Other workers have investigated other thermal spraying variables, such as coating chemistry and spraying parameters to improve on the inherent corrosion resistance of the coating. Kretschmer et al<sup>36</sup> studied a series of nickel based flame sprayed coatings with varying amounts of molybdenum. They found that the corrosion resistance improved with increasing molybdenum content as it has an ability to preferentially form borides and carbides leaving more chromium in the dissolved state to protect against corrosion. Furthermore, initial tests with similar HVOF sprayed coatings, indicated a further increase in corrosion resistance.

The other aspect of improving the corrosion properties of thermally sprayed coatings was investigated by Harvey et al<sup>37</sup>. They carried out anodic polarisation tests on HVOF sprayed Inconel 625 coatings which were sprayed using different settings on the HVOF gun. The variables that had the most prominent effect were the oxygen to fuel ratio and the combustion chamber size. An increase in oxygen is thought to increase the amount of chromium oxide formed during spraying and decrease the corrosion resistance of the coating. No explanation was given for the effects from decreasing the chamber size to give better corrosion resistance. This is most likely due to the residence time in the chamber and the reactions occurring within.

Guilemany et al<sup>38</sup> investigated the corrosion properties of HVOF sprayed WC-Co and TiC/Ni-Ti on commercial steel (UNS G41350). And found that they both had a better corrosion resistance than the steel and also that the TiC/Ni-Ti coating was better than the WC-Co coating. The corrosion attack in the WC-Co coating initiated at the WC/Co interface whereas the Ni-Ti matrix was uniformly corroded.

Other TiC based HVOF coatings were investigated<sup>39</sup>; TiC+Ni (where the powder had been previously coated with Ni), (TiW)C+22%Ni and (TiW)C+11%Ni. It was ascertained that the TiC+Ni coating had the best corrosion resistance followed by the (TiW)C+11%Ni and the remaining one was least corrosion resistant. In all cases there was a layer of iron oxide between the coating and substrate after corrosion as well as some on the surface of the coating involving corrosion of the substrate and transporting the products to the surface. When this

was brushed off, it was found that the principal mechanism of corrosion was uniform matrix dissolution in all cases but higher levels of nickel reduced the corrosion rate. In a comparison with other commercially available HVOF coatings; WC-Co, WC-Co-Cr and Inconel, these TiC coatings had a polarisation resistance up to 18 times higher.

The quality of thermal spray coatings have improved insofar as porosity levels have decreased and the coatings can now act as effective barriers against corrosion. Recent research has concentrated on assessing the inherent corrosion properties of the coatings as opposed to the initial studies where there was interference from galvanic interactions of coating and substrate under study. Post spray sealing does not seem to provide adequate resistance to corrosive attack on a long-term basis. It would appear that the way to improve these coatings' corrosion resistance is to expand our knowledge on the mechanisms of corrosive attack and to develop the coatings chemistry in line with those of high-grade alloys and to achieve the optimum spraying parameters for each coating.

### **3.5 Erosion-Corrosion**

Erosion-corrosion describes material degradation which occurs due to the combination of corrosive deterioration and mechanical wear of the material. A moving liquid (containing solids or free from solids<sup>40</sup>) can increase the corrosion rate of a material due to increased mass transfer<sup>41</sup>. Initial postulations that wall shear stresses can be a correlating factor for the effect of flow on erosion corrosion<sup>42</sup> have been refuted by Poulson<sup>43</sup> who claims that the stresses only aid corrosion product removal. This erosion-corrosion attack can occur within pipes, elbows, turbines, pumps and other structural features that alter flow direction and induce turbulence. Erosion-corrosion takes the form of grooves, horse-shoes, waves, gullies and depressions on the surface of the material. Another form of erosion-corrosion is cavitation corrosion which involves the initial form of vapour bubbles at locations where the pressure falls beneath the vapour pressure of the liquid followed by implosion of the bubbles on equipment surfaces at sites where the local pressure exceeds the vapour pressure.

Fretting is another wear process which can be enhanced by corrosion. The erosion is provided by repeated small movements (or vibrations), between the corroding metal and another contacting solid under load. The motion abrades surface oxide films off the metal surface, exposing the reactive metal to oxide formation.

Flow induced corrosion is the term often used to describe the enhancement of corrosion rates due to convective effects. Erosion-corrosion, in contrast, is often used to describe the situation where additional mechanical effects occur. Erosion-corrosion can occur under many hydrodynamic regimes but the one of most interest to this study is that of impingement of a surface by a liquid or liquid-solid jet. To appreciate the phenomenon of jet impingement the hydrodynamics of the jet should be considered.

### 3.5.1 The Hydrodynamics of a Submerged Turbulent Jet

The flow geometry in a submerged impinging jet is complex. The velocity within the liquid jet varies with the diameter of the nozzle and height of the nozzle from the wall as shown in Figure 3-2<sup>44</sup>. This produces variations in the wall shear stress. Rajaratnam<sup>44</sup> reported that the wall shear stress increases linearly from the centreline with  $r$  to a maximum at  $r/H \cong 0.14$  then subsequently decreases. The maximum shear stress ( $\tau_m$ ) can be found from:

$$\tau_m \equiv \frac{0.16\rho U_o^2}{\left(\frac{H}{d}\right)^2} \quad (3.7)$$

Giralt and Trass<sup>45</sup> have proposed that the wall shear stress ( $\tau_w$ ) follows the equation

$$\tau_w \equiv \frac{0.0447\rho U_o^2 \text{Re}^{-0.182}}{\left(\frac{r}{d}\right)^2} \quad (3.8)$$

in the region away from the stagnation point.

Where ' $U_o$ ' is the nozzle exit velocity, ' $d$ ' is the nozzle diameter, ' $r$ ' is the distance from the stagnation point, ' $\rho$ ' is the liquid density, ' $\tau_w$ ' is the shear stress and ' $H$ ' is the distance of the plate away from the nozzle.

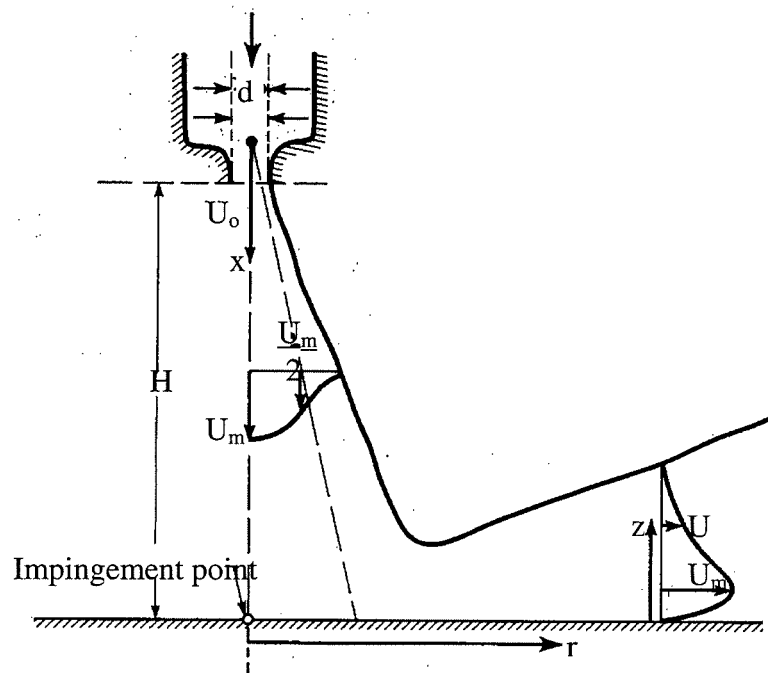


**Figure 3-2 Radial Wall jet produced by a submerged impinging circular jet.<sup>44</sup>**

Efrid et al<sup>46</sup> have correlated the wall shear stress, which they define as “a force within the flowing fluid rather than a force on the wall from the flowing fluid,” with the corrosion rate ( $I_{corr}$ ), where

$$I_{corr} \equiv a\tau_w^b \quad (3.9)$$

Where the coefficient  $a$  and exponent  $b$  are dependant on the specific environment and solution chemistry. This correlation was found in pipe flow, jet impingement and a rotating cylinder.

### 3.5.2 ‘Flow Induced Corrosion’

In flow induced corrosion, the following parameters are important: velocity,

hydrodynamics, surface and shear stress. It has been ascertained<sup>47</sup> that mass transfer has the most dominant hydrodynamic effect. Mass transfer can involve ions and molecules reaching the surface by diffusion due to a concentration gradient i.e. the higher the concentration of reactive species, the higher the mass transfer. If there is any flow, then the reactants are transported by convection, reach the surface quicker and the reaction rate is increased. Mass transfer has been also found to be dependant on surface roughness<sup>48</sup>, whereby it increases with increasing surface roughness. Mass transfer coefficients are often expressed as the non-dimensional Sherwood number,

$$Sh \equiv Const \times Re^x Sc^y \quad (3.10)$$

a combination of the Reynolds number ( $Re = V/d\gamma$ ), incorporating inertia and friction forces and the Schmidt number ( $Sc = \gamma/D$ ), incorporating momentum and mass transfer. Equation 3.10 can be simplified into

$$C \approx u^a \quad (3.11)$$

where  $C$  is the corrosion rate (mm/year) and  $u$  is the flow velocity and the exponent  $a$  is indicative of the rate controlling mechanism. Where  $0.03 < a < 1$ , corrosion is controlled by transport processes. When  $a > 1$  mechanical deterioration of the material is occurring<sup>49</sup>.

Heitz<sup>41</sup> categorised the main characteristics of flow-induced corrosion into four areas as shown in Figure 3-3. These included mass transfer, as explained earlier and phase transfer, where corrosion is dependent on the corrosive phases in a multiphase fluid. Also, erosion-corrosion where mechanical influences such as shear stresses, surface roughness, concentration of reactive species, high flow velocities, and particle impacts combine with corrosion processes to enhance material damage. Cavitation corrosion can be distinguished from the others by the sharp-edged craters on the metal surface.

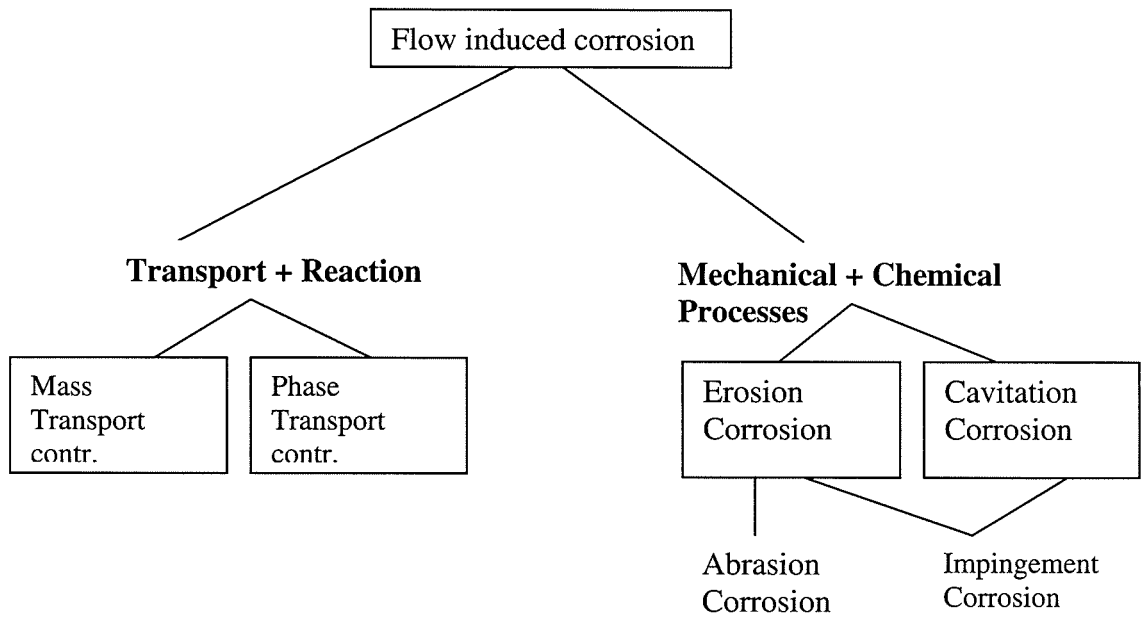


**Figure 3-3 Classification of flow induced corrosion**

Exposure to flowing conditions can be both beneficial and detrimental<sup>49</sup> depending on the hydrodynamic regime, the fluid and the material. Beneficial effects can result from prevention of solids settling on the surface which may promote localised attack and the passivation of alloys through supply of oxygen from the fluid to the surface. Detrimental effects exist when the surface layers are deteriorated, such as the removal of passive films or by direct attack (electrochemical and/or mechanical) on film-free surfaces.

### **3.5.3 Effect of flow/impingement on metals**

Under flowing conditions, more specifically an impinging jet, it has been found<sup>50</sup> that on a range of stainless steels and some Co- and Ni- based alloys the breakdown potential was lowered and the surface of the materials had evidence of more pits, in the form of comets, than in static conditions. In other, similar, studies<sup>51, 52</sup>, it was found that an impinging jet decreased the corrosion resistance of grey cast iron and an HVOF Ni-Cr-Si-B-C cermet coating. However, while the stainless steel remained passive at high velocities (up to 100 ms<sup>-1</sup>), until solids were added and became active, in contrast the grey cast iron is active in both static and erosion conditions. Corrosion mechanisms differed in areas under and

out with the jet stream. On grey cast iron, at velocities of 38m/s, in the area directly under the jet there was no evidence of pitting attack but matrix attack was accentuated. In the outer region, severe pitting at the graphite/matrix boundaries was observed and the matrix had similar attack to that in the central region. In another study<sup>52</sup>, on stainless steel, again the hydrodynamics of the jet altered the corrosion mechanisms. Comet-shaped attack, associated with flow direction, was observed in outer regions but not directly under the jet.

Lush et al<sup>53</sup> attempted to model the corrosion rates under a submerged jet from normal impingement. Since the wall shear stresses were not easy to calculate, the local velocity was measured as it was assumed there was a relationship between the two. They found that the differing flow regimes, laminar or turbulent, had differing corrosion currents; in the central region, where flow was laminar, the corrosion varied with velocity (U) by the relationship  $U^{1/2}$ , and in the outer, turbulent, region it varied with  $U^{2/3}$ . In the transition zone, a slight decrease in current was found.

#### **3.5.4 Dry Solid Erosion**

Dry solid erosion usually occurs when solid particles entrained in a gas impact a surface. The subsequent deterioration of the material is dependant on the number, direction and velocity of particles striking the surface<sup>54</sup>. It is also very much dependant on the material's mechanical properties. Most materials can be put into one of two categories: ductile or brittle. These can be identified by the method in which erosion occurs. Ductile materials are said to undergo weight loss by plastic deformation i.e. the material is removed by a cutting action from the eroding particle. Brittle material is removed by the intersection of cracks that radiate out from the point of impact of the eroding particle.

Finnie<sup>54</sup>, in the 1960's, solved equations of motion for a particle hitting a brittle material and found relationships relating angle and velocity to erosion:  $W \propto V^2$ . Further work with Sheldon<sup>55</sup> generated the well-known diagram indicating the peak of ductile erosion at low impact angles and the higher erosion rate of brittle

materials at high impact angles (Figure 3-4).

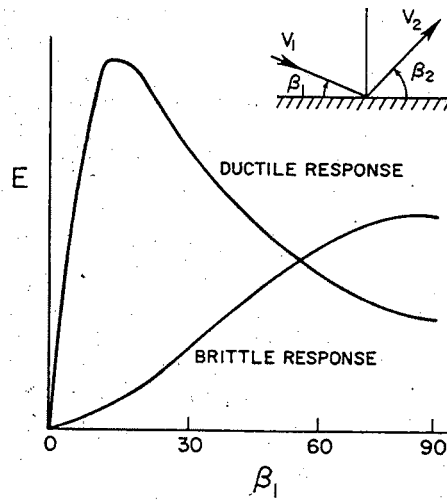


**Figure 3-4 Typical erosion curves for ductile and brittle materials as a function of particle incidence,  $\beta_1$ , from Sheldon and Finnie<sup>55</sup>.**

The way in which the material is removed differs in both cases and depends on the geometry of the particle<sup>56</sup>. For ductile materials impacted by round particles, the material is displaced to the side and in front like a ploughing action. When hit by angular particles, the particle indents the surface and raises the material to a prominent lip, in a cutting action. In brittle materials, rounded particles cause elastic deformation in the form of a conical Hertzian fracture. When angular particles impact the surface they cause some plastic flow around the point of contact. As the load increases to a critical value, tensile stress across the vertical mid-plane initiates a median vent crack. As the load decreases, a lateral vent crack is initiated. As the load decreases to zero, the lateral crack curves upward, terminating at the free surface. Median cracks, like Hertzian cracks, propagate down into the bulk solid. Initially they are not associated with material removal, unlike lateral cracks.

The plastic zone around the point of contact of an impacting particle has been investigated by Sundararajan<sup>57</sup> who proposes a correlation between plastic zone size,  $L$ , and erosion rate, i.e. erosion varies with  $L^3$ . Where 'L' is the distance from the eroded surface to the point at which the hardness value equals the original base value. Tests carried out on a selection of copper alloys and stainless

steels have shown that the plastic zone is dependant on the angle and velocity of the impacting particle; it increases with both variables. Sundararajan also proposed models for determining the erosion rate, one for erosion at normal impacts, based on localised plastic deformation (3.11) and another for oblique angles based on the energy absorbed in shear (3.12)<sup>58</sup>.

$$E_m = \left( \frac{5.5 \times 10^{-2}}{(T_m - 436)^{0.75}} \right) \frac{2^{n_c} f(t) U_1^2 \sin^2 \alpha (1 - e^2)}{n_c C_p} \quad (3.12)$$

$$E_m = \left( \frac{5.5 \times 10^{-2}}{(T_m - 436)^{0.75}} \right) \times \frac{(n_c + 1) \left( \frac{\mu_f}{\mu_{f,c}} \right) \left( 2 - \frac{\mu_f}{\mu_{f,c}} \right) U^2 \cos^2 \alpha}{2^{2-n_c} (1 + \lambda) n_c C_p} \quad (3.13)$$

where

$$\mu_{f,c} = \frac{1}{(1 + \lambda)(1 + e) \tan \alpha}$$

The effect of particle size on brittle and ductile materials is as yet unexplained. While particle size does not affect the behaviour of ductile material, Finnie<sup>59</sup> had noted a brittle-ductile transition in glass when the particle size was reduced from 127µm and 21µm to 9µm. He proposed that the transition is due to a change in mechanism for the material removal. It changes from lateral fracturing to scribing, where the particles move along the surface and scratch it.

Liebhard and Levy<sup>60</sup> conducted a study on how variable erodent particle characteristics affected the erosion of metals. Angular and spherical particles portrayed very different erosivity. While at low velocities (20m/s) the weight loss was immeasurable for spherical particles, it was an order of magnitude greater at the same velocities with angular particles. When the diameter of the spherical particle was >300µm, the mass loss decreased. This was thought to be due to its inability to penetrate the surface to cause plastic deformation. For angular particles the effect of changing the particle size was different at the two velocities. At low velocities (20 m/s) the mass loss reached a plateau whereas at 60m/s the mass loss increased steadily. To determine the extent of particle

erosivity, a number of characteristics must be evaluated; particle size, the number of particles striking the surface per unit time, the kinetic energy of the particles and the interference between the particles.

In a study of some alloys in dry erosion conditions by Levy<sup>61</sup>, it was speculated that the temperature affected the ranking of the alloys. At ambient temperatures, eroded by SiC particles, stainless steel 316L<sup>a</sup> had higher erosion rates than Ultimet<sup>b</sup> and Haynes alloy 6B<sup>c</sup>, while at 850°C, eroded by Al<sub>3</sub>O<sub>3</sub> particles, 316L's erosion rate was by far the lowest. It should be pointed out that, the authors carried out these tests at different impact angles, 30° at the lower temperature and 60° at the upper temperature and they also show a dependence on angle which alters for each erodent material. This would indicate that their results at the two temperatures are incomparable and cannot be conclusive.

Dry erosion tests were performed on carbide-metal composites<sup>62</sup> of varying carbide content from 0 to 88.8%. The carbides were divided into two groups, those with less than 30% carbide volume, carbon steels, and those with greater than 60% volume, cermets. It was found that the erosion rate increased with increasing carbon content with the lower carbon content composites and decreased with increasing carbon content in the cermets. While in the low carbon content alloys, the carbides cause an inhomogeneous plastic flow in the matrix and high strains close to the carbides resulting in the formation of voids; the cermets behave in a brittle manner. The proposed erosion mechanism is that individual carbide grains are removed by an impact and cracks in the carbide skeleton allow clusters of grains to be dislodged. The authors also propose that maximum erosion would occur at intermediate angles (45°-60°) as a "gouging" action would remove the grains more efficiently.

Thermally sprayed cermets have been the subject of dry erosion studies. Hawthorne et al<sup>63</sup> investigated the dry erosion resistance of HVOF WC cermets

---

<sup>a</sup> Composition Ni21%-Cr17%-Mo2.5%-Fe Bal

<sup>b</sup> Composition Ni9%-Fe3%-Cr26%-Mo5%-W2%-C0.06%-N0.08%-Si0.3%-Mn0.8%-CoBal

<sup>c</sup> Composition Ni3%-Fe3%-Cr30%-Mo1%-W4.5%-C1%-Si1%-Mn1%-CoBal

with Co- or Ni- based matrices with 50µm alumina particles at 84 m/s. He found that all coatings exhibited a ductile response to erosion with WC-12Co having the best erosion resistance due to the high carbide content. While the Co based coatings increased erosion resistance occurred at higher carbide content at impact angles, 20° and 90°, the Ni- based coating did not display the same trend at 90°. This was thought to be due to the poor bonding between the matrix and the WC particles caused this. Analysis of the surface of the WC-Co coating after erosion showed evidence of cutting, platelet formation and occasional carbide particle removal.

Many studies have been conducted to measure the erosion rate of a range of materials and models proposed to predict the erosion rate. These were, however, too case specific so Oka et al<sup>64</sup> have proposed a more general equation developed from dry erosion tests on metallics, plastics and ceramics:

$$E \equiv k' (\sin \alpha)^{n1} \left[ \frac{k_2 - \sin \alpha}{k_2 - 1} \right]^{n2} \quad (3.14)$$

Where  $k'$  is the erosion rate at normal impact expressed as a function of hardness, impact velocity and particle type,  $k_2$ ,  $n1$  and  $n2$  are constants determined by mechanical properties of the material and  $\alpha$  is the impingement angle. This equation has been shown to fit a range of materials: metallic, plastic and ceramic and can predict the erosion rate at a specific angle given the normal erosion rate. It is based on the assumption that mechanical wear can be expressed as one action of a combination of plastic deformation and cutting.

### 3.5.5 Liquid-Solid Erosion

Slurry erosion-corrosion causes significant material wastage in drilling applications<sup>65</sup>, fluidised bed combustors<sup>66</sup>, aircraft compressor blades<sup>67</sup>, paper and pulp<sup>5</sup>, and pumps<sup>40</sup>. The variations of parameters such as particle size and concentration, carrier fluid velocity, temperature and salinity, and the impacting angle of the slurry all affect the severity of the impinging conditions and the



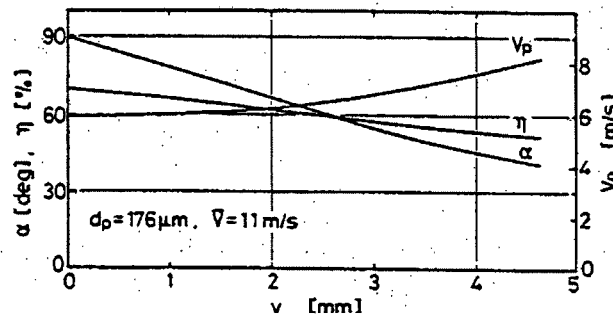


**Figure 3-7 Variation in impact velocity  $V_p$ , impact angle  $\alpha$  and collision efficiency  $\eta$  for a water jet containing  $176\mu\text{m}$  diameter glass beads for an average jet velocity of  $11\text{ ms}^{-1}$  after Clark<sup>68</sup>**

Turenne et al<sup>71</sup> also noted this range of impact angles from a nominally  $90^\circ$  impingement, whereby eroded surfaces of glass and aluminium had a maximum in the centre of the wear scar surrounded by a trough (Figure 3-8) in agreement with the dry erosion behaviour of ductile materials as did Zhou et al<sup>72</sup>. The authors also noted that brittle material had a maximum erosion depth at the central point from surface profiles.

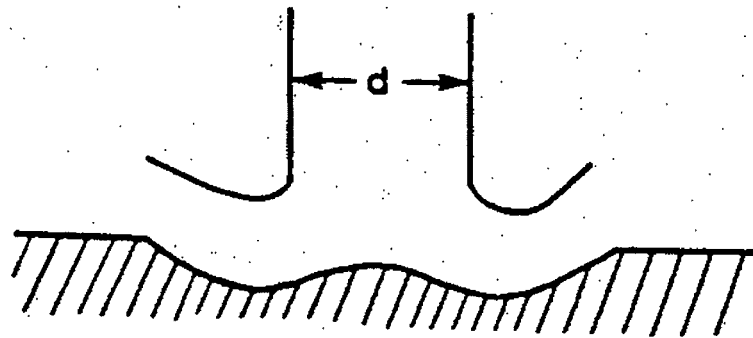


**Figure 3-8 Schematic diagram showing the profile of a wear scar of aluminium and glass at normal impingement from sand-water slurry<sup>68</sup>**

Particle-particle interactions become another variable at increased solid concentrations. After one particle has hit the surface it must be able to flow away before another can impact the surface, hence if the solid loading is too high ( $>5\text{ wt.}\%$ )<sup>68</sup>, not all particles will strike the surface and the erosion rate will be affected.

### **3.5.6 Slurry Erosion of Thermally Sprayed WC Coatings**

Thermally sprayed cermet coatings have been studied in slurry conditions. Karimi et al<sup>73</sup> investigated HVOF sprayed WC- coatings with Co, CoCr and Ni binders at low impingement angles with 0.3wt% sand in tap water with velocities in the range 20-145 ms<sup>-1</sup>. The erosion tests showed that a Co matrix resisted erosion better than a Ni matrix and alloying the Co with Cr increased the resistance by a factor of 4 to 6. The mechanism for material removal by the tangential impacts was principally by scratching effects. The abrasive particle scratched the soft binder phase and was disrupted by the carbide which would deflect the erodent. However, the carbides can be too small to deflect the erodent. In this situation they can aid in increasing the hardness of the matrix and reduce the scratch depth. Velocity was also found to affect the erosion mechanisms. At low velocities the carbides can deflect the particle impacts whereas at high velocities the carbides can be removed with the matrix.

Thermally sprayed (by a D-Gun) 86WC-10Co-4Cr coatings were tested in jet impingement (30° and 90°) conditions with 2.1 wt.% sand in tap water at velocities in the range 2-32 ms<sup>-1</sup> <sup>74</sup>. Two differing erosion mechanisms for low and high-energy impact, corresponding to low and high impingement angles, were found. At low impact energies, the impacting particles caused micro cutting and ploughing within the binder phase exposing the carbide particles. These were gouged out by the erodent and lead to further cutting. At higher impact energies, the coating was susceptible to sub surface cracks caused by fluctuating stresses. The cracks initiated at defects within the coating and they can propagate to splat removal. Hence within different regions of jet impingement, different mechanisms of erosion can occur.

### **3.5.7 Erosion-Corrosion-Synergy: Definitions and Mechanisms**

During aqueous erosion-corrosion it is well known that the overall material loss exceeds the sum of the separate mechanical erosion and electrochemical corrosion contributions; in other words synergistic effects are involved. There have been essentially two ways employed to analytically describe this complex

interactive phenomenon. One approach, following the definition by ASTM<sup>75</sup> where the total weight loss ( $T$ ) is defined by:

$$T = W_o + C_o + S \quad (3.15)$$

where  $W_o$  = material loss under pure erosion conditions, in the absence of corrosion

$C_o$  = the corrosion rate in the absence of erosion

$$S = S' + S''$$

$S'$  = the increase of mechanical wear due to corrosion

$S''$  = the increase of corrosion rate due to mechanical wear

The components can be determined by a set of experiments. The total material loss,  $T$ , is found by weighing the test specimen before and after an erosion-corrosion test.  $W_o$  is also determined by weighing the test specimen before and after an erosion-corrosion test but when the specimen is cathodically protected i.e. corrosion processes are stopped.  $C_o$  is determined from electrochemical tests when no mechanical wear is acting on the specimen.  $C_w$  is determined from electrochemical tests during an erosion-corrosion test, and  $S'' = C_w - C_o$ .

The other approach is:

$$\leftarrow T = E + C + S \quad (3.16)$$

where  $E$  is  $W_o$  above and  $C$  is the contribution from electrochemical deterioration under erosion-corrosion conditions ( $C_w$  above) and all the parameters can be directly obtained during an impingement experiment. The synergistic component,  $S$ , can be calculated from equation 3.17 where  $S$  is the increase in erosion due to corrosion. This equation is incorporated in work by Neville et al<sup>40</sup>, Hodgkiess et al<sup>52</sup> and Bjordal et al.<sup>84</sup>

$$S = TWL - E - C \quad (3.17)$$

Wood and Hutton<sup>76</sup> reviewed experimental results and showed a linear relationship, on a log-log plot, of the ratios of synergy and corrosion (S/C) to erosion and corrosion (E/S). It was thought that this would help give engineers an idea to how the wear rate would be affected in certain corrosive environments. Three groups were identified; high synergistic effects ( $S > 60\%$ ), medium synergistic effects ( $S \approx 30\%$ ) and low synergistic effects ( $S < 10\%$ ) and the relative increase in wear rate due to the synergistic effect for each group is  $> 2.5$ ,  $1.5$  and  $1.11$  respectively. Their findings, from limited resources, hoped to be a framework for future development.

Madsen<sup>77</sup> in 1988 identified a synergism on three alloys: A514 steel, 316 stainless steel and REM 500 in a slurry pot test with tap water,  $0.06\text{M Na}_2\text{SO}_4$  and  $2\%$  silica sand at velocities of  $5.8\text{m/s}$  and  $15.6\text{m/s}$  at  $26^\circ\text{C}$  and  $60^\circ\text{C}$ . The synergistic effect accounted for between  $23\%$  and  $33\%$  of the overall material degradation and up to  $62\%$  on stainless steel at low velocities.

Studies carried out at by Zhou et al<sup>78</sup>, involved a modified rotating cylinder electrode (RCE) system. Tests were carried out on mild steel in a solution of  $0.5\text{M NaHCO}_3 + 0.5\text{M Na}_2\text{CO}_3$  containing  $300\text{g/l}$  of  $100\mu\text{m Al}_2\text{O}_3$  particles. The peripheral velocity of the RCE ranged from  $2\text{m/s}$  to  $8\text{m/s}$ . Corrosion and erosion rates were measured over this range of velocities and potentials of  $-0.67\text{V}_{\text{SCE}}$  to  $+0.2\text{V}_{\text{SCE}}$ . The enhancement of erosion by corrosion was only seen in the same potential range where intergranular stress corrosion cracking occurs. The mechanism proposed for the synergy was that the impacting particles induced tensile stresses and hence corrosion cracks leading to material removal. The contribution from corrosion increased with velocity but decreased significantly with the introduction of the passive film.

Passive films on stainless steels are well known for providing protection against active dissolution in static conditions. However, when they are introduced to an erosive media the passive film can break down and the addition of corrosive and mechanical wear accelerates material degradation<sup>79</sup> namely synergism.

This (synergy) had been quantified by Neville et al<sup>50</sup> and Hodgkiess et al<sup>52</sup> on

UNS S31603 stainless steel to be 30% under an impinging jet of 800 mg/l solids at 17m/s and 25°C, and 17% in similar conditions with 1000mg/l solids at 25 m/s and 50°C with erosion contributions at 67.6% and 80.7% respectively. In the presence of solids, the passive film is penetrated causing dissolution of the substrate and wear by the erosive particles<sup>80</sup>.

The passive film breakdown in stainless steels is often associated with the initiation of pits<sup>81</sup> (but not in slurry conditions). Experiments carried out<sup>82</sup> measuring the current when particles in a slurry of 0.6M NaCl solution impacted the surface of 304L stainless steel showed an increase in current (at a constant potential of +120mV), associated with the nucleation of a metastable pit. Increases in current were also noted without jet particle impact, generated from sulphide inclusions. The solid particles were thought to “denude the passive film on the surface and allow direct contact between the inclusions and the electrolyte.” A rise in current with time was also noted by Neville et al<sup>50</sup> when sand was added to an impinging jet, and a marked decrease when the slurry jet was switched off.

Erosion-corrosion mechanisms were studied on other alloys: W-alloy white cast iron<sup>83</sup> and grey cast iron<sup>51</sup>. The white cast iron deteriorates by corrosion weakening the carbide/matrix bond, cavitation holes forming and aggravating the wear and the carbides, subjected to repeated impact eventually fall off. Hence by increasing the chromium and tungsten content, the corrosion resistance and hardness of the alloy increases, reducing the erosion-corrosion rate. Corrosion, both direct and indirect, had a large effect on the erosion-corrosion of the grey cast iron. It contributed up to 55% of the overall weight loss when subjected to an impinging jet of 500 mg/l solids at 50°C. The matrix was mechanically eroded by a ploughing action as well as electrochemically corroded which was accentuated near the graphite flakes.

As illustrated in the previous paragraphs, the corrosion resistance of alloys plays a large role in determining the extent to which they deteriorate in erosion-corrosion conditions. The synergistic effect becomes apparent when the mechanisms, either breakdown of passive films or the weakening of matrix/hard

phase bonds, are identified.

HVOF thermal spray coatings have proved<sup>52, 84</sup> to have increased erosion-corrosion resistance compared with that of conventional alloys, namely stainless steel. In conditions of an impinging jet at 17m/s containing 800 mg/l solids, a Ni-Cr-Si-B coating had about 50% reduction in weight loss compared with the stainless steel in a three hour test period. The synergistic effect (23% of the overall weight loss), on the coating, was attributed to the roughening of the surface on a micro scale and the corrosion of the matrix leading to the faster removal of protruding hard particles by the impacting sand.

Extensive studies<sup>84, 85, 86, 87, 88, 89,</sup> into the erosion-corrosion behaviour of WC-cermet coatings rotating in slurry of sand and seawater were carried out. These assessed the erosion, corrosion and synergy contributions and the effects of varying matrix composition and hard phase particle size.

These experiments show a time dependency on the erosion rate of coatings, this was thought to be attributed to the initial rough surface smoothing out and then the erosion rate reaching a steady state. The actual erosion and corrosion rates differed with each coating. The metallic matrix had a large effect, particularly on corrosion related deterioration. A pure cobalt matrix had very active corrosion behaviour and reflected in the erosion-corrosion behaviour. As the cobalt was replaced by chromium, the corrosion improved by a factor of 10 as the amount of chromium increased from 1% to 5%. A further increase to 8.5% improved the corrosion resistance further but when subjected to erosion-corrosion environment, this had a detrimental effect; undermining the good binding properties of Co. Other nickel-based matrices did not have as good erosion-corrosion resistance as the cobalt-chromium ones.

The WC hard phase particle size also affected the erosion-corrosion performance. As the particle size increased from 1 $\mu$ m-2.5 $\mu$ m-5 $\mu$ m, the erosion-corrosion resistance decreased so much so that the material loss halved on 86WC-10Co-4Cr by decreasing the particle size from 5 $\mu$ m to 2.5 $\mu$ m. This was

because the larger areas of binder associated with the larger hard phase particles give rise to a higher corrosion rate as the passive oxide layers are easily broken down. And as the sand particles hit the surface, larger chunks of the hard phase are removed.

The relative contributions of pure erosion, pure corrosion and synergy vary with conditions and coating. In low sand concentrations (0.025% w/w), corrosion dominates the material loss and as the sand increases (up to 2.5% w/w) mechanical erosion and the synergistic effect (to a lesser extent) contribute more to the material loss. The synergy mechanism is thought to be the matrix corroding and undermining the hard phase particles, causing them to fall out.

Wentzel and Allen<sup>90</sup> investigated cermets with 94% WC and varying compositions of the matrix: 6%Co, 6% Ni, 5.4%Ni+0.6%Cr and 3%Ni+0.6%Co+2.4%Co. The coatings were tested in a pump-like tester at 6.5m/s with 7%w/w sand and with 1M H<sub>2</sub>SO<sub>4</sub> in distilled water. A maximum erosion rate was found at an impact angle of 75° with all the binder compositions. However, the erosion-corrosion rate decreased as the corrosion rate of the binder decreased i.e. when chromium was added to the matrix, which also increases the hardness. The erosion resulted in attack on the matrix but corrosion left the WC particles standing proud to be dislodged by impacting particles (a synergistic effect).

Wood and Hutton<sup>76</sup> have defined mechanisms for erosion-enhanced corrosion: local acidification in erosion pit, accelerating corrosion rates and prohibiting film formation, increased ion transportation by high turbulence levels caused by surface roughening effects and lowering of the fatigue strength of the metal by corrosion. And for corrosion-enhanced erosion: the removal of work-hardened surfaces by corrosion, exposing a softer base metal, the preferential corrosive attack at grain boundaries, resulting in grain loosening and the increase in the number of stress-concentrating defects resulting from corrosion micropitting. However, this thesis will focus on the latter of the two synergies: corrosion-enhanced erosion.

### 3.5.8 Mapping of Erosion-Corrosion Regimes.

Erosion-corrosion regimes were identified during the study<sup>91</sup> of high temperature alloy corrosion resistance in FBC's. The study investigated the effect of velocity and temperature on the erosion resistance of mild and 310 stainless steels eroded by alumina particles. Weight loss was measured against increasing velocity and temperature and the dominant regimes were observed. These were split into four categories:

- (i) erosion dominated – erosion of the alloy substrate
- (ii) erosion-corrosion dominated – corrosion enhancement of the erosion rate
- (iii) corrosion dominated-1- erosion enhances the corrosion rate
- (iiii) corrosion dominated-2- erosion is negligible compared with corrosion

Corrosion dominated-1 can be separated from corrosion dominated-2 by its high dependence on velocity during material wear. It was found that the corrosion resistance of the alloy had a significant effect on the ranking of the alloys when considering the velocity exponent; a lower weight loss was found at low velocity for mild steel while the weight loss was greater at high velocities.

Tests performed on mild steel RCE in an aqueous slurry environment found the existence of similar regimes<sup>92</sup> adjusted to:

- (i) erosion dominated
- (ii) erosion-corrosion dominated:
  - (a) erosion-dissolution-dominated
  - (b) erosion-passivation-dominated
- (iii) corrosion-dominated:
  - (a) dissolution-dominated
  - (b) passivation-dominated.

These were determined by altering the erosion parameter (the rotating velocity) and corrosion parameter (the potential) and determining the erosion-corrosion rate. The results were then plotted on a potential versus velocity graph and regimes identified. At high potentials the regime changed from 'passivation' to 'erosion-dominated' as a function of velocity, and at the lower potentials it changed from 'dissolution' to 'erosion-dominated', as a function of velocity.

Since the corrosion of metals can involve the dissolution of metal as well as the breakdown of a passive film<sup>93</sup>, it was thought that the regimes would be better defined as ratios of corrosion rate ( $K_c$ ) to erosion rate ( $K_e$ ): ( $K_c/K_e$ ) where the regimes would be described as:

- |                                   |                        |
|-----------------------------------|------------------------|
| (i) erosion dominated             | $K_c/K_e < 0.1$        |
| (ii) erosion-corrosion dominated  | $0.1 \leq K_c/K_e < 1$ |
| (iii) corrosion-erosion dominated | $1 < K_c/K_e \leq 10$  |
| (iv) corrosion dominated          | $K_c/K_e > 10$         |

The relative contributions of  $K_c$  (3.17) and  $K_e$  (3.18) can be determined from Faraday's Law and models of solid particle erosion at 90° impingement<sup>94</sup> and a map, velocity versus applied potential, of the different regimes can be constructed following the flow chart adopted by Stack et al<sup>94</sup>.

$$K_c = \frac{M}{nF} i_{anet} \quad (3.17)$$

$$K_e = \frac{0.65 D_p^{0.25} c v^{3.5}}{C_p T_m^{0.25} H_s^{0.25}} \quad (3.18)$$

These models do not however take into consideration the elastic rebounds of solid particles and the subsequent effects on the boundaries within the erosion-corrosion maps. By incorporating the elastic rebound effects, i.e. the kinetic energy minus the particle rebound kinetic energy; a more accurate model can be derived<sup>95</sup>. Differences in the models were only significant at low velocities (less than 10m/s in a pipeline). However, when these are taken into consideration on a 'wastage map' (a map showing high, medium and low regions of wastage on a particle size versus velocity graph) the boundaries between the various wastage regimes moved somewhat.

Erosion-corrosion wastage maps (slurry velocity or velocity exponent versus particle size) were constructed from data on a range of materials tested under an impinging jet of aqueous slurry<sup>96</sup>. The velocity exponent was calculated and

shown to differ with particle size and erodent type (alumina or silicon carbide) where it is generally higher for silicon carbide and large particle although in some cases it is highest for intermediate size, alluding to the fact that some of the larger particles do not impact the surface. The exponent variation with material was dependant on the method of deformation. High exponents found on the ceramic material were associated with brittle fracture and the low exponents found on the polymeric material (Teflon) were due to elastic deformation. The erosion-corrosion wastage maps generated from the results demonstrate how material choice can be optimised in various conditions.

### 3.6 Summary

To date, the majority of studies relating to HVOF WC-CoCr thermally sprayed coatings have focused on how the process variables such as WC particle size and the nominal grain size<sup>85, 103</sup> contribute to the coatings' erosion-corrosion performance. In addition studies on how the effect of differing matrix composition effects the coatings' behaviour have been conducted<sup>86</sup>.

Other studies<sup>97 98 99</sup> have concentrated on ranking the coatings performance in erosion and/or erosion-corrosion studies with other coatings and metals. In these studies 86WC-10Co-4Cr HVOF sprayed coatings have shown to have a better resistance to erosion-corrosion than 316L stainless steel and other WC- HVOF coatings with pure Co or Ni based matrixes.

Hence, the focus of this study is to concentrate on one particular WC-CoCr HVOF sprayed coating and to conduct an in-depth study designed to provide information on the basic mechanisms of its deterioration in an aqueous erosion-corrosion environment. The environment chosen provided a reasonable simulation of marine systems in which moderate solid loadings may be present. The impinging jet simulates an environment analogous to industrial applications in pumps, impellers and offshore valves (e.g. ball and gate) for which cermet coatings are receiving attention. This study defines the complex mechanistic

aspects of the interactions of erosion corrosion and quantifies each contribution in different aqueous-solid environments.

# Chapter 4

## Experimental Procedure and Analysis

### 4.1 Introduction

This chapter details the experimental techniques and apparatus used within the test programme. It initially describes the specimen preparation for the tests which involve electrochemical monitoring both in a beaker and in situ, in the erosion rigs. It also details calculations used to determine the weight loss due to corrosion. A detailed description of the apparatus used after erosion-corrosion testing is also given. The overall objective of the research was to study the durability of WC-Co-Cr HVOF coatings in 3.5% NaCl.

### 4.2 Methodology

The experiments carried out within this programme incorporated static corrosion tests with the use of DC polarisation and additionally AC Impedance tests. These tests detailed the corrosion rates and the mechanisms were observed via an Atomic Force Microscope, Scanning Electron Microscope and optical microscopes.

Erosion-corrosion tests comprised a submerged impinging jet test in closed loop circulating rigs. Three tests were carried out to quantify the contributions of the total material loss:

- (1) Measurement of the weight loss by weighing the specimen before and after a test at the free erosion-corrosion conditions to give the total weight loss ( $T$ ).
- (2) Application of cathodic protection during a similar test to give the pure erosion weight loss ( $E$ )
- (3) Experiments in which polarisation scans were conducted at the end of a free erosion-corrosion test to yield the pure electrochemical corrosion rate during erosion-corrosion ( $C$ ).

Extensive post-test analysis by use of microscopes, Scanning Electron and optical, and by surface profiling were undertaken to provide information on the detailed mechanisms of erosion-corrosion.

#### 4.3 Specimen Preparation.

The specimens were received in an as-sprayed condition i.e. with a very rough surface and were subsequently ground and polished to achieve a smooth surface so that the microstructure of the coatings could be examined. This involved a grinding process using 60 grit SiC paper on a dry flatbed grinder, with intermediate cooling, followed by wet grinding with 240 grit SiC paper on a rotating wheel. The specimens were then polished using 6-micron diamond polish on a lubricated cloth. The specimens, for use in electrochemical monitoring, were soldered on the rear side to an electrical conducting wire and encapsulated in non-conducting resin so that only the polished face of the coating was exposed (Figure 4-1).

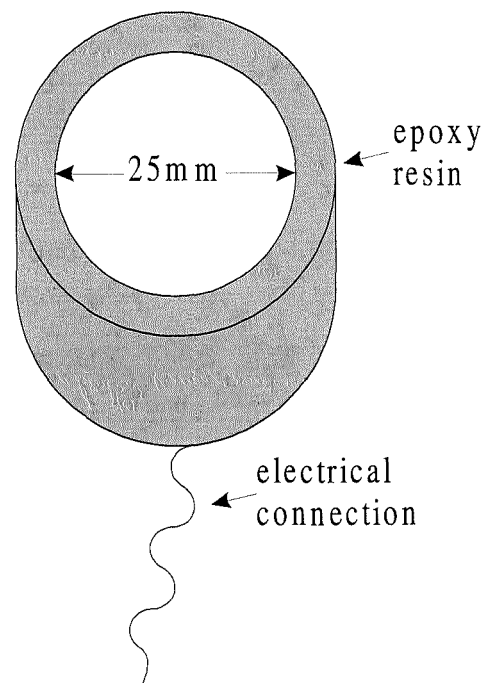


**Figure 4-1 Specimen prepared for electrochemical monitoring**

Other, concentric specimens (coating 2) were prepared by inserting an inner (6mm diameter specimen) inside a plastic tube and soldering the uncoated face to insulating

wire, this was inserted into the centre of a ring specimen (inner diameter 14mm and outer diameter 25mm), which was also soldered to insulating wire. The two specimens were then mounted in epoxy resin (Figure 4-2).

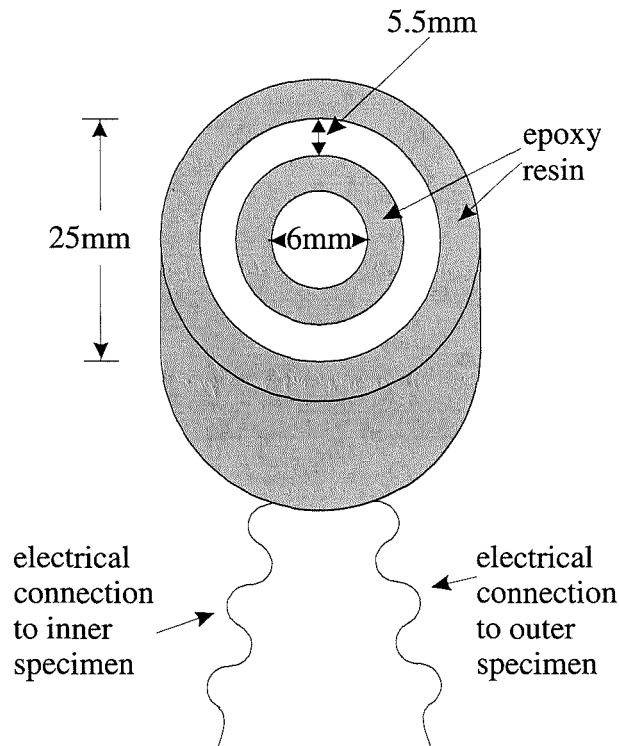


**Figure 4-2 Concentric specimen for electrochemical monitoring**

#### 4.4 Electrochemistry

All electrochemical experimentation was carried out using a 3-electrode cell. The specimen, a counter (platinum) electrode and a reference electrode (a saturated calomel electrode-SCE) are placed in a common aqueous solution- either simulated seawater from 'Ocean Salt' or made from 3.5% NaCl. The reference electrode is used in connection with a voltmeter to measure potential while the auxiliary electrode is used in conjunction with ammeter to measure current. In all electrochemical tests, a computer driven potentiostat (Sycopel Multistat 2/1739) that logged all potential and corresponding current data points, was used and scanned the potential at a rate of 15mV/min (Figure 4-3).

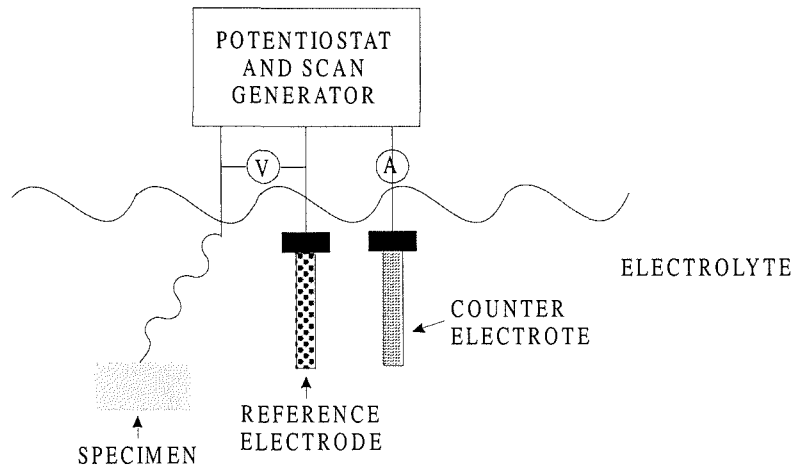


**Figure 4-3 Three-electrode electrochemical cell**

#### 4.5 Liquid Erosion Testing

Liquid impingement tests were carried out in a closed loop-circulating rig as shown in (Figure 4-4). The aqueous fluid was 3.5% NaCl, in distilled water, filtered through a 25 micron filter to exclude solids. The jet emerged from a 4mm nozzle at  $10 \pm 2 \text{ ms}^{-1}$  at an angle of  $90^\circ$  onto the specimen which was at a distance of 5mm. In-situ electrochemical monitoring was carried out.

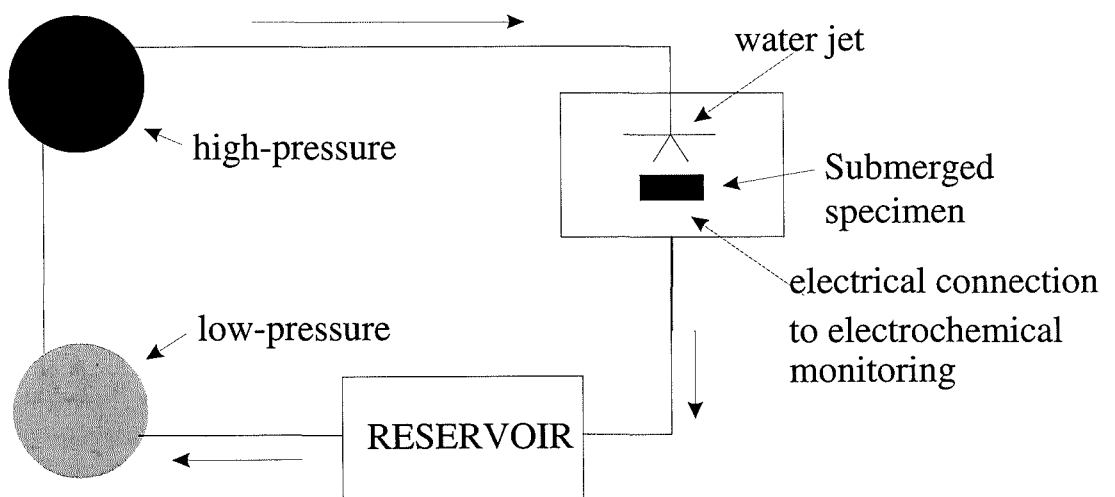


**Figure 4-4 Schematic diagram of liquid erosion rig**

## 4.6 Liquid-Solid Erosion-Corrosion

The solid-liquid erosion-corrosion experiments also used a closed loop-circulating rig (Figure 4-5) using 3.5% NaCl as the working fluid. The nozzle was 4mm in diameter and the stand-off distance was 5mm. Variations on impingement angle (within the range  $90^{\circ}$ - $30^{\circ}$ ) were achieved by rotating the specimen on a calibrated specimen holder. The temperature was maintained by the use of a controlled thermostat with accuracy of  $\pm 1^{\circ}\text{C}$ .

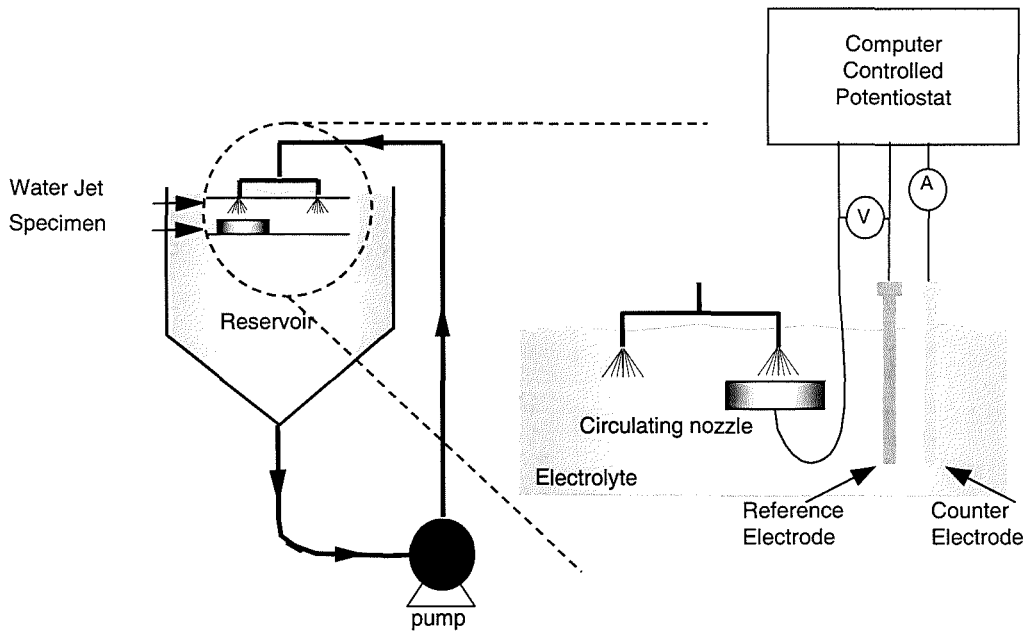


**Figure 4-5 Schematic diagram of liquid-solid apparatus**

The solids added to the working fluid were spherical silica sand (supplied by Hepworth Minerals) with a size range as shown in Table 4-1. The sand content, varying from 170mg/l to 2000mg/l, was measured in each experiment by filtering and weighing samples collected at intervals during and at the end of the experiments. While a specimen was impinged by the slurry from one nozzle, the other nozzle did not impinge onto a specimen and could aid the circulation of the slurry mixture.

During cathodic protection, the potential was held at  $-800\text{mV}$  which is sufficient to suppress any anodic current, as shown in Figure 4-6. By extrapolation of the Tafel slope to  $-800\text{ mV}$ , the currents are less than  $0.01\ \mu\text{A}/\text{cm}^2$ . At this potential, the specimen does not encounter any hydrogen embrittlement.

Size ( $\mu\text{m}$ )	>425	300-425	250-300	180-250	106-180	<106
Mass (%)	6.8	20.0	20.5	36.2	15.9	0.6

**Table 4-1 Size distribution of sand used in this study.**

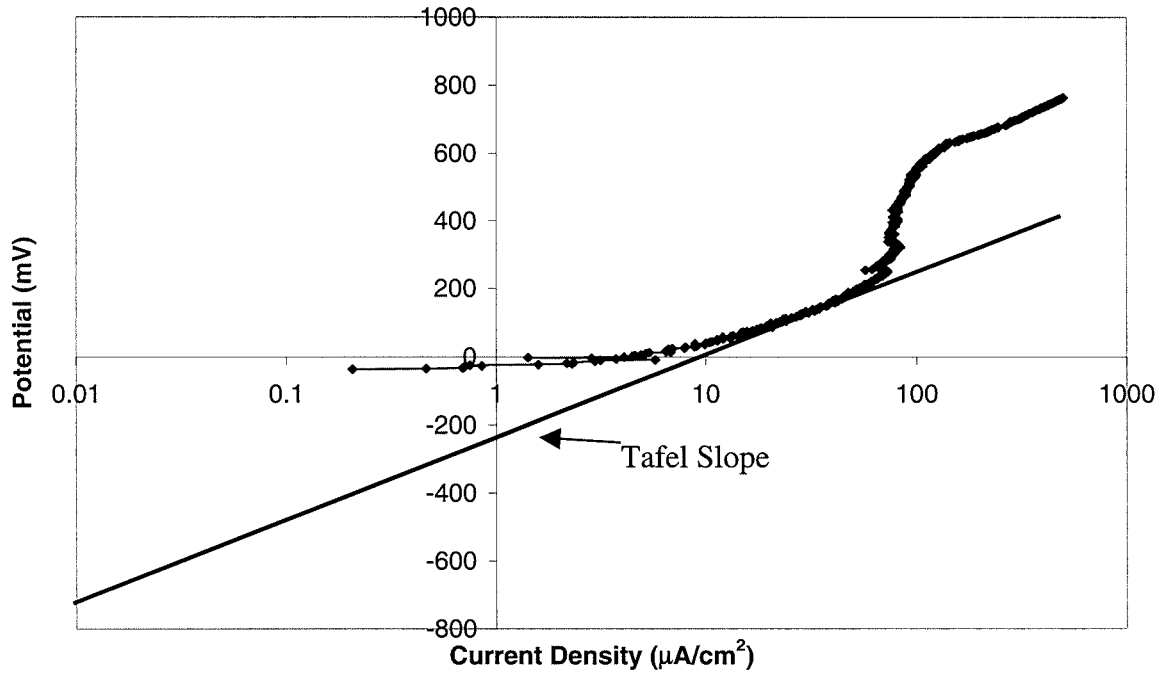


**Figure 4-6 Anodic Polarisation after 4 hours impingement with 500 mg/l solids at 18°C and 12 ms<sup>-1</sup>**

#### 4.7 Tafel Extrapolation

To determine corrosion current densities ( $i_{\text{corr}}$ ), and hence corrosion rates, Tafel extrapolation of anodic polarisation data was used extensively. This basically involves identifying the linear section on a semi-log plot of current and potential and extrapolating back to intersect with  $E_{\text{corr}}$  to determine the corrosion current density (Figure 4-7).

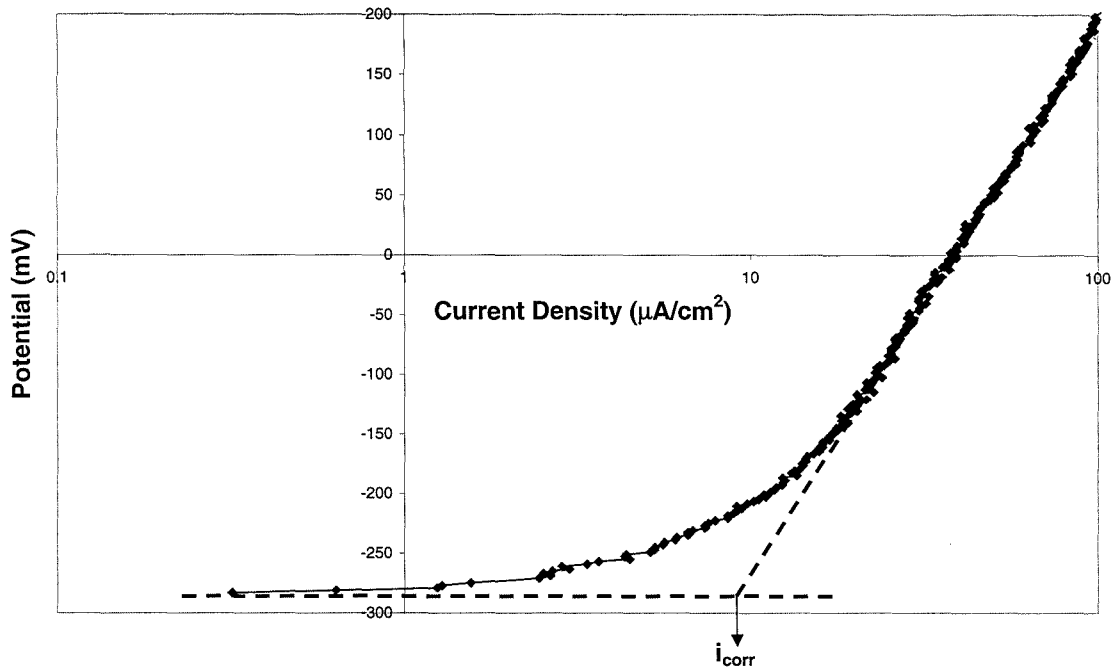


Figure 4-7 Tafel Extrapolation from anodic polarisation curve

From the corrosion current density, a thickness loss or weight loss can be calculated from the following equation:

$$\frac{dm}{dt} = \frac{iAM}{nF} \quad (4.1)$$

Where 'i' is the corrosion, current density, 'A' the surface area of the specimen (5.2 cm<sup>2</sup>), 'M' is the molecular weight of the material, 'n' is the valency and 'F' is Faradays constant (96500 coulombs/equivalent).

#### Sample Calculation

For Cobalt :

$$\frac{dm}{dt} = \frac{i_{corr} \times 5.2 \times 58.93}{2 \times 96500} \text{ (g/s)}$$

For Chromium:

$$\frac{dm}{dt} = \frac{i_{corr} \times 5.2 \times 51.99}{3 \times 96500} \text{ (g/s)}$$

Since the matrix consists of 71.5% cobalt and 28.5%chromium and the duration of an experiment is *t* seconds, the weight loss of the matrix due to the corrosion processes, *C*, is:

$$C = t \times \left[ (0.285 \times \frac{dm}{dt}(\text{chromium})) + (0.715 \times \frac{dm}{dt}(\text{chromium})) \right] \quad (4.2)$$

In order to improve the reliability of identification of the linear part of the semi-log anodic polarisation data in the region close to  $E_{corr}$ , the measured anodic polarisation currents,  $i_m$ , were “corrected” to compensate for the influence of the residual cathodic currents,  $i_c$ , on  $i_m$ . The basis of this approach can be found in the paper by Stern and Geary<sup>107</sup> where they state that at  $E_{corr}$ ,  $i_a = i_c = i_{corr}$ . As the specimen is polarised anodically from  $E_{corr}$ ,  $i_a$  increases,  $i_c$  decreases and the measured current is expressed as:

$$i_m = i_a - i_c \quad (4.3)$$

Thus, the true anodic current can be found from:

$$i_a = i_m + i_c \quad (4.4)$$

Under liquid-solid conditions, the “corrected” anodic current was calculated from this theory. Due to the slightly different  $E_{corr}$ 's obtained from the separate anodic and cathodic polarisation tests, the  $E_{corr}$ 's were normalised to an arbitrary value of zero. Tafel Extrapolation of the cathodic curve to potentials positive to 0mV yeild the residual cathodic currents incorporated in  $i_m$  (Figure 4-8). Thus  $i_a$  was calculated at 10mV intervals until the residual cathodic current became negligible. The way in which this procedure facilitated improved definition of the linear part of the anodic polarisation plot is clear in Figure 4-8.

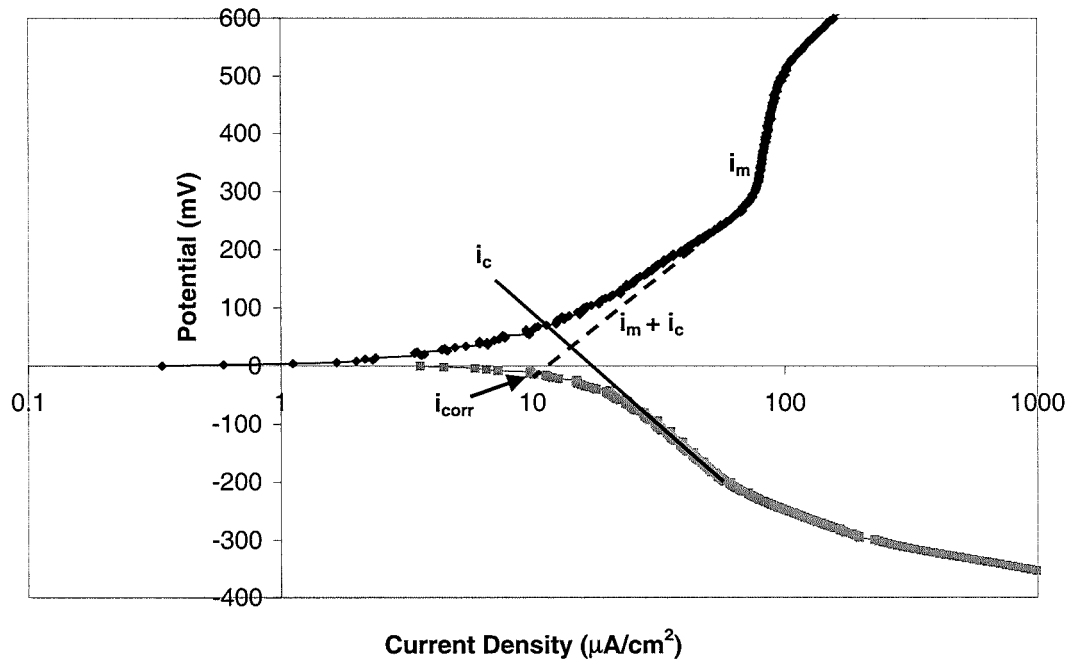


**Figure 4-8 Schematic diagram showing the determination of  $i_{corr}$  in erosion-corrosion conditions**

#### 4.8 Linear Polarisation

Linear polarisation tests were carried out by scanning the potential from 30 mV less positive than  $E_{corr}$  to 30 mV more than  $E_{corr}$ . The results were plotted on a linear current density v potential plot (Figure 4-9) and a best-fit straight line was drawn.  $R_p$  was then calculated from the gradient of the line i.e.

$$R_p = \frac{\Delta E}{\Delta I} \quad (4.5)$$

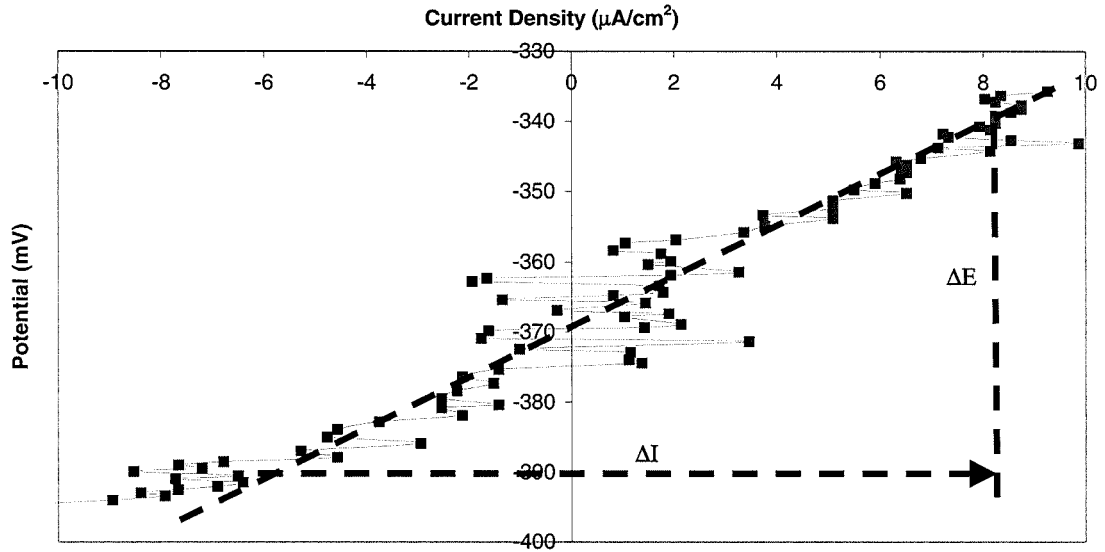


**Figure 4-9 Schematic diagram showing calculation of polarisation resistance**

#### **4.9 Post Test Analysis**

The microstructure, characterisation and corrosion behaviour were analysed with optical microscopes, a scanning electron microscope (SEM) [Leica Cambridge Stereoscan 360] atomic force microscope (AFM)- Topomatrix Explorer, an X-ray diffractometer (XRD) [Siemens D500] and surface profiling equipment, a Taylor Hobson Talysurf (Form Talysurf Series 2).

##### **4.9.1 Scanning Electron Microscopy (SEM) and Energy Dispersive X-Ray (EDX)**

The samples for SEM analysis are coated with carbon to enable conduction on the surface and are then placed in a vacuum chamber. The SEM uses electrons rather than light to focus on the sample and therefore gives a much greater depth of field. Secondary electrons, produced from a primary beam, (from a tungsten filament) are collected by a secondary electron detector in the chamber this is processed by the attached computer to produce the micrograph.

Chemical analysis can be performed on the specimen by Energy Dispersive X-ray analysis (EDX) to find the elements present. The electron beam in the SEM ionises the metal atoms, exciting and losing electrons in the inner shell. The electrons in the outer shells replace the lost electrons to regain stability. As the electrons move shells they emit X-rays which identify the difference in energy between the shells. These energies, and the associated wavelengths of the X-rays, can be used to identify an element. All elements can be detected except carbon using a standard of cobalt.

#### **4.9.2 X-Ray Diffraction (XRD)**

XRD can identify phases of compounds present in the powder and coating samples. The X-ray diffraction patterns were scanned between the 2-Theta values of 0-120° at a speed of 1°min<sup>-1</sup>. The pattern produced can be identified by cross-referencing it to a database containing reference phase patterns.

#### **4.9.3 Surface Profiling**

Surface profiling was used to determine the depth and shape of erosion wear scars. The sample is placed beneath a stylus which is at one end of a beam. The beam is pivoted in the middle with an armature at the other end which moves between two coils, changing their relative inductance. The coils are connected in an ac circuit bridge so that there is no output when the armature is balanced. When there is movement, the bridge produces an output signal proportional to the displacement. The signal is amplified and compared with an oscillator signal to determine the direction of movement. The signal is then fed into a computer which generates the profile. The spacial resolution is 16nm at 1mm range and the diameter of the tip is 4microns.

#### **4.9.4 Atomic Force Microscopy (AFM)**

AFM was used to characterise the microstructure of the coatings during static anodic polarisation tests. While the specimen was submerged in artificial seawater with an

electrical connection to a computer driven potentiostat and scan generator with a reference and counter electrode, the AFM recorded an image of the specimen during an anodic polarisation test. Each image took 6 minutes to produce which covered a potential range of 90mV.

The AFM maintains a constant force between a stylus probe (cantilever) and the sample (Figure 4-9). A laser is focused on the rear of the AFM probe and as it scans the tip moves in the z direction to follow the profile of the material. The laser is reflected off the tip to the mirror and onto a photodiode split into 4 quadrants. The signal from the photodiode is calibrated to accurately measure z deflections and then a topographical map is built up.

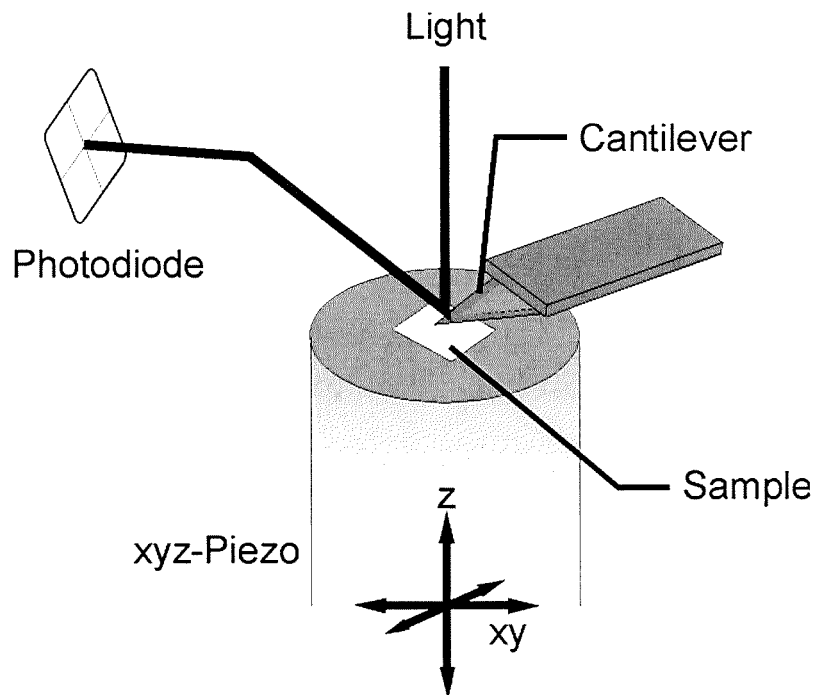


**Figure 4-10 Schematic diagram of AFM**

# **Chapter 5**

## **Coating Characterisation and Static Corrosion Behaviour**

### **5.1 Introduction**

This chapter deals with the characterisation of the feedstock powder, the microstructure and composition of the coating and the subsequent corrosion behaviour in static saline conditions. The coatings investigated within this thesis come from three different companies. Companies I and II supplied the same type of coating, a WC-Co-Cr (coatings 1 and 2) and company III supplied a WC-Co coating (coating 3). The properties of the three coatings are presented then a comparison is made in section 5.5. Where polarisation curves are shown, only one, showing the typical response, of three experiments conducted in each case is shown. The replicate curves can be found in the Appendix.

### **5.2 Coating I**

#### **5.2.1 Characterisation**

The WC-Co-Cr powder (Figure 5-1) consists of fine particles, in the size range 10-50 $\mu$ m, which are sprayed, using a Hobart Tafa gun, onto a stainless steel UNSS S31603 (316L) substrate and forms the coating with a distribution of WC particles, typically less than 5 $\mu$ m in size (Table 5-1), within a metallic matrix as shown in Figure 5-2. The coating has a nominal composition WC86%-Co10%-Cr4% and microanalysis over several areas of 30 $\mu$ m x 30 $\mu$ m yielded a composition range as shown in Table 5-2.

Thickness	300 $\mu\text{m}$
Hardness	1157-1488 Hv
Carbide size range	<5 $\mu\text{m}$

Table 5-1 Parameters of Coating 1

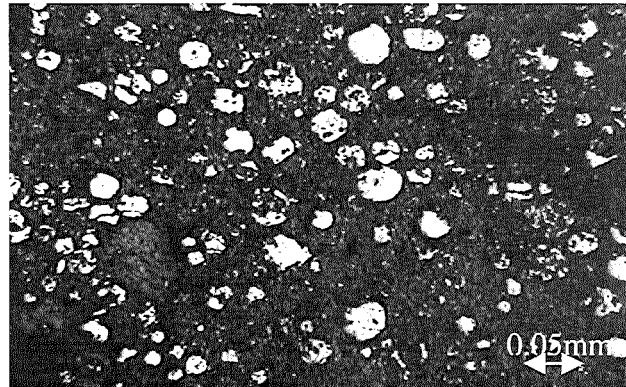


Figure 5-1 Picture of WC-Co-Cr powder particles

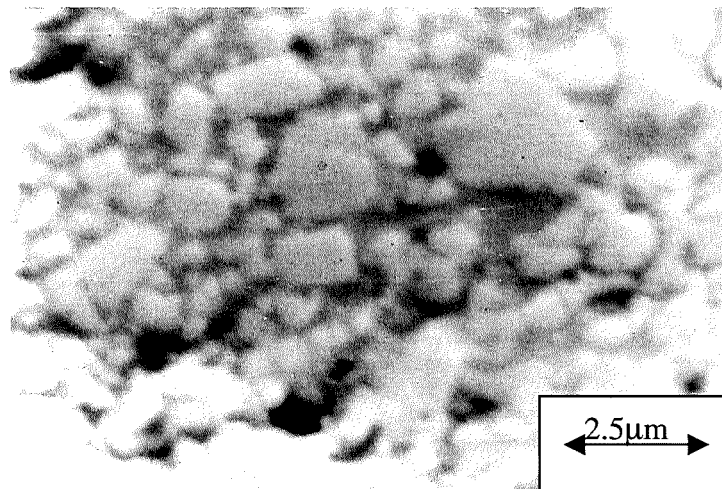
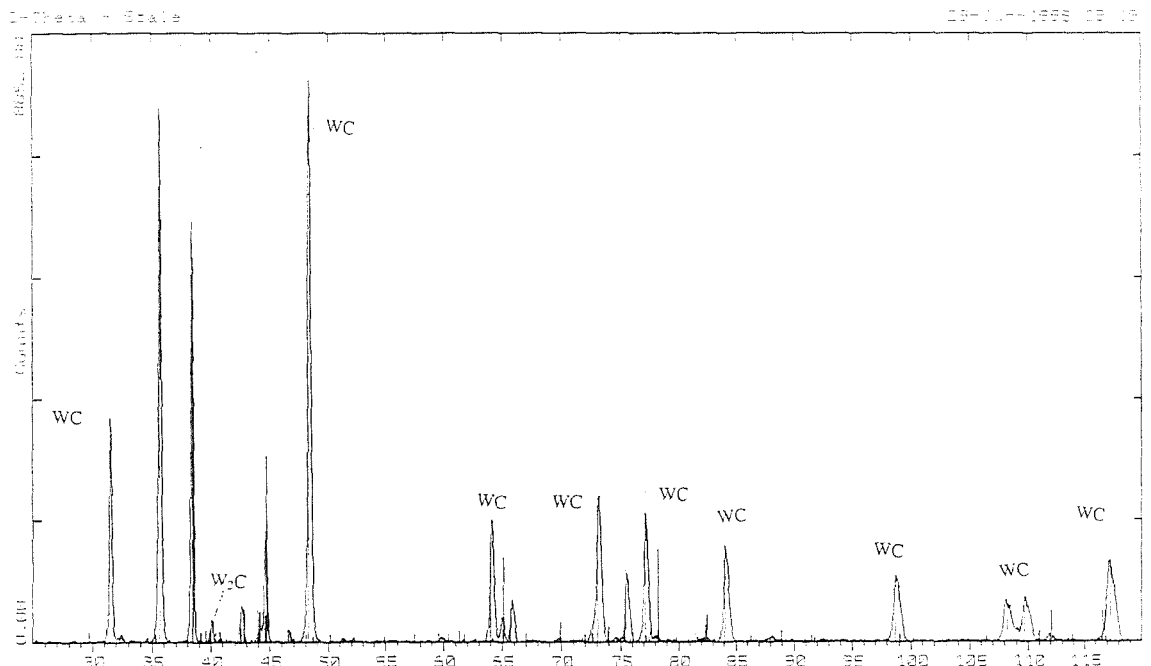


Figure 5-2 SEM micrograph of sprayed coating 1

Element	Weight %
Cr	2-4
W	85-91
Co	7-9

**Table 5-2 Chemical composition of the WC-Co-Cr coating 1 measured using the EDAX facility on the SEM**

On a comparison of the feedstock powder and the sprayed coating by XRD (Figure 5-3 and Figure 5-4) it is apparent that some decarburisation had taken place during spraying since the  $W_2C$  peak is larger in the coating than in the feedstock trace. However, this is not extensive. The coating had a thickness of 250-400 $\mu$ m (Figure 5-5) and a porosity level of 2-6% determined through image analysis.



**Figure 5-3 XRD trace for the constituent WC-Co-C powder**

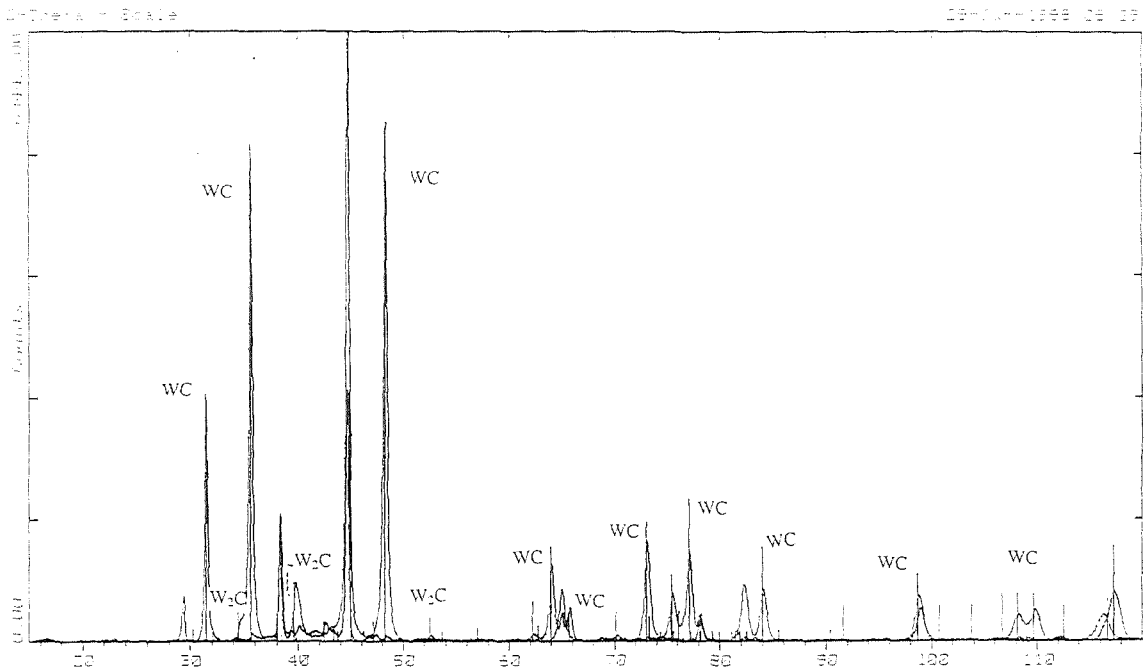


**Figure 5-4 XRD trace for the sprayed WC-Co-Cr coating**

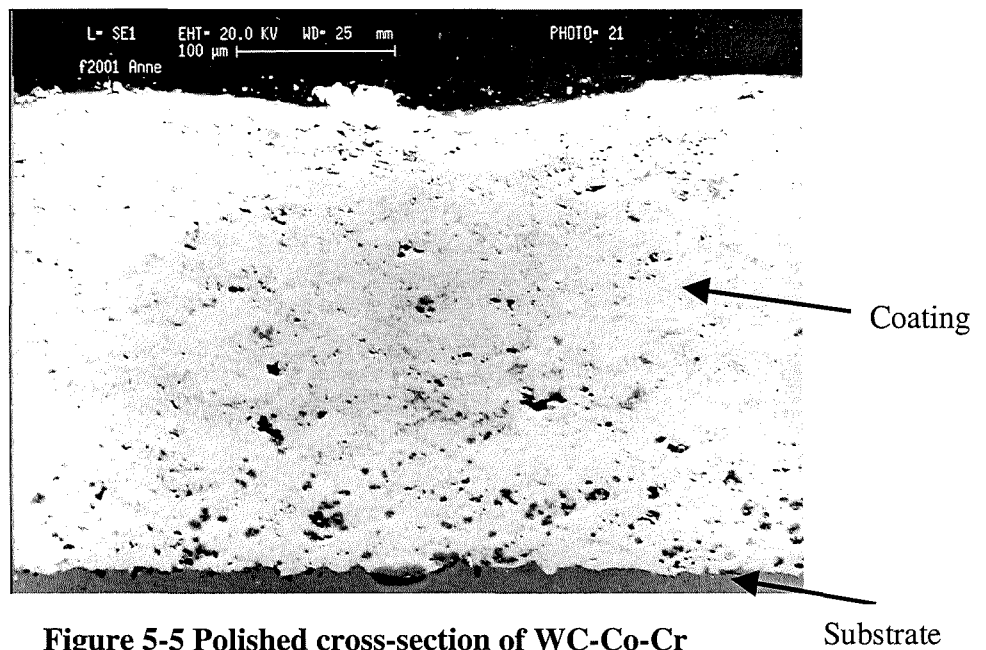


**Figure 5-5 Polished cross-section of WC-Co-Cr**

### 5.2.2 Static Corrosion Behaviour

The anodic polarisation plot on the coating at 18°C, after one hour immersion in artificial seawater, is shown in Figure 5-6. Also incorporated in Figure 5-6 is the anodic polarisation response for a 'passive' material, stainless steel UNS S31603 and carbon steel (EN 8) which shows 'active' corrosion behaviour. Interestingly

the coating displays an electrochemical response which is neither truly active nor truly passive. As the potential is shifted more positive from  $E_{\text{corr}}$  the current rises to a stable value of around  $50\mu\text{A}/\text{cm}^2$ . At a potential of about +500mV the first rapid rise in current density is observed, labelled the first breakdown potential ( $E_{b1}$ ) and a second breakdown potential ( $E_{b2}$ ) is evident at around +800mV. Examination of the specimen after anodic polarisation by SEM (Figure 5-7) showed that the corrosive attack resulted in extensive removal of the carbide particles, the corrosion initiating at the carbide/metal interface.

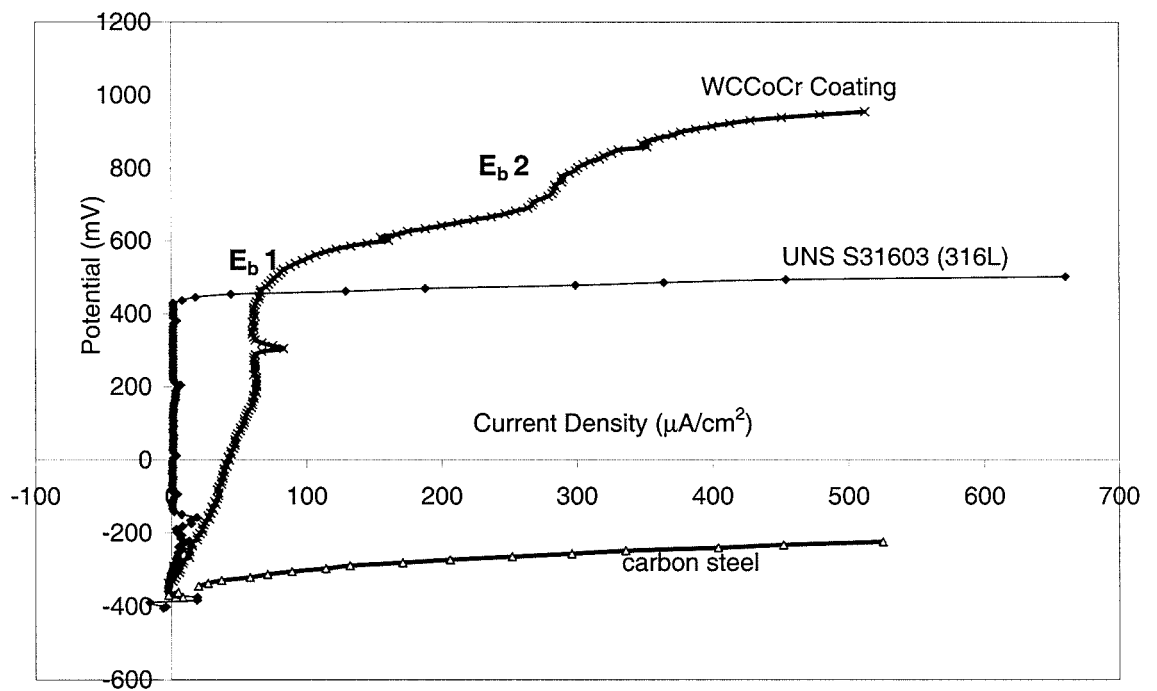


**Figure 5-6 Anodic polarisation curve on the WC-Co-Cr coating in static artificial seawater at 18°C**

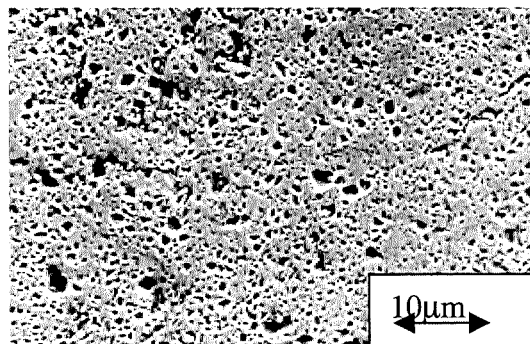


**Figure 5-7 SEM image of the surface of the WC-Co-Cr HVOF coating after anodic polarisation at 18°C.**

At 50°C, as expected, the corrosion rate increases as shown by the more rapid increase of current as the potential increase (Figure 5-8). The anodic polarisation at 50°C is more characteristic of a material which displays active corrosion behaviour unlike the complex behaviour at 18°C. In addition to the loss of carbide phase observed at 18°C, it is interesting to note that at 50°C severe localised regions of deep corrosion attack are evident where removal of the matrix resulted in unsupported carbides being left in these regions (Figure 5-9).

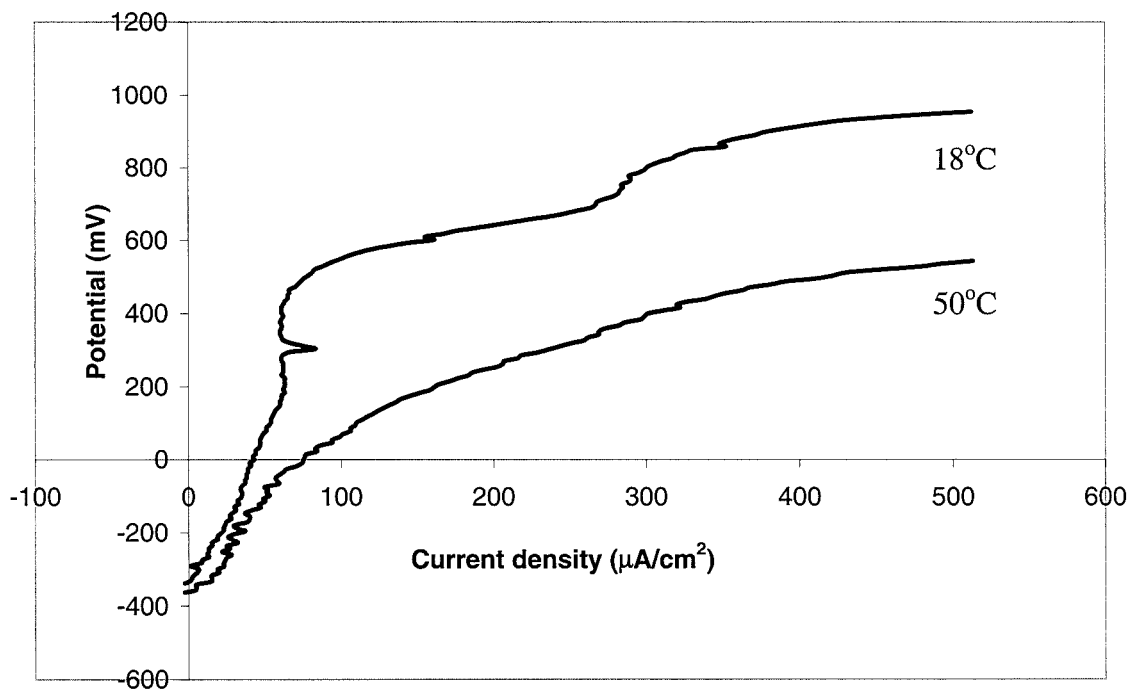


**Figure 5-8 Comparison of the anodic polarisation curves at 18°C and 50°C in static conditions**

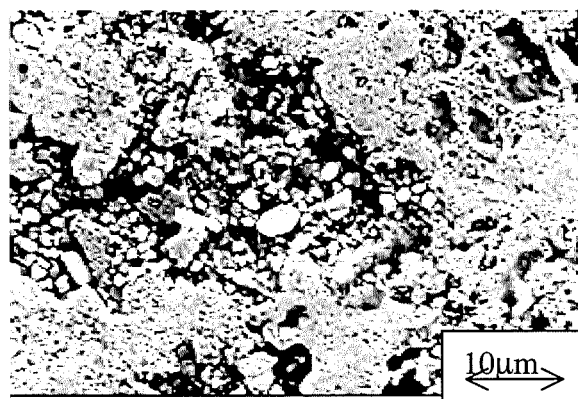


**Figure 5-9 SEM micrograph of deep localised region of corrosion attack where extensive matrix dissolution has occurred**

### 5.2.3 Cathodic Polarisation Tests

Figure 5-10 shows the cathodic polarisation tests after one-hour immersion at 18°C and 50°C on a E/log I plot. After an initial sharp increase in current (Tafel behaviour), the controlling reaction is a mix of activation and concentration polarisation. A current of 90 $\mu\text{A}/\text{cm}^2$  is reached at 18°C before hydrogen evolution becomes the predominant cathodic reaction around -1000mV. At 50°C, a similar story emerges although the current reaches 100 $\mu\text{A}/\text{cm}^2$  before hydrogen evolution proceeds.

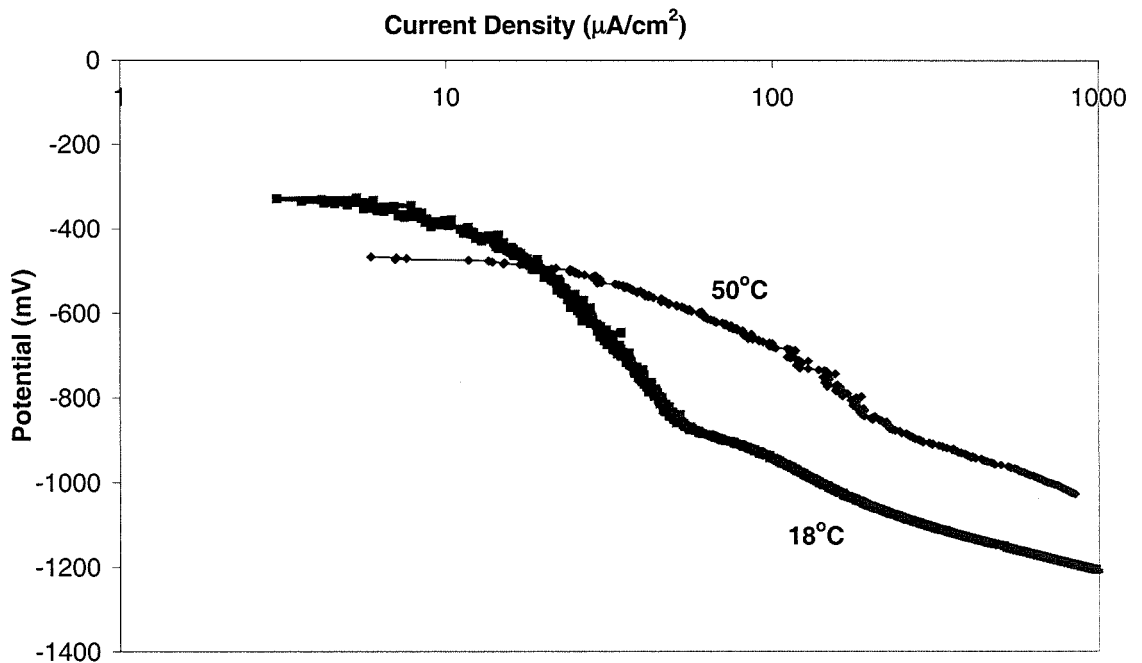


Figure 5-10 Cathodic Polarisation tests after 1 hour immersion

### 5.2.4 Long-term tests

Anodic polarisation tests were carried after immersion for one month at 18°C (Figure 5-11) and 50°C (Figure 5-15) in artificial seawater. After an initial lower increase in current with potential after one month compared with one hour at 18°C (Figure 5-11), the current then rapidly increases and has a much lower breakdown potential. After one month immersion at the free corrosion potential at 18°C there was deep attack around the hard phase/matrix interfaces over the

entire surface (Figure 5-12) and more severe attack of the same mechanism occurred at the coating/lacomit interface, indicative of crevice corrosion (Figure 5-13). A higher corrosion rate was also shown in the polarisation tests at 50°C (Figure 5-15) by the rapid increase in current with potential. At 50°C the more severe corrosive attack at the free corrosion potential manifested itself as the matrix beginning to open up in some localised areas leaving the carbide particles more pronounced in other areas (Figure 5-16).

The AC impedance data when plotted as a Nyquist plot showed a response typical of a resistor component in parallel with a capacitor, as usually used to model activation-controlled corrosion. The partial semi-circles shown in Figure 5-17 were extrapolated onto the real axis and a value for the polarisation resistance  $R_p$  (inversely proportional to the corrosion current) was obtained. The values for two samples are tabulated in Table 5-3 and Table 5-4 for 18°C and 50°C respectively. As a function of time no specific trend was observed in  $R_p$  values for the sample immersed at 18°C (Figure 5-14) but, in contrast at 50°C, a significant progressive increase in the polarisation resistance, and hence a decrease in corrosion, was seen (Figure 5-17).

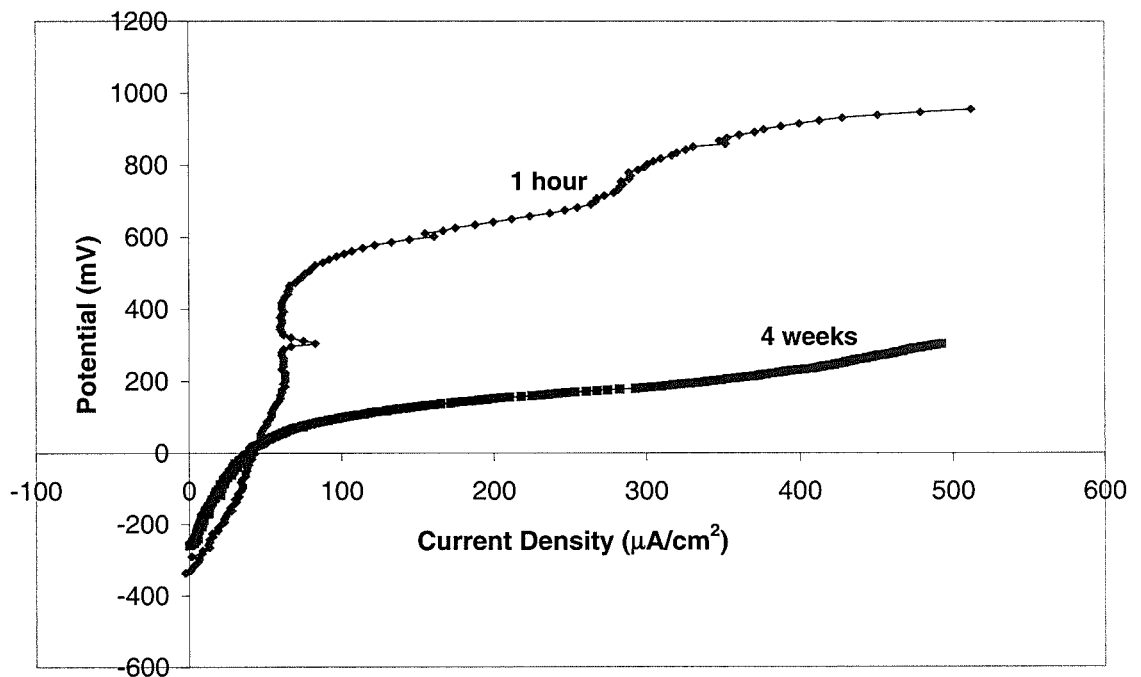


**Figure 5-11 Anodic Polarisation after one month at 18°C**

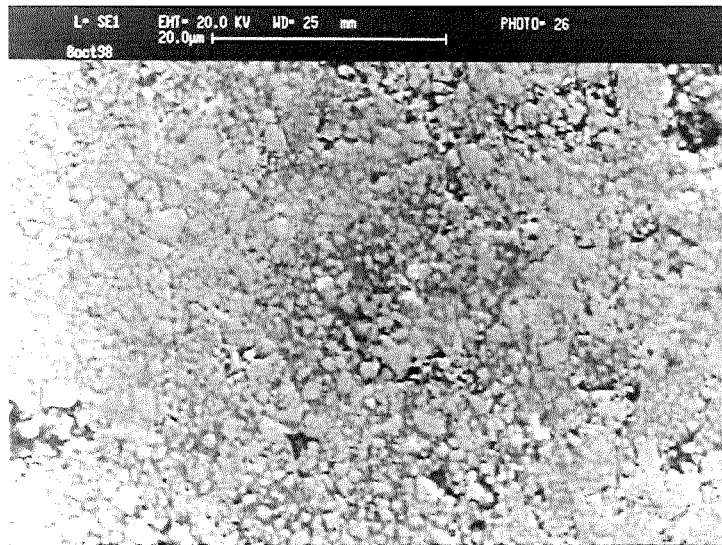


**Figure 5-12 Corrosion attack on WC-Co-Cr coating after exposure to artificial seawater at 18°C for one month at the free corrosion potential**

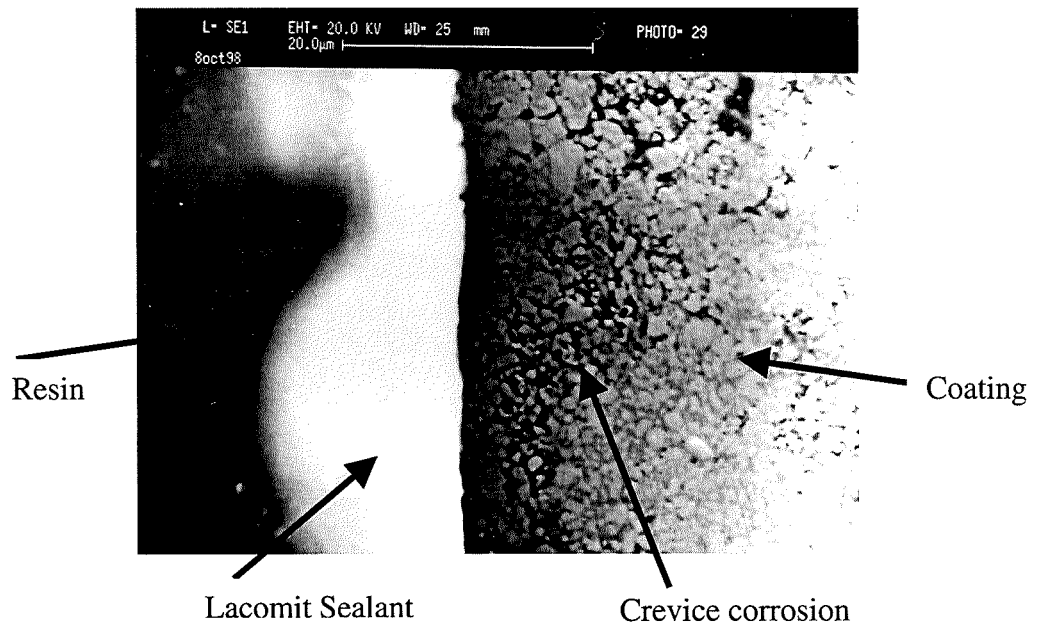


**Figure 5-13 Crevice corrosion at coating/lacomit interface after one month immersion at 18°C**

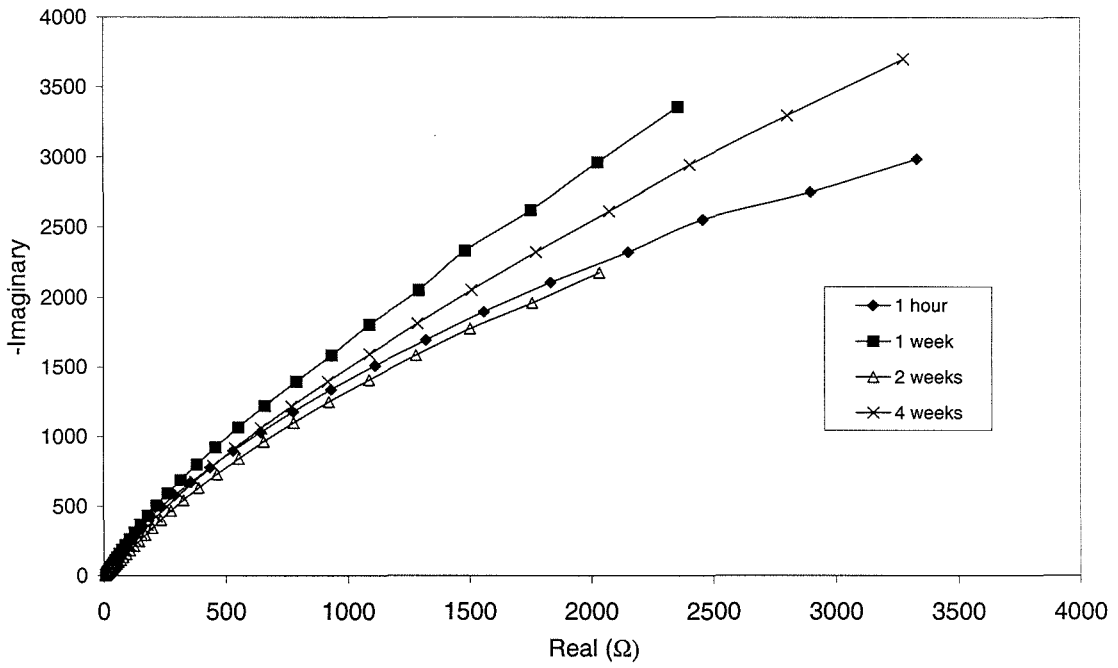


**Figure 5-14 AC Impedance as a Nyquist after exposure to artificial seawater for upto one month at 18°C**

Exposure Time	R <sub>p</sub> (ohms)	
1 hour	15180	9728
1 week	10617	12555
2 weeks	10108	14518
1 month	8364	13267

**Table 5-3 Table of duplicate R<sub>p</sub> values over one month at 18°C on separate samples**

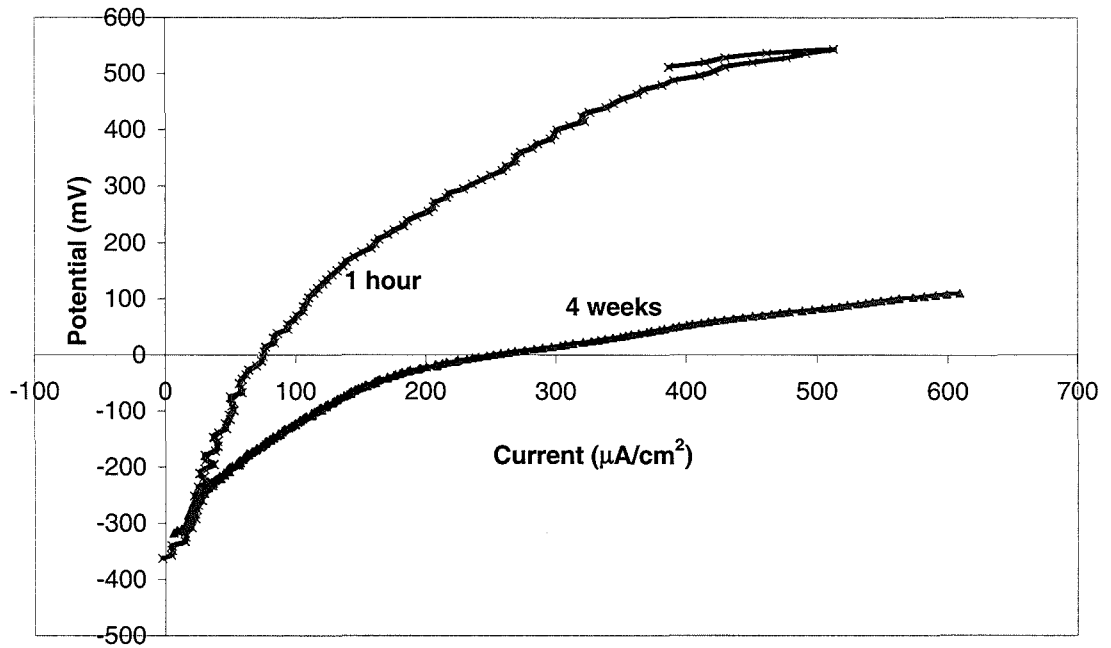


**Figure 5-15 Anodic Polarisation after one month immersion at 50°C**



**Figure 5-16 Unsupported carbide particles on the coating surface after exposure to artificial seawater at 50°C for one month at the free corrosion potential**

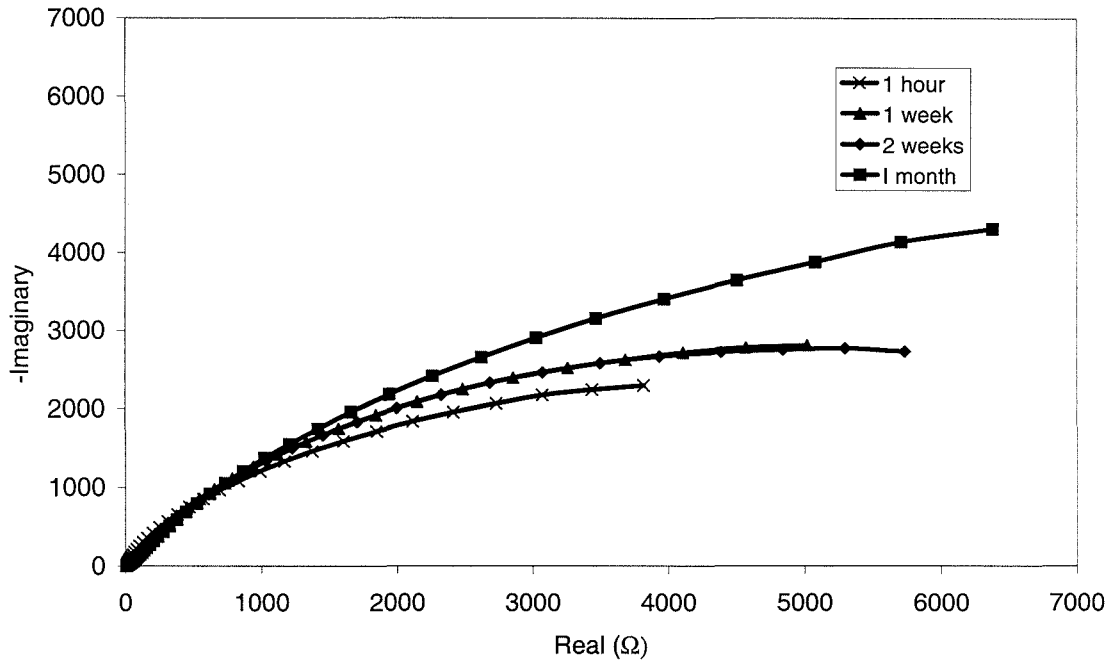


**Figure 5-17 AC Impedance as Nyquist plot for immersion in seawater at 50°C over a one month period**

Exposure Time	$R_p$ (ohms)	
1 hour	4908	7441
1 week	7300	9270
2 weeks	11896	9579
1 month	12294	16387

**Table 5-4 Table of duplicate  $R_p$  values over one month at 50°C on separate samples**

## 5.3 Coating 2

### 5.3.1 Characterisation

Coating 2 (Table 5-5) is also of nominal composition 86%WC-10%Co-4%Cr and an average analysis carried out by EDAX on a  $30\mu\text{m} \times 30\mu\text{m}$  area gave the composition shown in Table 5-6. It was sprayed by a JK IIA system with hydrogen fuel at  $0.01 \text{ m}^3/\text{s}$  and oxygen at  $5 \times 10^{-3} \text{ m}^3/\text{s}$  depositing  $0.03\text{mm}$  per pass on to a stainless steel UNS S31063 (316L) substrate. A polished plan specimen of the coating is shown in Figure 5-18. It shows the white tungsten carbide blocky particles encased in a Co-Cr metallic matrix. Again some decarburisation has occurred due to the presence of small  $\text{W}_2\text{C}$  peaks in the XRD pattern (Figure 5-19).

<b>Thickness</b>	<b>300<math>\mu\text{m}</math></b>
<b>Hardness</b>	<b>1021-1442 Hv</b>
<b>Carbide size range</b>	<b>&lt;5<math>\mu\text{m}</math></b>

**Table 5-5 Parameters of Coating 2**

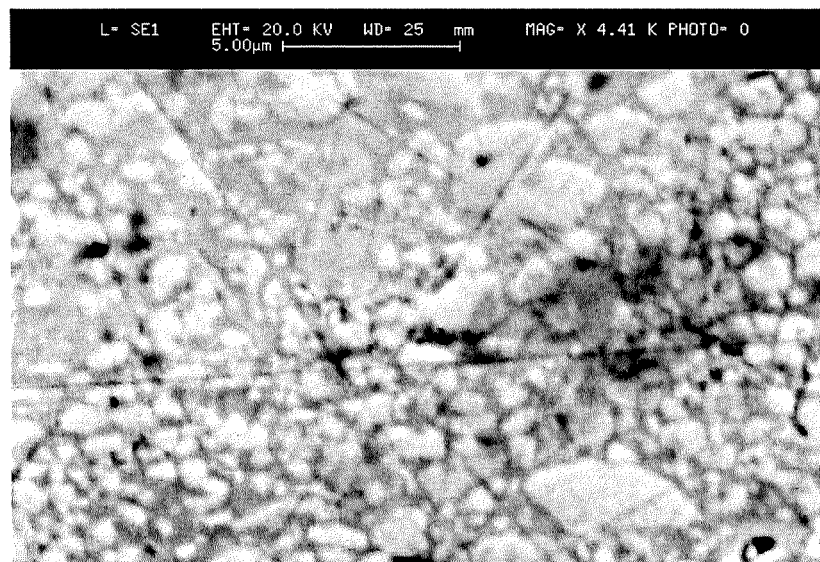


**Figure 5-18 SEM micrograph of WC-Co-Cr as polished**

Element	Weight %
W	83-85
Co	9-11
Cr	3-5

**Table 5-6 Chemical composition of the WC-Co-Cr coating 2 measured using the EDAX facility on the SEM**

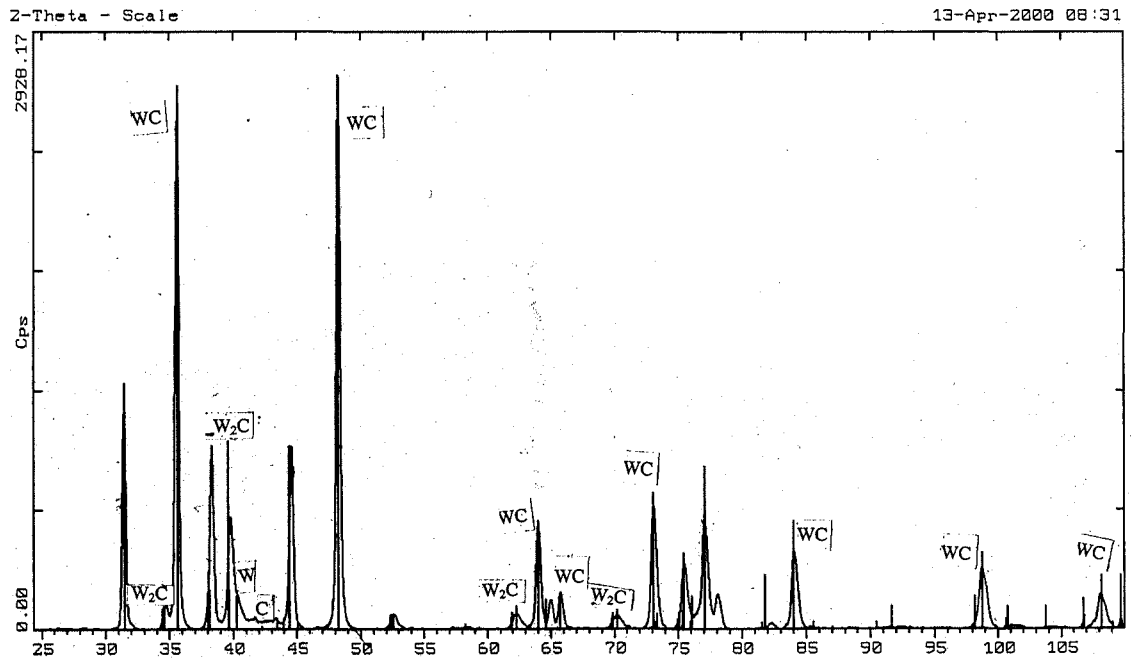


**Figure 5-19 XRD trace for the WC-Co-Cr coating II**

### 5.3.2 Static Corrosion Behaviour

Anodic polarisation tests conducted after 1 hour immersion at 18°C and 50°C in artificial seawater are shown in Figure 5-20. At 18°C the coating shows a general loss of hard phase as shown in Figure 5-21 and at 50°C there is more deep localised attack focused on the matrix at the hard phase/matrix interface (Figure 5-22).

In an attempt to determine the mechanisms of corrosive attack, at 18°C, as the potential increased, and hence as the current increased, in-situ AFM scans were

conducted at intervals during the anodic polarisation. A scan was taken at the beginning and then at intervals during the test. The time to complete each scan covered a potential range of 90mV.

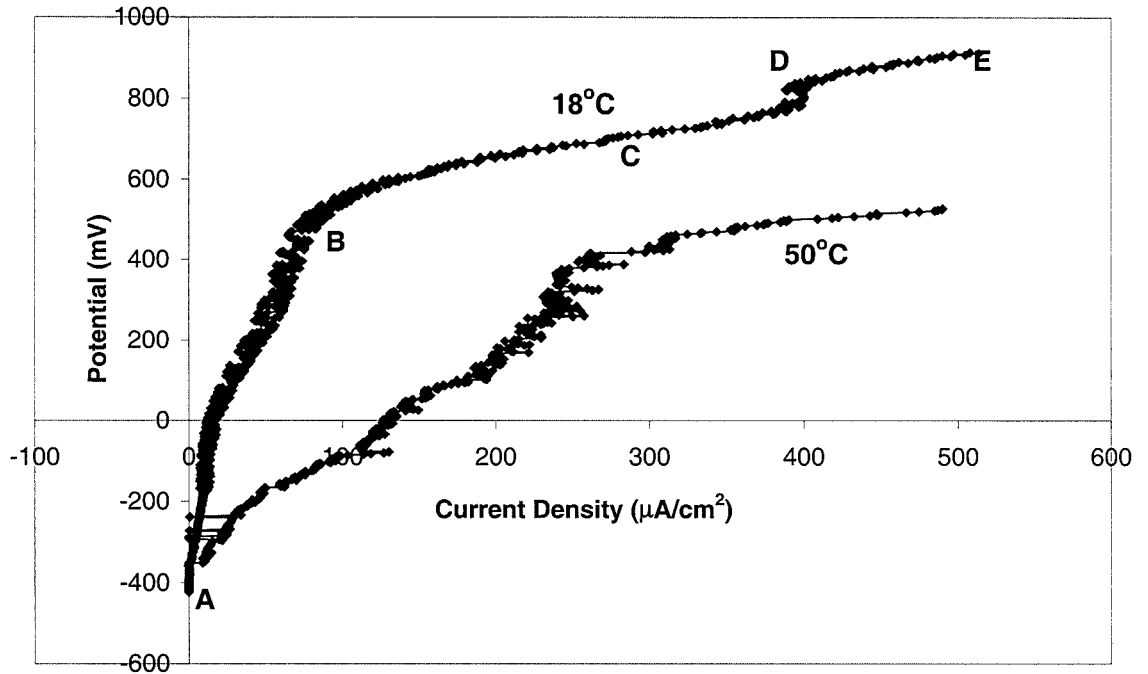


Figure 5-20 Anodic polarisation of WC-Co-Cr in artificial seawater

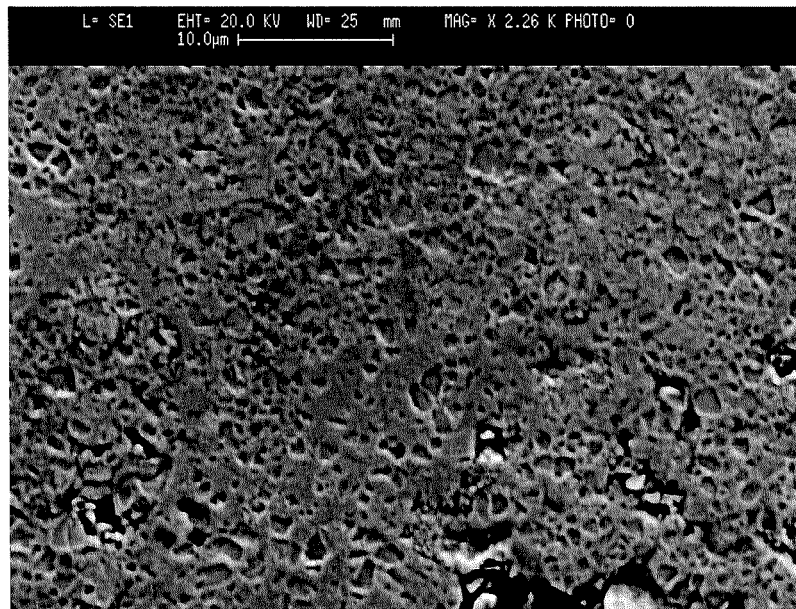
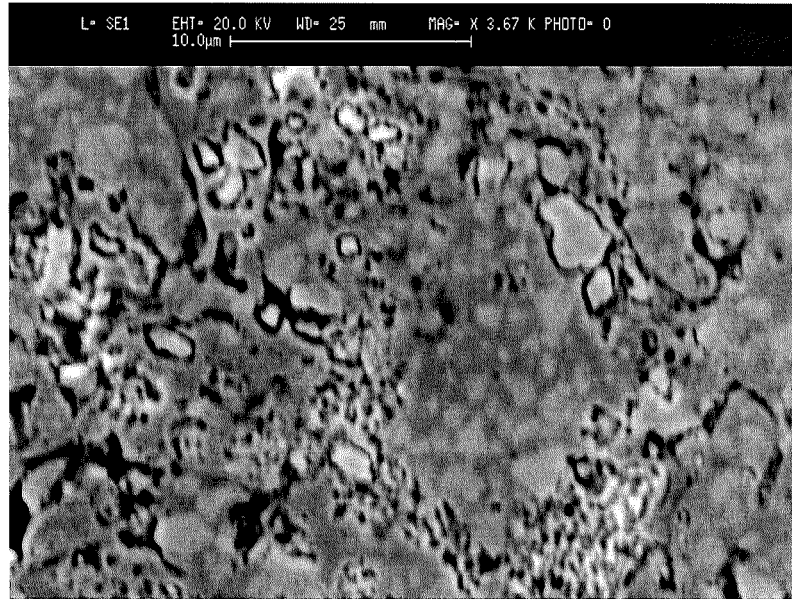
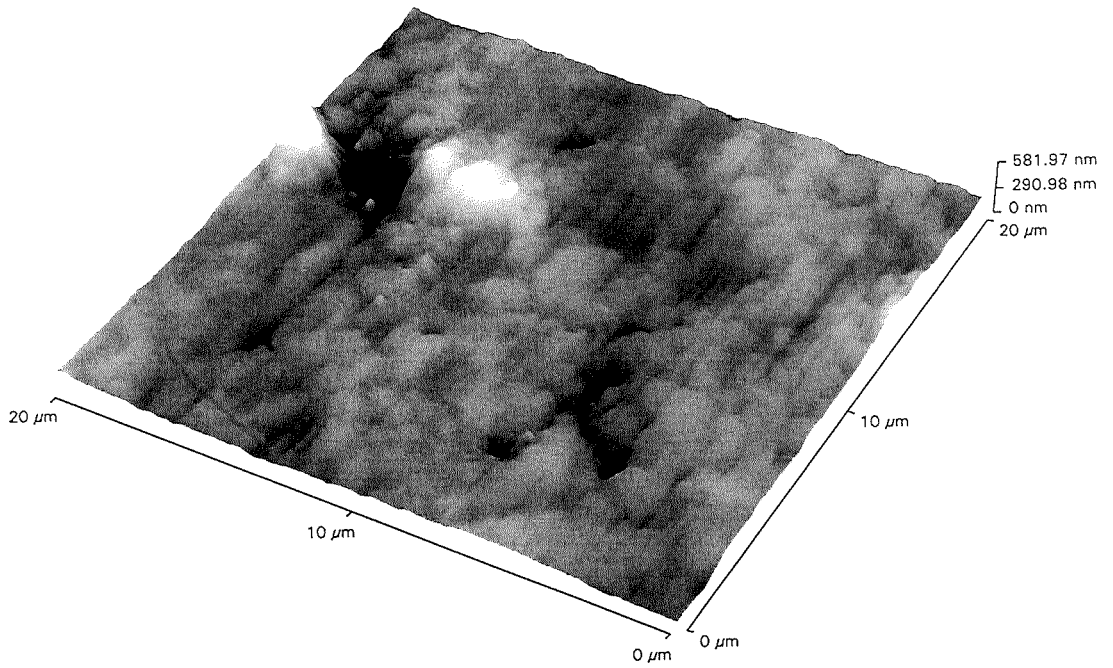


Figure 5-21 SEM Micrograph of WC-Co-Cr after polarisation at 18°C



**Figure 5-22 SEM micrograph of WC-Co-Cr after polarisation at 50°C**

The 3-D AFM images show the progression of the corrosive attack as a function of applied potential after immersion in seawater for 1 hour at 18°C. The scan covers a 20µm x 20µm area of the coating with the height taken from a constant arbitrary zero. The initial scan (Figure 5-23) at the rest potential shows the lighter grey hard phases encased in a darker grey matrix with an overall height of 581nm. As the potential is scanned more positive than  $E_{\text{corr}}$ , the current increases slowly to point B on Figure 5-20 and smaller carbide particles are more pronounced within the matrix (Figure 5-24) and the overall depth has not altered much (470nm). A more rapid rise in current with potential to point C, with an increase in depth (730nm) corresponds to dramatic matrix dissolution and leaves the hard phase protruding from the matrix (Figure 5-25). As the current stabilises at point D carbides begin to fall out from the matrix and leave voids behind also increasing the overall depth to 818nm (Figure 5-26). This progresses until the end of the scan at point E where the matrix consists mainly of voids left by the carbide particles and a few carbides on the next layer are visible and the overall depth has now decreased to 448nm (Figure 5-27). A line scan (Figure 5-28) highlights the voids left by the carbides.



**Figure 5-23 AFM Image of WC-CoCr coating at point A**

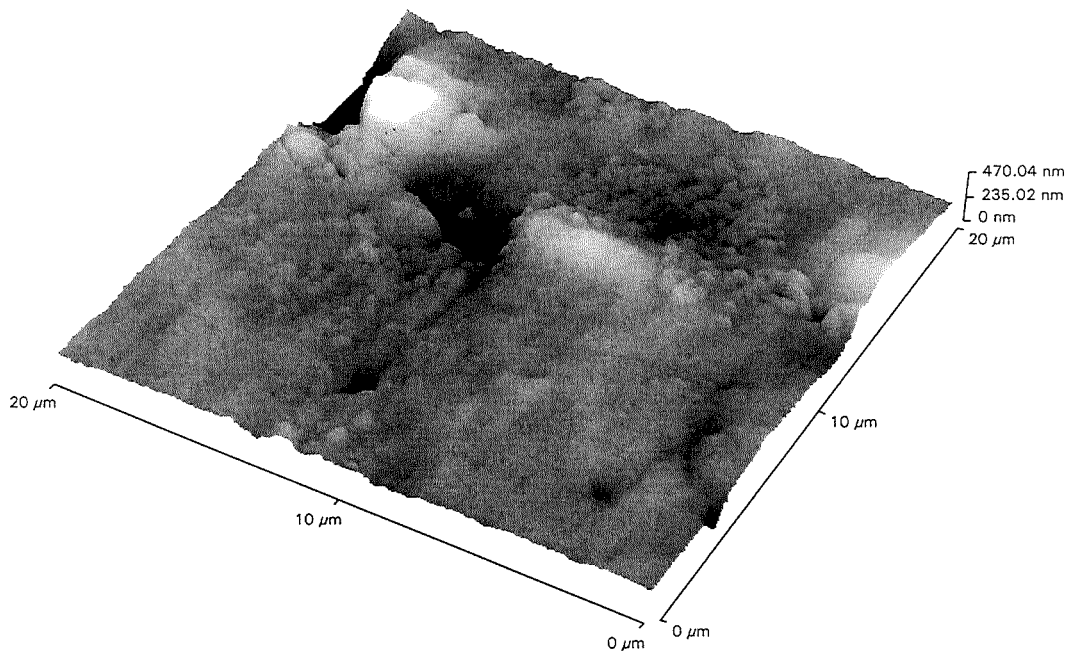


**Figure 5-24 AFM image of WC-CoCr coating a point B**

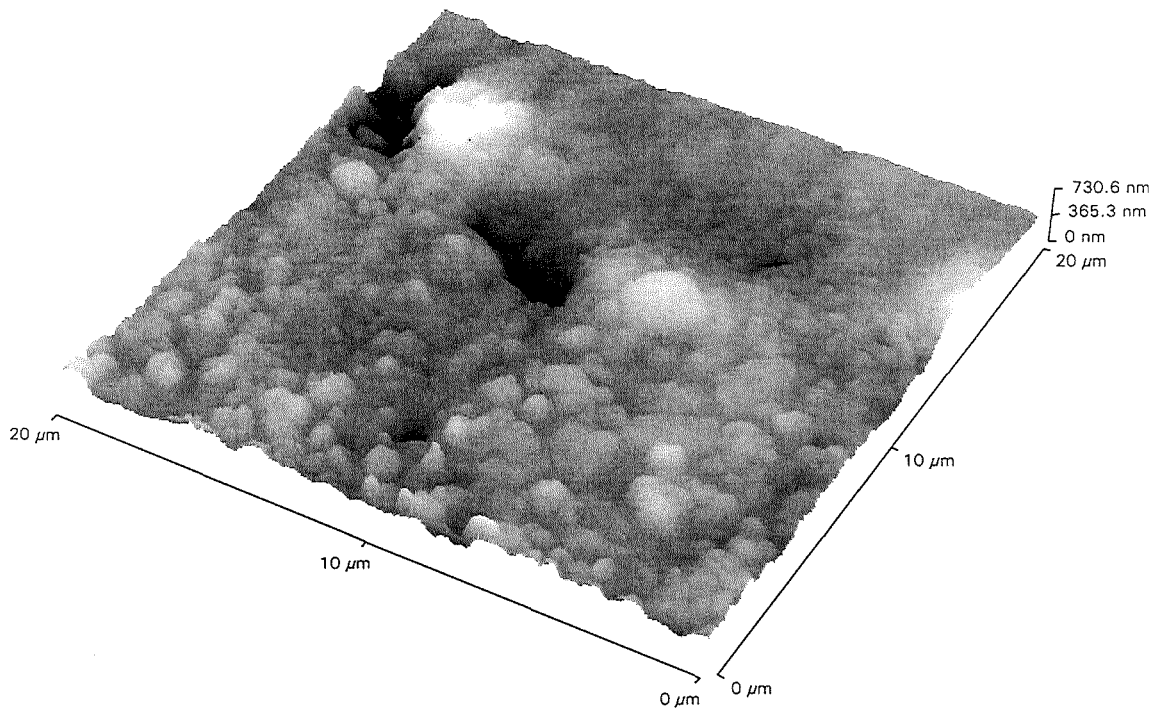


**Figure 5-25 AFM image of WC-CoCr coating at point C**

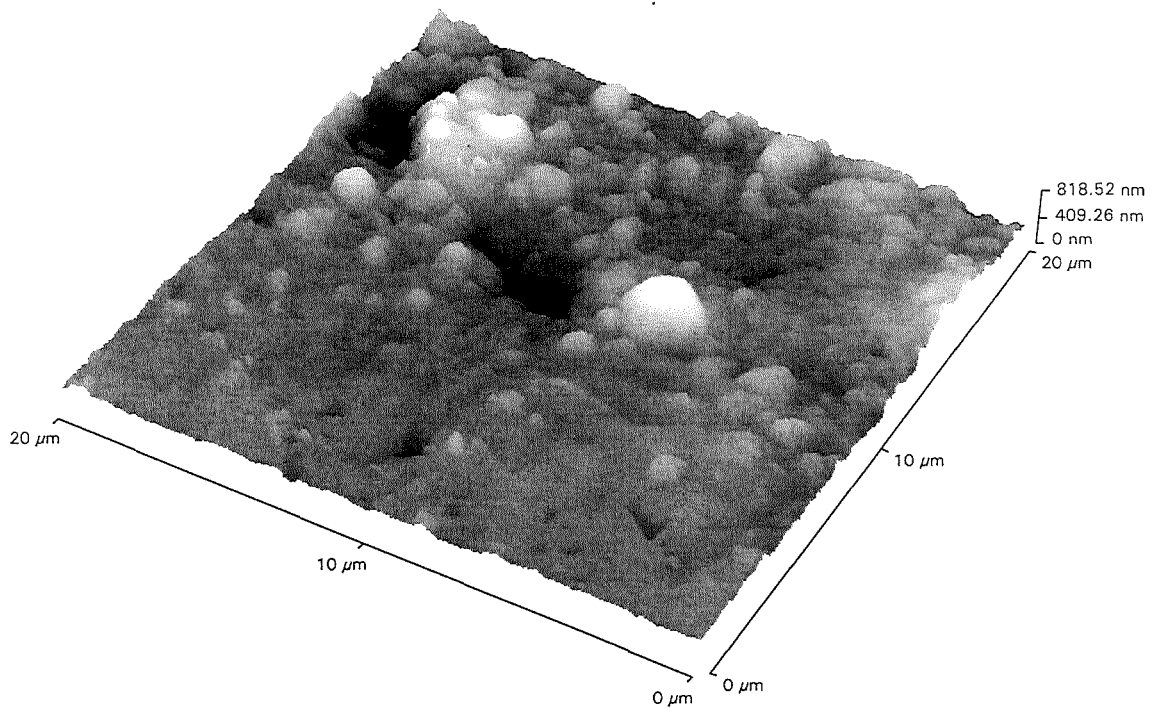


**Figure 5-26 AFM image of WC-CoCr coating at point D**

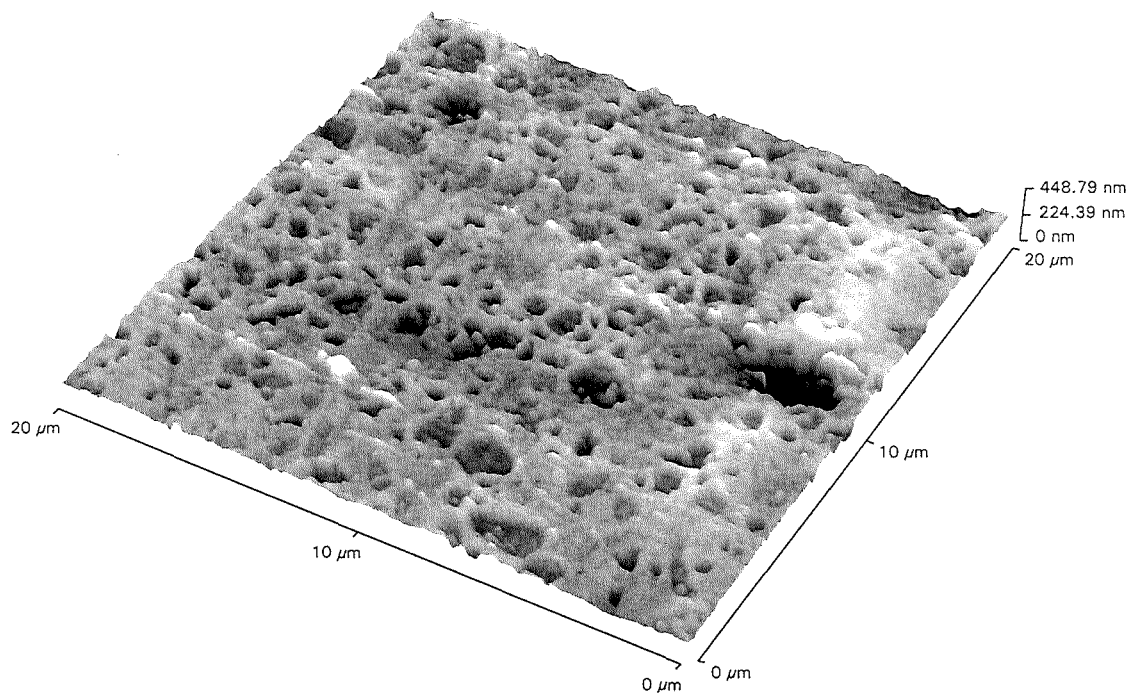


**Figure 5-27 AFM image of WC-CoCr coating at point E**

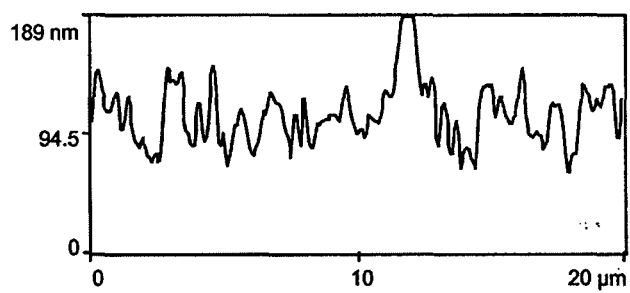


**Figure 5-28 Line scan of coating 2 after anodic polarisation at 18°C**

### 5.3.3 Cathodic Polarisation Tests

Figure 5-29 shows cathodic polarisation tests after one hour immersion at 18°C and 50°C. At 18°C the graph shows a typical response for concentration polarisation, with a limiting current density at 20  $\mu\text{A}/\text{cm}^2$ . The cathodic current then increases as the potential is pushed further negative and the onset of hydrogen evolution occurs. At 50°C the curve is initially indicative of Tafel behaviour and again hydrogen evolution enhances the cathodic current.

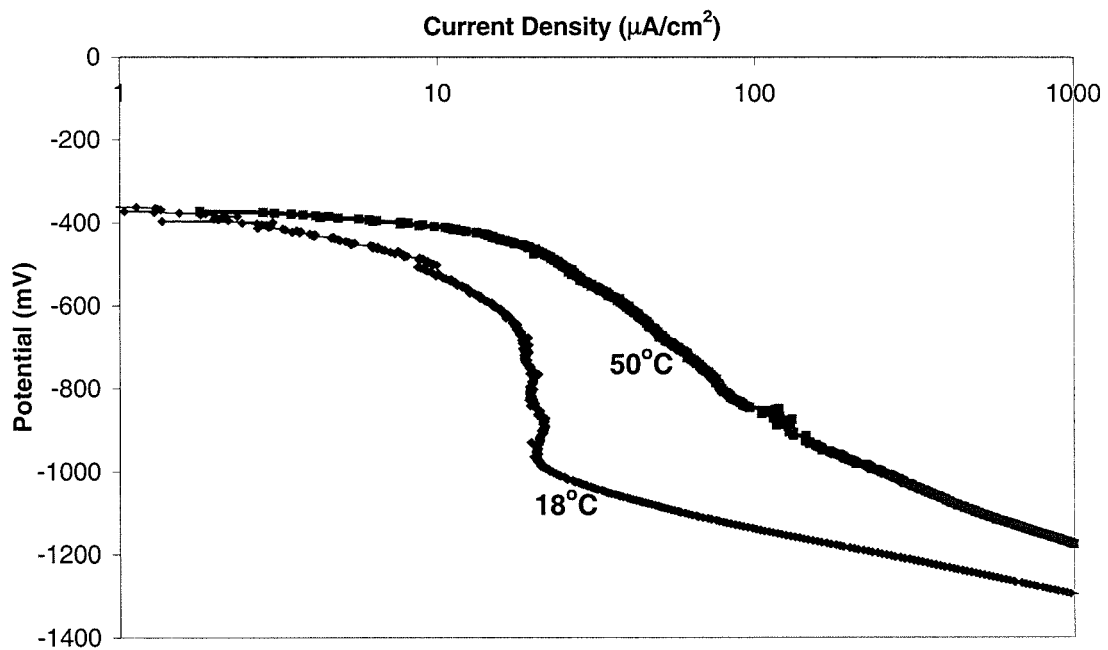


**Figure 5-29 Cathodic Polarisation of WC-Co-Cr after one hour immersion**

## 5.4 Coating 3

### 5.4.1 Coating Characterisation

Coating 3 is a WC-Co coating of nominal composition WC-86%-Co14%. The results from EDX analysis, over a  $30\mu\text{m} \times 30\mu\text{m}$  area, are shown in Table 5-7. Figure 5-30 shows a polished cross-section of the coating with a range of size of hard phase particles ( $<5\mu\text{m}$ ) distributed within the matrix. The XRD trace for the sprayed coating is shown in Figure 5-31 again shows evidence of limited decarburisation by the presence of  $\text{W}_2\text{C}$ .

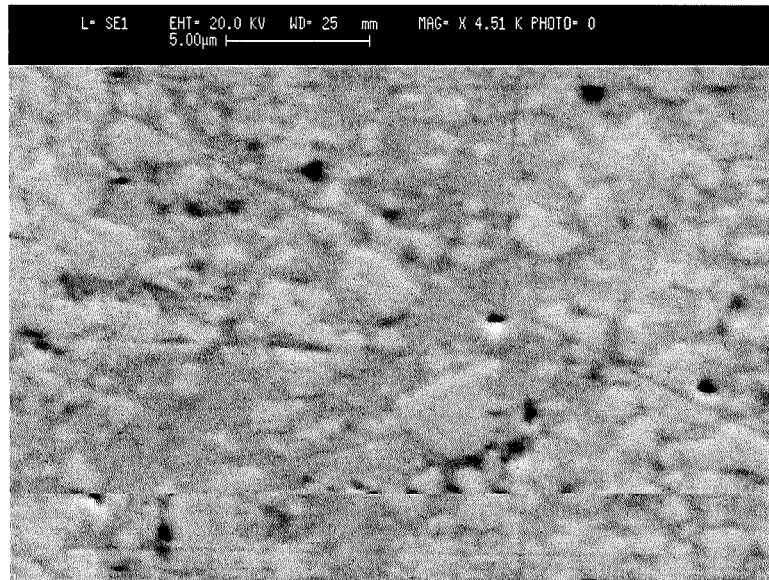


**Figure 5-30 Polished cross-section of WC-Co coating**

Element	Weight %
W	87-88
Co	12-13

**Table 5-7 Chemical composition of the WC-Co coating 3 measured using the EDAX facility on the SEM**

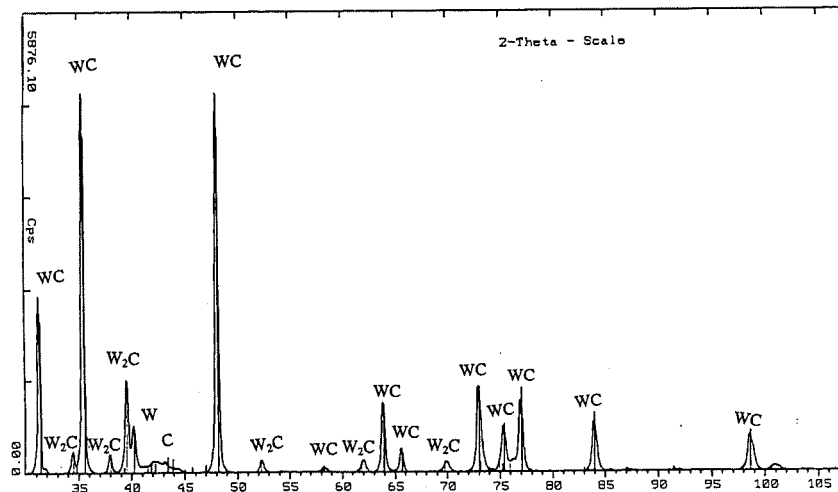


**Figure 5-31 XRD of WC-Co-Cr spray coating**

#### 5.4.2 Static Corrosion Behaviour

The response when the coating is anodically polarised after immersion for one hour in artificial seawater at 18°C and 50°C is shown in Figure 5-32. At 18°C, after an initial relatively slow rise in current with potential the current then increases more rapidly with potential to a value of 590 $\mu$ A/cm<sup>2</sup> (behaviour akin to active corrosion) but then the corrosion current reduces until a potential of +400 mV then increases at a constant rate until +600 mV which is a breakdown potential and an increase in corrosion current. SEM examination after the polarisation tests found general attack on the surface (Figure 5-33) and crevice attack initiating at the carbide/hard phase interface. When the temperature is increased to 50°C, the increase in current with potential is more rapid, quite similar to an active material. This results in extensive attack on the matrix with the hard phase particles standing proud of the matrix (Figure 5-34).

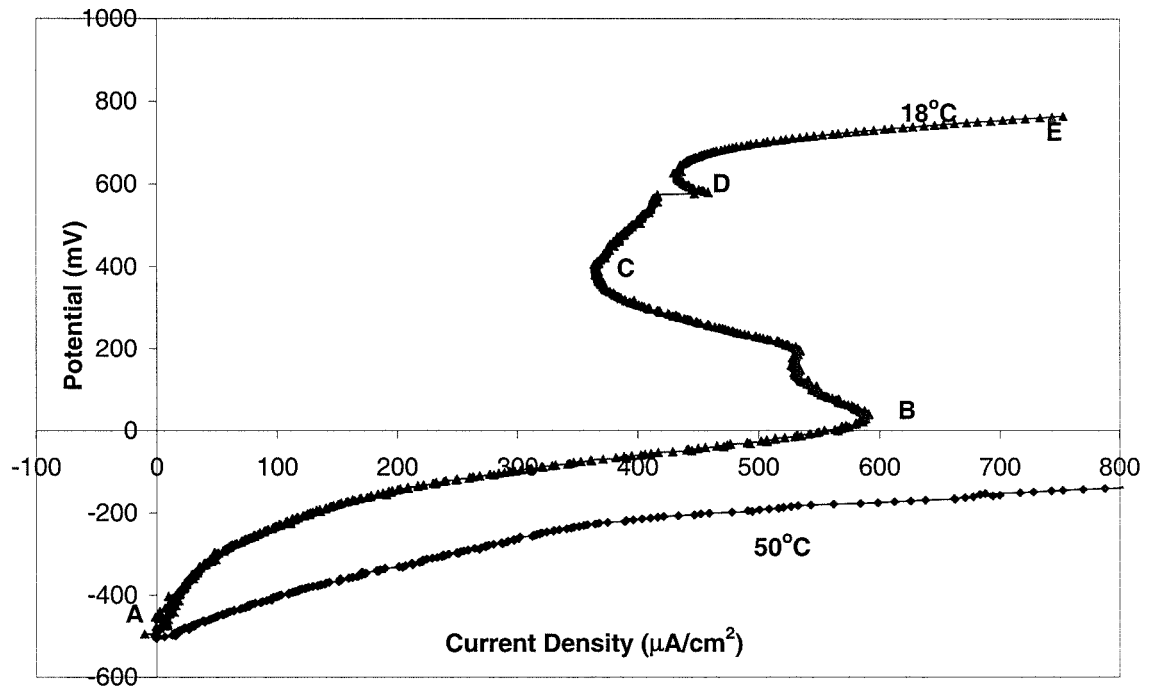


**Figure 5-32 Anodic polarisation of WC-Co coating**

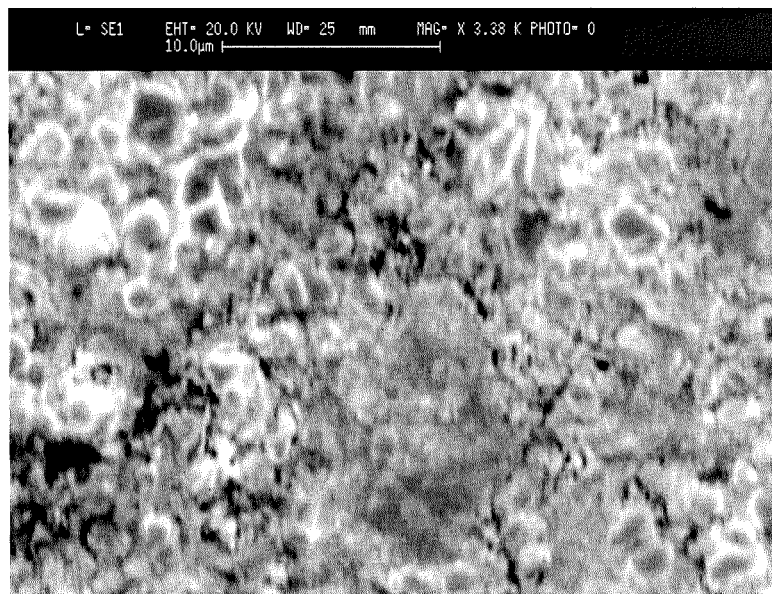


**Figure 5-33 SEM micrograph after anodic polarisation at 18°C of WC-Co coating**

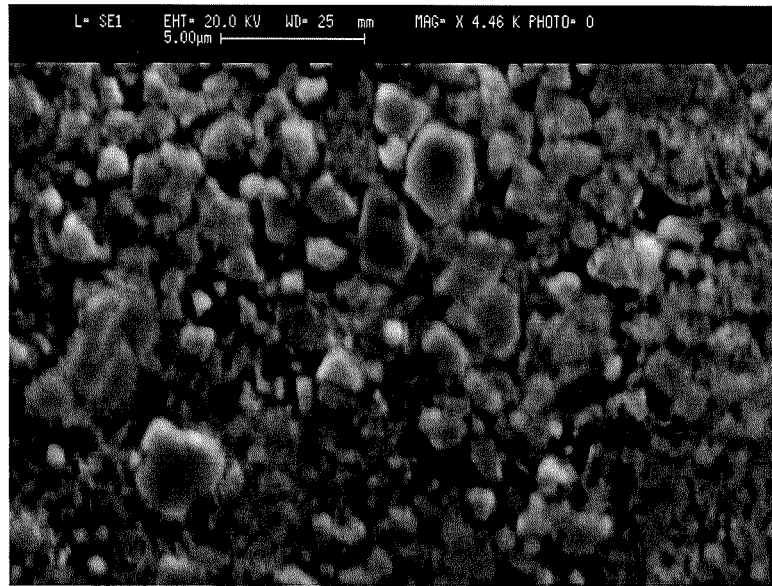


**Figure 5-34 SEM micrograph of WC-Co coating after anodic polarisation at 50°C**

In an attempt to determine the mechanisms of corrosive attack, a scan of the surface topography with an AFM was taken during the anodic polarisation. The initial scan at the free corrosion potential (Figure 5-35) shows the surface of the polished coating with slight spikes due to polishing effects. As the potential is scanned more positive up to point B in Figure 5-32, the surface is smoothed and extensive matrix dissolution has occurred, showing clearly the hard phase particles (Figure 5-36). During the decrease in current range (B to C), the matrix is dissolving at a steady rate, defining the hard phase particles more clearly (Figure 5-37). As the current rises (C to D), the matrix dissolves further revealing the smaller hard phase particles (Figure 5-38) and even more so from D to E (Figure 5-39). Again at the end of the scan, areas where the matrix has dissolved in some regions and attack around the matrix hard phase/interface can be seen (Figure 5-40).

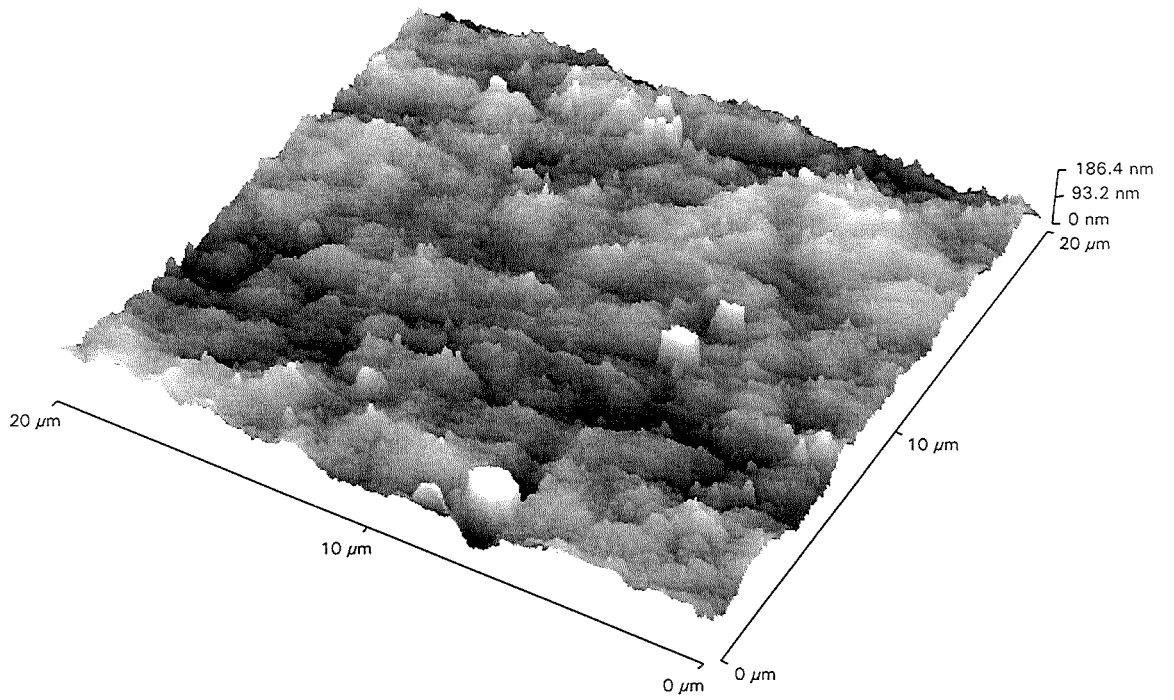


**Figure 5-35 AFM Image of WC-Co coating at point A**

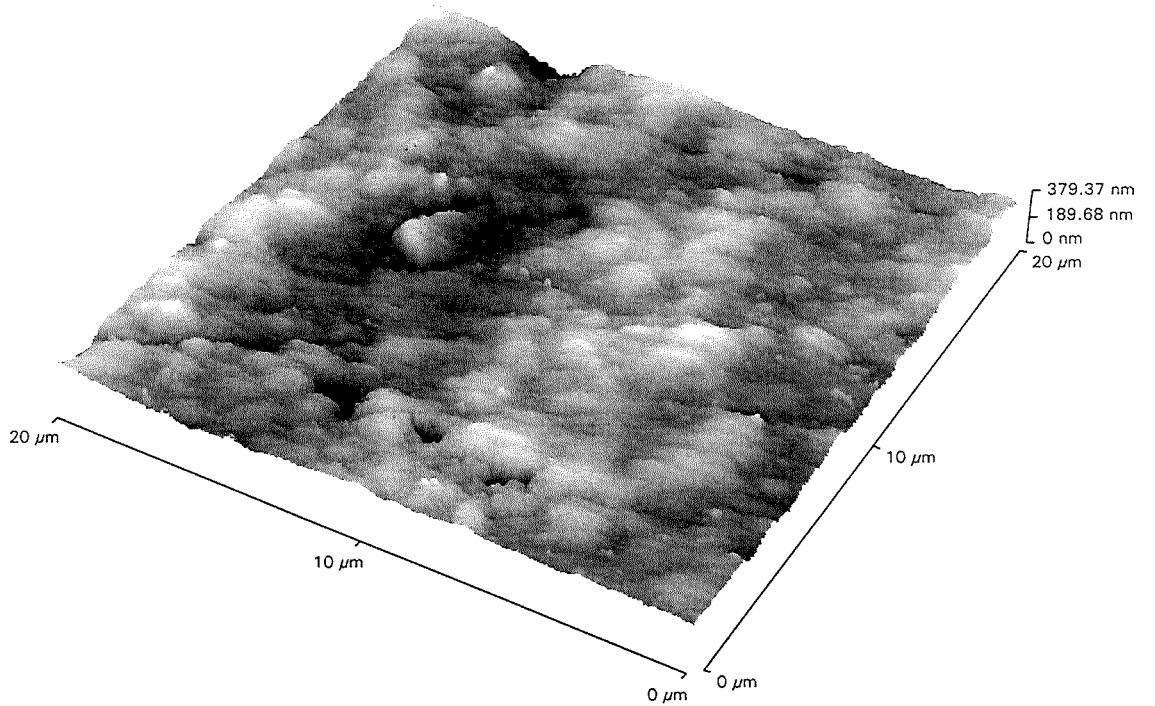


**Figure 5-36 AFM image of WC-Co coating at point A to B**

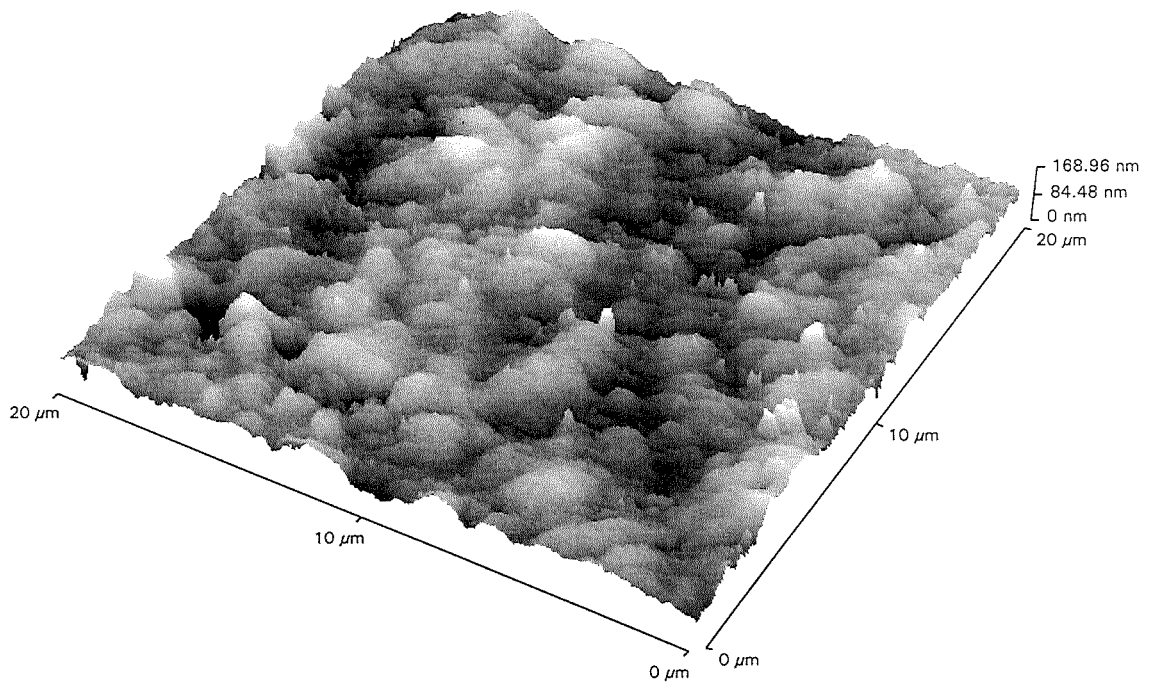


**Figure 5-37 AFM image of WC-Co Coating at point B to C**

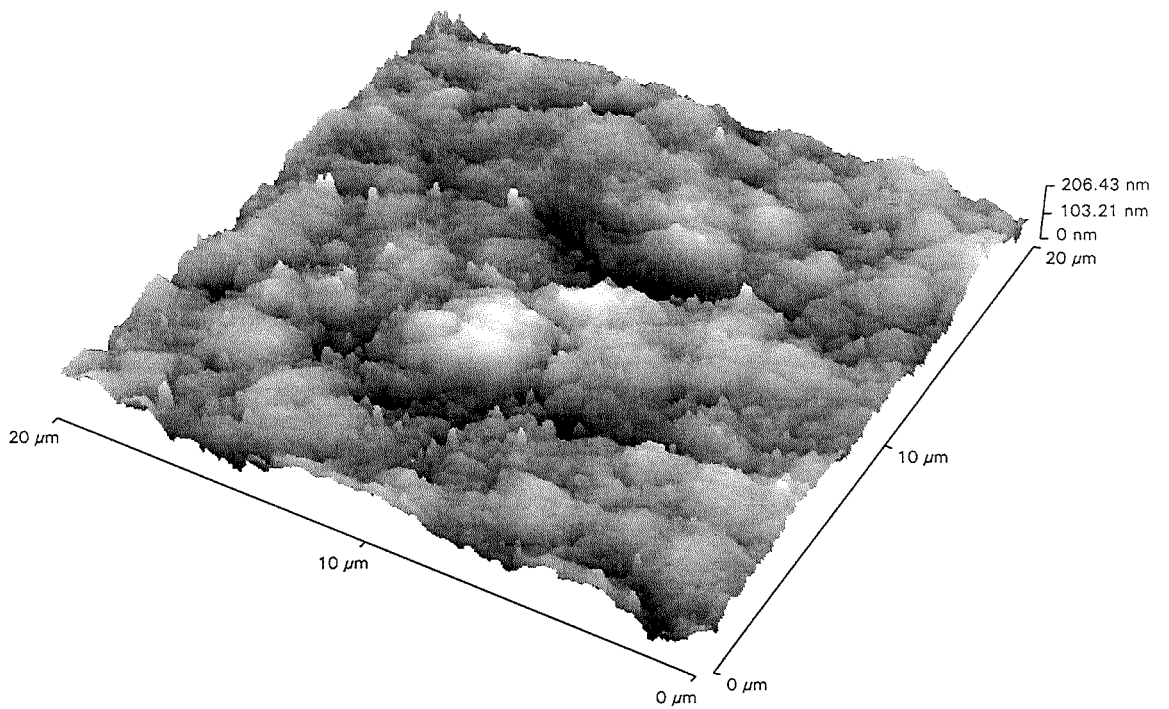


**Figure 5-38 AFM image of WC-Co coating at point C to D**

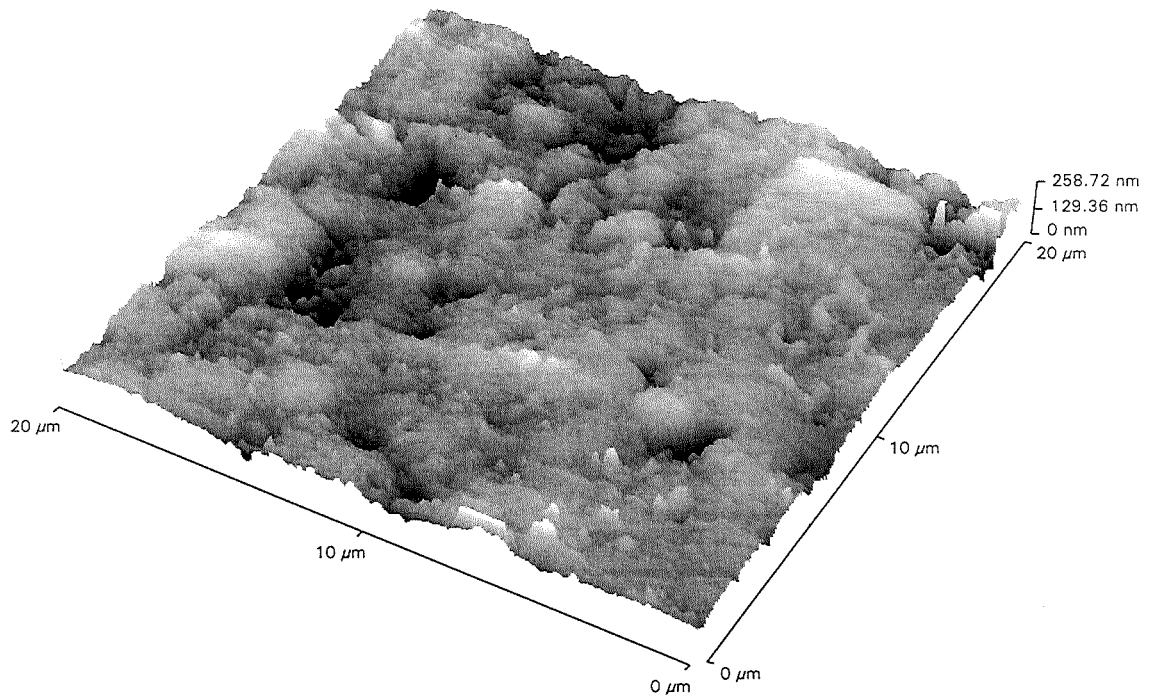


**Figure 5-39 AFM image of WC-Co coating at point D to E**

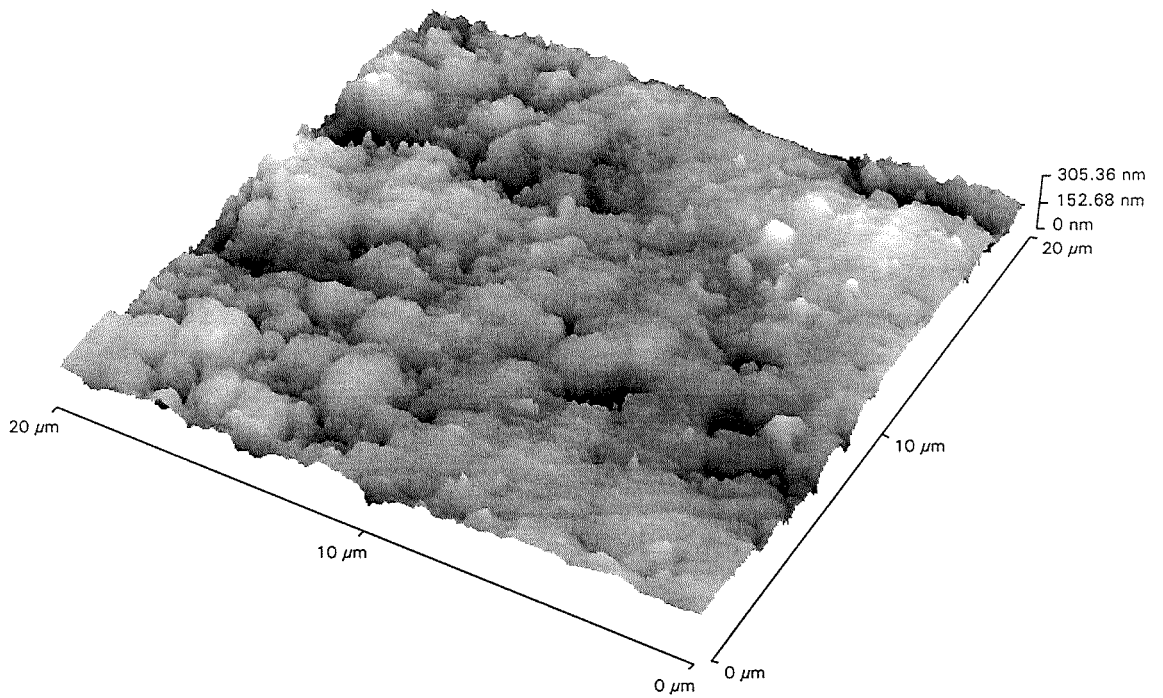


**Figure 5-40 AFM Image WC-Co coating at point E**

### 5.4.3 Cathodic Polarisation Tests

Figure 5-41 shows the cathodic polarisation scan after one hour immersion at 18°C and 50°C. The limiting current density at 18°C is in excess of 30 $\mu\text{A}/\text{cm}^2$  and at 50°C is 200 $\mu\text{A}/\text{cm}^2$  before the onset of hydrogen evolution. This will be discussed later.

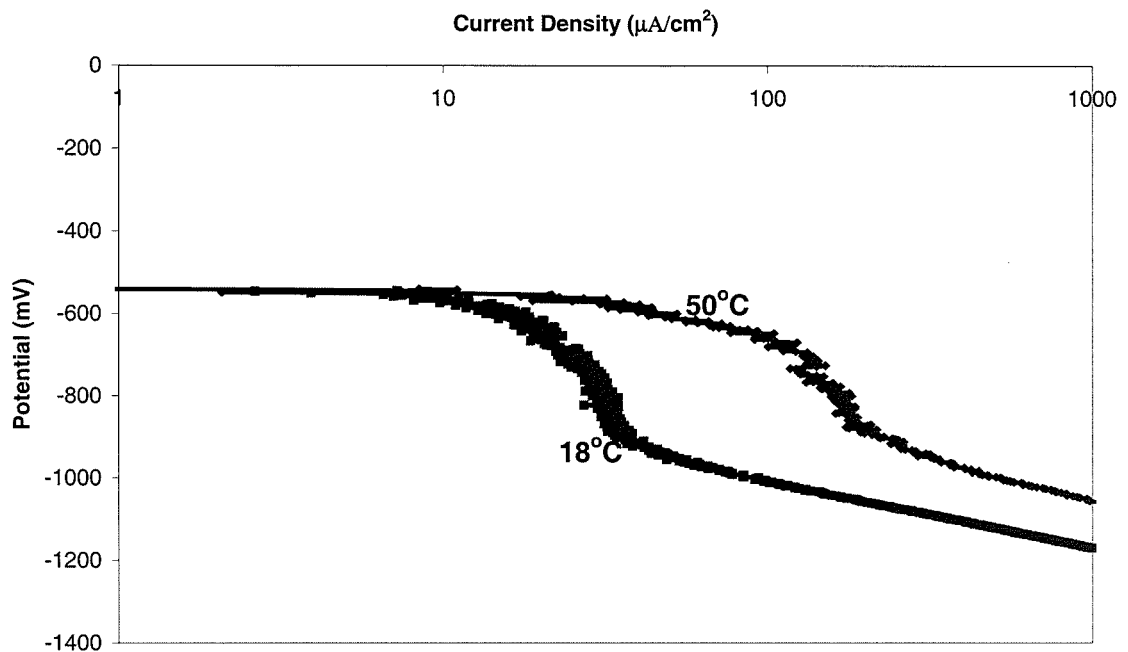
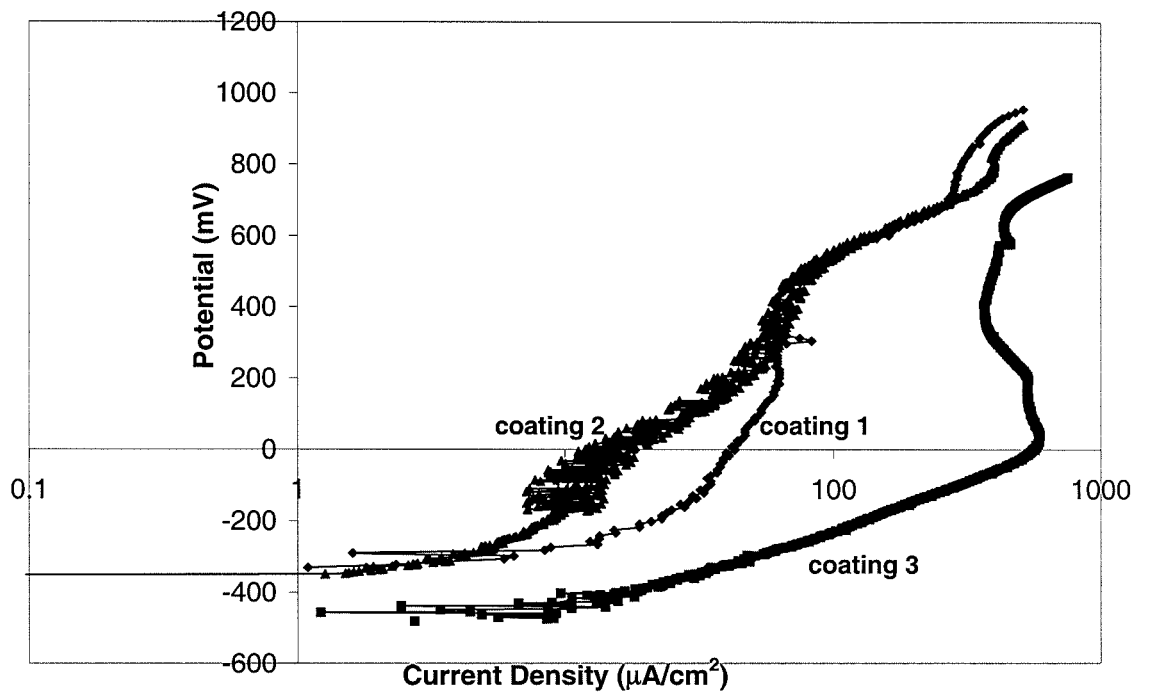


Figure 5-41 Cathodic polarisation tests of WC-Co after one hour immersion

### 5.5 Summary and Comparison of Coatings

Of the three coatings presented here, the two WC-CoCr coatings can be considered the same since they have similar composition, microstructure and corrosion behaviour. Figure 5-42 shows a semi-log plot of the coatings' corrosion behaviour during anodic polarisation. Coating 1 and 2, the WC-CoCr coatings show similar complex behaviour during the anodic polarisation with lower corrosion currents than coating 3- the WC-Co coating. This coating shows more general attack on the matrix (Figure 5-43) and some attack at the hard phase matrix interface. The matrix has dissolved leaving the carbides standing proud. The WC-CoCr coating (Figure 5-44) has attack focused on the hard phase matrix interface resulting in general loss of carbides.



**Figure 5-42 Semi-log plots of anodic polarisation of all three coatings after one hour immersion at 18°C**

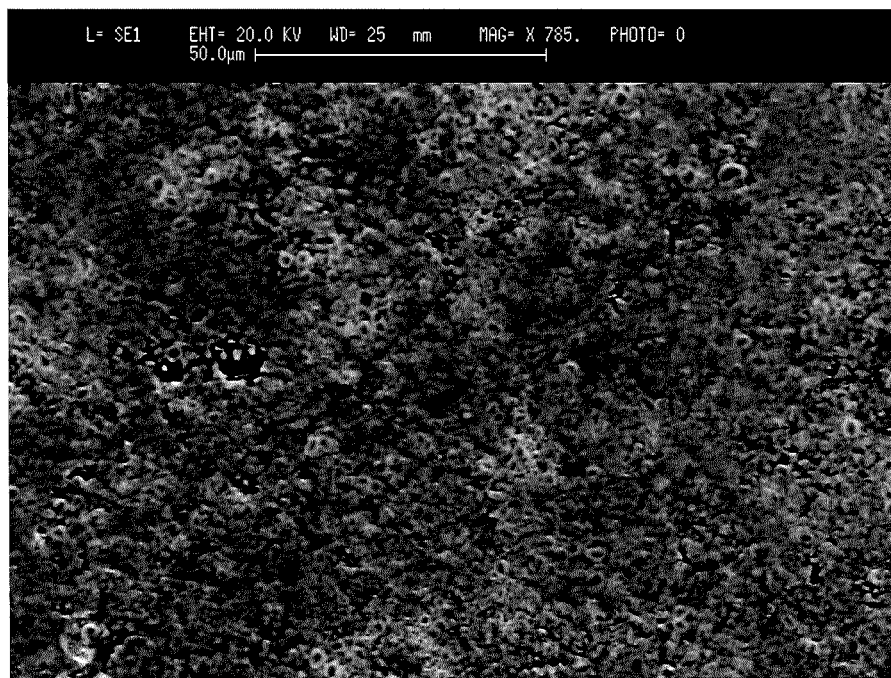


**Figure 5-43 Micrograph of WC-Co after anodic polarisation at 18°C showing general corrosion**



**Figure 5-44 Micrograph of WC-CoCr coating after anodic polarisation at 18°C showing the removed hard phases**

At 50°C, again the two WC-Co-Cr coatings behave similarly during anodic polarisation (Figure 5-45) having a notably higher corrosion rate compared to that at 18°C. Again, the WC-Co coating has more general attack on the surface (Figure 5-46) due to general matrix dissolution, whereas the WC-CoCr coating has areas of localised attack (Figure 5-47).

Table 5-8 summarises the corrosion rates for all three coatings at the two temperatures. The two WC-CoCr coatings corrosion rates all fall within similar ranges, with the corrosion rates falling predominantly in the 3-6µA/cm<sup>2</sup> range with a scatter of one point on each case reaching 9µA/cm<sup>2</sup> and 10µA/cm<sup>2</sup>. At 50°C, the corrosion rate is almost double that at 18°C (not including the highest rates found). The coating with only a cobalt matrix has a higher corrosion rate (9 to 11µA/cm<sup>2</sup>), which is accentuated at 50°C where the corrosion rate is 16µA/cm<sup>2</sup>.

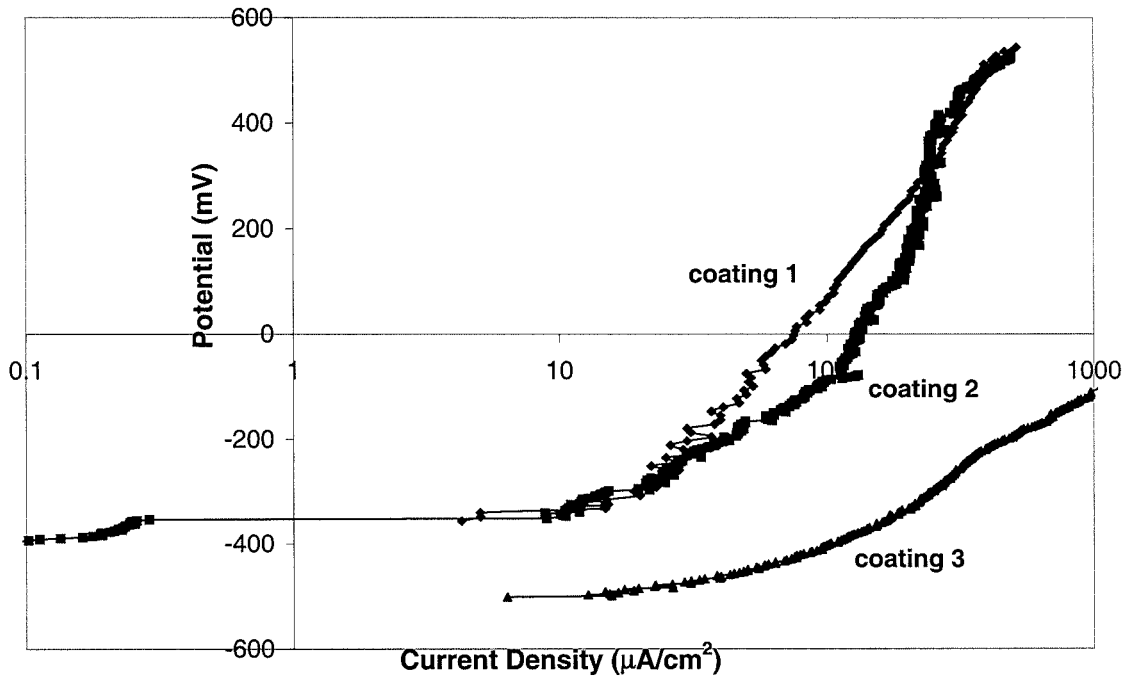


**Figure 5-45 Semi log plot of anodic polarisations of all three coatings after one hour immersion at 50°C**

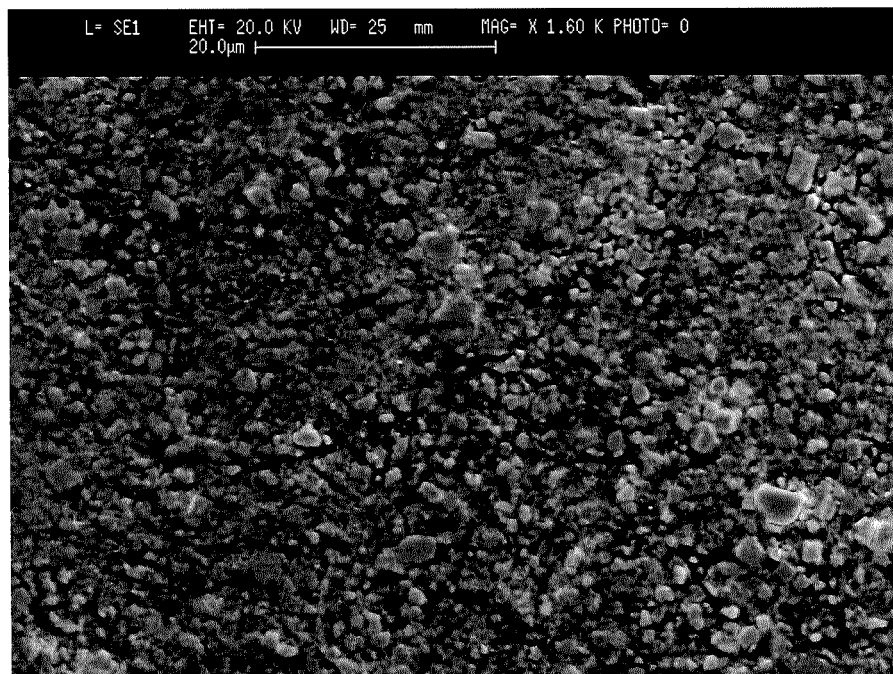


**Figure 5-46 Micrograph of WC-Co coating after anodic polarisation at 50°C showing severe matrix dissolution**

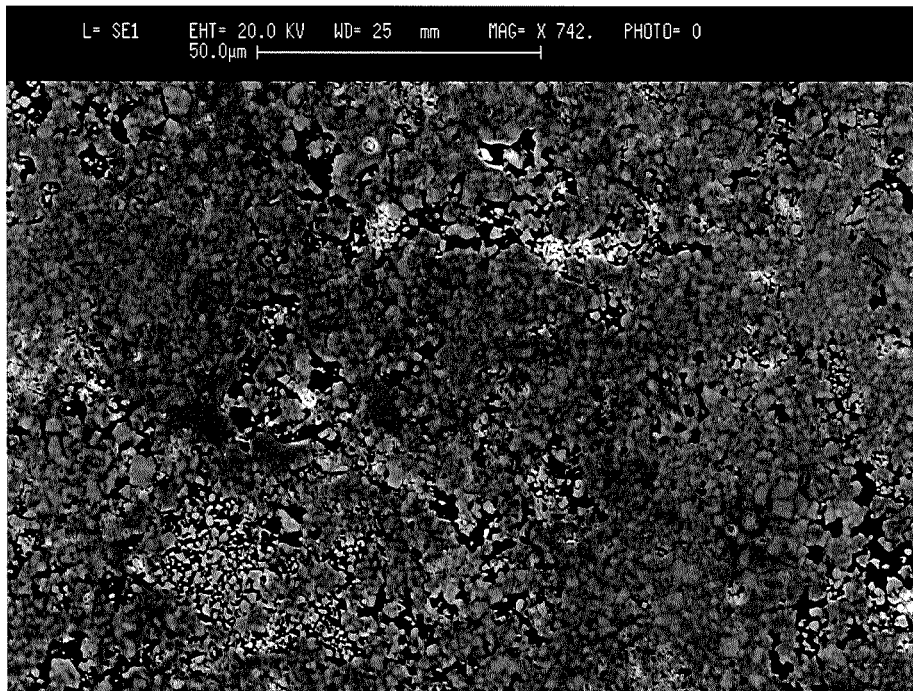


**Figure 5-47 Micrograph of WC-CoCr coating after anodic polarisation at 50°C showing localised areas of attack**

Coating	$I_{\text{corr}}$ ( $\mu\text{A}/\text{cm}^2$ )	
	18°C	50°C
WC-Co-Cr I	5, 6, 10	9, 12
WC-Co-Cr II	3, 4, 9	10, 12
WC-Co	9, 10, 11	16

**Table 5-8 Static corrosion rates for replicate experiments on all three coatings**

# Chapter 6

## Erosion-Corrosion under Liquid Impingement and Liquid-Solid Impingement

### 6.1 Introduction

This chapter initially assesses the corrosion rates under liquid and liquid solid impingement conditions on coating 1, the WC-Co-Cr coating. These corrosion rates are calculated by taking into consideration any residual cathodic currents assumed to exist as the potential is pushed in the anodic direction as explained in section 4.5. An example of how residual cathodic currents are taken into account is shown in Figure 6-1. This shows an extrapolation from the Tafel region on the cathodic polarisation curve into the anodic polarisation region. The residual cathodic currents which were in the region of  $0-9 \mu\text{A}/\text{cm}^2$  in the normalised potential range  $0-200\text{mV}$  are then added to the measured anodic currents. This clarifies the Tafel region which gives rise to a more accurate measurement of  $I_{\text{corr}}$ . In some instances, the residual cathodic currents amount to low currents at low potentials which do not transfer any significant changes in the measured anodic currents. A collection of all the cathodic scans and 'corrected' anodic scans are presented in Appendix 1.

Corrosion rates at  $18^\circ\text{C}$  and  $50^\circ\text{C}$  under liquid impingement conditions are assessed and the effect of time is quantified. The corrosion rates when solids are added to the liquid stream are then determined, and the corrosion rates as a function of time are assessed. Subsequently, the overall degradation of the material under liquid-solid erosion-corrosion is quantified which incorporates the contributions from pure mechanical erosion, pure corrosion and the indirect contribution from corrosion on erosion – referred to as synergy. In the later parts of this chapter, assessment of the erosion-corrosion damage through microscopy and surface profiling techniques are presented. As with previous chapters, replicate polarisation curves are collated in Appendix 1.

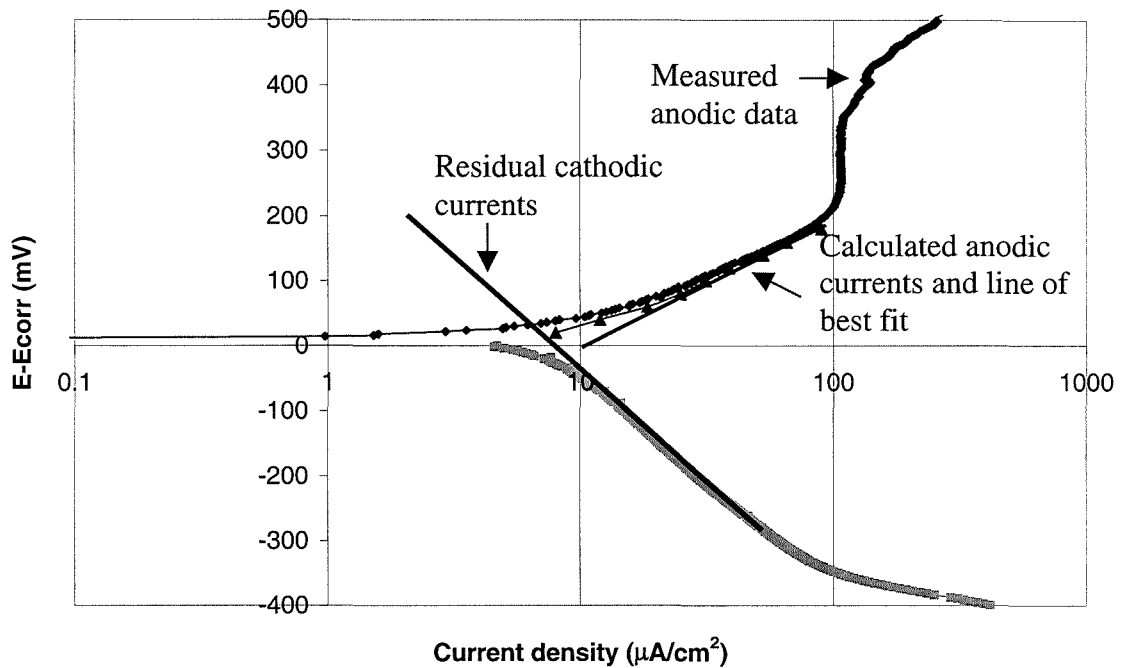


**Figure 6-1 Example of corrected anodic currents incorporating residual cathodic currents at 4 hours impingement with 170 mg/l solids in 3.5% NaCl at 18°C**

## **6.2 Corrosion effects under liquid (no solids) impingement at 18°C and 50°C**

### **6.2.1 Anodic Polarisation**

Figure 6-2 shows in-situ anodic polarisation scans after one and four hours at 18°C and 50°C at 90° impingement; also incorporated is the anodic polarisation curve after one hour in static conditions for comparison. The anodic polarisation curve associated with this coating under liquid impingement conditions is similar in form to that observed in static conditions. After one hour impingement, a more rapid rise in current to reach a stable current was observed than in static conditions and only one breakdown potential was observed at a more negative potential (+400mV) in comparison with the two breakdown potentials in static conditions (at +500 mV and +800mV). As the impingement time is extended to four hours, the characteristic shape disappears and the current continues to increase without any stabilisation of the current or noticeable breakdown

potential. As in static conditions, as shown in the previous chapter, increasing the temperature to 50°C in impingement conditions induces an increase in corrosion rate as shown in Figure 6-2.

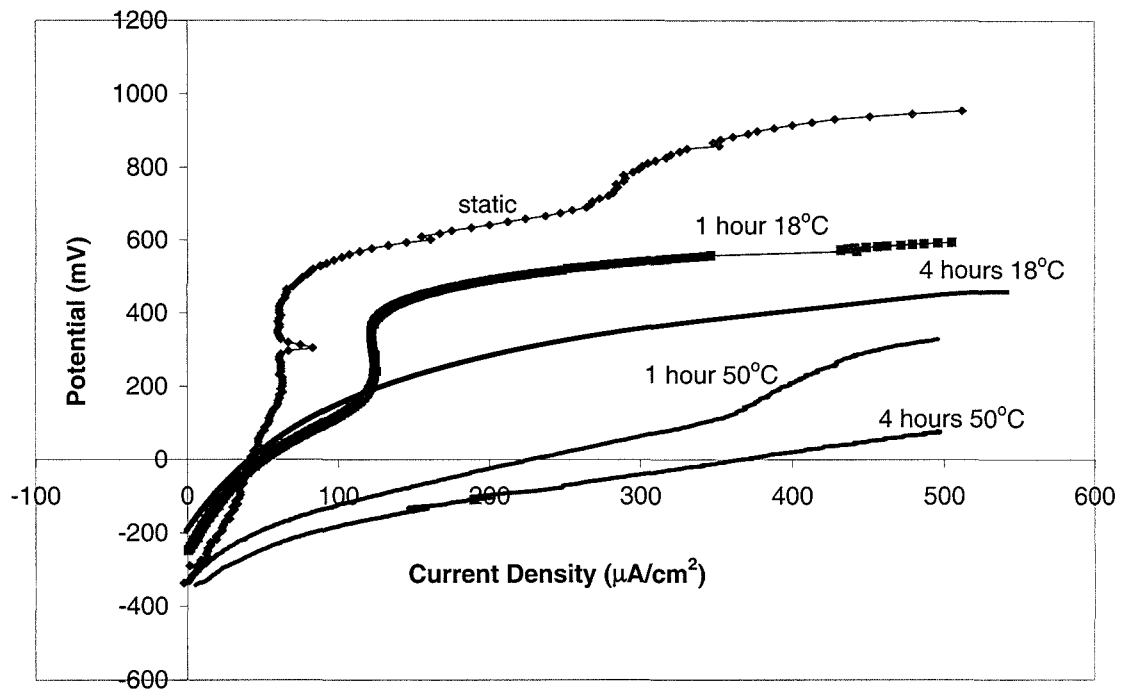


**Figure 6-2 Anodic polarisation scans under liquid impinging jet at  $12\text{ms}^{-1}$  in 3.5% NaCl**

### 6.2.2 Cathodic Polarisation

The corresponding cathodic polarisation scans are shown in Figure 6-3. The cathodic currents under liquid impingement conditions are higher than in static conditions, as expected, due to the highly turbulent conditions minimising limiting current effects. The temperature in impingement conditions does not seem to have an effect on the depolarisation process however, there appears to be an increase in cathodic current as the time is extended to 4 hours.

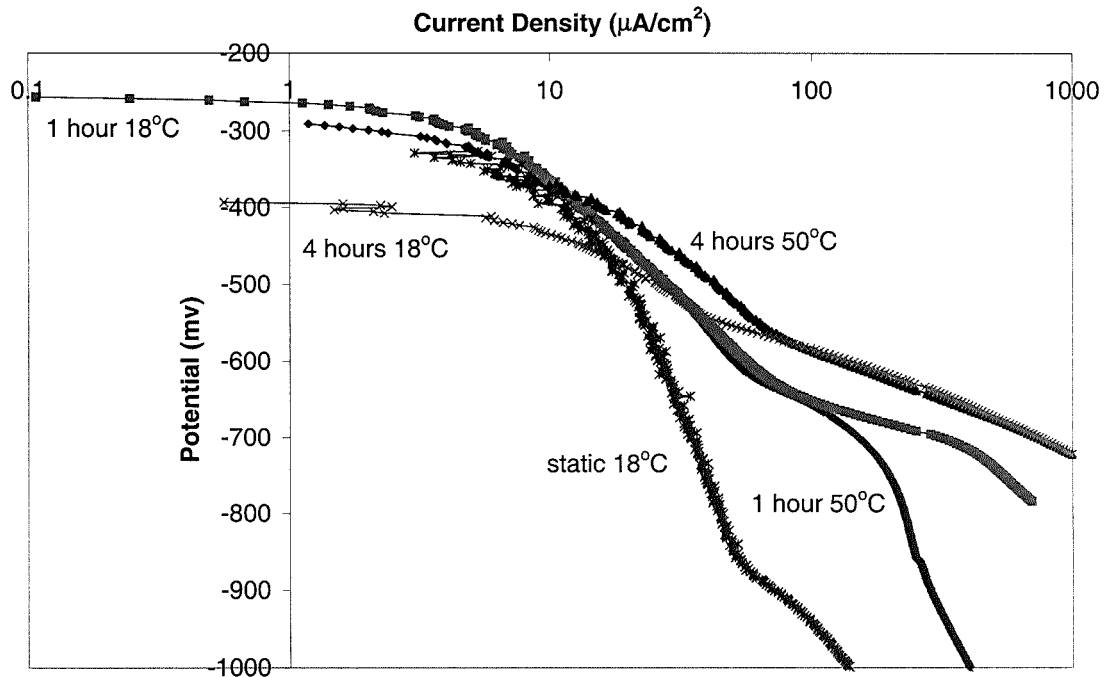


**Figure 6-3 Cathodic polarisation scan under a liquid impinging jet at  $12\text{ms}^{-1}$  in 3.5% NaCl**

### 6.2.3 Corrected Tafel Extrapolation

The corrosion current densities were determined by Tafel Extrapolation using the method described in section 4.7 and 6.1 which takes into consideration the residual cathodic current. The results of this procedure are shown in Figure 6-4 where clear linear relationships are apparent. The corrosion rates are found at the intersection of 0mV (i.e.  $E_{\text{corr}}$ ) and the line of best fit through the points. As can be seen, the corrosion rates increase when the time is extended from one hour to four hours at 18°C and at 50°C the corrosion rate at both 1 and 4 hours is substantially higher than at 18°C and a slight increase is noted after 4 hours impingement.

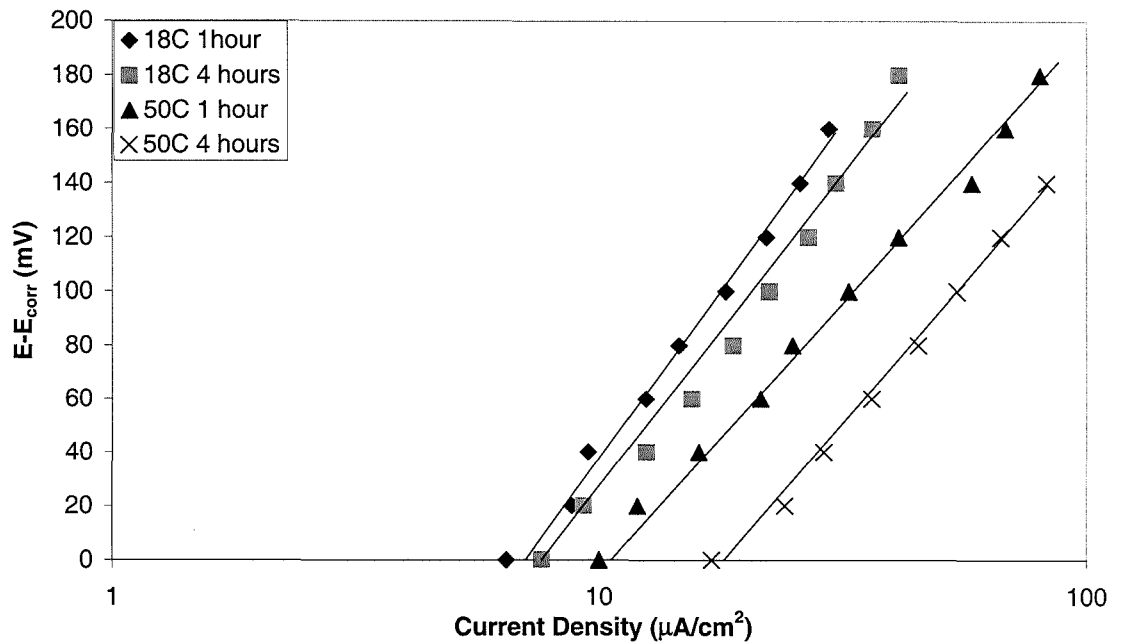


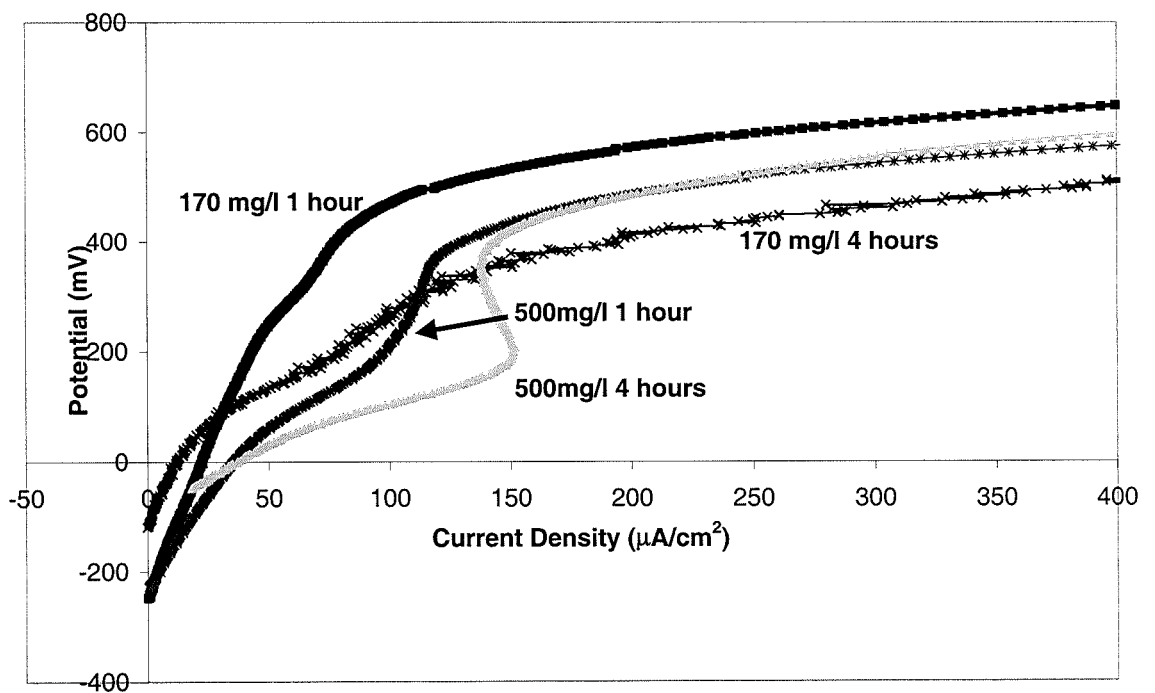
**Figure 6-4 Corrected corrosion currents under liquid impingement conditions**

### 6.3 Corrosion Effects under Solid-Liquid Impingement

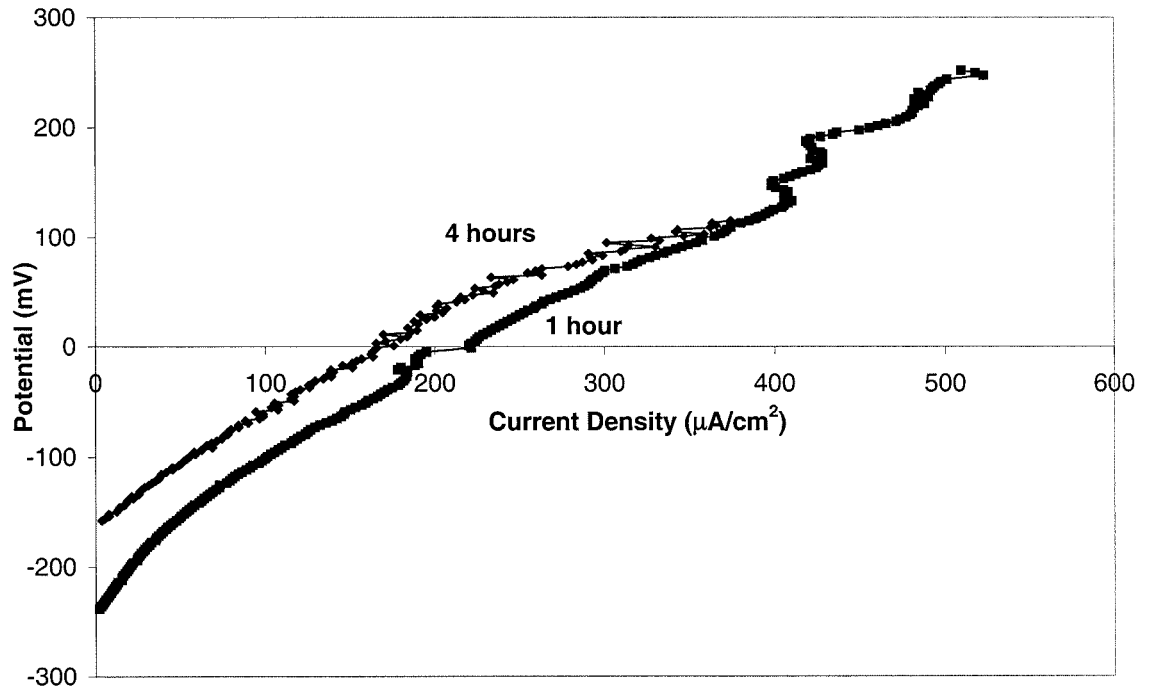
#### 6.3.1 Anodic and Cathodic Polarisation

Figure 6-5 shows the anodic polarisation curves in liquid-solid erosion-corrosion conditions at two solid loadings with 3.5% NaCl solution and impinging at  $90^\circ$ . It can be seen that the characteristic shape of an increasing current, a subsequent constant current, followed by a final breakdown remains even after 4 hours. The corrosion rate measured after 1 hour and 4 hours at 170mg/l remained constant and, when corrected for any residual cathodic current, was comparable with that under liquid impingement conditions (Figure 6-11). After 1 hour at the higher sand loading of 500 mg/l, an increase in the corrosion current was observed, and further increased as the time extended to 4 hours. In addition, at all solid levels (as under liquid impingement conditions) the final breakdown was lowered to +400mV compared with +750mV in static conditions.

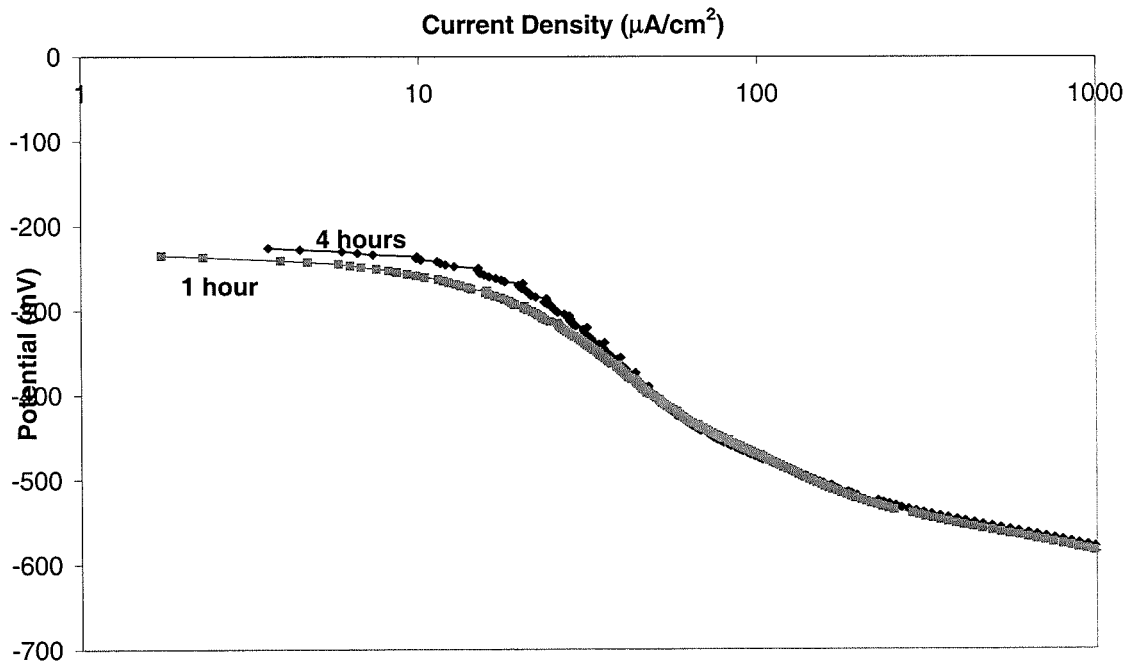
On increasing the temperature to 50°C (Figure 6-6) under liquid-solid conditions at 500mg/l solids, no definite breakdown potential existed; instead an active corrosion response of increasing current with scanning of potential from  $E_{\text{corr}}$  was observed. Again this is rather similar to the behaviour (Figure 6-2) in liquid impinging conditions. Both the anodic (Figure 6-6) and the cathodic (Figure 6-7) polarisation curves indicate no significant difference in corrosion behaviour with the passage of time from 1 hour to 4 hours. However, the higher corrosion currents obtained after 4 hours impingement are indicative of a higher corrosion rate (Figure 6-15).



**Figure 6-5 Anodic polarisations scans under a liquid-solid impinging jet at 18°C at 12 ms<sup>-1</sup>**

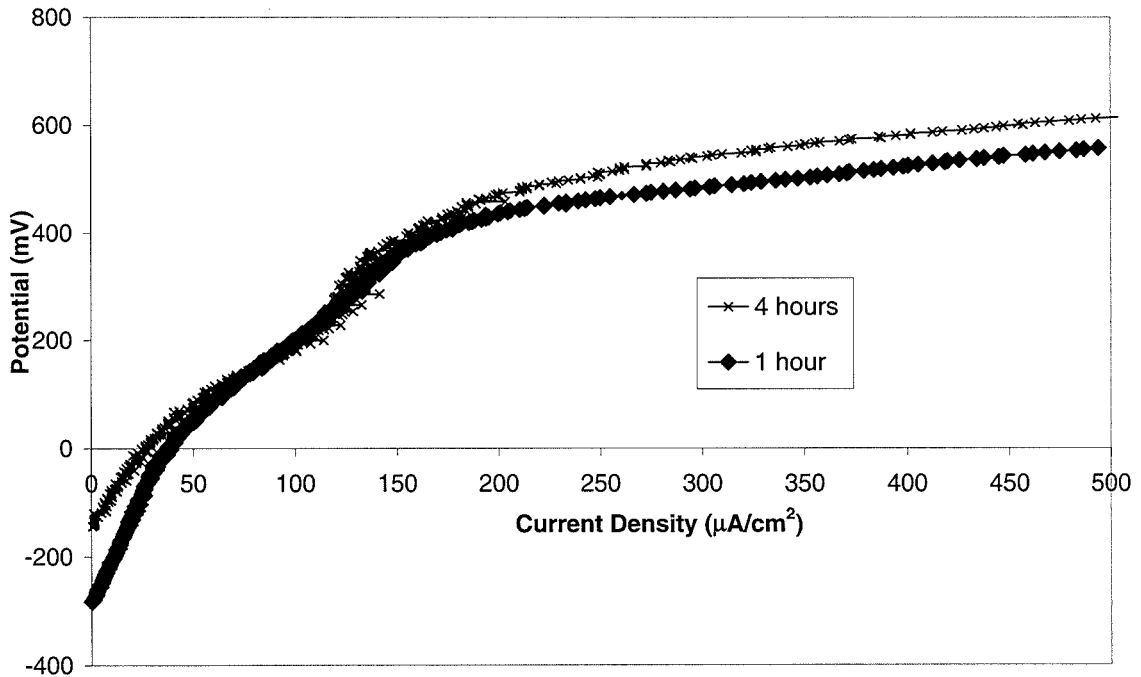


**Figure 6-6 Anodic polarisation scans under a liquid-solid impinging jet of 500mg/l solids at 50°C and 12 ms<sup>-1</sup>**



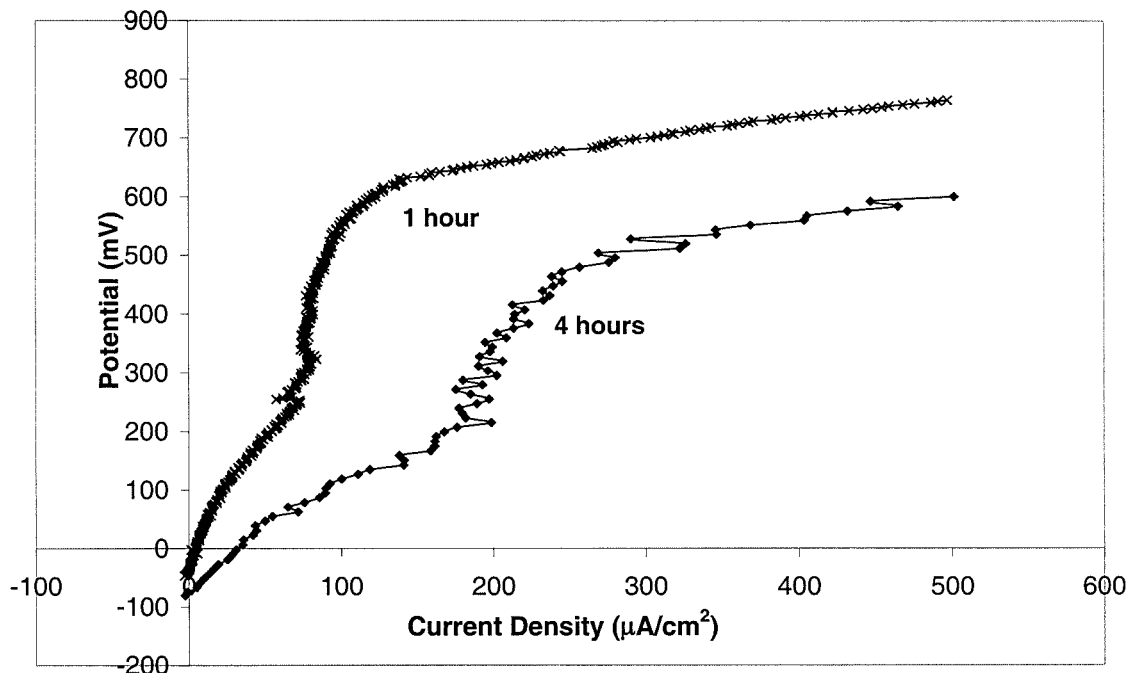
**Figure 6-7 Cathodic polarisation scans under a liquid-solid impinging jet containing 500 mg/l solids at 50°C and 12 ms<sup>-1</sup>**

Figure 6-8 shows the anodic polarisation curves after one and four hour exposure to a liquid-solid jet containing 650 mg/l solids. Both curves exhibit similar corrosion behaviour of increasing current with potential which is greater after 4 hours impingement. Although no definite stabilisation of current exists, there is a change in the rate of increase of current before a breakdown at +400 mV, in both cases.



**Figure 6-8 Anodic polarisation curves under liquid-solid jet with 650 mg/l solids 18°C, 12 ms<sup>-1</sup>**

When the solids concentration is increased to 1500 mg/l (Figure 6-9) there is a notable effect of time on the corrosion behaviour of the coating. After one hour impingement, the current rises then stabilises at about 80 $\mu\text{A}/\text{cm}^2$  over a potential range of 250 mV before a breakdown potential is reached. After four hours impingement there is a much higher initial increase of current with potential until a stabilisation current of about 200 $\mu\text{A}/\text{cm}^2$  is reached and is also maintained over a potential range of 250mV. This is can also be found when the impingement angle is rotated to 45° impingement (Figure 6-10).



**Figure 6-9 Anodic Polarisation curves under liquid-solid jet with 1500 mg/l solids 18°C, 12 ms<sup>-1</sup>, and 90° impingement.**

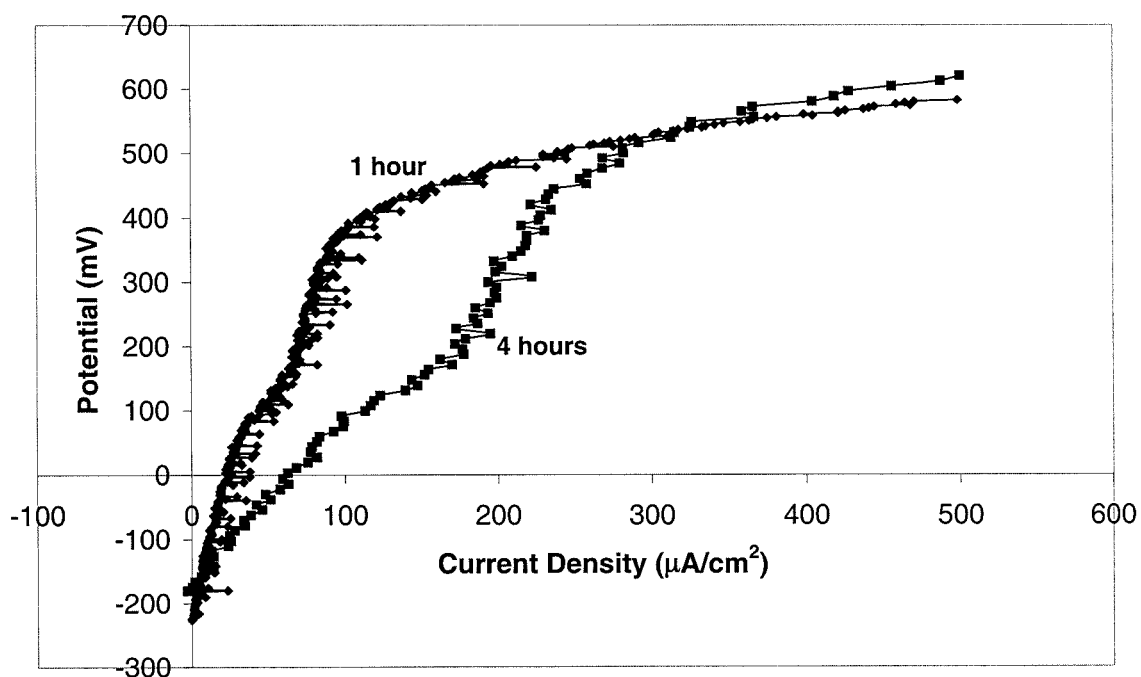


**Figure 6-10 Anodic Polarisation curves under liquid-solid jet with 1500 mg/l solids 18°C, 12 ms<sup>-1</sup>, 45° impingement**

### 6.3.2 Corrected Tafel Extrapolation

The corrected Tafel plots for liquid-solid erosion (up to 500mg/l solids) conditions up to a period of 4 hours and temperatures of 18°C and 50°C are shown in Figure 6-11 where good linear relationships of current and potential are found. Figure 6-12, Figure 6-13 and Figure 6-14 show the Tafel Extrapolation after impingement with a liquid-solid jet containing 650 mg/l and 1500 mg/l solids at 90°, and 1500 mg/l solids at 45° respectively. Good linear relationships can be found on these semi-log current against potential plots. These extrapolations, and replicate tests shown in Appendix 1, give rise to corrosion currents listed in Table 6-1. These do not incorporate any residual cathodic currents, since the residual cathodic currents were negligible (see Appendix 1).

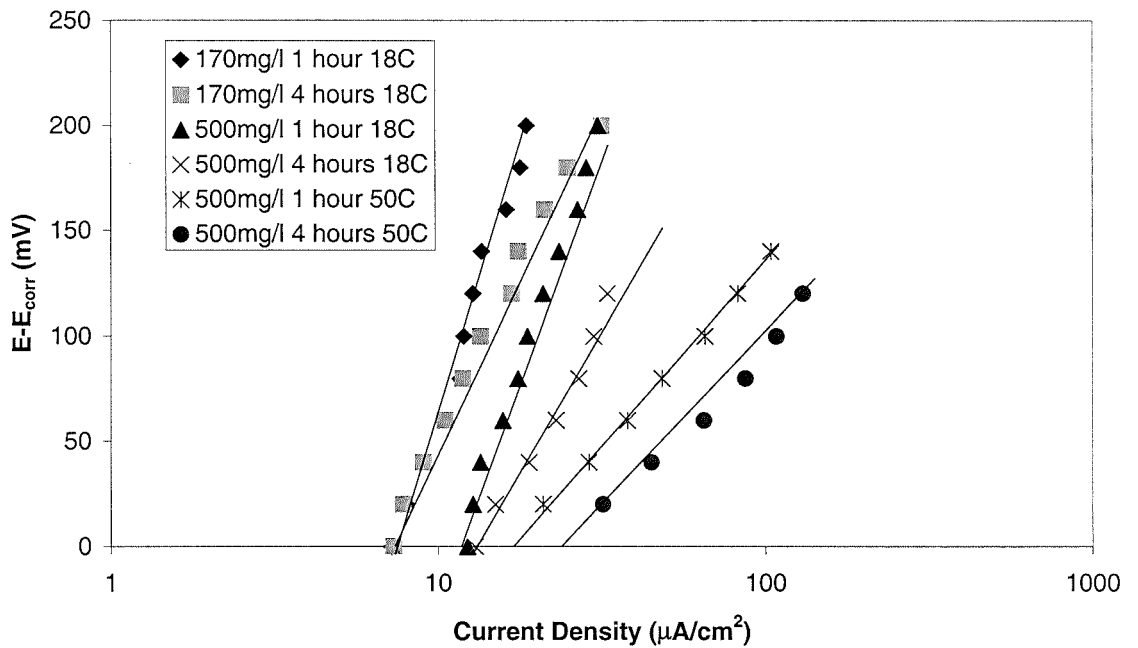
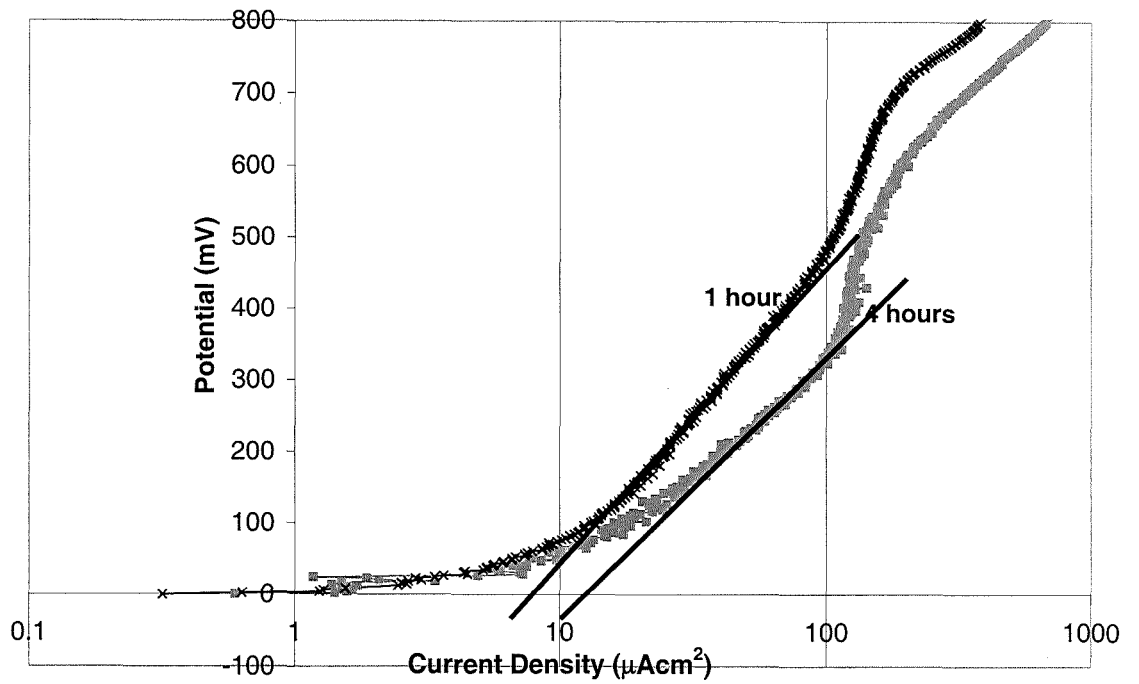
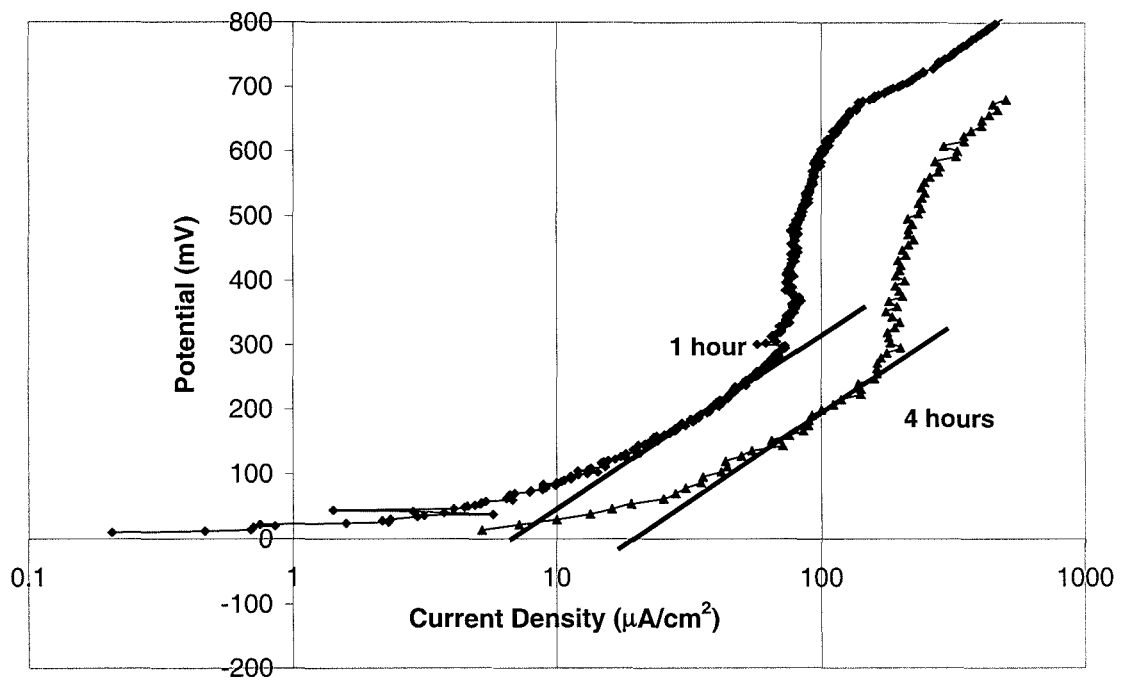


Figure 6-11 Corrected corrosion currents under liquid-solid conditions



**Figure 6-12 Tafel Extrapolation for liquid-solid impingement with 650 mg/l,  $12 \text{ ms}^{-1}$ ,  $18^\circ\text{C}$**



**Figure 6-13 Tafel Extrapolation for  $90^\circ$  liquid-solid jet impingement with 1500 mg/l solids  $12 \text{ ms}^{-1}$   $18^\circ\text{C}$**

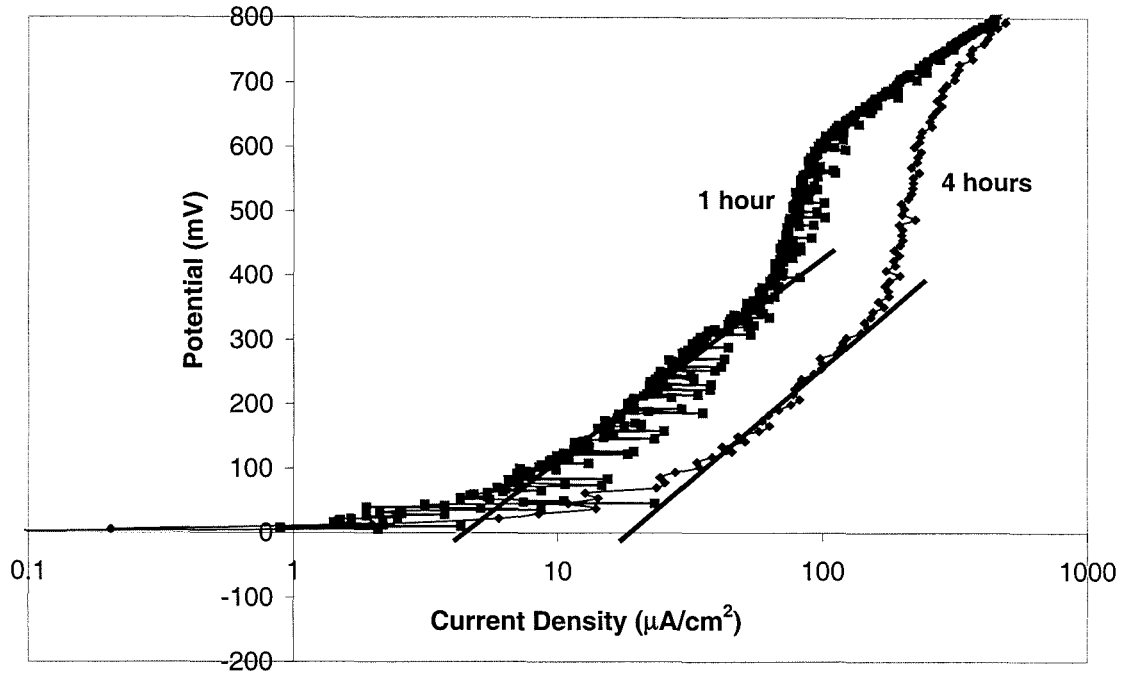


**Figure 6-14 Tafel Extrapolation for 45° liquid-solid jet impingement with 1500mg/l solids 12 ms<sup>-1</sup> 18°C**

Solid content (mg/l)	I <sub>corr</sub> (μA/cm <sup>2</sup> )		
	1 hour	4 hours	Ave.
170	7	7, 7	7
500	12	12, 14, 15	14
650	8, 8	10, 12, 14	12
1500 (90°)	6	20, 20, 20	20
1500 (45°)	4.5	14, 14, 20	16

**Table 6-1 Corrosion currents under liquid-solid impingement conditions**

The actual corrected corrosion current densities of all static, liquid and liquid-solid erosion-corrosion conditions for this coating presented thus far are shown in Figure 6-15. As can be seen, the temperature of the environment influences the corrosion rate even in static conditions. As the aqueous fluid changes from being stagnant to a flowing jet impinging on the surface of the specimen, the corrosion rate increases slightly. On increasing the temperature, the corrosion rate is significantly increased. The corrosion rate almost doubles at 50°C to from what it

was at 18°C, and on increasing the impingement time to four hours, it further increases.

When solids (170mg/l) are added to the liquid jet, the corrosion rate does not change from when no solids are in the jet, for up to a period of four hours. However, when 500mg/l of solids are added for up to a period of one hour, the corrosion rate increases by fifty percent, and as the impingement time is extended to four hours, the corrosion rate increases slightly. On increasing the temperature of the solid-liquid steam to 50°C, the corrosion rate increases threefold after one-hour impingement and by a further 7 $\mu$ A/cm<sup>2</sup> after four hours impingement.

The corrosion current densities obtained at the highest solid (Figure 6-15) content exhibit lower values than those obtained at the lower concentration of solids after one-hour impingement but as the time is extended to four hours, the corrosion currents are higher than those at the lower levels.

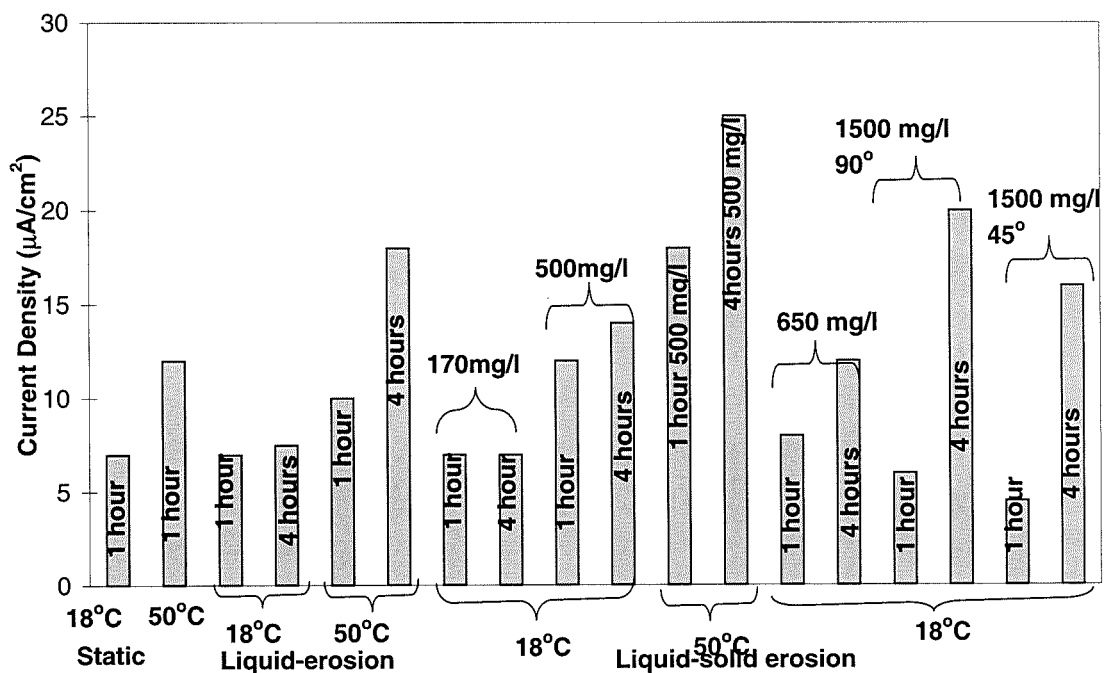


**Figure 6-15 Corrosion current densities measured in liquid and liquid-solid conditions**

## 6.4 Overall solid-liquid effects on material degradation

Thus far, the tests carried out have focused on the effect of liquid and liquid-solid erosion-corrosion conditions on the corrosion rate. This section concentrates on the overall degradation of the material, incorporating the weight losses under free erosion-corrosion conditions and when cathodic protection is applied hence assessing only the pure mechanical erosion process in the absence of corrosion. It subsequently addresses the contributions of erosion, corrosion and the synergistic effect in differing conditions.

### 6.4.1 Weight losses under liquid-solid conditions

Table 6-2 shows the weight losses under free erosion-corrosion conditions of normally three replicate experiments with the average value shown in bold. Table 6-3 shows the weight losses obtained in the same conditions when cathodic protection has been applied. The currents measured during cathodic protection are shown in Figure 6-16 where the currents increase for a period of one hour and then remain constant, and are higher for increasing solid content. The average weight losses in each instance are plotted on Figure 6-17. (Here E denotes the contribution from pure erosion). When cathodic protection is applied there is a substantial decrease in weight loss (almost 50%) in almost all cases.

It can be seen that as the solid content is increased, there is an associated increase in weight loss as would probably be expected. By extending the time from one hour to four hours, a more dramatic increase is seen at the highest solid content (1500mg/l) where a quadrupling of weight loss is seen opposed to a 2-3 times increment at 500 mg/l and 650 mg/l. This is also seen when only the pure erosion component is taken into consideration, with similar factorial increases.

Table 6-4 and Table 6-5 show the replicate and average weight losses under free erosion corrosion conditions and under cathodic protection when the impingement angle is rotated to 45°. The average weight loss for each condition is shown graphically in Figure 6-18 where a threefold increase in weight loss is

seen when the exposure time is extended from one to four hours. The rate of erosion, under cathodic protection, increases with increasing solid content.

It should be noted that, as with the lowest solid content level at 90° impingement, the weight loss was not measurable with the resolution of the digital balance at an impingement time of one hour, the weight loss was also not measurable at an impingement time of one hour with 500 mg/l solids content at 45°.

Time	Sand Loading (mg/l)							
	170		500		650		1500	
	Ave.		Ave.		Ave.		Ave.	
1 hour (mg)	Not measurable		0.2		0.2		0.4	
			0.2	<b>0.2</b>	0.2	<b>0.26</b>	0.4	<b>0.4</b>
			0.2		0.4		0.4	
	Ave.		Ave.		Ave.		Ave.	
4 hours (mg)	0.2		0.3		0.7		1.6	
	0.2	<b>0.2</b>	0.4	<b>0.36</b>	0.7	<b>0.73</b>	1.7	<b>1.7</b>
			0.4		0.8		1.8	

**Table 6-2 Total Weight Losses in free erosion-corrosion conditions of a liquid-solid jet at 18°C, 90° impingement and 12ms<sup>-1</sup>**

Time	Sand Loading (mg/l)			
	170	500	650	1500
1 hour (mg)	Ave.	Ave.	Ave.	Ave.
	Not measurable	0.1	0.1	0.2
		0.1	<b>0.1</b>	<b>0.16</b>
4 hours (mg)	Ave.	Ave.	Ave.	Ave.
	Not measurable	0.2	0.3	1.0
		0.2	<b>0.2</b>	<b>0.4</b>

**Table 6-3 Weight losses under cathodic protection from a liquid-solid jet at 12ms<sup>-1</sup>, 90° impingement and 18°C**

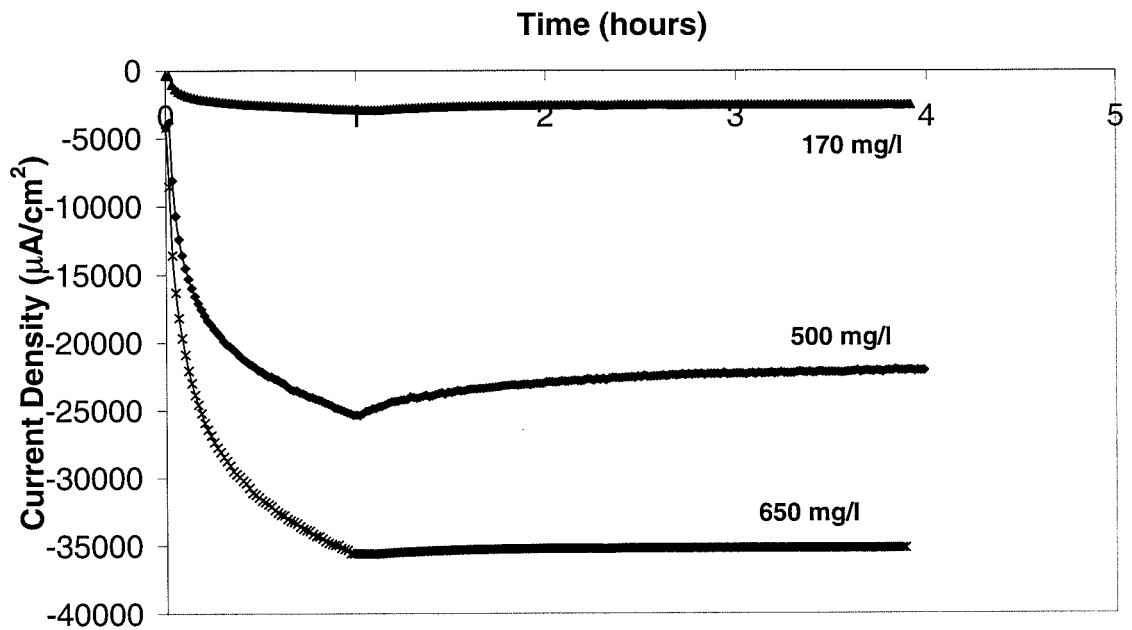


**Figure 6-16 Currents measured during cathodic protection (-800mV) at 90° solid-liquid impingement**

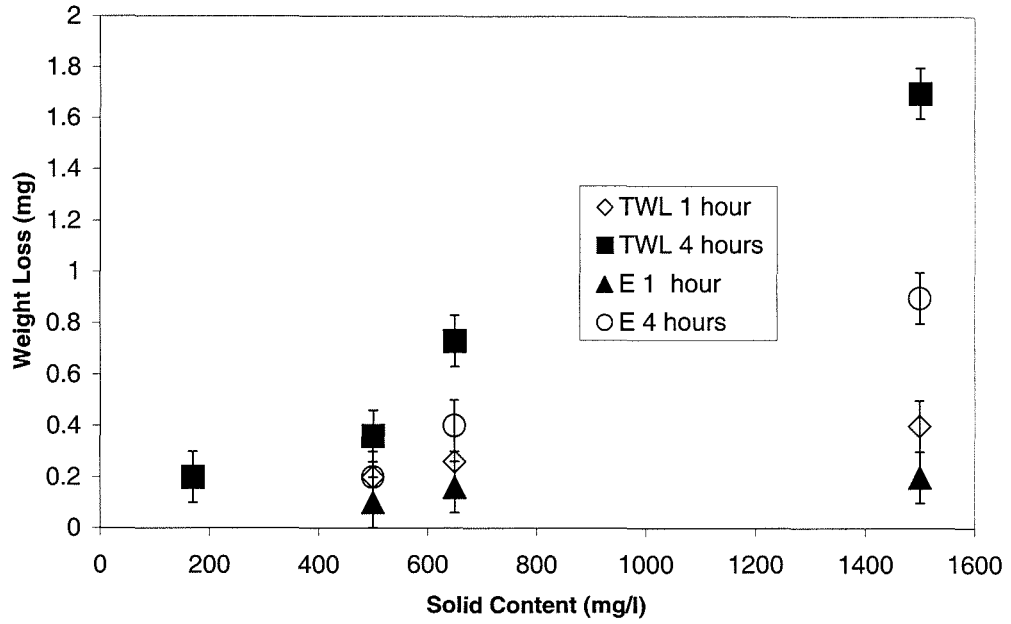


Figure 6-17 Graph of average weight losses under solid-liquid impingement at 90°

		Sand Loading (mg/l)			
		500	650	1500	
1 hour (mg)	Ave.		Ave.	Ave.	
	Not Measurable	0.2	0.3		
		0.2	<b>0.2</b>	0.3	<b>0.33</b>
4 hours (mg)	Ave.		Ave.	Ave.	
	0.3	0.6	1.1		
	0.3	<b>0.3</b>	0.6	<b>0.63</b>	1.0
	0.3	0.7	1.2		

Table 6-4 Weight losses from free erosion-corrosion under a liquid-solid jet at 45° impingement at 12ms<sup>-1</sup> and 18°C

Time	Sand Loading (mg/l)					
	500		650		1500	
1 hour (mg)	Ave.		Ave.		Ave.	
	Not Measurable		0.1	<b>0.1</b>	0.1	<b>0.17</b>
			0.1		0.2	
4 hours (mg)	Ave.		Ave.		Ave.	
	0.1	<b>0.17</b>	0.4	<b>0.33</b>	0.6	<b>0.7</b>
	0.2		0.4		0.7	
	0.2		0.2		0.8	

**Table 6-5 Weight losses from cathodic protection under a liquid-solid jet at 45° impingement at 12 ms<sup>-1</sup> and 18°C**

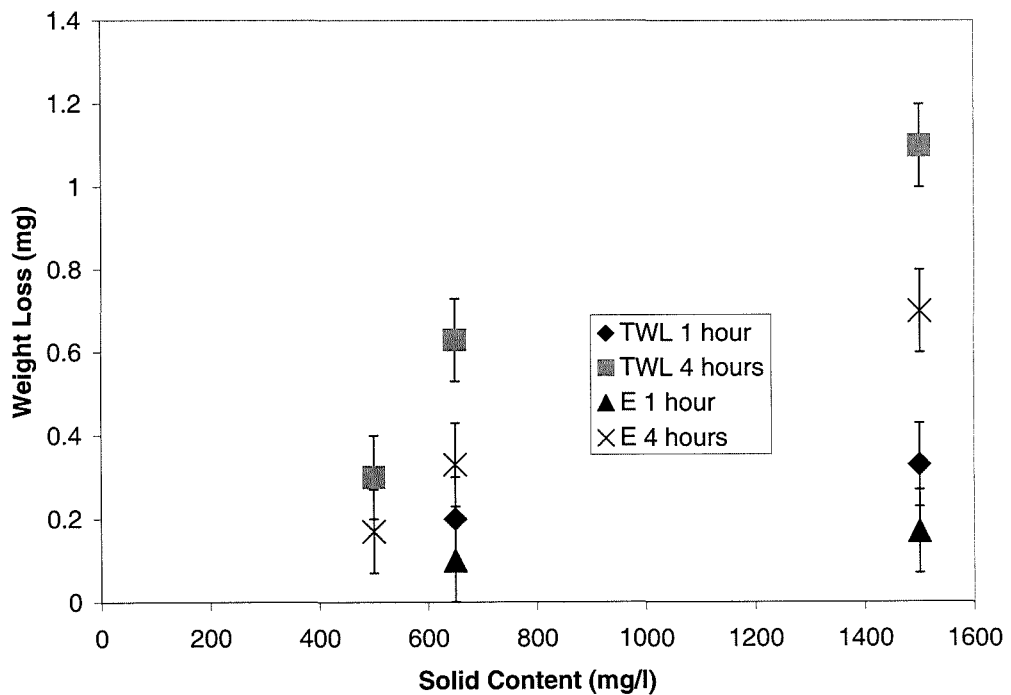


**Figure 6-18 Graph of weight losses under solid-liquid impingement at 45°**

Figure 6-19 shows the comparison of the total weight losses at three different sand loadings at 45° and 90° impingement angle. The effect of having a more oblique impact angle is to reduce the weight loss and the difference becomes more pronounced as the solid content increases.

Using Equation 4-2, as stated previously, the corrosion current densities are transferred into weight losses which can be seen in Table 6-6. Since the corrosion rate is shown to increase during the four hour impingement time, the corrosion rate found after the four hour impingement cannot be taken as the corrosion rate which has occurred over the duration of the test. Based on an assumption that the corrosion rate increases linearly from one to four hours, the total corrosion weight loss after four hours is taken as the sum of the weight losses found during each hour of exposure.

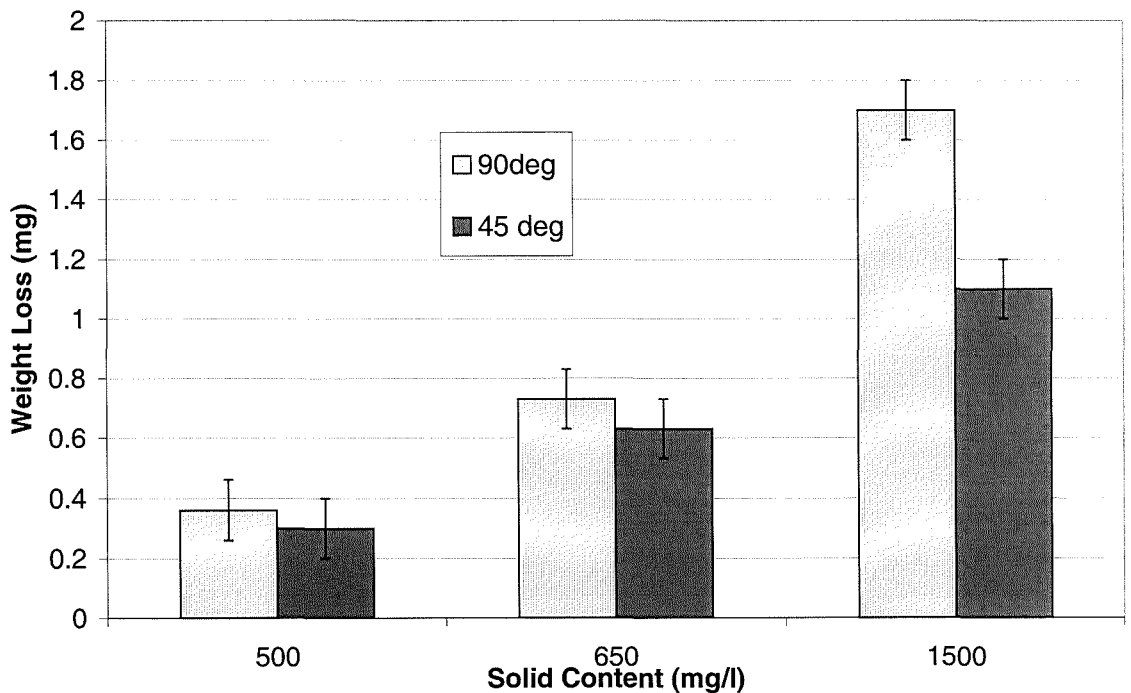


**Figure 6-19 Comparison of effect of impingement angle on total weight losses under solid-liquid jet for four hours at 18°C, 12ms<sup>-1</sup>**

Condition (mg/l)	1 hour		4 hours	
	$I_{corr}$ ( $\mu A/cm^2$ )	Corrosion weight loss during test(mg)	$I_{corr}$ ( $\mu A/cm^2$ )	Cumulative Wt. Loss (mg) for 4 hour test
<b>90° Impingement</b>				
170	7	0.03	7	0.22
500	12	0.06	14	0.25
650	8	0.04	12	0.22
1500	6	0.03	20	0.25
<b>45° Impingement</b>				
1500	4.5	0.02	16	0.20

**Table 6-6 Corrosion rates and corresponding weight losses under a solid-liquid jet at  $12ms^{-1}$ .**

## 6.5 Material Degradation Quantification

### 6.5.1 Erosion, Corrosion and Synergy.

From Equation 3-13 where the contributions of the total weight loss (TWL) were defined as erosion, E, corrosion, C, and a synergistic component, S, Figure 6-20 to Figure 6-23 show the contributions from each component and each component as a percentage of the total weight loss.

At the lowest sand loading (170 mg/l), the measured total weight loss was found to be only 0.2 mg after 4 hours impingement. From calculations using Tafel Extrapolation and Equation 4.2, the corrosion component is found to be approximately 0.24 mg. The measured weight loss under CP (the pure erosion component) was found to be negligible. Due to the small weight loss measured and the large amount of error ( $\pm 0.1$  mg), the calculated contributions of E, C and S at this solid content will be unreliable.

However, as the solid content is increased to 500 mg/l (Figure 6-20), the corrosion component is still very dominant at 59% after four hours impingement, incurring a negative synergistic component. After one-hour impingement, the corrosion component is only 30%. In contrast to the previous negligible

contribution from pure erosion at 170 mg/l, at 500 mg/l the pure erosion component contributes to 50%-55% of the overall weight loss.

At 650 mg/l solids content (Figure 6-21), the corrosive component still has a fairly significant contribution to the total weight loss (15% after one hour and 30% after 4 hours impingement), as is the indirect corrosive component's (synergy) contribution (23% after one hour and 15% after 4 hours impingement). While at both solid loadings, (650mg/l and 1500mg/l, Figure 6-22) the pure mechanical damage is 50% or more, the pure corrosive component both as an absolute value and as a percentage is reduced at the higher solid loading (7% after 1 hour and 14% after 4 hours impingement. This results in a higher contribution from the synergistic component at 1500 mg/l solid content (43% and 32% after 1 and 4 hour impingement respectively).

The lower corrosive component, after 1 hour, at the higher sand loading (1500 mg/l) is still evident when the impingement angle is 45° (Figure 6-23). Here the corrosive component is only 6% in contrast to 18% after 4 hours impingement. Again the pure erosive component has the most dominant contribution (64% and 52% after 1 and 4 hours respectively) and the synergistic component is more prominent after 1-hour impingement (42%) than after 4 hours (18%).

Figure 6-24 and Figure 6-25 summarise the percentage contributions of erosion, corrosion and synergy at all the conditions presented thus far. Figure 6-24 shows the percentage contributions after 1-hour impingement, where the pure erosion component accounts for ~50% of the total material loss at all solid contents and similarly after 4 hours impingement (Figure 6-25). A general trend of decreasing corrosion component, after both one and four hour impingement, with increasing solid content exists while the synergistic component decreases.

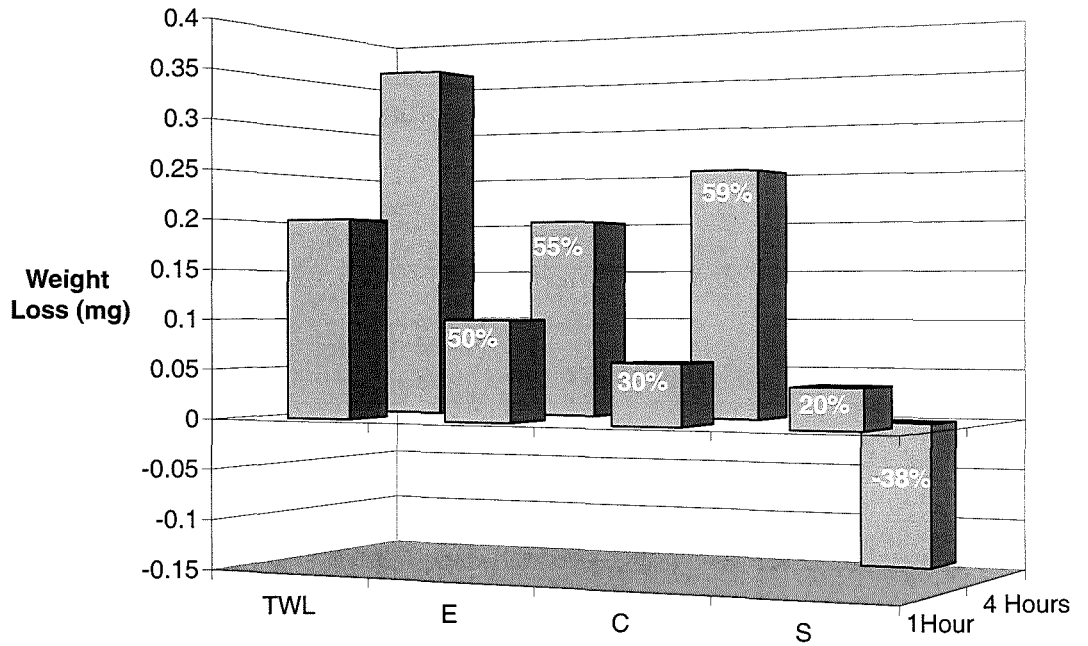


**Figure 6-20 Contributions to total weight loss from a 500 mg/l liquid-solid jet at 90° impingement**

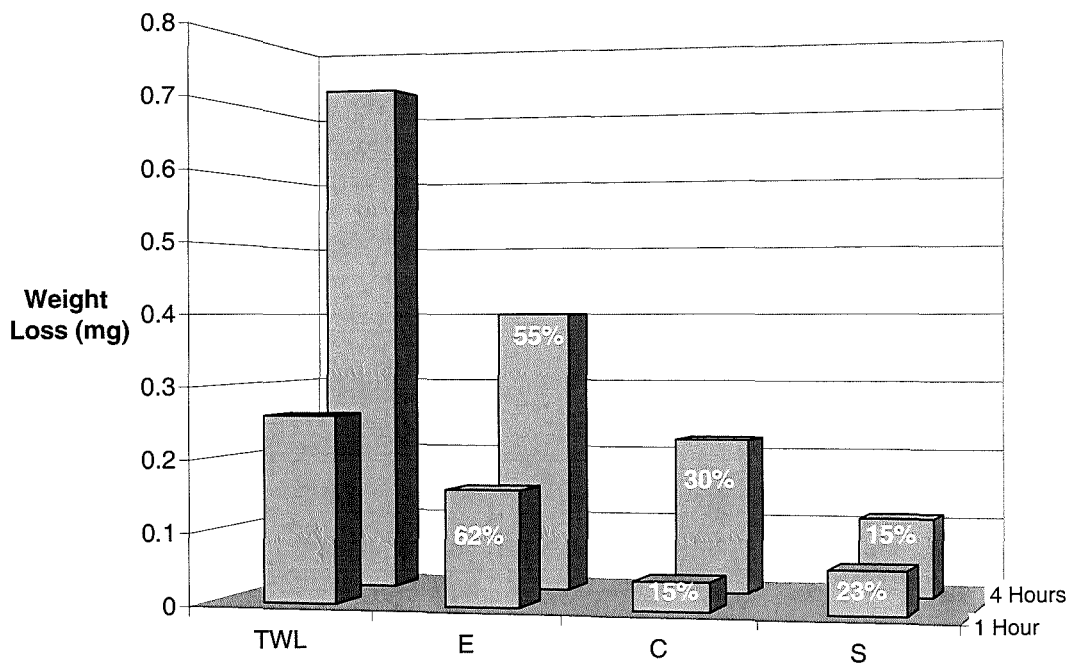


**Figure 6-21 Contributions to total weight loss with a 650 mg/l liquid-solid jet at 90° impingement**

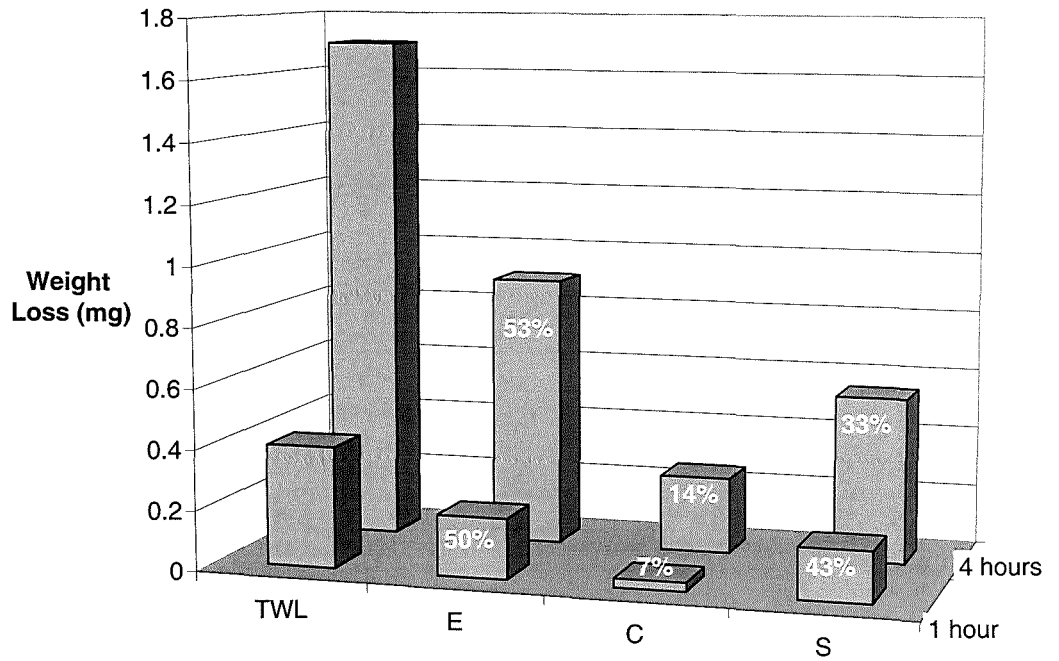


**Figure 6-22 Contributions to total weight loss with a 1500 mg/l liquid-solid jet at 90° impingement**

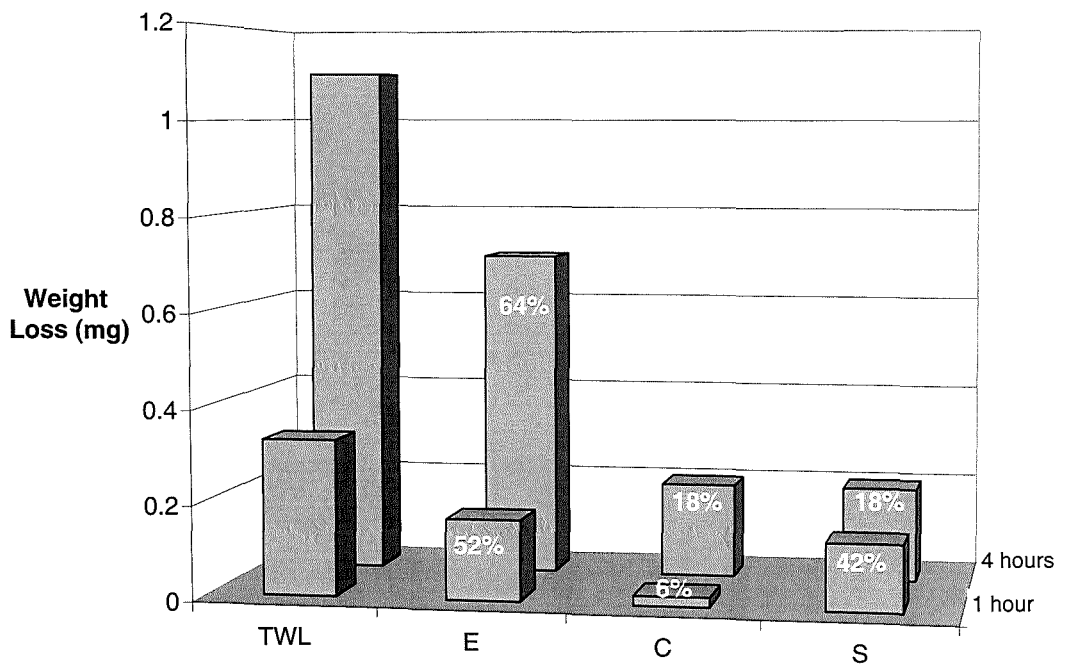


**Figure 6-23 Contributions to total weight loss from a 1500 mg/l liquid-solid jet at 45° impingement**

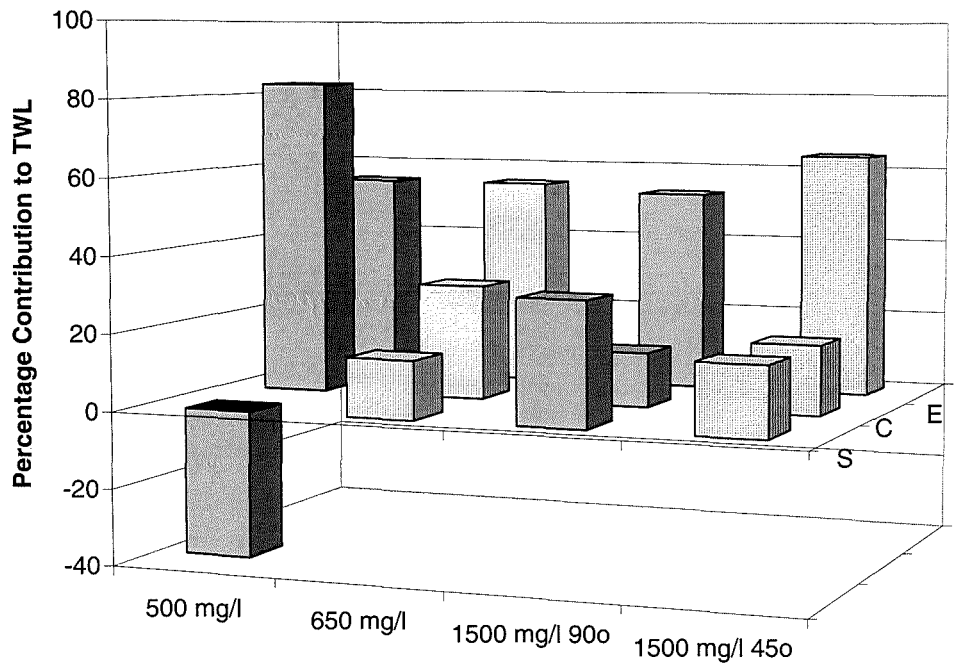


**Figure 6-24 Percentage contributions of E, C and S after 1 hour impingement**

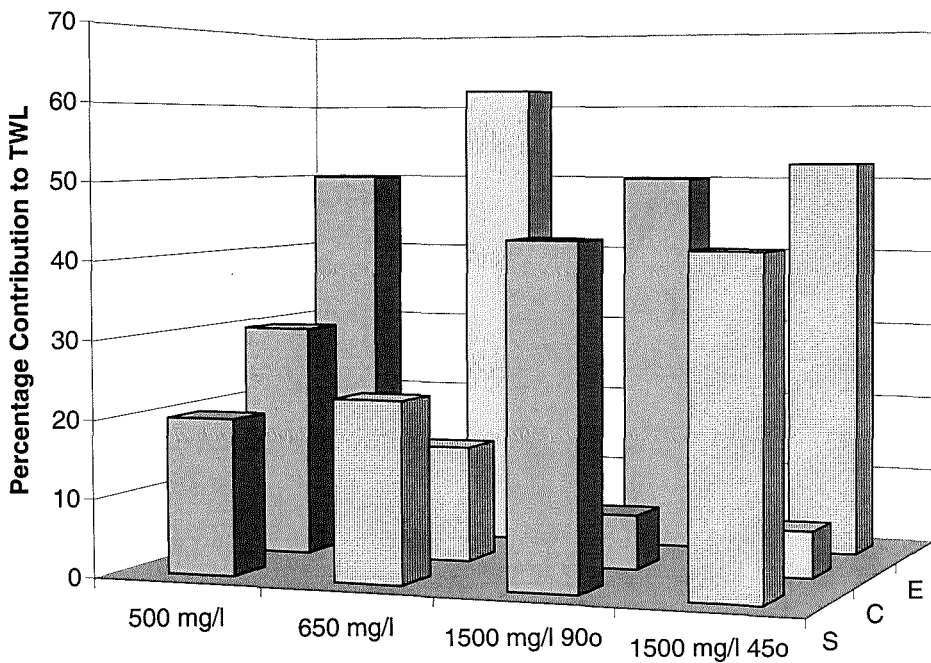


**Figure 6-25 Percentage contributions of E, C and S after 4 hours impingement**

## 6.6 Post Test Surface Analysis

### 6.6.1 Liquid Impingement

After impingement with the liquid jet for 1 and 4 hours both at 18°C and 50°C no evidence of a wear scar is apparent. After one-hour impingement at 18°C, the surface of the specimen has a dulled surface similar to that after static anodic polarisation. As the impingement time is extended to 4 hours, over the surface of the specimen, the matrix began to open up at discrete areas where carbides are pronounced Figure 6-26.

When the temperature is increased to 50°C, the corrosive attack, as indicated by the measured increased corrosion rates, is more severe. This manifested itself as areas where the coating had broken up (Figure 6-27) and then these areas progressed into macro-holes (Figure 6-28).

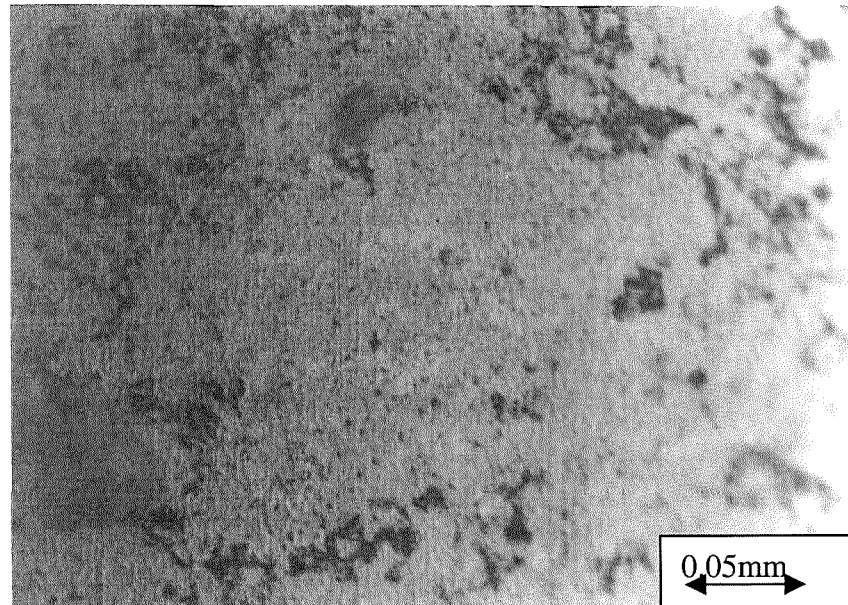


**Figure 6-26 No wear scar after anodic polarisation under impinging jet for 4 hours at 18°C**

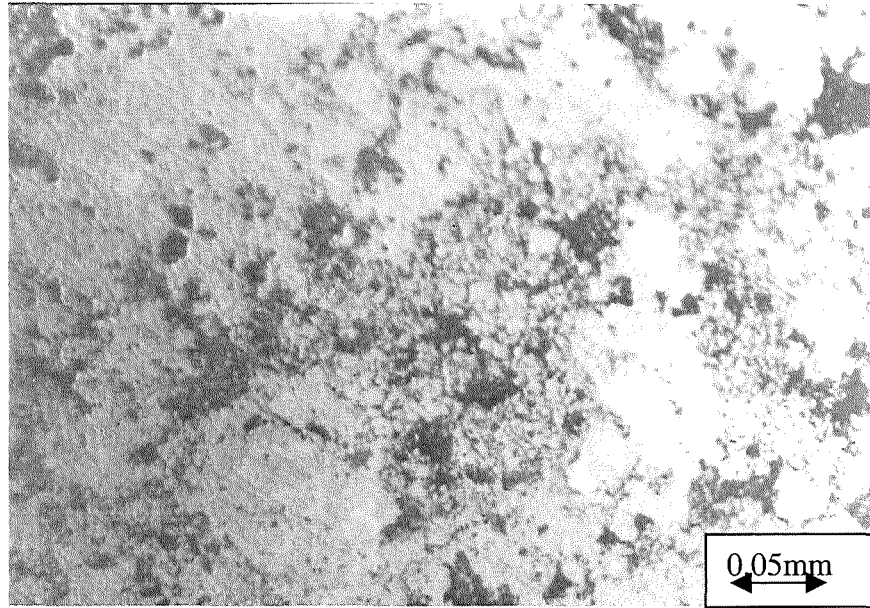


**Figure 6-27 Coating breaking up after anodic polarisation under impinging jet 1-hour 50°C**

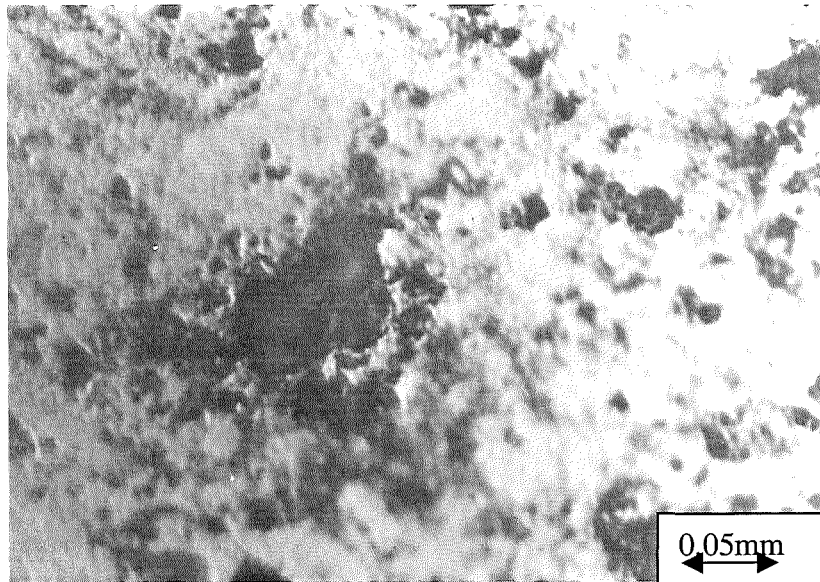


**Figure 6-28 Macro holes after anodic polarisation under impinging jet for 4 hours at 50°C**

## 6.6.2 Liquid-Solid Impingement

When solids are added to the liquid jet, a wear scar is evident on the surface of the specimen – as defined by the lighter grey area in Figure 6-29. This is in the region under the nozzle of the jet. On closer inspection of the wear scar (Figure 6-30) a roughened surface of the surface is apparent, where parts of the surface have been removed by the impacting sand particles.

When the wear scar, after free erosion-corrosion conditions at  $E_{\text{corr}}$ , is examined in profile (Figure 6-31) a depth loss of about  $2\mu\text{m}$  in this instance is measured, with an array of spikes extruding from the bottom of the trough boring deeper into the surface of the coating to a maximum depth of  $7\mu\text{m}$ . When cathodic protection is applied (Figure 6-32) a lower mean depth of the wear scar is revealed ( $0.7\mu\text{m}$ ) as are less protracting spikes (protruding to about  $2.5\mu\text{m}$ ).



**Figure 6-29** Wear scar on surface of specimen after 4 hours impingement with 650 mg/l liquid-solid jet at  $90^\circ$  impingement

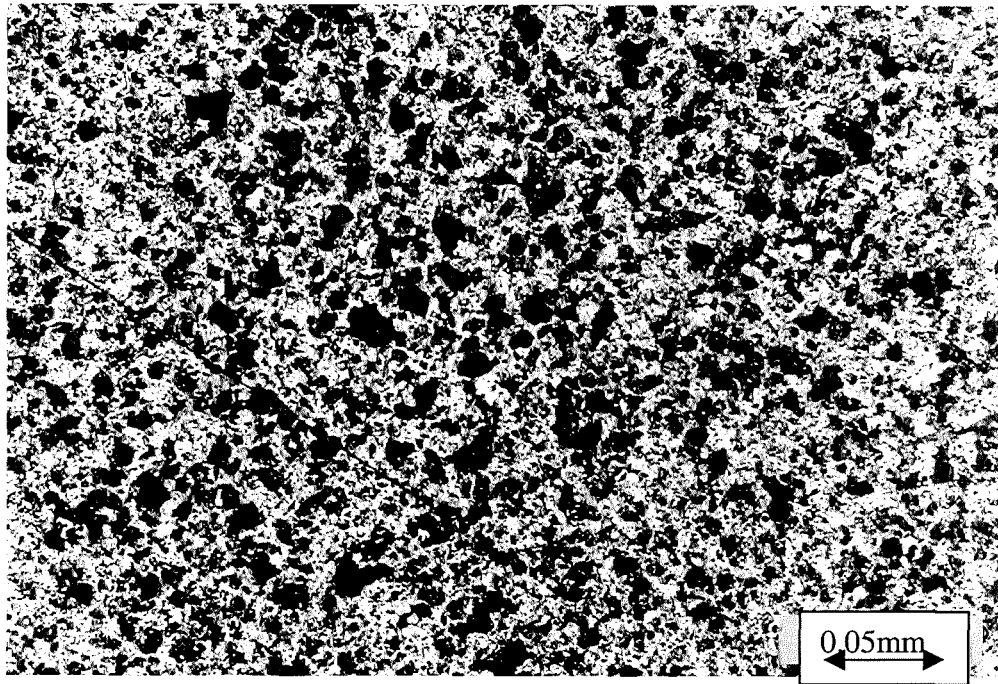


**Figure 6-30 Magnified photograph of wear scar at 90° impingement**

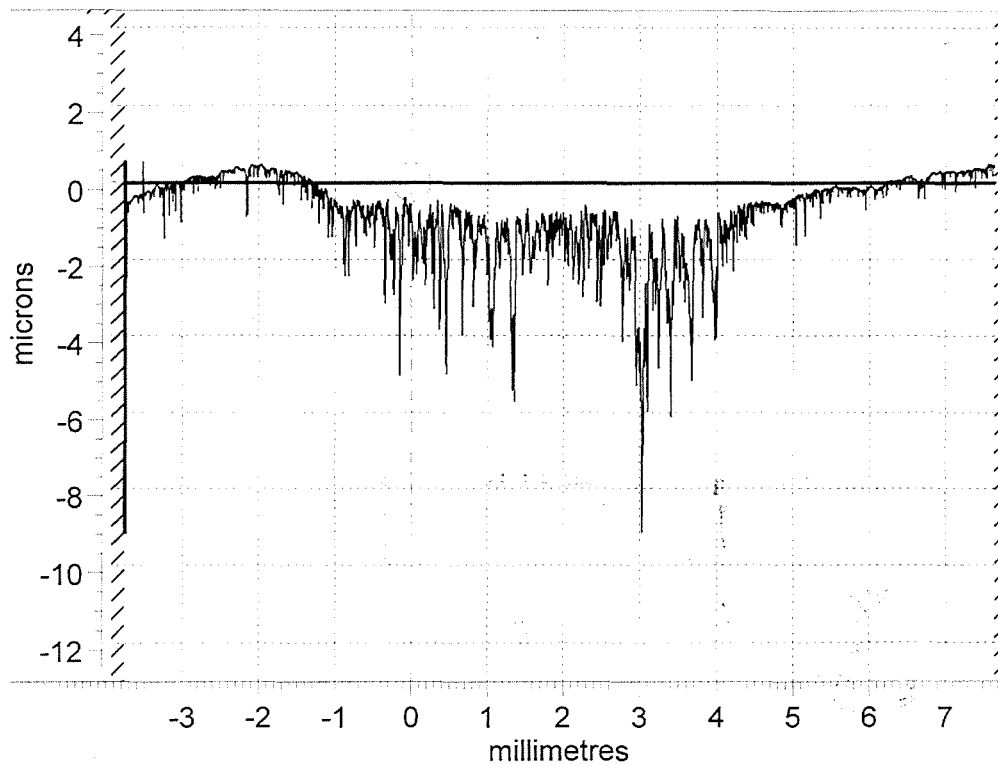


**Figure 6-31 Surface profile after 4 hours impingement at free erosion-corrosion with 650 mg/l solids at 90°**

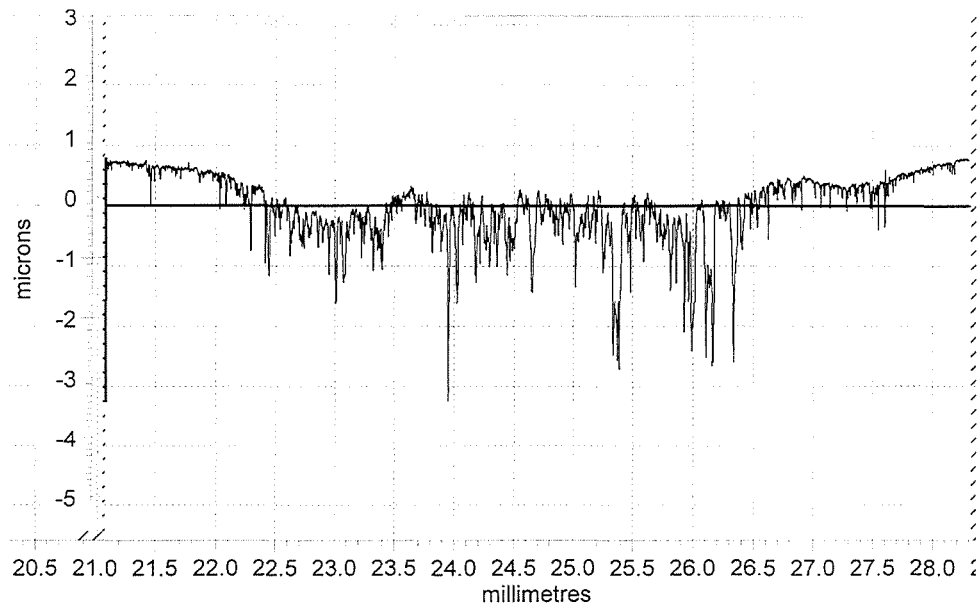


**Figure 6-32 Surface profile after 4 hours impingement with 650 mg/l solids at 90° with cathodic protection**

At the lower solids loading of 170 mg/l, a reduction in the average depth of the wear scar to  $\sim 0.5\mu\text{m}$  as opposed to a depth of  $2\mu\text{m}$  with 650 mg/l solids (Table 6-7) can be seen in Figure 6-33. The spikes extruding from the bottom of the wear scar are also reduced at the lower sand loading, now only extending to a maximum of  $\sim 4\mu\text{m}$  (in contrast to  $7\mu\text{m}$  at 650 mg/l solids). Even when no weight loss is recorded, when cathodic protection is applied (Figure 6-34), there is still evidently some mechanical erosion occurring. Again, the average depth has decreased, this time to  $\sim 0.25\mu\text{m}$  with spike lengths of  $\sim 1.5\mu\text{m}$ . It is obvious from the material loss shown on the wear scar profiles, that while pure mechanical erosion is detrimental to the coating, the combination of erosion and corrosion conditions is worse!

When the impingement angle is  $45^\circ$ , the wear scar becomes more elongated as shown in Figure 6-35 and in the surface profile (Figure 6-36) where the wear scar has been extended to 10mm long opposed to the 5mm at  $90^\circ$  impingement. Also as a result of the reduction in angle of impact, the depth of the wear scar is reduced. The average depth has reduced to  $0.5\mu\text{m}$ ; half of the depth at  $90^\circ$  impingement and the maximum depth to which the spikes end is about one third ( $2.5\mu\text{m}$ ) of the spike length at  $90^\circ$  impingement ( $7\mu\text{m}$ ). Although a larger scar in

terms of surface area is produced, the reduction in weight loss from 0.73 mg at 90° impingement to 0.4 mg at 45° impingement can be attributed to the reduction in depth of the scar and a reduction in length of the spikes.

Solid Content (mg/l)	Scar Depth from TWL ( $\mu\text{m}$ )	Scar Depth with CP ( $\mu\text{m}$ )
170	0.5	0.25
650	1	0.75

**Table 6-7 Scar Depths (estimated by eye) from Surface Profiles**

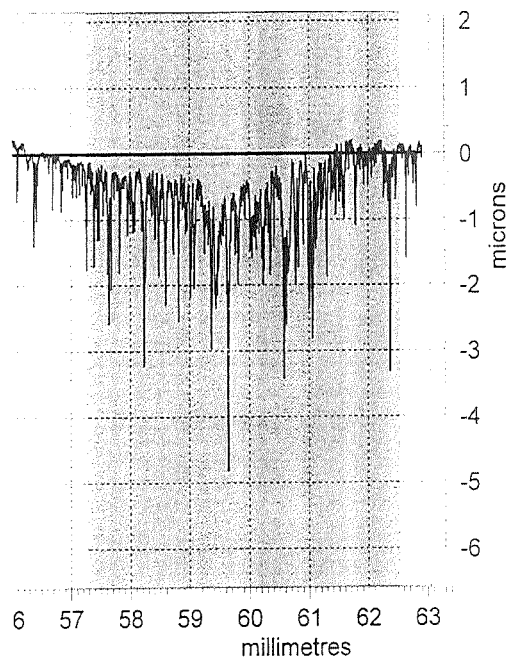


**Figure 6-33 Surface profile of after 4 hours impingement with 170 mg/l at free erosion-corrosion conditions**

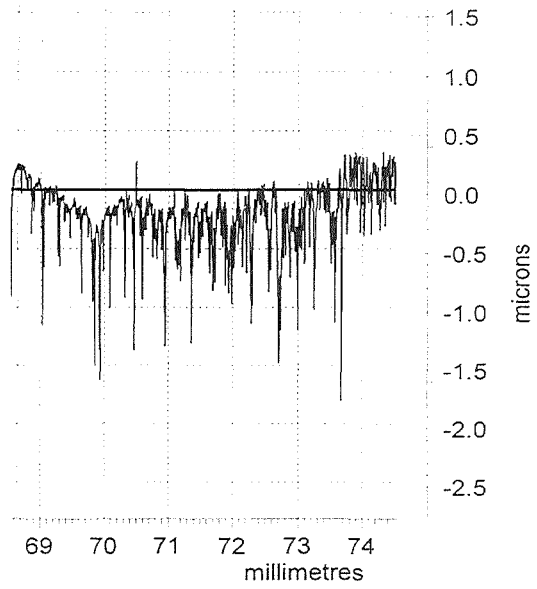


**Figure 6-34 Surface profile after 4 hours impingement with 170 mg/l under cathodic protection**



**Figure 6-35 Photograph of wear scar at 45° impingement**

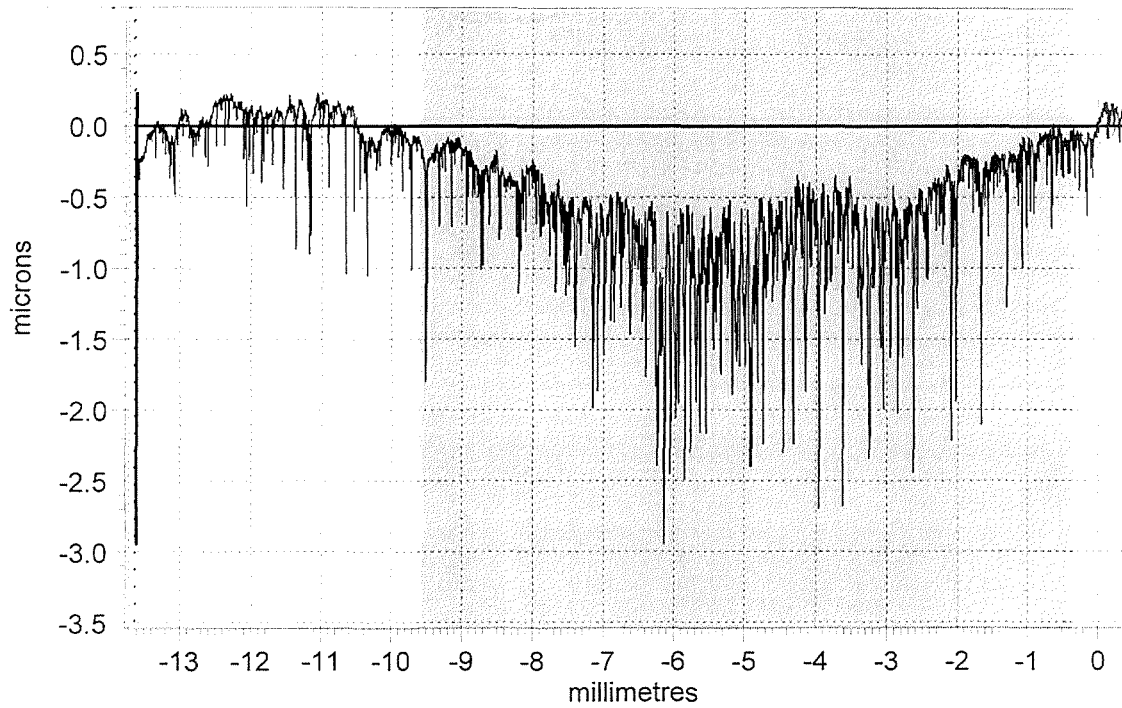


**Figure 6-36 Surface profile of wear scar at 45° impingement with 650 mg/l solids for 4 hours**

The effects of differing impact angles will be investigated further within the next chapter in terms of how the solids mechanically erode the surface.

## Chapter 7

# An Investigation of Erosion-Corrosion Under a Liquid-Solid Jet Incorporating Effects from Varying Impact Angle and on Concentric Specimens

### 7.1 Introduction

This chapter presents the results obtained from coating 2, the WC-Co-Cr coating produced by company II. It incorporates aspects such as the effect of solid loading on weight loss, the effect of impingement angle on weight loss and the subsequent erosion mechanisms and the corrosion rate. The corrosion monitoring includes linear polarisation to assess the time dependency of the corrosion rates both on composite and concentric specimens.

### 7.2 Weight Loss vs Solid Loading

Table 7-1 shows the weight losses of three replicate experiments after four hours impingement at  $90^\circ$  at ambient temperature with an increasing solid content. On investigation of wear scar, via surface profiling techniques, the average depth, starting roughly in the middle of the array of the spikes at the trough of the scar extending up to the flat surface, of each wear scar at each sand loading, is shown in Table 7-2. Also incorporated into Table 7-2 is the maximum spike depth. This is an important factor when considering the ability of the surrounding solution to penetrate to the substrate. Both weight loss data and scar depth data are incorporated into Figure 7-1, where both data sets increase as a function of solid content.

Solid Content (mg/l)	Total Weight Loss (mg)		
	Test 1	Test 2	Test 3
250	0.3	0.4	0.4
650	0.7	0.7	0.9
1250	1.4	1.5	1.6
1500	2.3	2.4	2.5
2000	3.6	3.5	3.5
2700	4.8	4.9	5.0

**Table 7-1 Total weight loss of WC-CoCr coating under a solid-liquid jet at  $12\text{ms}^{-1}$  after 4 hours impingement at  $18^{\circ}\text{C}$  at  $90^{\circ}$ .**

Solid Content (mg/l)	Average Scar Depth	Maximum Scar Depth (by inspection)
	( $\mu\text{m}$ )	( $\mu\text{m}$ )
250	0.75	5
650	1	3.5
1250	2	3.5
1500	6	9
2000	10	15
2700	14	21

**Table 7-2 Average wear scar depth and maximum spike depth on WC-CoCr coating under a solid- liquid jet at  $12\text{ms}^{-1}$  after 4 hours impingement at  $18^{\circ}\text{C}$ .**

As well as increases in the scar depth as the solid content of the liquid stream increases, a change in the wear scar appearance becomes apparent. Figure 7-2 shows a surface profile of an as-polished specimen, i.e. post polishing with 6-micron diamond polish. It shows an almost smooth surface with some spikes which could be due to the combination of the occasional removal of a hard phase during polishing and the general contours of the matrix/hard phase surface.

When the polished coating is subjected to a liquid-solid jet, containing 250 mg/l (Figure 7-3) the original polished surface now contains an area where there is a

higher concentration of spikes, which extend, to a depth of  $4\mu\text{m}$ . The ‘dip’ on the surface of the specimen where material has been removed is  $\sim 1\mu\text{m}$ . As the solid content increases a similar wear scar pattern emerges, i.e. a concentration of spikes at the bottom of the scar, with the depth of the scars increasing with solid content until the solid content is  $1250\text{ mg/l}$ . At this solid content (Figure 7-4), the spikes do not appear so compact but are more defined, both in terms of width and depth. This also occurs at a solid content of  $1500\text{ mg/l}$  with an increased average scar depth. Then at a solid content of  $2000\text{ mg/l}$  (Figure 7-5), the random spikes apparently merge forming areas of high material loss. This continues with a further increase in solid content  $2700\text{ mg/l}$  (Figure 7-6) and the wear scar develops a definite trough.

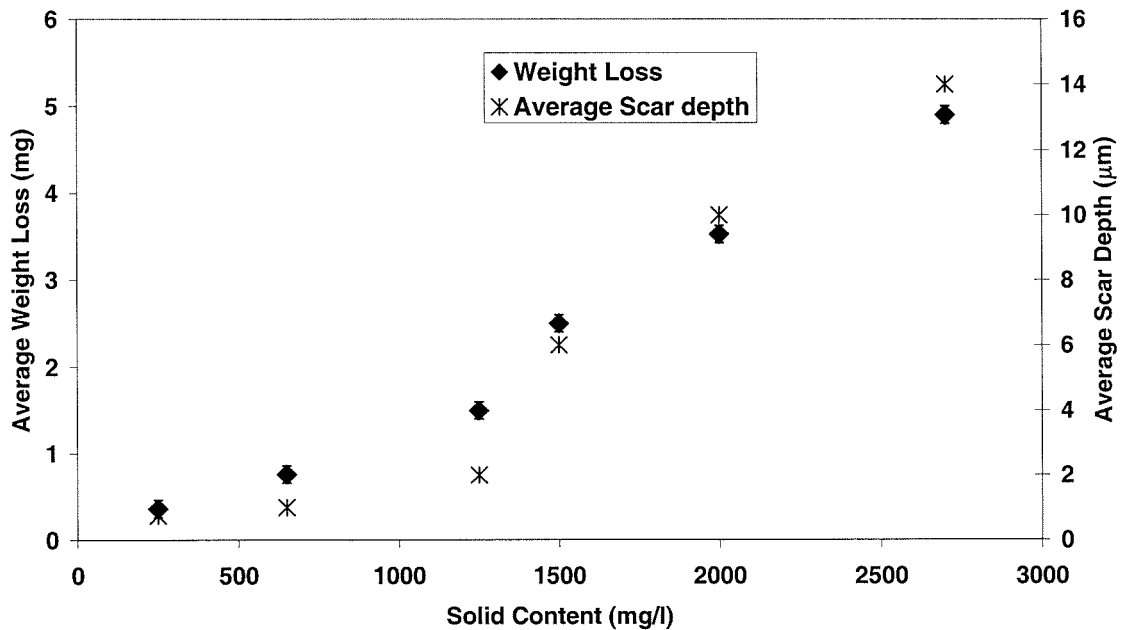


**Figure 7-1 Average weight losses and scar depths under liquid-solid Erosion-Corrosion after 4 Hours Impingement,  $12\text{ ms}^{-1}$  at  $18^\circ\text{C}$ .**

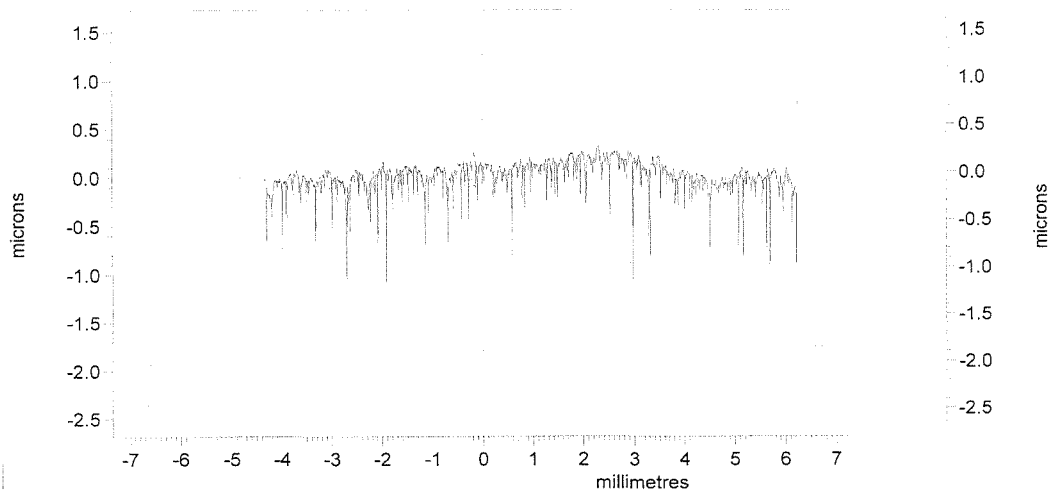


**Figure 7-2 Surface profile of as-polished specimen**

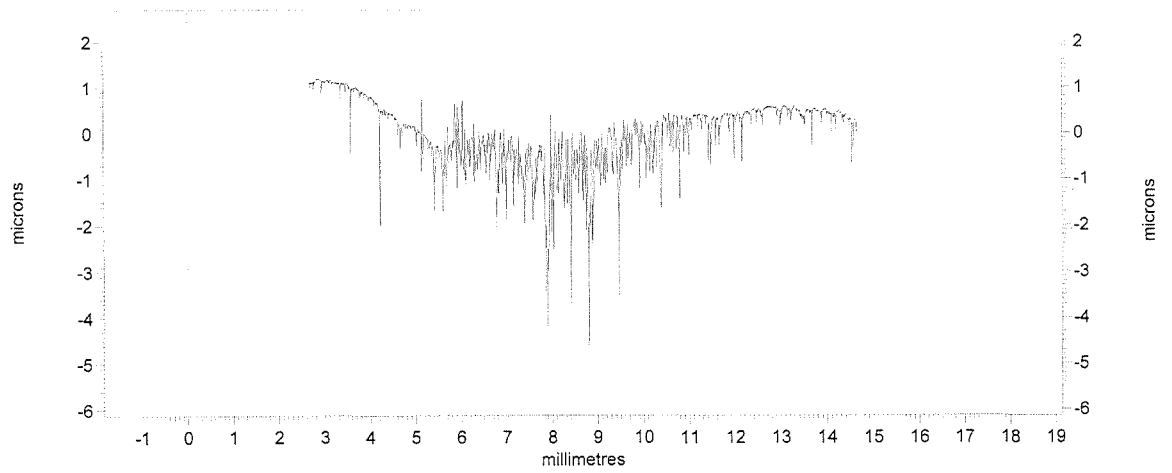


**Figure 7-3 Surface profile after 4 hours impingement with 250 mg/l solids at 90° and 12 ms<sup>-1</sup>**

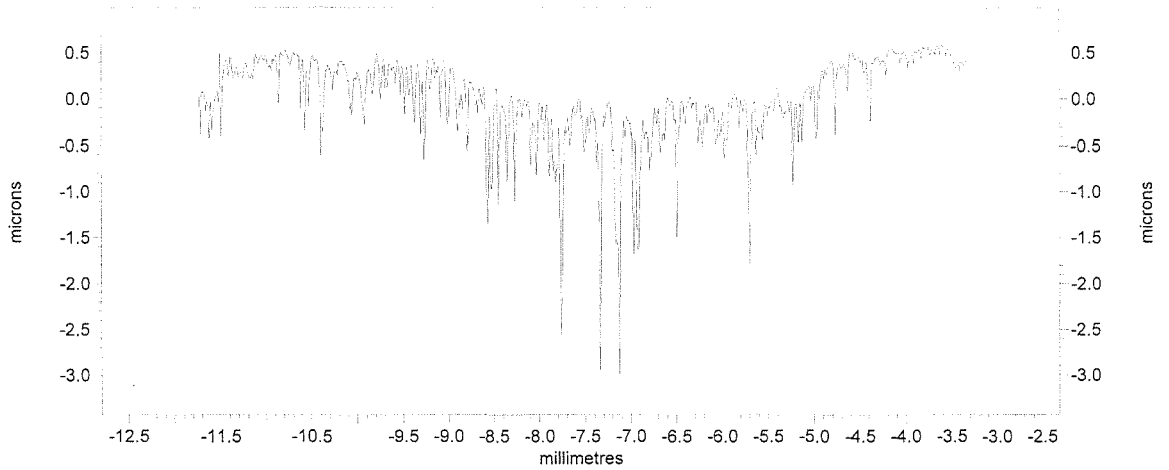


**Figure 7-4 Surface profile after 4 hours impingement with 1250 mg/l solids at 90° and 12 ms<sup>-1</sup>**

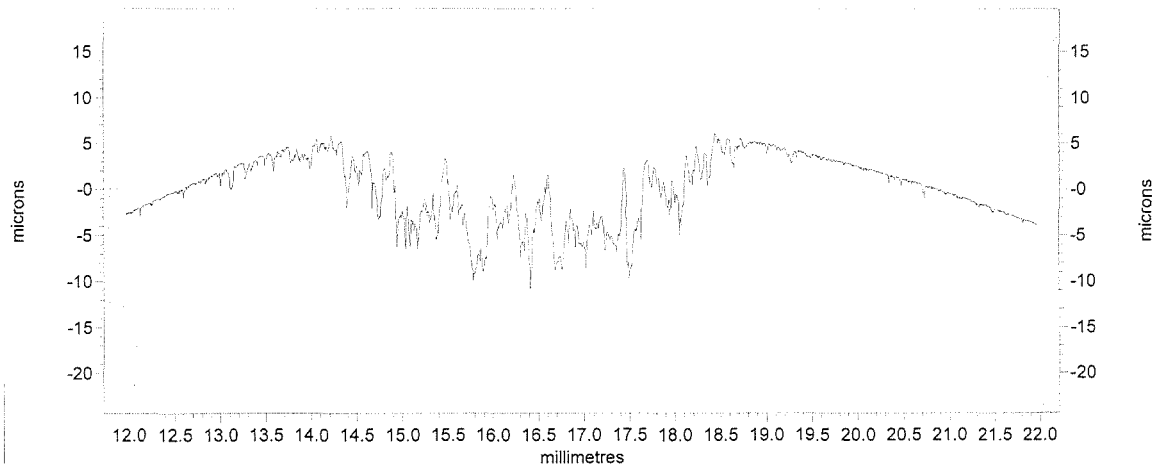


**Figure 7-5 Surface profile after 4 hours impingement with 2000 mg/l solids at 90° and 12 ms<sup>-1</sup>**

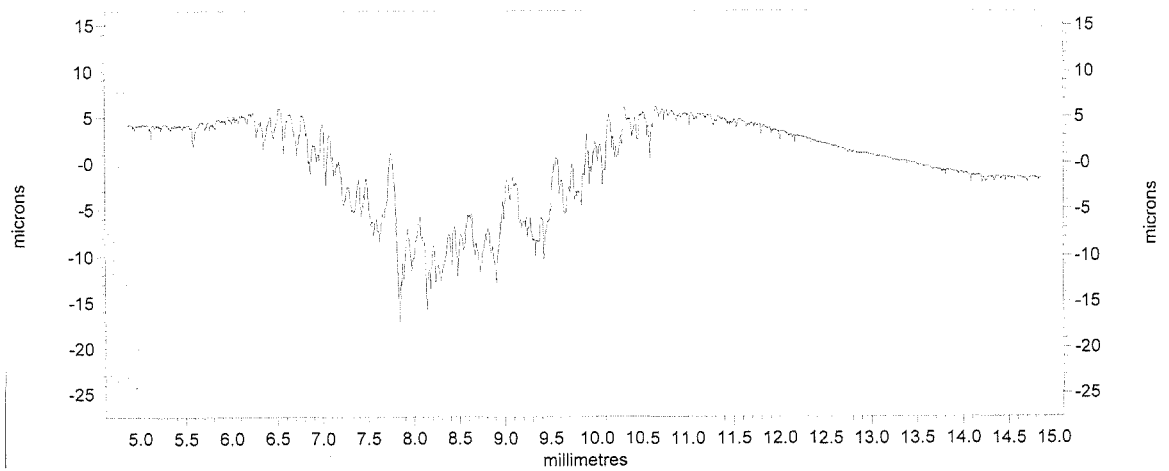


**Figure 7-6 Surface profile after 4 hours impingement with 2700 mg/l solids at 90° and 12 ms<sup>-1</sup>**

### 7.3 Effect of Impingement Angle

#### 7.3.1 Erosive Effects

A series of tests at a solid content of 2000 mg/l, were carried out to determine the effect the angle of impingement had on the total weight loss under free erosion-corrosion conditions, under cathodic protection and in anodic polarisation tests.

Figure 7-7 to Figure 7-11 shows photographs of the wear scars at all the various impact angles. At 90° impingement, the wear scar is circular in appearance on the surface of the specimen. At shallower impact angles, the wear scar becomes elongated, as illustrated in Figure 7-8 where the angle of impact is 30°. Then as the angle is increased to 45°, 60° and finally 75°, the wear scar reduces towards a more circular shape, akin to that at 90°.

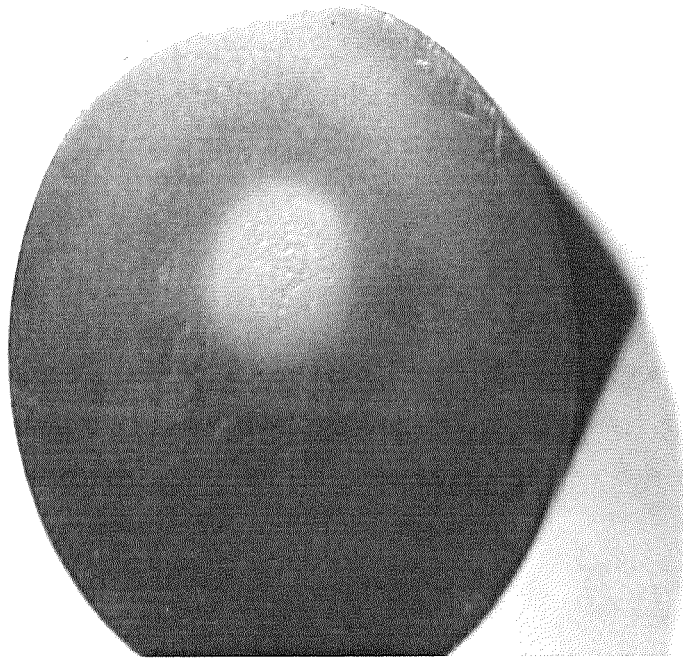


**Figure 7-7 Photograph of wear scar at 90° impingement 12 ms<sup>-1</sup>, 2000mg/l  
18°C**

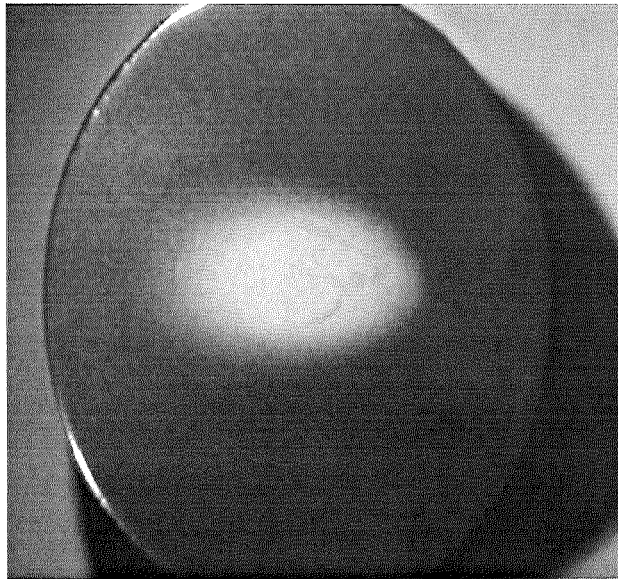
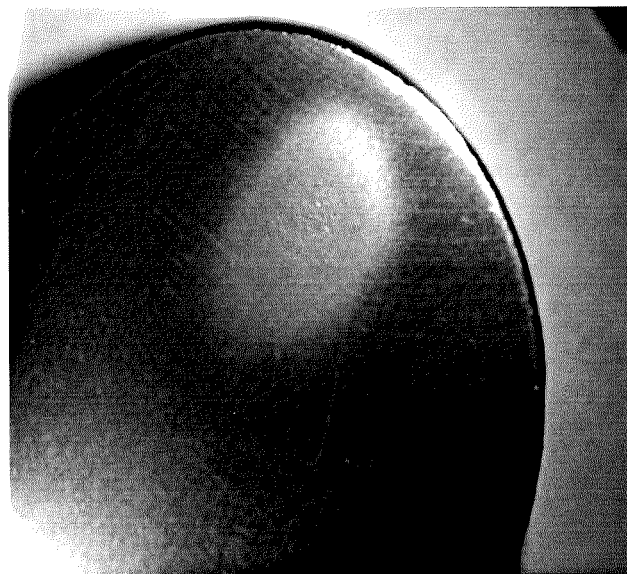


**Figure 7-8 Photograph of wear scar at 30° impingement 12 ms<sup>-1</sup>, 2000mg/l**



**18°C**

**Figure 7-9 Photograph of wear scar at 45° impingement 12 ms<sup>-1</sup>, 2000mg/l  
18°C**

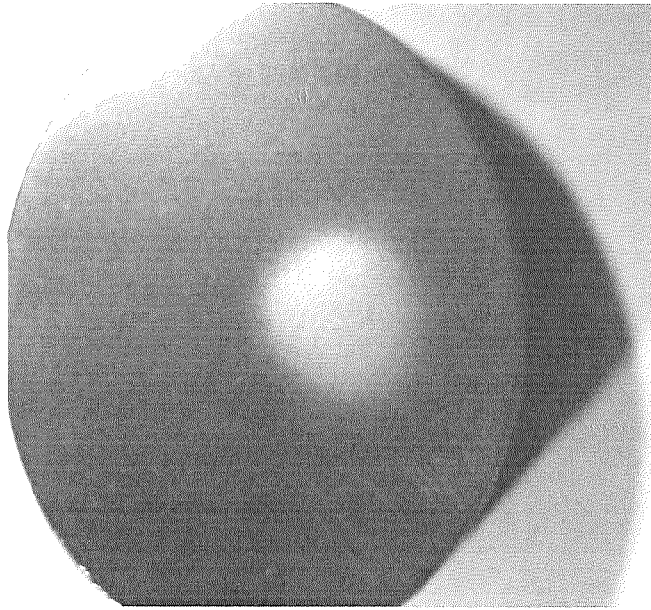


**Figure 7-10** Photograph of wear scar at 60° impingement 12 ms<sup>-1</sup>, 2000mg/l  
18°C

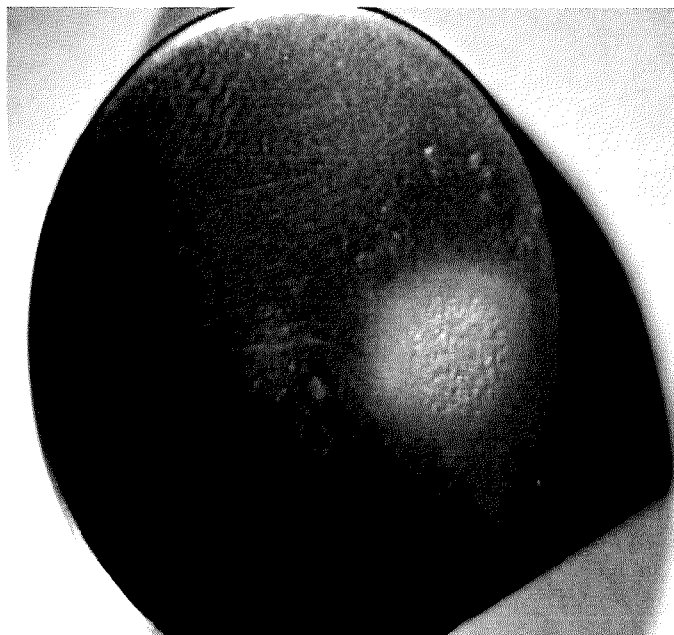


**Figure 7-11** Photograph of wear scar at 75° impingement 12 ms<sup>-1</sup>, 2000mg/l  
18°C

As can be seen in Table 7-3, the impact angle affects the amount of material removal. The shallower impact angles although they elongate the scar, do not

remove as much material. As depicted by Figure 7-12, the increasing impact angle increases material loss both under free erosion-corrosion conditions and cathodic protection.

Impingement Angle	TWL (mg)			E (mg)		
	Test 1	Test 2	Test 3	Test 1	Test 2	Test 3
30	2.2	2.1	2.0	1.0	1.0	
45	2.7	2.3	2.5	1.1	1.2	
60	3.0	2.9	2.9	1.3	1.3	
75	3.4	3.4	3.3	1.5	1.6	1.6
90	3.6	3.5	3.5	1.7	1.7	1.6

**Table 7-3 Weight loss on WC-CoCr coating after 4 hours impingement at 12 ms<sup>-1</sup> with 2000 mg/l solids at 18°C**

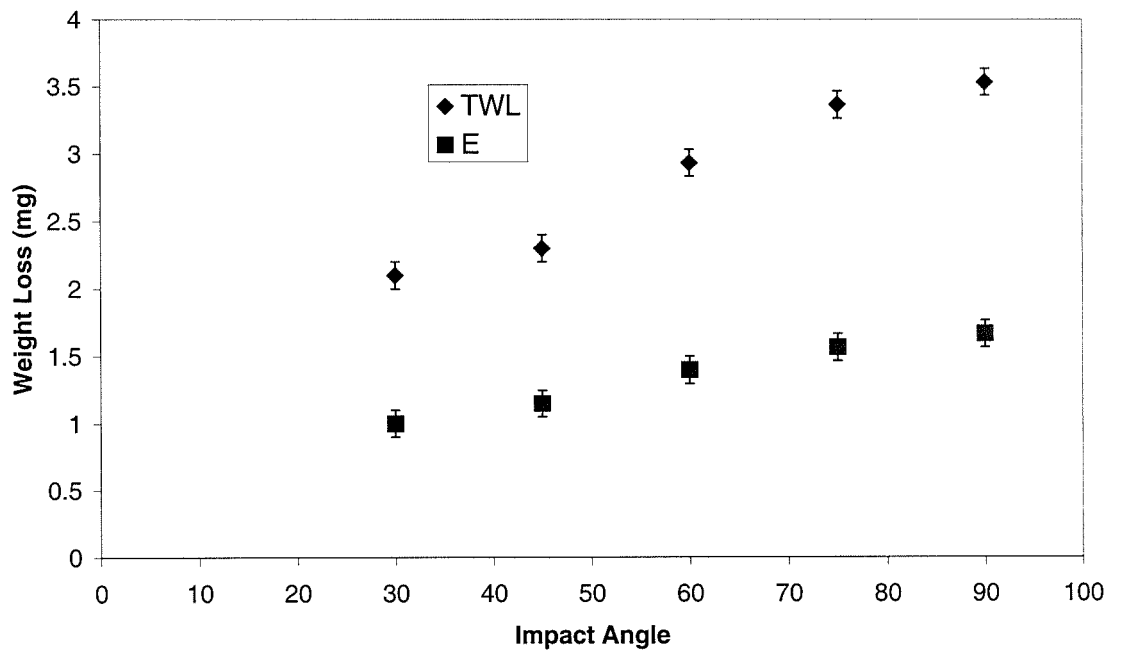


**Figure 7-12 Graph of weight loss versus impact angle with 2000 mg/l solids**

At 90° impingement, the impacts from the sand particles cause crater-like voids on the surface of the coating as shown in Figure 7-13. These, shown at a slightly higher magnification in Figure 7-14, are areas where chunks of coating have

been removed within areas where only small amounts of the original surface, denoted by the whiter areas, remain. Figure 7-15 shows the area near to the edge of the wear scar. Here the craters do not appear as deep or as frequent and a larger part of the surface remains. The edge of the wear scar is defined in Figure 7-16 where, on the right-hand side of the photograph, a larger part of the original surface remains. This surface has small, shallow areas where the coating has been removed (Figure 7-17), but in general has suffered from corrosion as seen by the pronounced hard phase particles due to matrix dissolution. In contrast (Figure 7-18), the area further away from the wear scar, where the solids from the jet have had little effect, has not suffered from such severe corrosive effects as the hard phases are still retained within the coating but the corrosion damage has manifested itself as macro-holes.

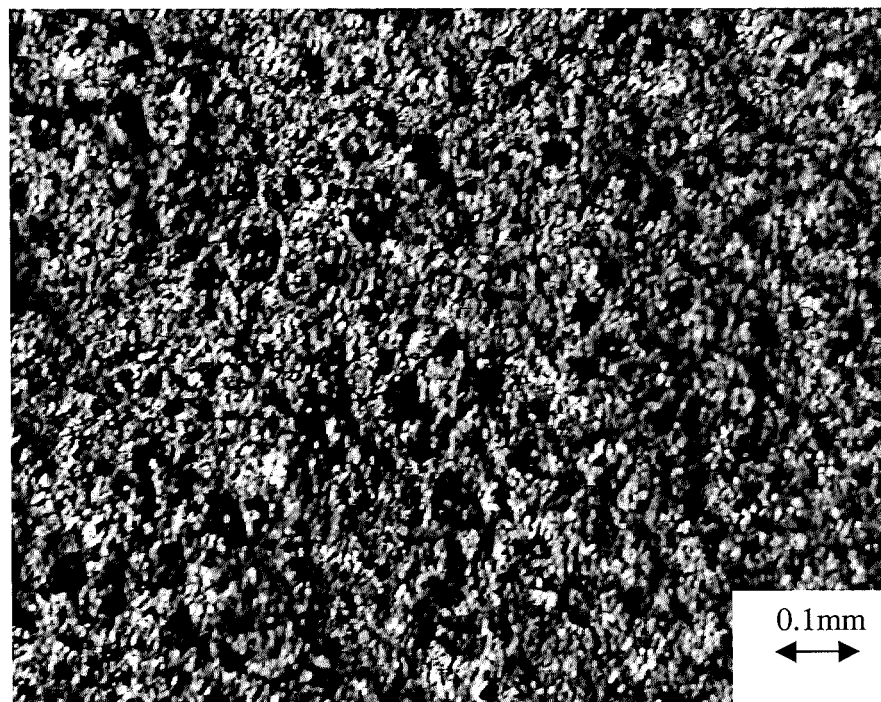


**Figure 7-13 Photograph of sand impacts at 90° impingement  $12 \text{ ms}^{-1}$ ,  
2000mg/l 18°C**

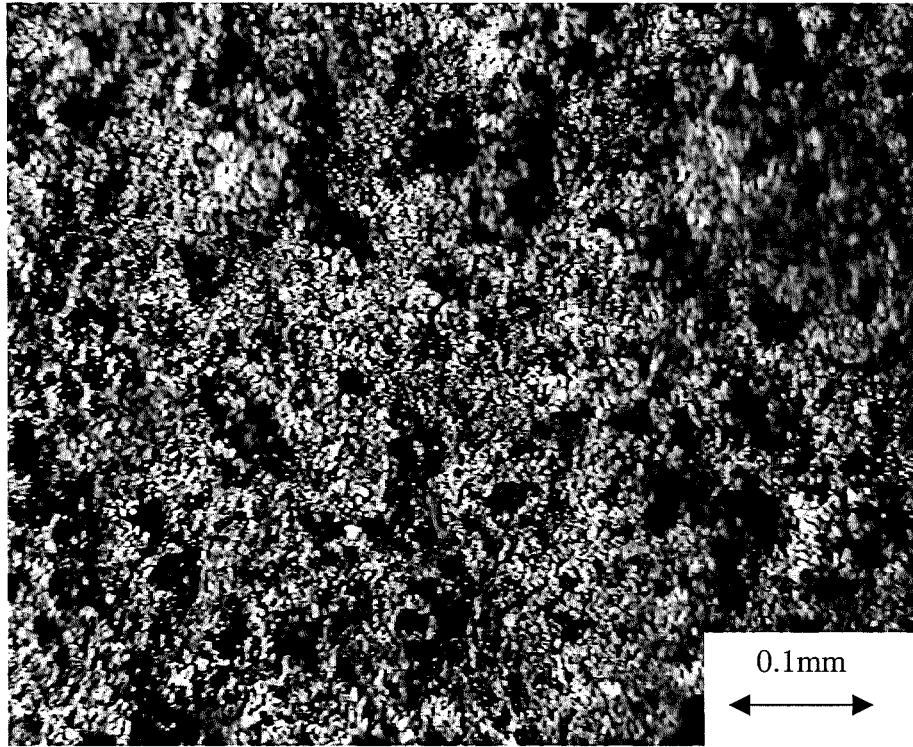


**Figure 7-14 Craters in the middle of the 90° wear scar  $12 \text{ ms}^{-1}$ , 2000mg/l  $18^\circ\text{C}$**

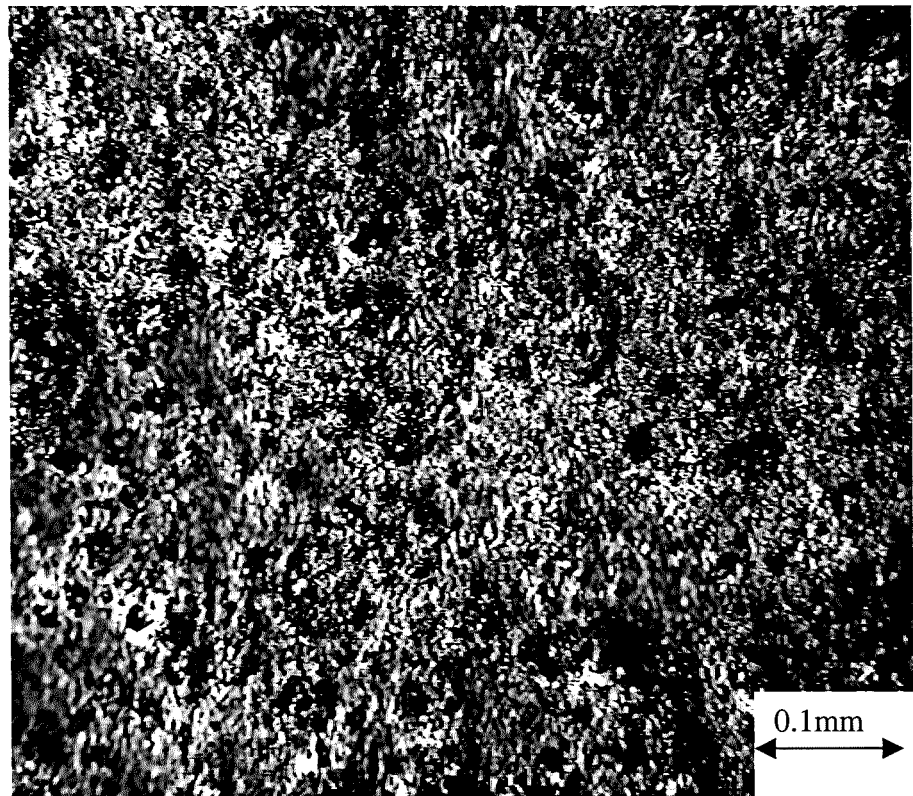


**Figure 7-15 Craters at the edge of the 90° wear scar  $12 \text{ ms}^{-1}$ , 2000mg/l  $18^\circ\text{C}$**

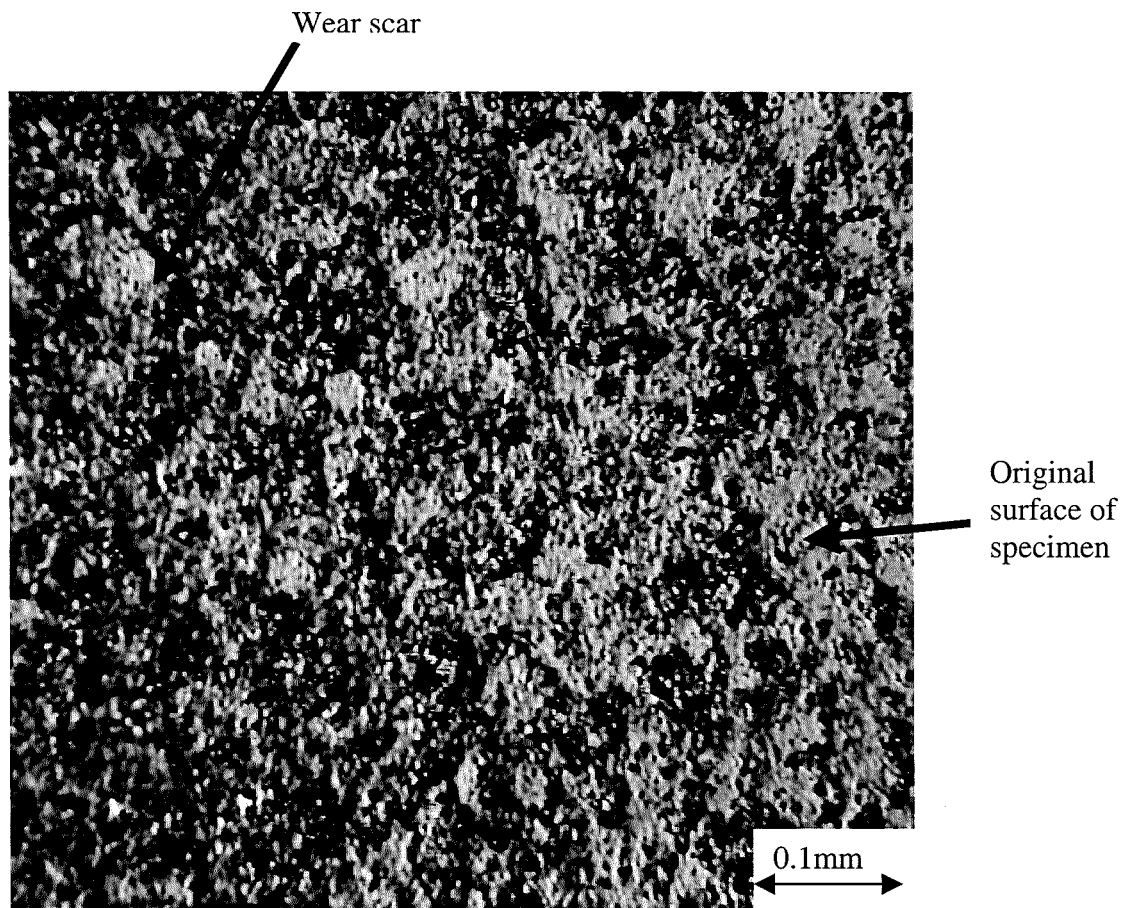


Figure 7-16 Diminishing craters at the edge of the 90° wear scar 12 ms<sup>-1</sup>, 2000mg/l 18°C

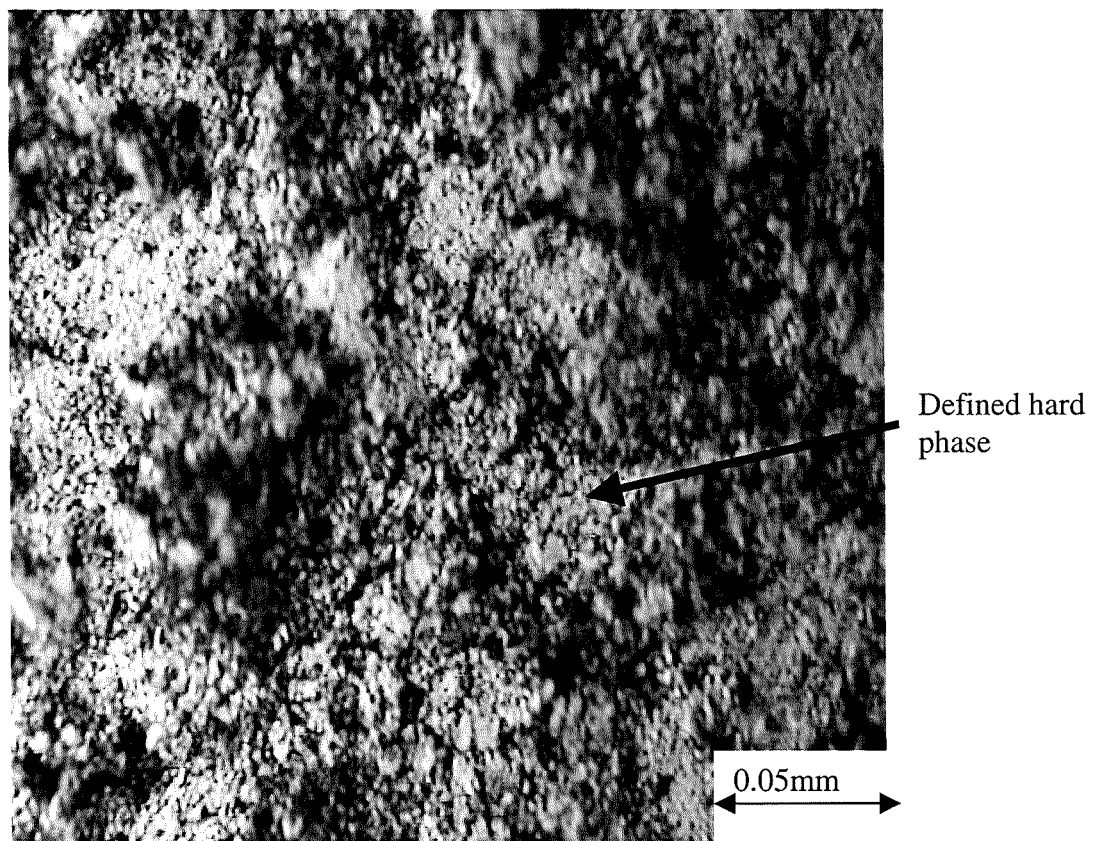
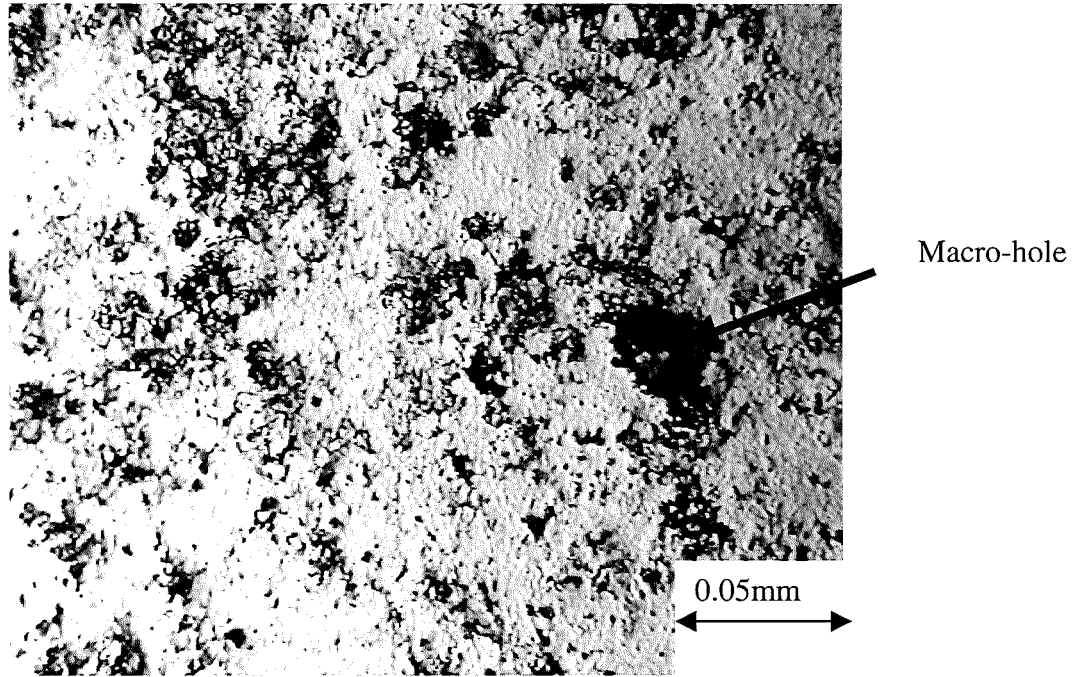
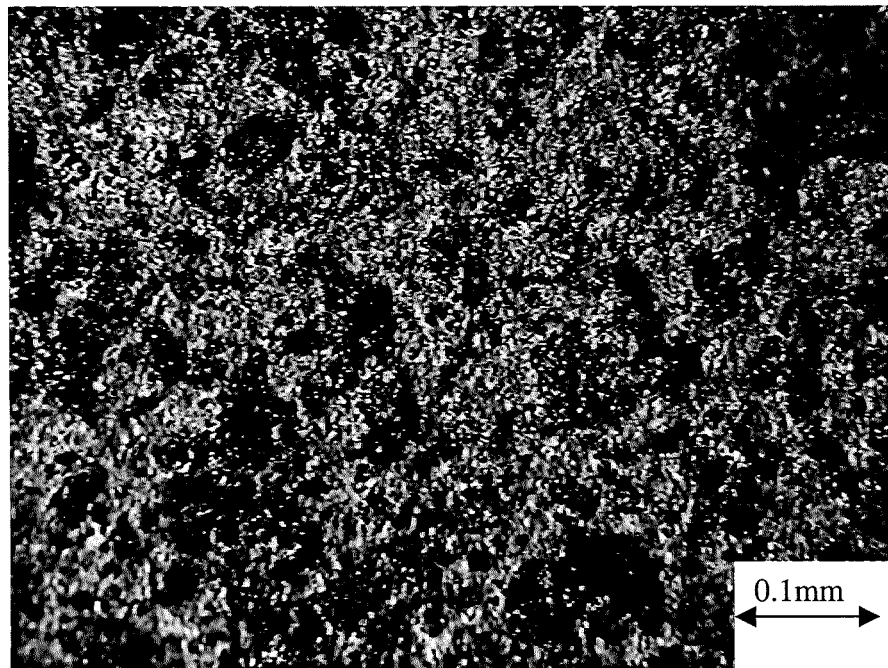


Figure 7-17 Area just outside wear scar defining hard phase 12 ms<sup>-1</sup>, 2000mg/l 18°C



**Figure 7-18 Area outside wear scar showing discrete corroded areas  $12 \text{ ms}^{-1}$ ,  $2000 \text{ mg/l}$ ,  $18^\circ \text{C}$**

When cathodic protection is applied to the sample, the surface still has craters on the surface, similar to those seen when there is no cathodic protection. However, there appears to be a reduction in the amount of craters and more hard phase is retained within the coating (Figure 7-19).



**Figure 7-19 Wear scar when cathodic protection is applied at  $90^\circ$ ,  $2000 \text{ mg/l}$  solids**

As previously shown, the surface of the coating sustains a different shape of wear scars as a result of varying the impact angle of the liquid-solid jet stream. Within these wear scars the effect from the liquid-solid jet stream varies, especially at low impact angles. At 30° impingement, the head (the broader part) of the wear scar consists of a roughened surface but not containing any obvious craters like those at 90° (Figure 7-20) and more hard phase is retained. Then at the middle part of the wear scar, the craters become more obvious (Figure 7-21). On the tail of the wear scar (the narrowest part) the impacts from the solid particles do not remove as much material as in the central part and the number of craters are reduced and more of the original surface remains (Figure 7-22).

When the angle of impingement is 45°, the wear scar does not appear to incorporate the 'craters' as before. Instead the surface has a rippled effect (Figure 7-23) as a result of the solid particles ploughing the surface. The gouging of the material by the sand particles is more apparent in the middle of the scar where the craters have been extended into a trough-like shape (Figure 7-24). At the tail of the wear scar (Figure 7-25) again, more of the original surface remains as the effects from the impacting particles have reduced.

As the impingement angle is increased to 60°, the ploughing action from the solid particles becomes less apparent and craters appearing where the material has been removed (Figure 7-26). At 75° impingement, the wear scar contains numerous craters (Figure 7-27) similar to the wear scar after impingement at 90°.

Also to be noted are the areas up and downstream of these wear scars. At the impact angles of 30°-60°, the surfaces above and below the wear scar differed. Above the wear scar the coating was not affected as much by corrosion as the area below. Figure 7-28 and Figure 7-29 show the region below and above (respectively) the wear scar where the matrix is more open - shown by the dark areas - below the wear scar and less affected by corrosion above the wear scar.

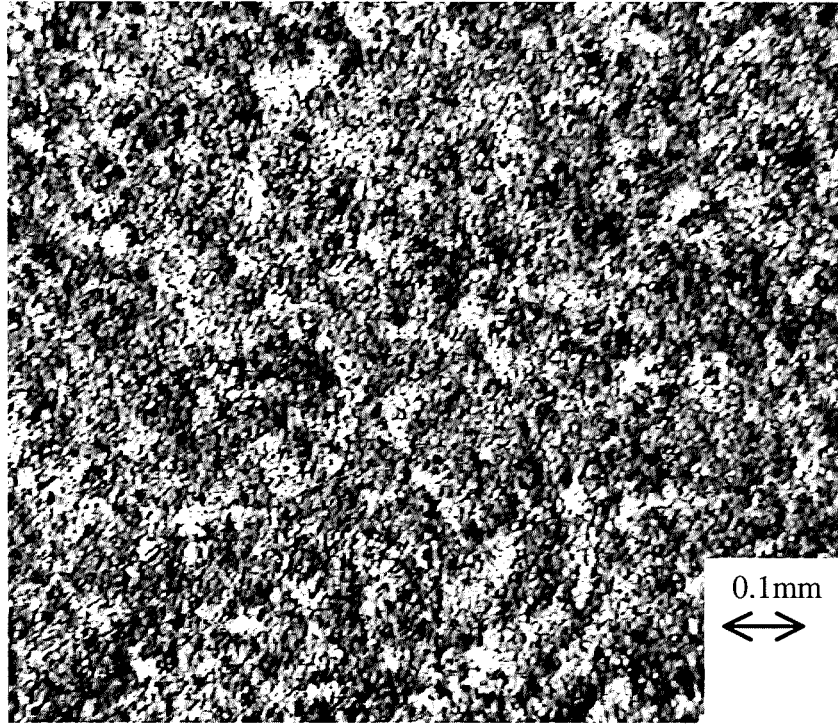


Figure 7-20 Roughened surface at head of 30° wear scar

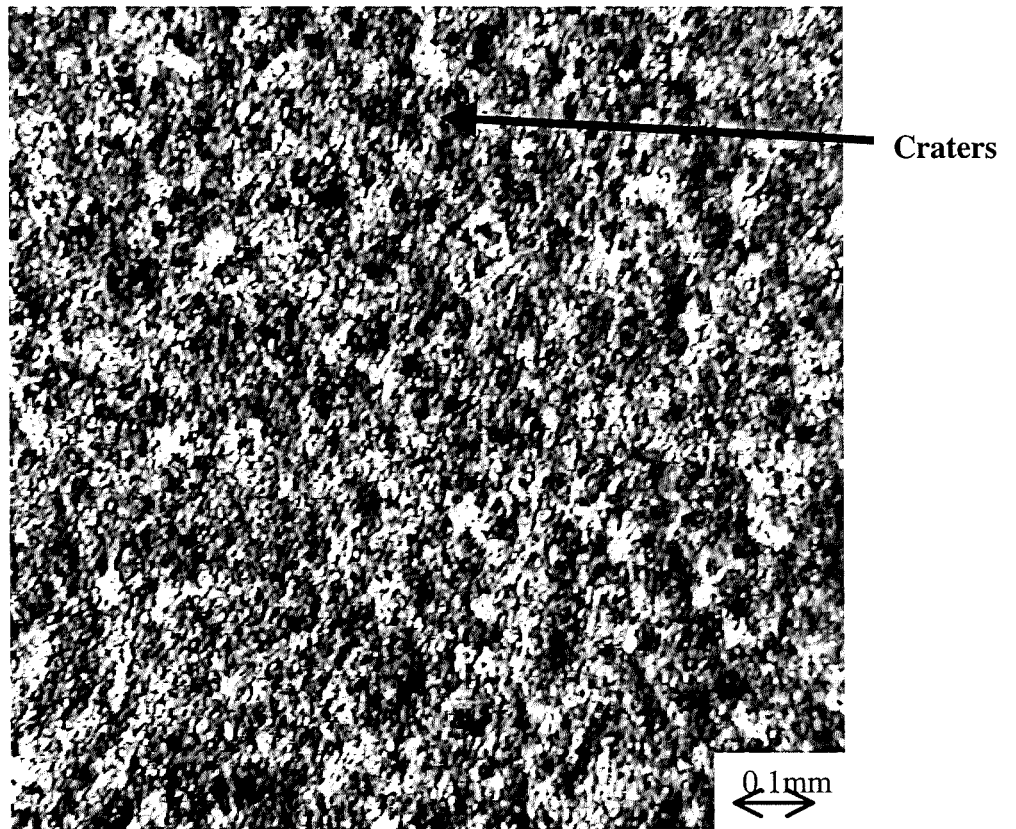


Figure 7-21 Middle of 30° wear scar

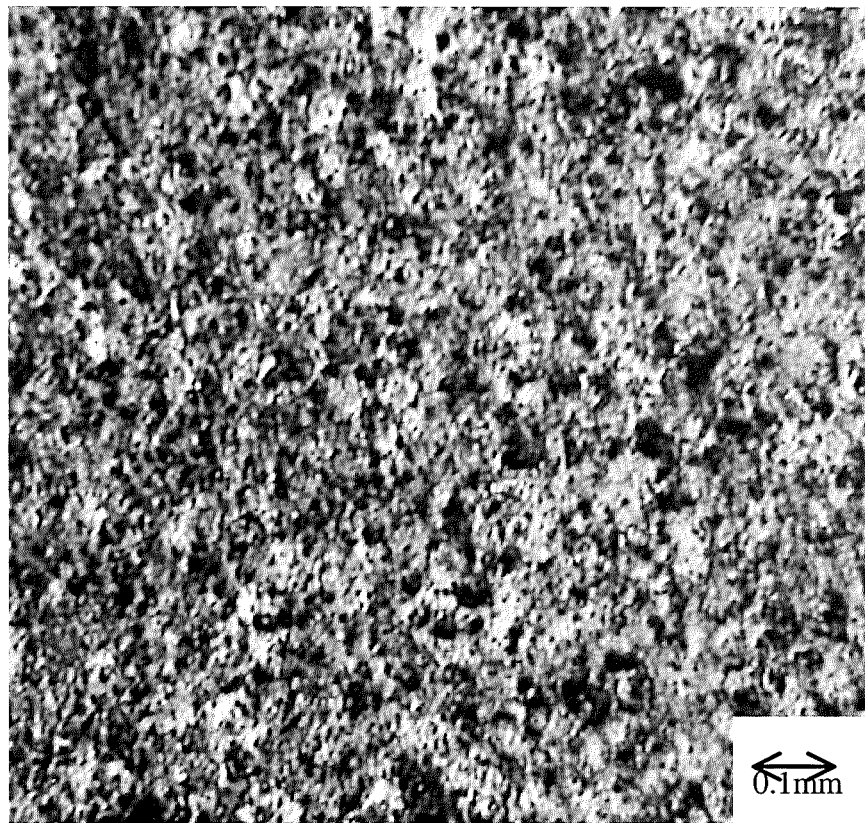


Figure 7-22 Tail of wear scar at  $30^\circ$ ,  $12 \text{ ms}^{-1}$ ,  $2000 \text{ mg/l}$ ,  $18^\circ \text{C}$

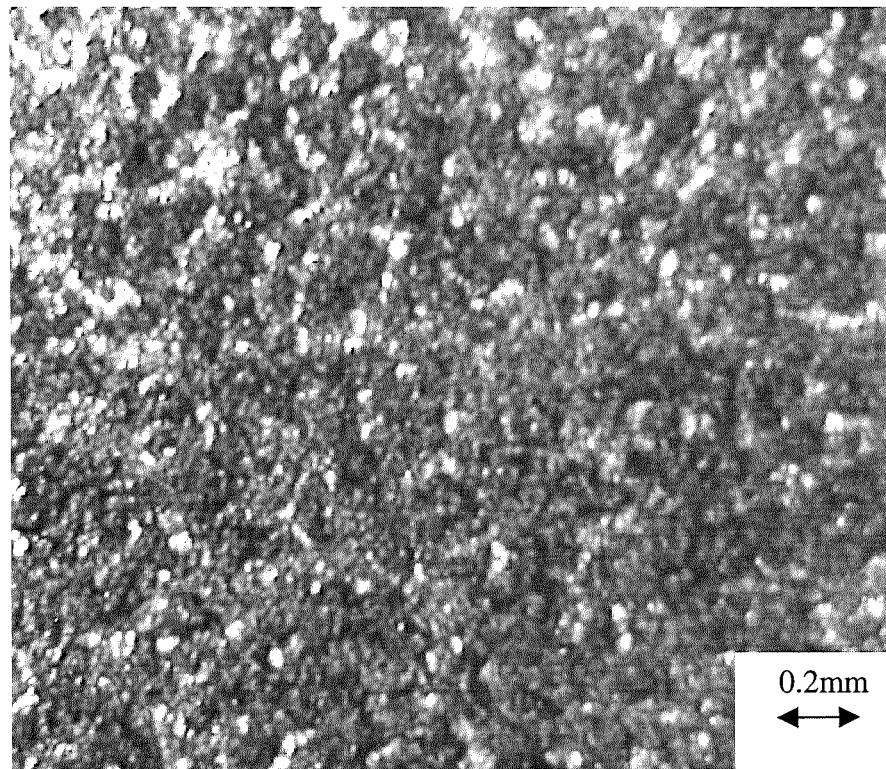


Figure 7-23 Ploughing effects at  $45^\circ$  impingement angle,  $12 \text{ ms}^{-1}$ ,  $2000 \text{ mg/l}$ ,  $18^\circ \text{C}$

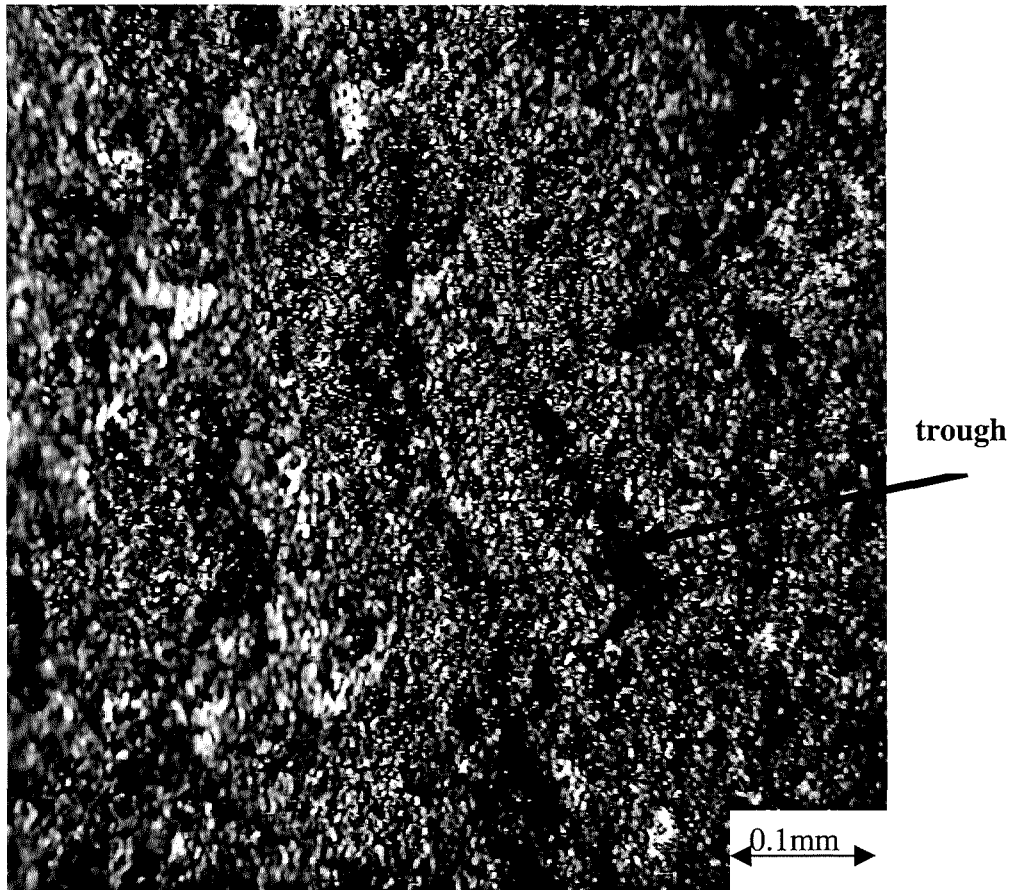


Figure 7-24 Middle of 45° impingement wear scar, 12 ms<sup>-1</sup>, 2000mg/l, 18°C

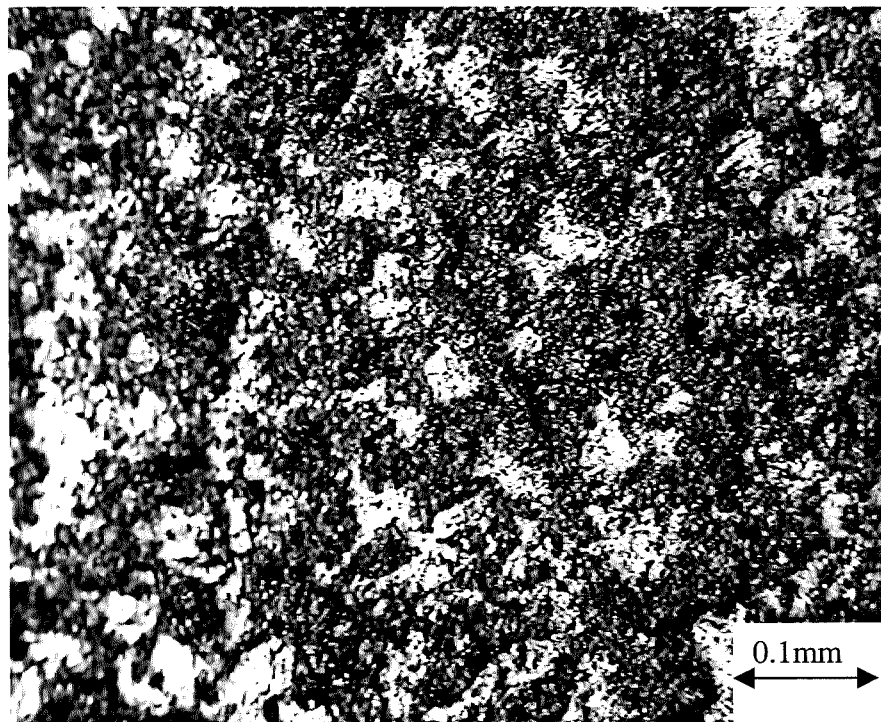
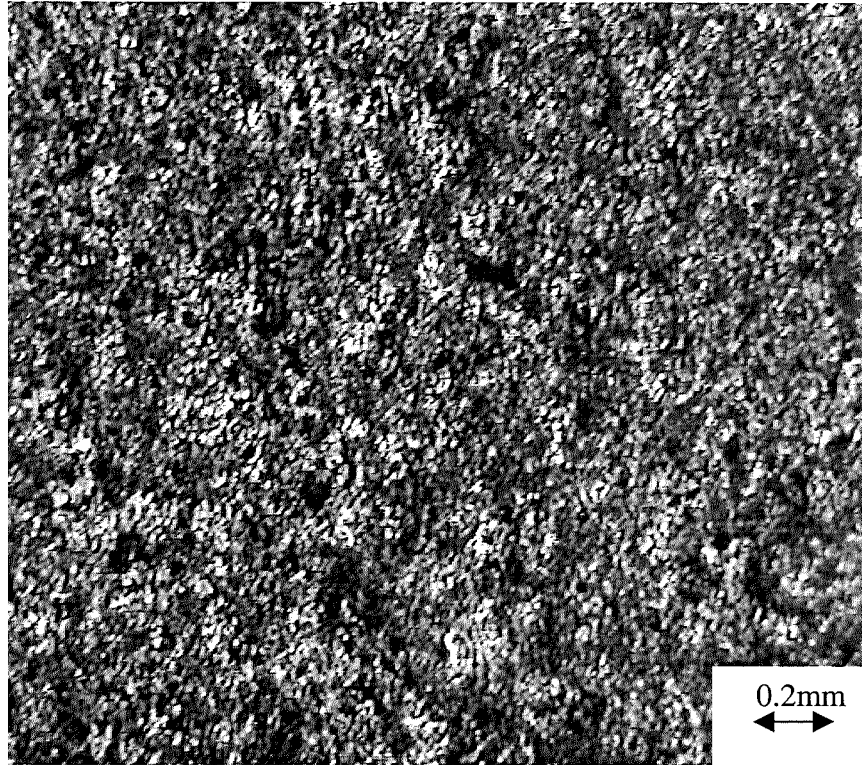
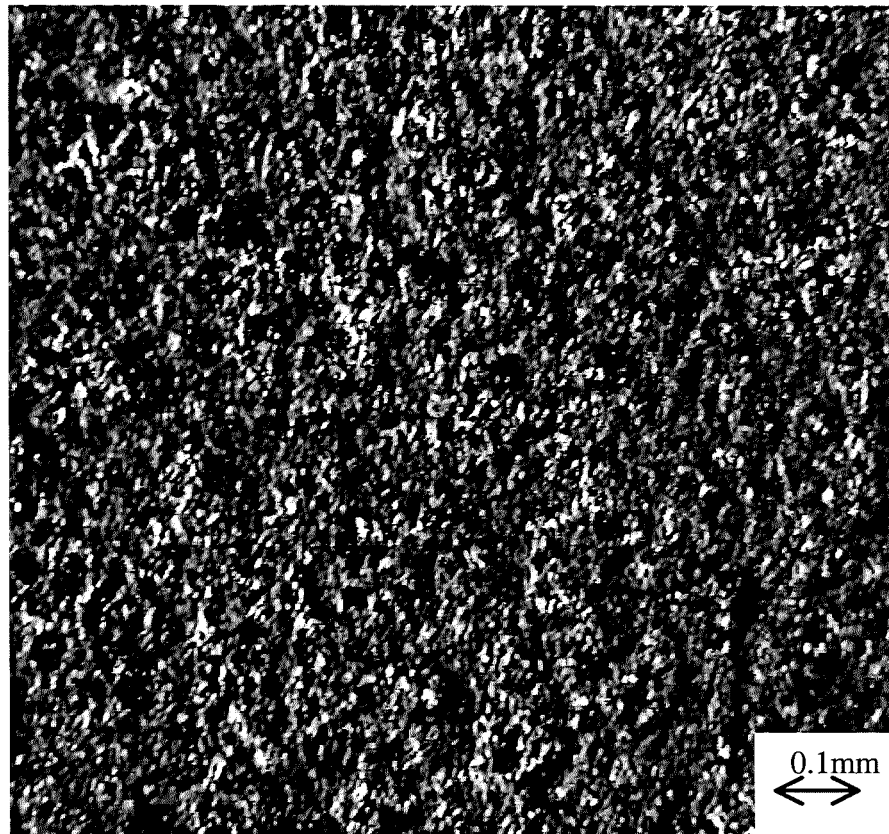


Figure 7-25 Tail of 45° impingement wear scar, 12 ms<sup>-1</sup>, 2000mg/l, 18°C



**Figure 7-26** Inside wear scar at 60° impingement, 12 ms<sup>-1</sup>, 2000mg/l, 18°C



**Figure 7-27** Inside wear scar of 75° impingement, 12 ms<sup>-1</sup>, 2000mg/l, 18°C

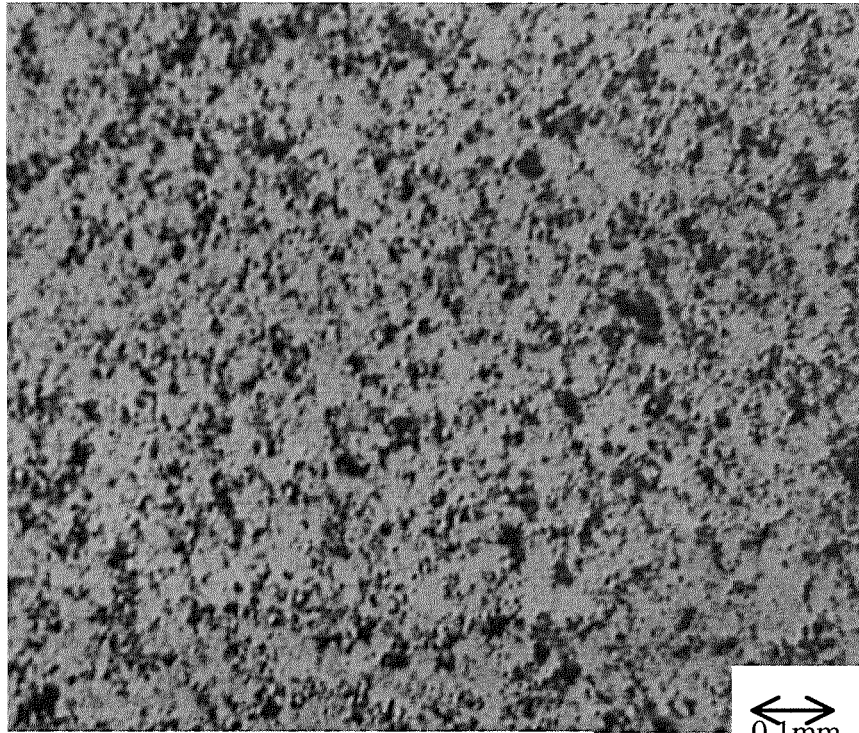


**Figure 7-28 Corroded area at bottom of wear scar at 60° impingement, 12 ms<sup>-1</sup>, 2000mg/l, 18°C**

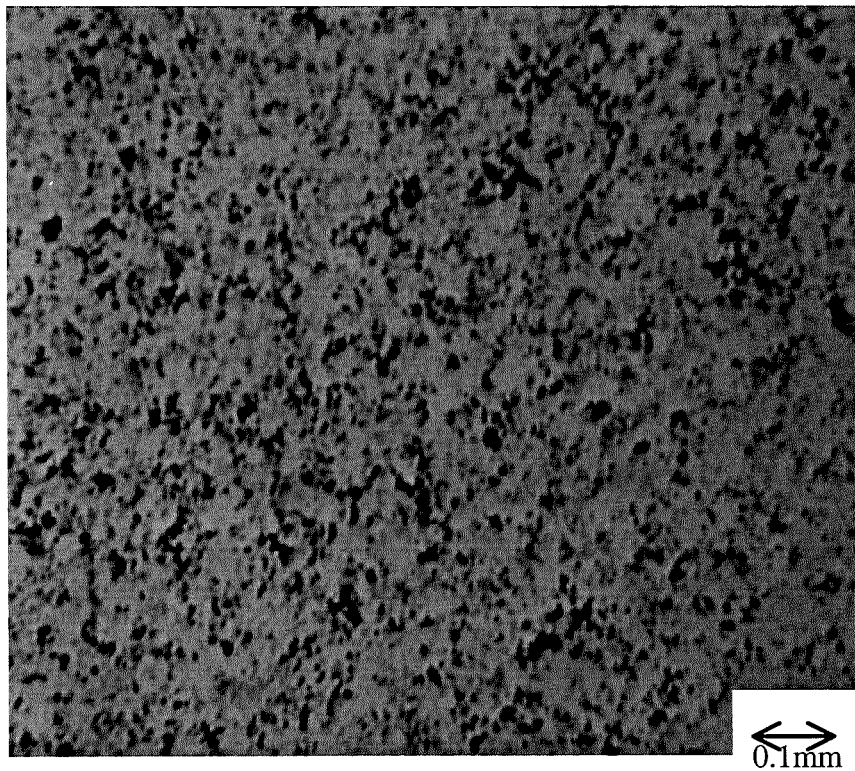


**Figure 7-29 Uncorroded area above wear scar at 60° impingement, 12 ms<sup>-1</sup>, 2000mg/l, 18°C**

### 7.3.2 Corrosion Effects with Differing Impact Angles

As can be seen in Figure 7-30, the anodic polarisation results of tests conducted after 4 hours impingement with 2000 mg/l at the various angles are not greatly different. The corrosion rates obtained from Tafel Extrapolation are shown in Table 7-4. The slight variation ( $20\text{-}24\mu\text{A}/\text{cm}^2$ ) in the corrosion currents at different angles does not reflect any systematic increase or decrease with angle change, but can be attributed to experimental error.

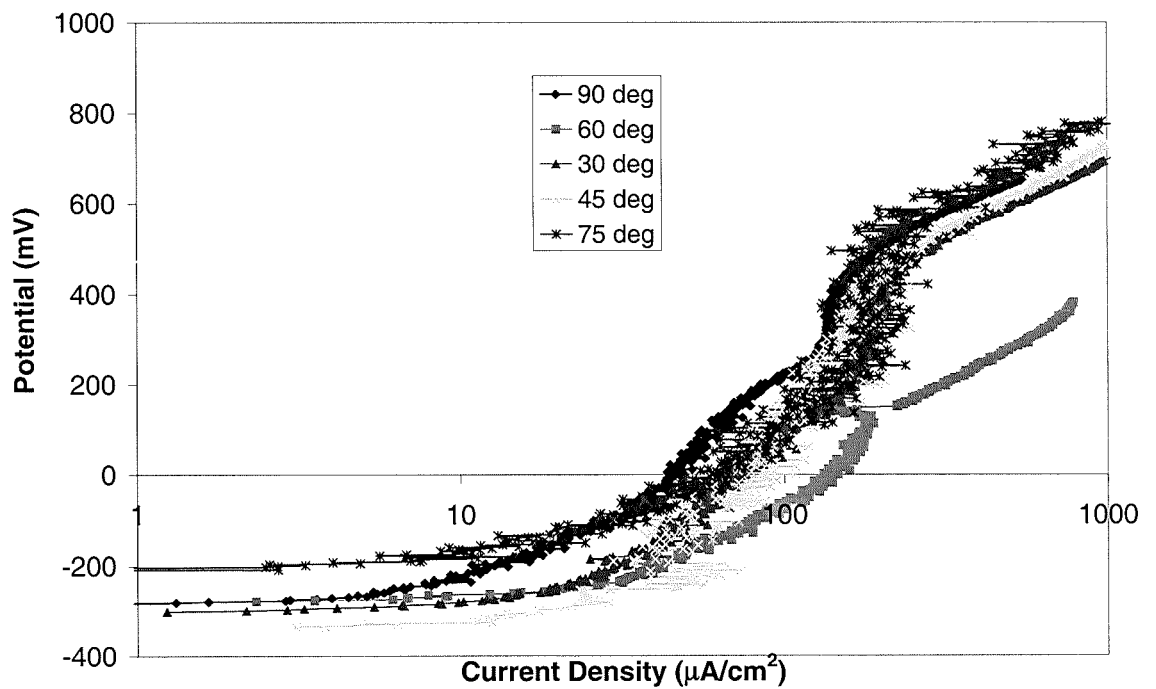
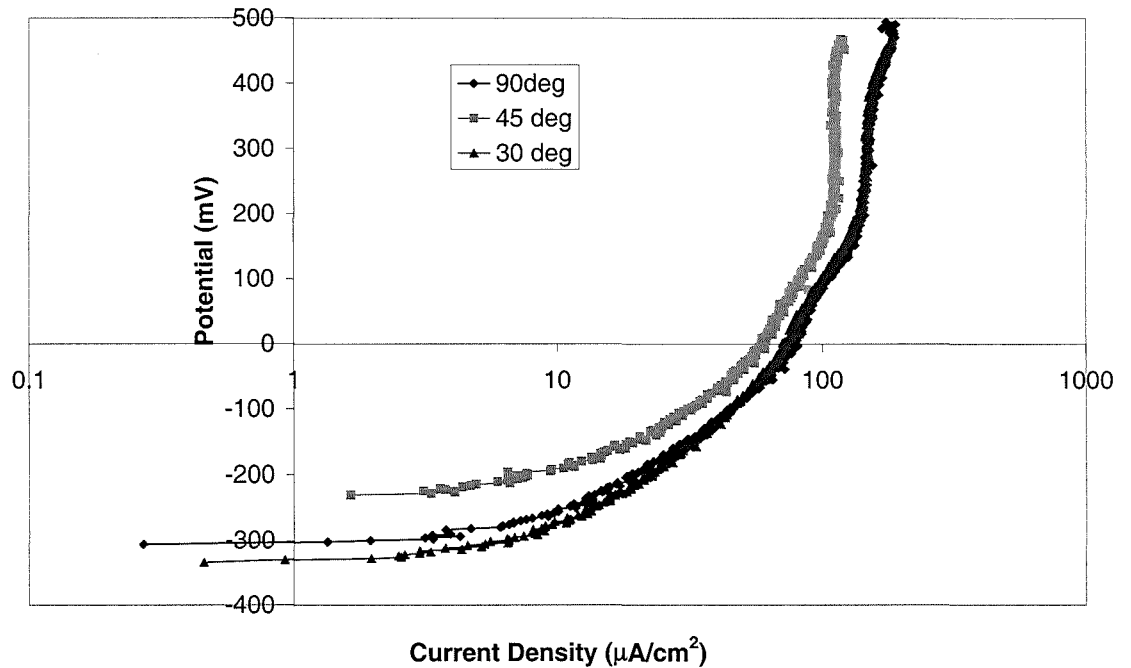


Figure 7-30 Anodic Polarisations at angles  $90^\circ$ ,  $75^\circ$ ,  $60^\circ$ ,  $45^\circ$  and  $30^\circ$  with 2000 mg/l solids after 4 hours impingement at  $12\text{ ms}^{-1}$

Impact Angle	$I_{\text{corr}}$ ( $\mu\text{A}/\text{cm}^2$ )
30	22
45	24
60	23
75	24
90	20

Table 7-4 Corrosion rates found at angles  $90^\circ$ ,  $75^\circ$ ,  $60^\circ$ ,  $45^\circ$  and  $30^\circ$  with 2000 mg/l solids after 4 hours impingement at  $12\text{ ms}^{-1}$

Similarly after one hour, the angle of impingement did not affect the corrosion rate of the coating. Figure 7-31 shows anodic polarisation curves conducted after one- hour impingement at 90°, 45° and 30° where the corrosion rate was found to be 8  $\mu\text{A}/\text{cm}^2$ , 10  $\mu\text{A}/\text{cm}^2$  and 9  $\mu\text{A}/\text{cm}^2$  respectively.



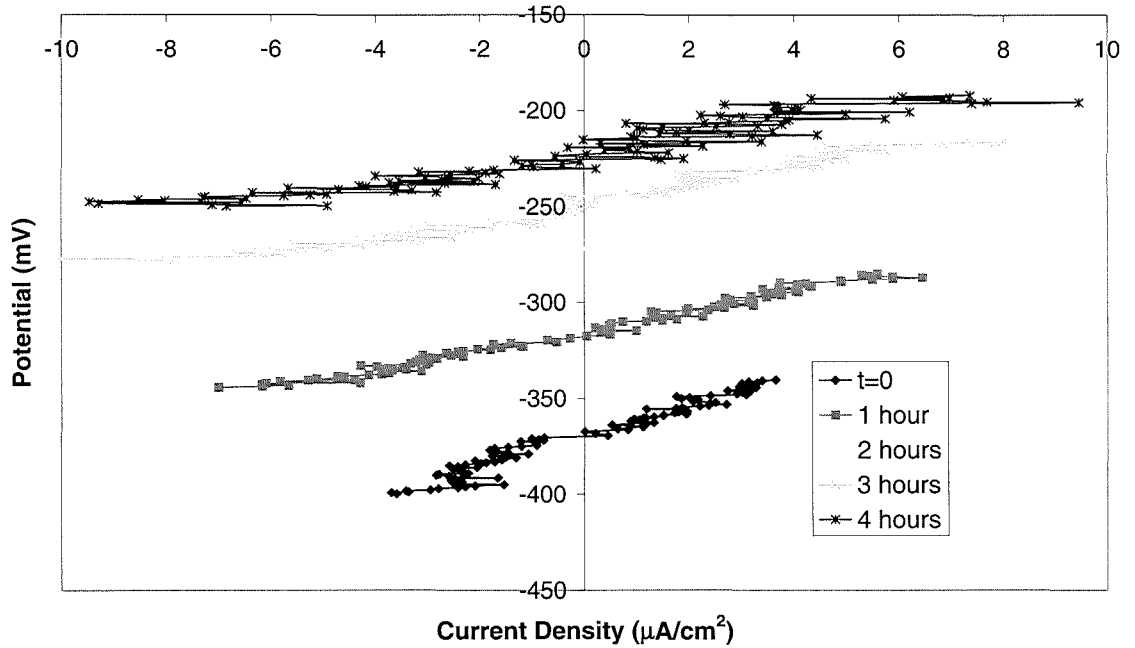
**Figure 7-31 Anodic polarisation curves at 90°, 45° and 30° after 1 hour impingement with 2000 mg/l solids at 12 ms<sup>-1</sup>**

Figure 7-32 shows typical results of linear polarisation tests during a 4-hour test at 75° impingement, the polarisation resistance values ( $R_p$ ) for this and other angles are shown in Table 7-5. The resistance of each specimen generally decreased with time with maximum resistance at time zero in the range 4-8  $\times 10^3 \Omega/\text{cm}^2$ , decreasing to the range 2-4  $\times 10^3 \Omega/\text{cm}^2$ .

Taking an average of the three corrosion current densities found after one hour impingement as 9  $\mu\text{A}/\text{cm}^2$  and an estimate of the corrosion current increasing to the average after 4 hours impingement of 22  $\mu\text{A}/\text{cm}^2$ , a weight loss due to corrosion of 0.30 mg (from Equation 4.2) during a four hour impingement with 2000 mg/l at all the angles can be estimated.

The contributions of each component of erosion, corrosion and synergy are shown in Figure 7-33 which shows that the absolute value of each component

decreases with impingement angle, except the corrosion component which is constant. As percentage values, the erosion component is always the most dominant in the region of 44-48% and the corrosion component is the least dominant at (8-14%). However, the indirect corrosion component, synergy, is significant accounting for 37-44% of the overall material loss.



**Figure 7-32 Linear polarisation results during 4 hours liquid-solid impingement at 75° at 12 ms<sup>-1</sup> with 2000 mg/l solids**

Time (hours)	Rp (x10 <sup>3</sup> Ω.cm <sup>2</sup> )				
	90°	30°	45°	60°	75°
0		6	7.6	4.3	8
1	5	5.3	4.7	4	4.7
2	4.7	5.0	3.6	3.4	5.5
3	4.1	3.6	3.2	3.3	5
4	4.1	3.0	2.0	3.0	4.5

**Table 7-5 Polarisation resistance values from the linear polarisation curves after 4 hours impingement with 2000 mg/l solids**

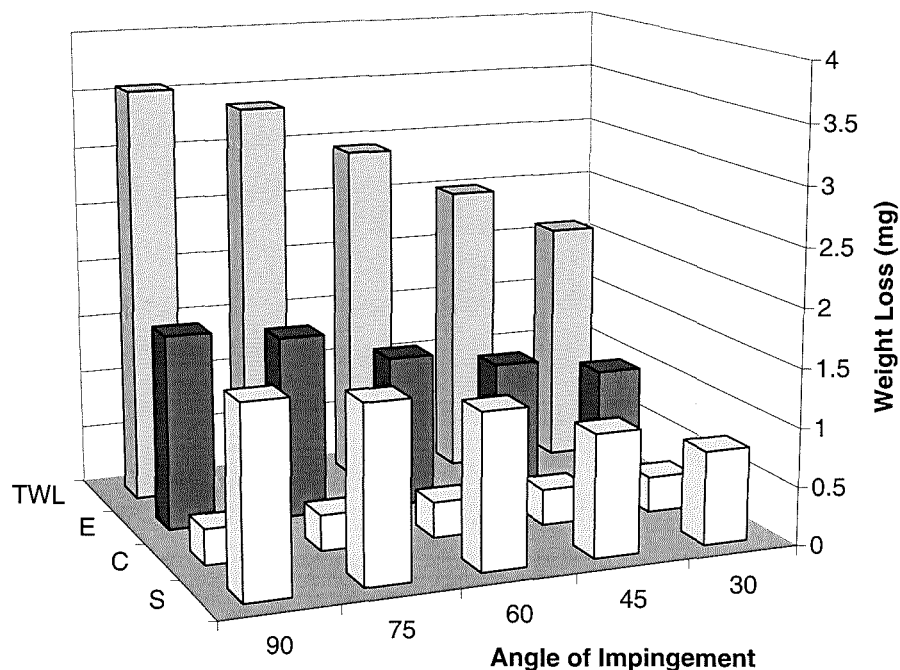


**Figure 7-33 Erosion, corrosion and synergy components at 30°, 45°, 60°, 75° and 90° impingements with 2000 mg/l solids at 12 ms<sup>-1</sup>**

## 7.4 Concentric Specimens

### 7.4.1 Introduction

Specimens of coating 2, as described in section 4.1 were subjected to a liquid-solid impinging jet, where the jet was mainly incident on the central specimen. Linear polarisation tests were conducted hourly during the course of the experiment on both the inner and outer parts to the specimen followed by full anodic polarisation scans after the four hour test with 2000 mg/l solids at 18°C at 12 ms<sup>-1</sup>. Galvanic currents were measured at half-hourly intervals during the course of separate four-hour experiments as well as measurement of the change in the free corrosion potential.

### 7.4.2 Galvanic Effects within Concentric Specimens

Table 7-6 shows the current from the central specimen (the anode) to the outer specimen (the cathode) and the variation of the free corrosion potential during

the test. It is clear that there is a substantial driving force for galvanic corrosion which displayed a generally increasing trend with time. In line with these electrode potential differences, the currents progressively rise from 6 to 31.5  $\mu\text{A}$  which, when taking into consideration the area of the inner specimen, 0.28  $\text{cm}^2$ , translates into current densities of 21 to 111  $\mu\text{A}/\text{cm}^2$ . In a replicate experiment the currents rise from 2.5  $\mu\text{A}$  to 17  $\mu\text{A}$  (Table 7-7) over a period of four hours which gives galvanic currents of 9  $\mu\text{A}/\text{cm}^2$  to 61  $\mu\text{A}/\text{cm}^2$ .

Time (mins)	I ( $\mu\text{A}$ )	$E_{\text{corr}}$ Inner Specimen (mV)	$E_{\text{corr}}$ Outer Specimen (mV)	Driving Potential (mV)
0	6	-399	-399	1
30	6.5	-351	-277	74
60	7.7	-320	-254	66
90	9.2	-300	-201	99
120	10.5	-270	-180	90
150	15	-250	-111	139
180	20	-222	-82	140
240	27	-180	-70	110
300	31.5	-165	-55	110

**Table 7-6 Galvanic currents and  $E_{\text{corr}}$  of concentric specimen**

Time (mins)	0	30	60	90	120	150	180	240	300
I ( $\mu\text{A}$ )	2.5	3	3.5	3.5	7.5	8.3	9.0	9.7	17

**Table 7-7 Galvanic currents of concentric specimen**

### 7.4.3 Linear Polarisation of Concentric Specimen

In addition to the galvanic currents measured between the two specimens, the self-corrosion rate of the inner specimen shows that it corrodes at a higher rate than the outer specimen. This can be seen by linear polarisation curves (Figure 7-34 to Figure 7-37) where the inner specimen shows higher currents than the outer specimen at comparable impingement times. This is in agreement with the polarisation resistances found (Table 7-8). These show a general decrease in resistance over the four hour experiment and also lower resistances on the inner specimen compared with the outer specimen.

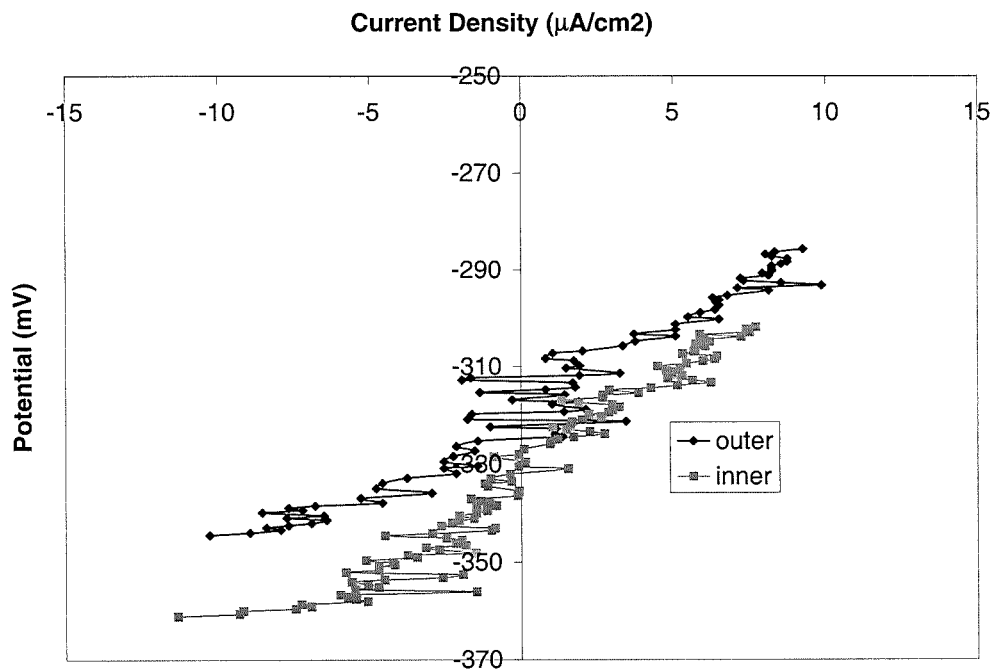


Figure 7-34 Linear polarisation curves of inner and outer concentric specimens at time zero with 2000 mg/l solids impinging at  $12 \text{ ms}^{-1}$

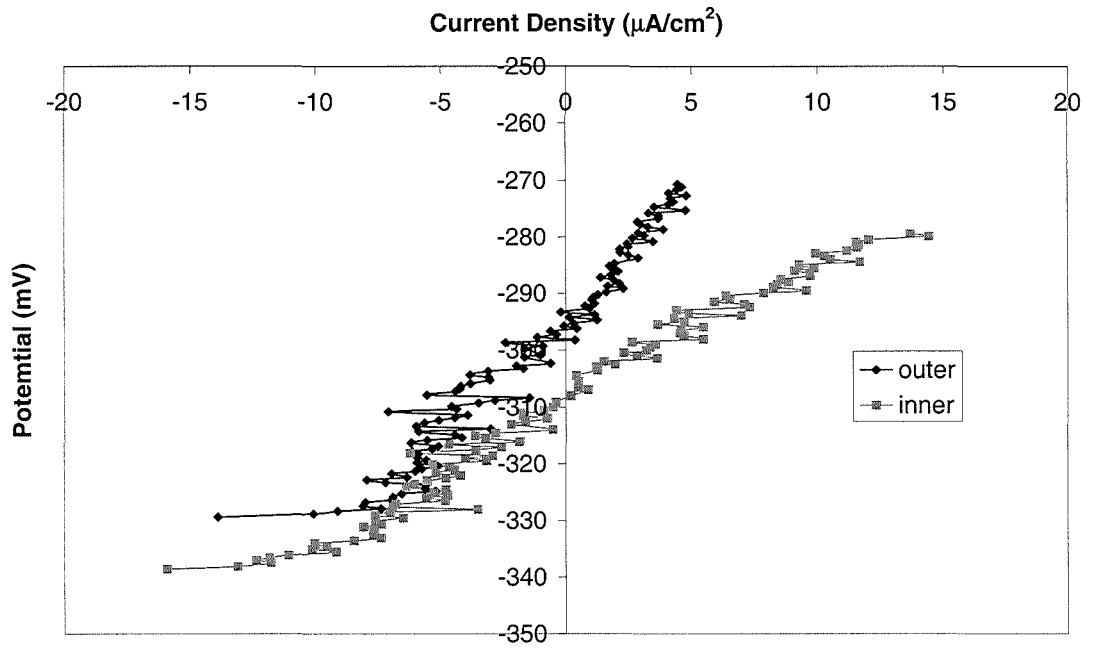


Figure 7-35 Linear polarisation curves of outer and inner concentric specimens after 1 hour with 2000 mg/l solids impinging at  $12 \text{ ms}^{-1}$

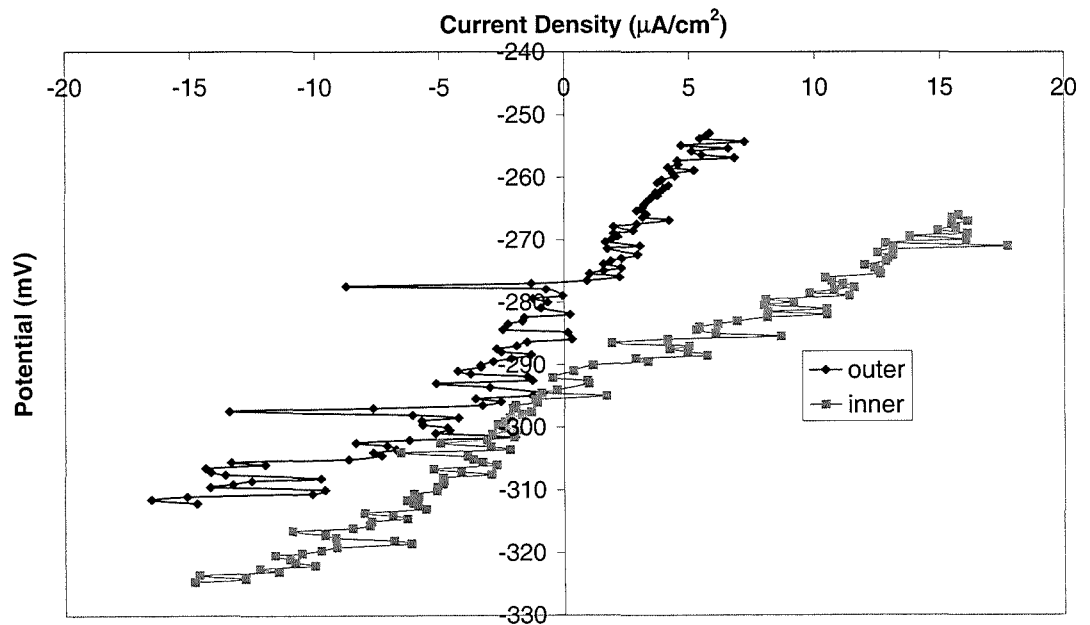
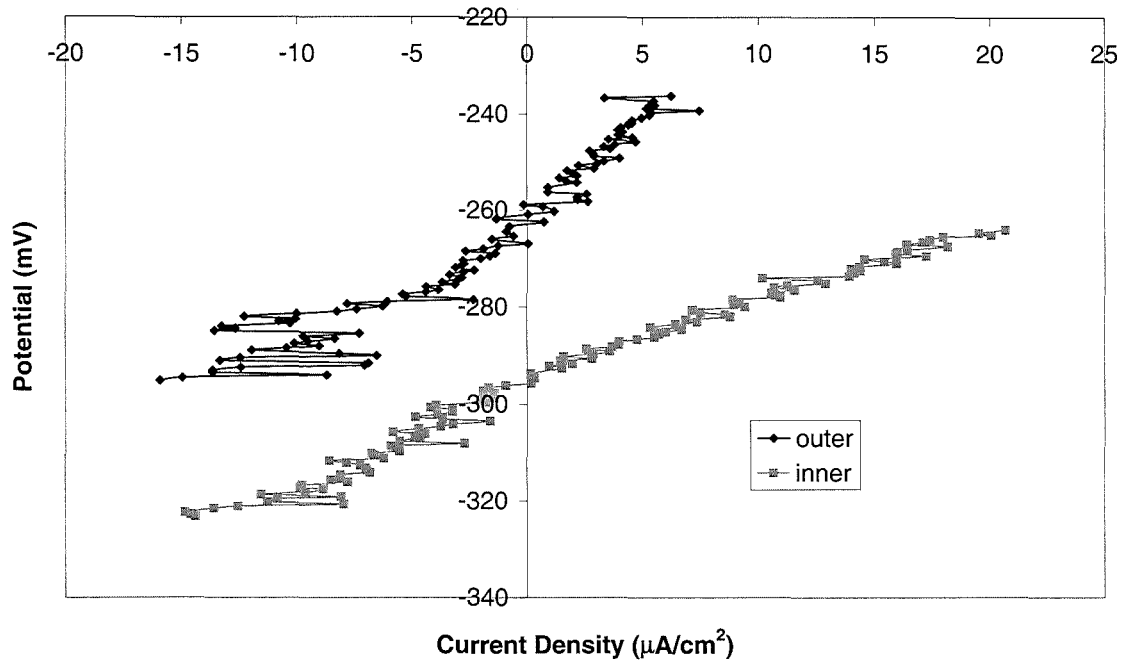


Figure 7-36 Linear polarisation of inner and outer concentric specimens after 2 hours with 2000 mg/l solids impinging at  $12 \text{ ms}^{-1}$



**Figure 7-37 Linear polarisations on inner and outer specimens after 3 hours impingement with 2000 mg/l solids impinging at 12 ms<sup>-1</sup>**

Time ( hours)	Rp (x 10 <sup>3</sup> Ω/cm <sup>2</sup> )	
	Inner specimen	Outer specimen
0	4.6	4.3
1	2.6	4.2
2	2.0	3.6
3	1.8	3.3

**Table 7-8 Rp values from linear polarisations on inner and outer concentric specimens**

#### 7.4.4 Anodic Polarisation of Concentric Specimens

Figure 7-38 shows the anodic polarisation curve, after four hours impingement with 2000 mg/l solids, of the inner and outer specimen. The inner specimen displays more active corrosion characteristics with a rapid rise in current with potential and a slight indication of a breakdown potential less than 100mV more

positive than  $E_{\text{corr}}$ . The outer specimen shows more passive corrosion behaviour with lower current densities and a breakdown potential at 350mV more positive than  $E_{\text{corr}}$ . In contrast to with a composite specimen, where the corrosion current density is  $\sim 24\mu\text{A}/\text{cm}^2$ , the inner specimen has a corrosion current density of  $32\mu\text{A}/\text{cm}^2$  while the outer specimen has a corrosion current density of  $6\mu\text{A}/\text{cm}^2$ . This indicates that the area directly under the impinging jet corrodes 5 times faster than the area outside the jet.

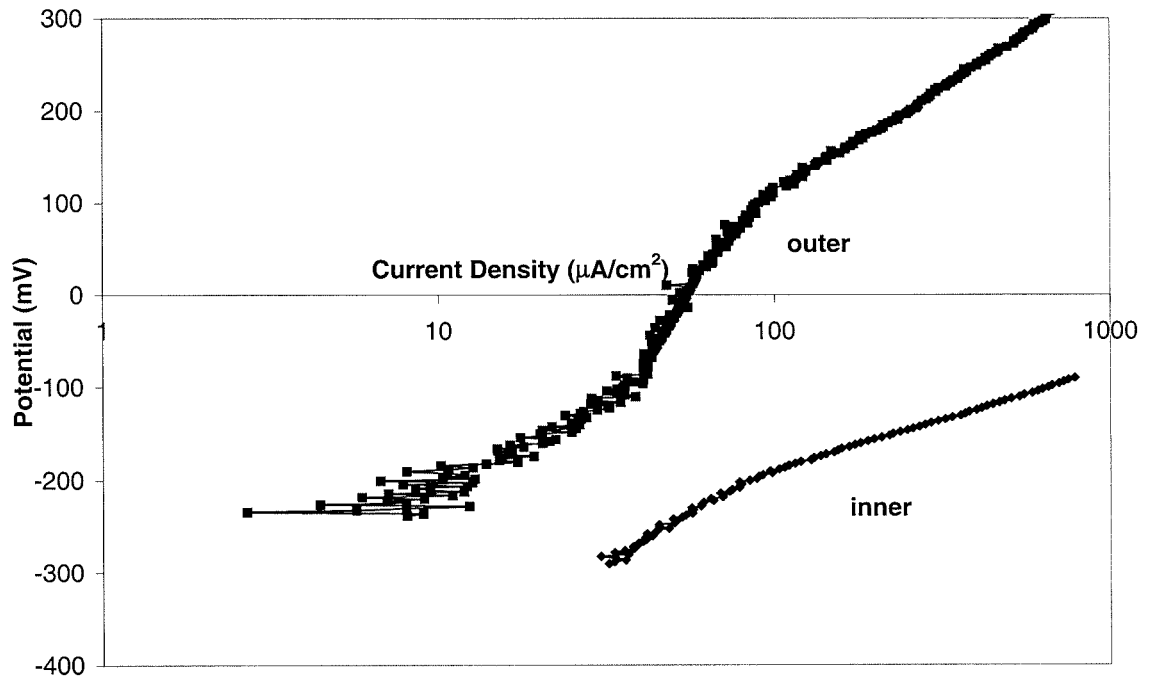


**Figure 7-38 Anodic Polarisation curves for inner and outer concentric specimens after 4 hours impingement at  $12\text{ ms}^{-1}$  with  $2000\text{ mg/l}$  solids**

#### 7.4.5 Post Test Analysis of Concentric Specimens

This section presents the microscopy of the concentric specimens. The inner specimen contains the wear scar as previously seen on the composite specimen (Figure 7-39) although no difference was noted on the light microscope to compensate for a reduction in corrosive effects due to the galvanic current. The outer ring of the specimen is unaffected by the sand particles as no obvious signs of impacts from solid particles were noted. However, the outer area of the ring

suffers more surface defects largely due to corrosion processes. Figure 7-40 shows that the corrosive effects result in macro-holes forming where extensive matrix dissolution has occurred. The macro-holes are shown more magnified in Figure 7-41.

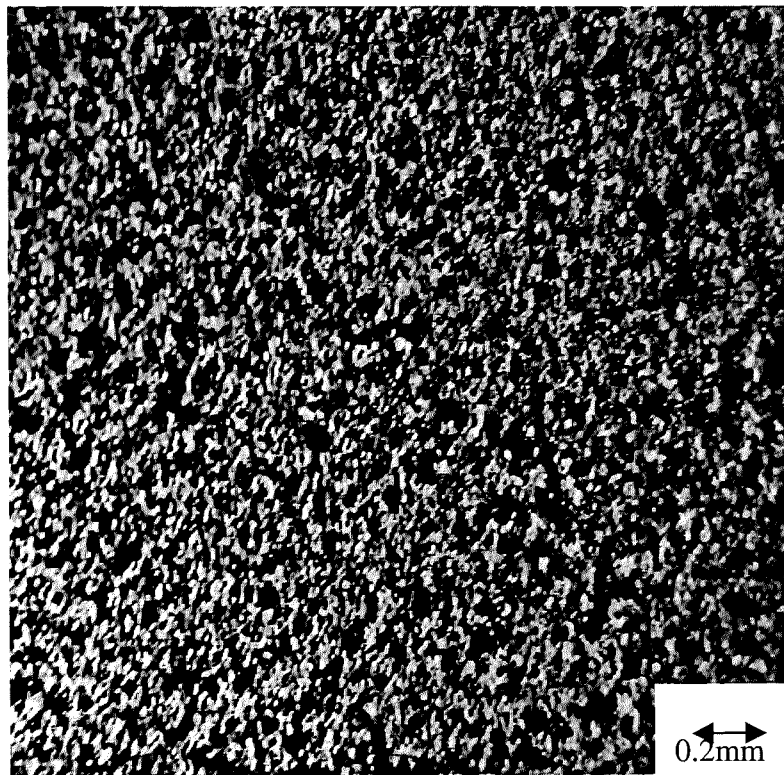


**Figure 7-39** Central specimen of concentric with eroded surface

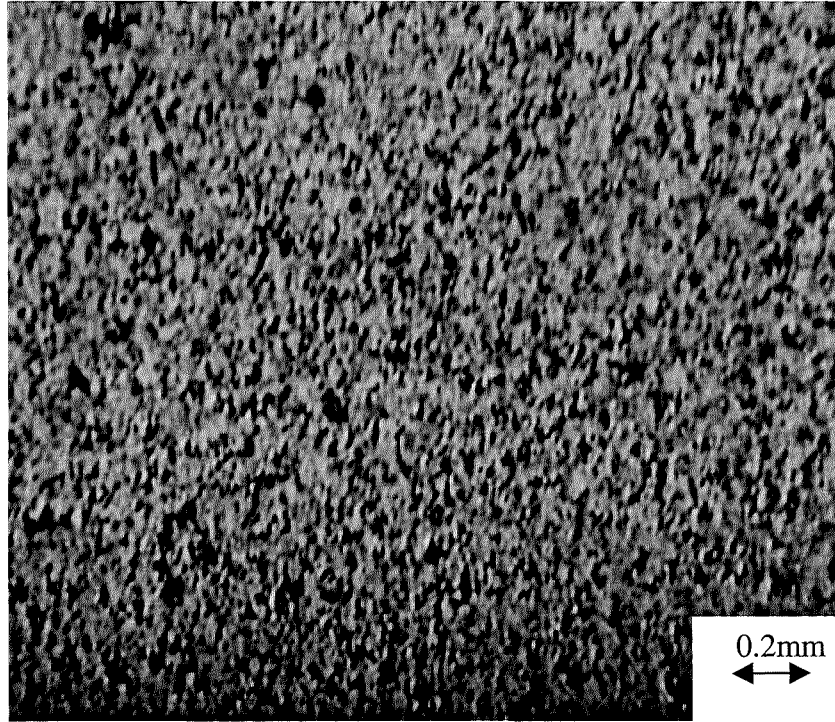


**Figure 7-40** Outer part of concentric specimen showing no erosion but more effect from corrosion

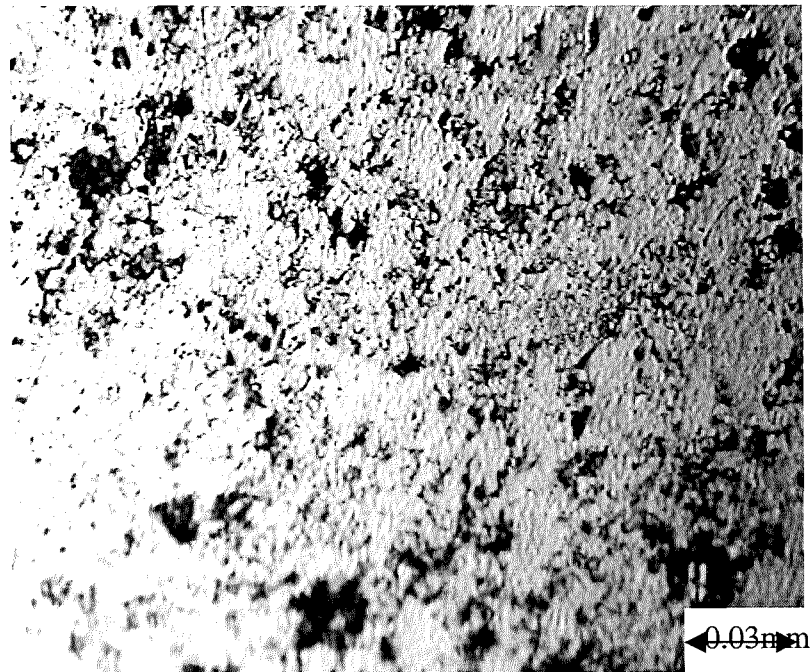


**Figure 7-41** The outer ring where the matrix is effected by corrosion

## 7.5 Effects of Anodic Potentials Under Erosion-Corrosion Conditions

Figure 7-42 shows the surface of a composite specimen which was held at 0 mV (SCE), ~250 mV more positive than  $E_{\text{corr}}$ , during the 4 hour impingement period. It shows a distinctive pattern of the wear scar surrounded by a darker ring. This darker ring is also evident, but not as pronounced, in specimens under erosion-corrosion conditions at the free corrosion potential (Figure 7-7). The darker ring is more evident in Figure 7-43, with lighter areas that spray outward from the wear scar. On inspection with a light microscope, no difference between this 'intermediate zone' and the outer area of the specimen can be determined. A substantial increase in the weight loss compared with free erosion-corrosion conditions was also noted (Table 7-9). Extremely large currents in the mA range were recorded in this anodic potentiostatic controlled experiment. These currents exhibited an initial increase in the current followed by a stabilisation.

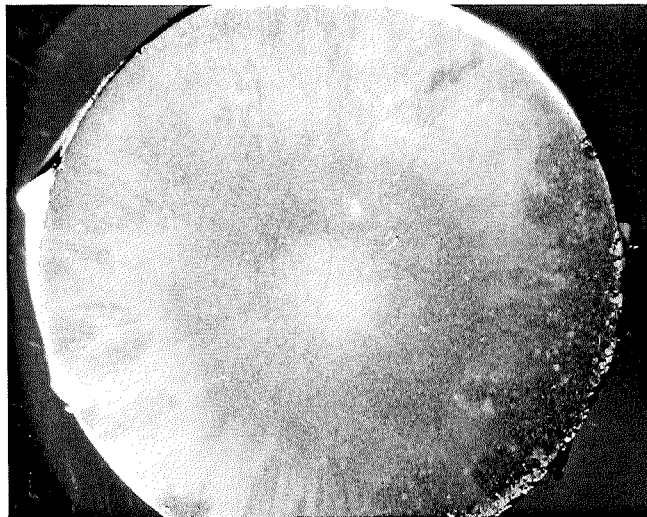


**Figure 7-42 Photograph of Specimen held at 0mV under impingement with 650 mg/l solids for 4 hours**

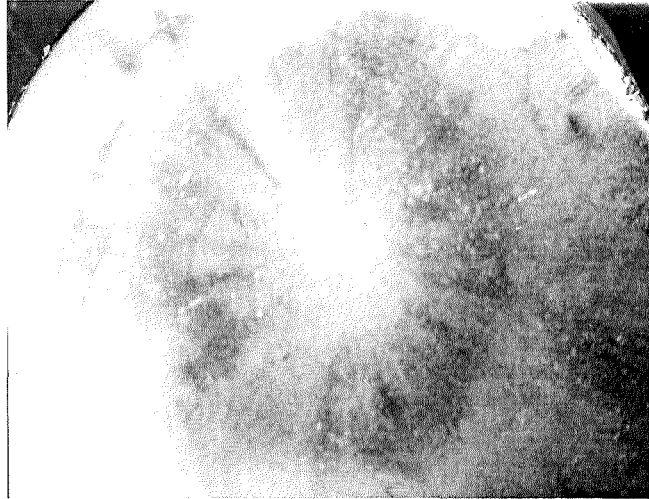


**Figure 7-43 Photograph of central wear scar area of specimen held at 0mV under impingement with 650 mg/l solids for 4 hours**

Potential	Weight Loss	Anodic Current
Free Corrosion	0.7, 0.7, 0.9	Not applicable.
+0mV (SCE)	1.9, 2.3*, 2.1	*t = 0, I = 3 mA t = 2 hrs I = 10.5 mA t = 4 hrs I = 10.5 mA

**Table 7-9 Weight Losses and Currents under 4 hours impingement with 650 mg/l solids**

The 'extra' weight loss can not only be attributed to the increase in scar depth from  $\sim 1 \mu\text{m}$  to  $\sim 2 \mu\text{m}$  (Figure 7-44) but also to the increase in material loss from the area outside the central wear scar where spikes extending to  $3 \mu\text{m}$  in length can be found (Figure 7-45).

The dark area on the surface of the specimen could be attributed to hydrodynamic effects where the impinging jet rebounds from the central wear scar and impinges the surface again after a certain distance, i.e. where the dark

area ends. Also within this area, there are complex galvanic currents occurring which are also affecting the surface. This aspect, is not fully understood and further work is required.

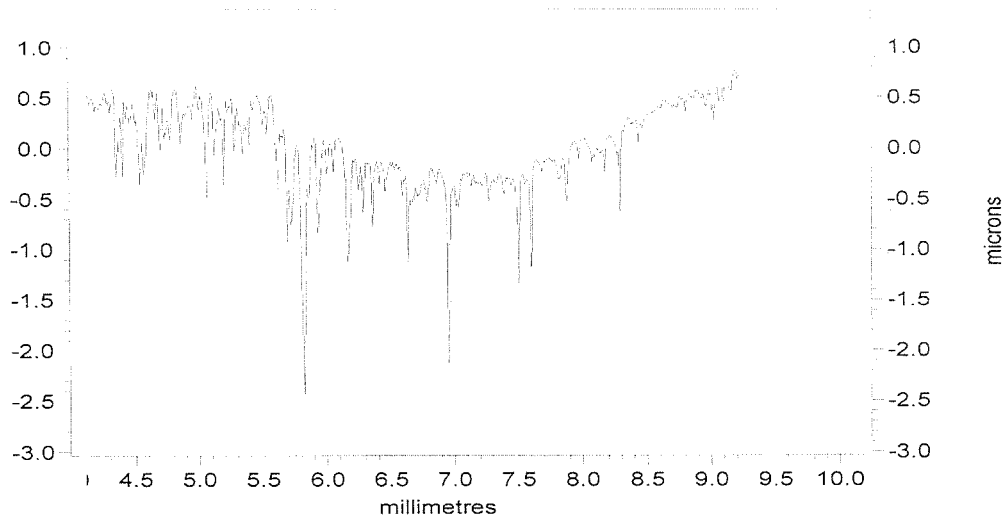


**Figure 7-44 Surface Profile of specimen held at 0mV after 4 hours impingement with 650 mg/l solids at 12 ms<sup>-1</sup>**

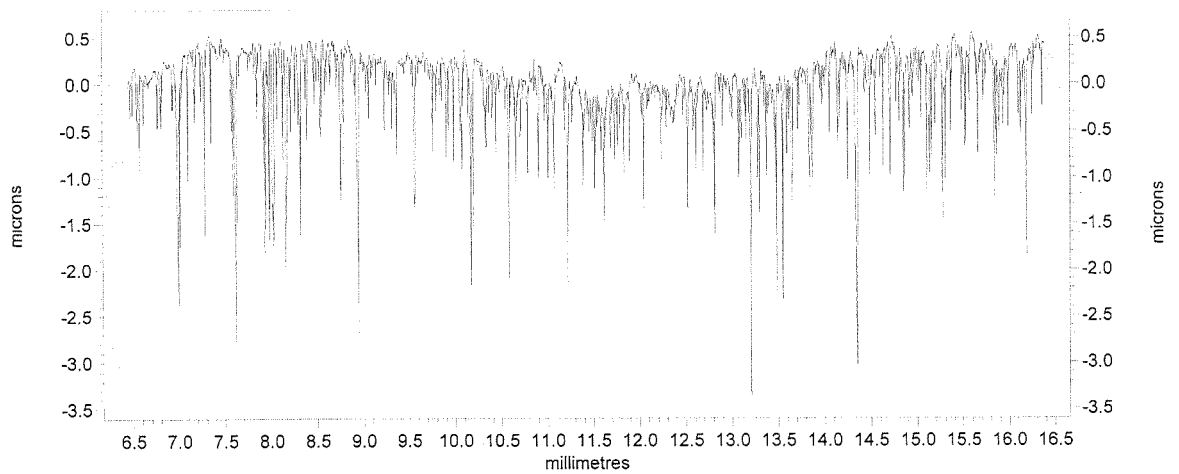


**Figure 7-45 Surface profile of area outside wear scar of specimen held at 0mV after 4 hours impingement with 650 mg/l solids at 12 ms<sup>-1</sup>**

## Chapter 8

### Discussion of Results

#### 8.1 Static Corrosion Behaviour

In contrast to initial electrochemical studies on plasma sprayed coatings where the interconnected porosity was an issue<sup>25</sup>, and galvanic interactions of the substrate and coating intervened with electrochemical results, this study has focused on the inherent corrosion, and subsequently the erosion-corrosion, characteristics of good quality, (i.e. low porosity, good adherent) coatings. The static corrosion behaviour of the coatings has been assessed by: (i) detailed electrochemical study of corrosion behaviour upon initial exposure to a saline environment and (ii) assessment of natural corrosion behaviour incorporating time trends. One feature of the corrosion studies was the use of AFM to reveal details of corrosion mechanisms under accelerated corrosion conditions. This demonstrated some success, in this respect, by showing details of corrosion mechanisms on a micro scale and in particular providing good correlation with findings from longer-term natural corrosion tests and demonstrating clearly the difference in corrosion mechanisms between WC-Co and WC-Co-Cr.

##### *(i) Accelerated Corrosion*

The complex anodic polarisation response of each coating, WC-Co and WC-CoCr, distinguishes them from the carbon and stainless steel substrates as these show distinctive active and passive responses, respectively, whereas the two coatings lie somewhere between, with the WC-CoCr displaying more corrosion resistant behaviour<sup>100</sup>. Many of the static corrosion studies already carried out on WC-CoCr<sup>29, 31</sup> have focused on the mechanisms of corrosive attack and have not included the corrosion current densities. This study includes these details and highlights the better static corrosion resistance of the CoCr matrix over the Co, which has also been documented elsewhere<sup>84, 86</sup> in erosion-corrosion studies. While the corrosion current densities of the CoCr lies predominantly in the 3-6

$\mu\text{A}/\text{cm}^2$  range, the Co matrix corrodes about twice as fast having a corrosion current density in the 9-11  $\mu\text{A}/\text{cm}^2$  range. Increasing the temperature to 50°C almost doubles the corrosion rate of the Co-Cr matrix and increases the corrosion rate of the Co matrix to 16  $\mu\text{A}/\text{cm}^2$ .

Depolarisation of the anodic reaction at 18°C (Figure 5-20) when the temperature is increased to 50°C can be attributed to higher matrix dissolution. As depolarisation occurs on both the anodic and cathodic reactions on increasing the temperature from 18°C to 50°C, it can be said that the increased corrosion rates, at 50°C, are as a result of increased anodic and cathodic reactions (Figure 5-29). Associated with the depolarisation of the cathodic reaction is an increased limiting current density. The cathodic reaction:



is controlled by the rate of diffusion of oxygen molecules, which is governed by

$$D = D_0 \exp\left(\frac{-Q}{RT}\right) \quad (8.2)$$

An increase in temperature induces an increase in the diffusion coefficient, but it also decreases the amount of dissolved oxygen in solution, so the limiting current, denoted by,

$$i_L = \frac{DnFC_B}{\delta} \quad (8.3)$$

is a balance between the amount of oxygen available and the rate at which it moves. As the limiting current density increases with increasing temperature, the diffusion process is therefore the most dominating.

Since the corrosion of the WC phases is very minimal<sup>101</sup> it can be deduced, and indeed was observed in this study, that the corrosion processes focus mainly on the binder phases. The different binder phases (Co and Co-Cr) have resulted in

two corrosion mechanisms for the coatings. At 18°C, the Co-Cr binder corrodes uniformly across the surface of the specimen, but is obviously accentuated at hard phase matrix interface as it eventually causes the hard phase to fall out (Figure 5-44). The Co binder has more localised area of corrosion, around the matrix/hard phase (Figure 5-43). At 50°C, the attack on the Co-Cr matrix is more localised with regions of deep corrosion (Figure 5-47) where the removal of the matrix has resulted in unsupported hard phases in these regions. Corrosive attack focused at the hard phase/matrix interface could be as a result of micro-galvanic effects. Presuming that the  $E_{\text{corr}}$  of WC-Co lies between the  $E_{\text{corr}}$  of WC and Co (and similarly with WC and Co-Cr), and noting that the WC-Co coating has been observed to have a more negative  $E_{\text{corr}}$  than the WC-CoCr coating (Figure 5-42), thus indicating Co has a more negative  $E_{\text{corr}}$  than Co-Cr, it is understandable that the WC-Co system would suffer more from micro-galvanic effects since the potential driving force between the WC and Co is greater than between the WC and Co-Cr.

Additional factors contributing to the complex electrochemical response of the WC-CoCr coating are the possibility of micro-crevices between the hard phase and matrix and the presence of elemental tungsten or  $W_2C$  as well as amorphous material caused by the diffusion of carbon and tungsten into the matrix as a result of decarburisation of WC during spraying<sup>16</sup>. Thus the phases within the corroding matrix could contribute to the non-uniform rate at which it corrodes.

In addition, it is not inconceivable that a passive film could exist on this Co-Cr matrix. Stainless steels' corrosion resistances improve on the addition of more than 12%Cr, which supports a chromium-rich, passive oxide film. The coatings' matrix, where the corrosion processes are focused, consists of 28%Cr and 72% Co, which might be considered to be enough chromium to induce a passive film. However, complexities arise by the intermediate WC particles which would cause discontinuation in the protective film and crevices between the hard phase and matrix and hence explain why the electrochemical response is not fully passive and why hard phases fall out.

*Micro-pitting*, removal of the hard phase particles was also found on a Ni-Cr-Si-B coating<sup>35</sup> which was also thought to be due to micro-galvanic effects. This coating also deteriorated due to *macro-pitting* which involves the removal of splat particles. Splat particles were not observed in either the WC-Co or WC-CoCr coatings after corrosion tests, thus suggesting that these had a more uniform microstructure than the Ni-Cr-Si-B coating. The latter coating also displayed passive corrosion behaviour even under liquid impingement conditions.

Having ascertained that the WC-CoCr coating is superior to the WC-Co coating in terms of corrosion resistance in the short term, and that the two WC-CoCr coatings have similar corrosion properties, the remainder of the study focused on the properties of the WC-CoCr coating. The similar corrosion properties of the two WC-CoCr coatings is a very noteworthy finding from an industrial perspective since they were sprayed by two companies on different systems, one by a Hobart Tafa and the other by a JK II gun.

*(ii) Corrosion Behaviour as a Function of Time*

Adding to the complex corrosion behaviour during an anodic polarisation after one-hour immersion in aqueous solution at 18°C, are the oscillating Rp values obtained during one-month exposure from AC Impedance tests. Having ascertained that the coating more or less uniformly corrodes, the proposition is that this process eventually leads to loss of hard phase thus revealing a previously unexposed layer of matrix, which could account for the variation in corrosion behaviour. In the long-term the coatings probably corrode in a continual cycle of:

1. Dissolution of binding matrix (Figure 8-1), leading to
2. Loss of hard phase particles (Figure 8-2) which
3. Unveils a new layer of matrix, and so the cycle continues.

After one month exposure, deep attack around the hard phases and protruding hard phases (Figure 5-12) resemble, to an extent, the type of attack found during AFM examination under accelerated corrosion conditions in the potential region of 600-650 mV (SCE) (Figure 5-25). This is indicative of the useful correlation

between accelerated electrochemical tests upon initial exposure and longer-term natural corrosion.

The more localised form of attack identified at 50°C after anodic polarisation reflects in the AC Impedance response in the longer term as a progressive decrease in corrosion resistance. As seen after one month exposure, discrete areas of matrix are initially attacked (Figure 5-16) which eventually, as shown after accelerated corrosion tests (Figure 5-9), manifest into areas of matrix and hard phase loss. Thus, the progressive decrease in corrosion resistance is associated with the localised areas of attack propagating and dissolving larger areas of the matrix.

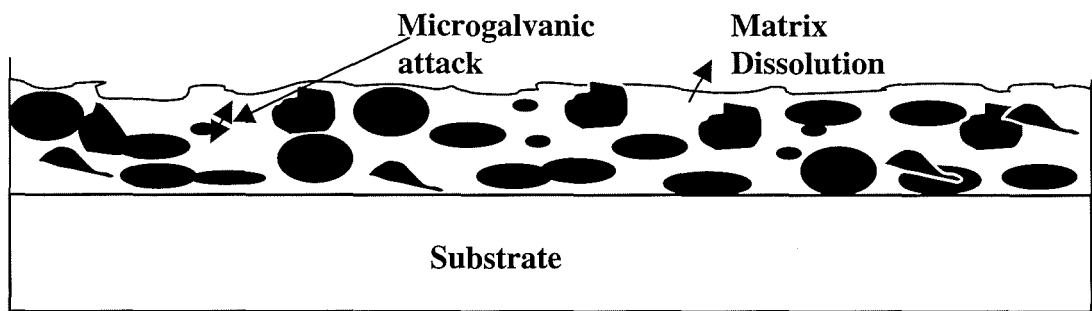


Figure 8-1 Schematic diagram of coating submerged in aqueous solution

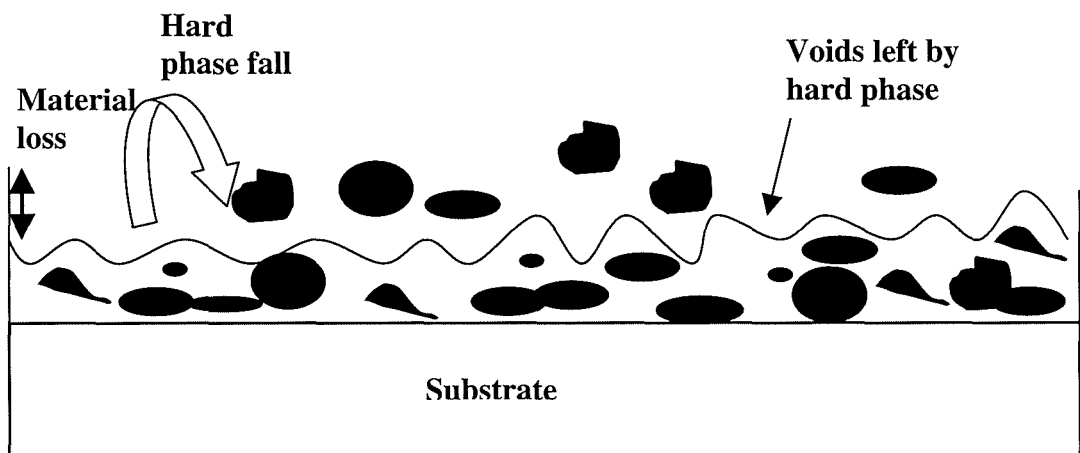


Figure 8-2 Schematic diagram of corroding coating

## 8.2 Liquid Impingement

Under liquid impingement conditions, at  $12 \text{ ms}^{-1}$ , the principal method of degradation is corrosion since only a minimal amount of mechanical erosion (which usually takes the form of a wear scar) can be seen on a micro scale. The effects from the impinging jet results in a smoothing-out of the characteristic shape of an anodic polarisation at  $18^\circ\text{C}$ , a lower breakdown potential after one-hour impingement, and eventual eradication of any breakdown potential after 4 hours impingement (Figure 6-2). Depolarisation of the cathodic reaction (Figure 6-3), which has also been found on alloys<sup>52</sup>, from static to impingement conditions is noted. These faster reactions, both anodic and cathodic, result in an increased corrosion rate from static (predominantly in the  $3\text{-}6 \mu\text{A}/\text{cm}^2$  range) to liquid impingement ( $8 \mu\text{A}/\text{cm}^2$ ), which is constant even after 4 hours impingement. On the coating, matrix dissolution occurs at discrete areas over the surface and did not appear to be accentuated on the area under the jet but was a more random attack.

This different type of attack seen under impingement conditions, compared with that in static conditions, may explain the different shapes of the anodic polarisation curve. The matrix is dissolving at localised areas over the specimen, corrosion processes will be less focused at matrix/hard phase interfaces as the impinging and deflecting jet can wash any vulnerable hard phase particles exposing more matrix. The faster rate of matrix dissolution can be associated with a faster cathodic reaction occurring on the surface.

Given that from the conditions in this study, the Reynolds Number:

$$\mathbf{Re} = \mathbf{V} \frac{\mathbf{d}}{\boldsymbol{\gamma}} \quad \mathbf{(8.4)}$$

falls into a turbulent regime (where  $v = 12 \text{ ms}^{-1}$ ,  $d = 4 \text{ mm}$ ,  $\gamma = \sim 10^{-6} \text{ m}^2\text{s}^{-1}$  and  $\text{Re} > 2500$ ), an increase in corrosion rate is not unexpected as the turbulent conditions of the jet increases the concentration of oxygen at the surface through

mass transfer processes which induces a faster reaction rate of oxygen reduction. The oxygen reduction reaction can occur on the surface of either the WC particles or the CoCr matrix which may induce differing reaction rates. As the matrix opens up after 4 hours impingement, exposing more hard phase particles and a rougher surface, this may speed up the reaction, accounting for the higher cathodic currents after 4 hours impingement. As the potential becomes more negative and hydrogen evolution reactions commence, the curves become more complex and difficult to rationalise. However, the more negative potentials of these cathodic curves are of little consequence in relation to the natural corrosion behaviour of the coating.

The main interest of the cathodic polarisation was incorporating the residual cathodic currents near  $E_{\text{corr}}$  in Tafel extrapolation procedures. Since the measured currents near  $E_{\text{corr}}$  include both anodic and cathodic currents, it is difficult to obtain the true corrosion current density simply from the anodic polarisation plot. By excluding the residual cathodic currents it was easier to identify the Tafel regions and thus obtain a more accurate  $I_{\text{corr}}$  (Figure 6-4). This is an approach which has not been incorporated by others conducting similar work<sup>103</sup>.

As in static conditions, the corrosion rate at 50°C under an impinging jet increases. At 50°C, the corrosion rate is almost double, compared to that at 18°C under an impinging jet after one hour and increases slightly after 4 hours. Since the cathodic polarisation reactions follow a linear  $E/\log I$  relationship, the concentration of oxygen in the bulk solution did not inhibit the oxygen reduction reaction, but was increased, from that at 18°C, by increased diffusion coefficients attained by the increased temperature. As a consequence the anodic reaction can proceed at a faster rate and resulted in the coating breaking up at localised areas and as time increased, and as matrix dissolution progressed, macro-holes formed on the coating where the jet had aided the removal of hard phases (Figure 6-30) and exposing more matrix to dissolve.

On other materials, such as stainless steel, impingement conditions did not have any significant changes to the anodic polarisation characteristics even up to velocities of 100 ms<sup>-1</sup> but the hydrodynamics of the jet introduced comet-shaped

attack on the surface of the specimen<sup>50</sup>. On another cermet coating, namely Ni-Cr-Si-B<sup>102</sup>, the coating remained passive under liquid conditions even after 6 days impingement but corrosion attack in the form of comets outside the impingement area was observed.

### **8.3 Liquid-Solid Erosion**

#### **8.3.1 Corrosive Effects under Liquid-Solid Erosion**

On the addition of solids to the liquid stream, there is no increase in corrosion current (Figure 6-17), compared with solid-free impingement, up to 1-hour exposure at 170 mg/l and 500 mg/l, which is not surprising as the solid particles should not affect direct corrosion processes. After an incubation period of 4 hours, at 500 mg/l, there is an increase in corrosion rate which further increases with a solid content of 1500 mg/l. An increase of corrosion rate with increases in solid content as also noted by Berget et al<sup>102</sup> on various WC- coatings rotating in liquid with 0.25% wt. solids. However, this increase in material deterioration due to corrosion is not as significant as the increase in erosion effects, which will be addressed later. As in pure liquid impingement, an increase in temperature induces an increase in corrosion rate, which also increases with time. The corrosion rate at 50°C is higher with solids (500 mg/l) added to the liquid stream; 35  $\mu\text{A}/\text{cm}^2$  after 1 hour compared to the 22  $\mu\text{A}/\text{cm}^2$  with no solids and 45  $\mu\text{A}/\text{cm}^2$  after 4 hours with solids and 25  $\mu\text{A}/\text{cm}^2$  with no solids. The general trend of increasing corrosion rate with solid loading from 170 mg/l to 500 mg/l and 1500 mg/l is found, but at 650 mg/l in replicate measurements the corrosion rate is smaller than at 500 mg/l but still larger than at 170 mg/l. This could be due to complex effects of the particles inhibiting the corrosion processes but is an aspect which requires some further investigation.

As indicated by the wear scar on the surface of the specimen, corrosion processes do not only contribute to the material degradation in these conditions but also interactions with erosion processes. The increased corrosion rates could be due to

surface roughening effects and an increase in exposed area and/or exposure to more metallic matrix when the hard phase particles fall out. An increase in corrosion rate on the addition of solids was also found on passive stainless steel materials<sup>82</sup> where the solid particles were thought to break down the passive film. However, if there is a passive film present on the coating, it would break down on the introduction of solids to the liquid stream and not, as the results suggest, after 4 hours.

The increase of corrosion rate with time could be due to increased turbulence within the wear scar as alluded to by Hodgkiess et al<sup>52</sup>. The solid particles impacting the surface of the specimen and remove material causing micro pits which can induce an increased local turbulence within the pits. This would then increase the mass transfer coefficient within the pits and hence increase the matrix dissolution. Thus after 4 hours impingement, when these pits are larger than after 1-hour impingement, the corrosion rates will be greater. The higher corrosion rates at 50°C maybe as a result of increased diffusion coefficients due to the increased temperature causing a higher matrix dissolution, particularly within the micropits where the turbulence will be increased.

The corrosion current densities found on coating 1, when translated into weight losses only contribute to a small part of the total weight loss in liquid-solid erosion corrosion conditions, counting for up to a maximum of 30%. At the lower solid contents, due to the small total weight losses and associated large errors, it is difficult to obtain a true value for the percentage weight loss due to corrosion. However, a general decrease in the percentage contribution of the pure corrosion component can be seen after both one and four hour impingement (Figures 6-26 and 6-27) with an increasing solid content. As the direct corrosion component decreases, the indirect corrosion component i.e. synergy, increases. These together account for generally 50% of the total weight loss. These corrosion rates were determined from composite specimens where the corrosion rates were found over the surface of the whole specimen. Subsequent tests on coating 2 with concentric specimens, so that the area which was directly under the impinging jet, containing all the damage from direct liquid-solid impact, and the outer area, unaffected from direct liquid-solid erosion, showed that a higher

corrosion rate on the central specimen existed. The corrosion rates found indicate a 33% increase (from  $24\mu\text{A}/\text{cm}^2$  to  $32\mu\text{A}/\text{cm}^2$ ) on the inner specimen and a 75% reduction on the outer part of the specimen (to  $6\mu\text{A}/\text{cm}^2$ ).

The mechanism of corrosion in these erosion-corrosion conditions, in relation to the higher corrosion current density on the inner specimen and the less positive free corrosion potential is very complex. One possibility is that the anodic reaction rate remains the same on both the inner and outer sections while the cathodic reaction on the inner section is depolarised. However, this would lead to an increased corrosion rate but more positive  $E_{\text{corr}}$ . The only way of achieving the situation is if both the anodic and cathodic reactions on the inner section are depolarised. The depolarisation of the cathodic reaction is understandable as concentration polarisation effects control it and the increased turbulence at the inner section increases the mass transfer. However, it is difficult to draw definite conclusions as to why the anodic reaction, which is activation controlled, increases in these conditions. Since the activation energy ( $\Delta G$ ) is a function of temperature and pressure, it is possible that the solid particles increase the energy through increases in local temperature and/or pressure as the solid particles strike the surface of the specimen hence increasing the ion transfer from the metal into solution.

#### *Galvanic Interactions*

A short study in the latter stages of this research, investigated the galvanic interactions resulting from the concentric specimens under the liquid-solid impinging jet. Measured galvanic currents found between the inner and outer concentric specimens (Tables 7-6 and 7-7) were quite substantial. These galvanic currents indicate that the  $I_{\text{corr}}$  values measured on the inner specimen are an underestimate of the actual dissolution rate, that would occur on a composite specimen. As shown in Figure 7-39, the inner section of the specimen corrodes at a much faster rate than the outer section. In addition to the currents measured on the separate inner specimen, the inner part of a composite specimen will corrode at a higher rate due to the internal galvanic couple.

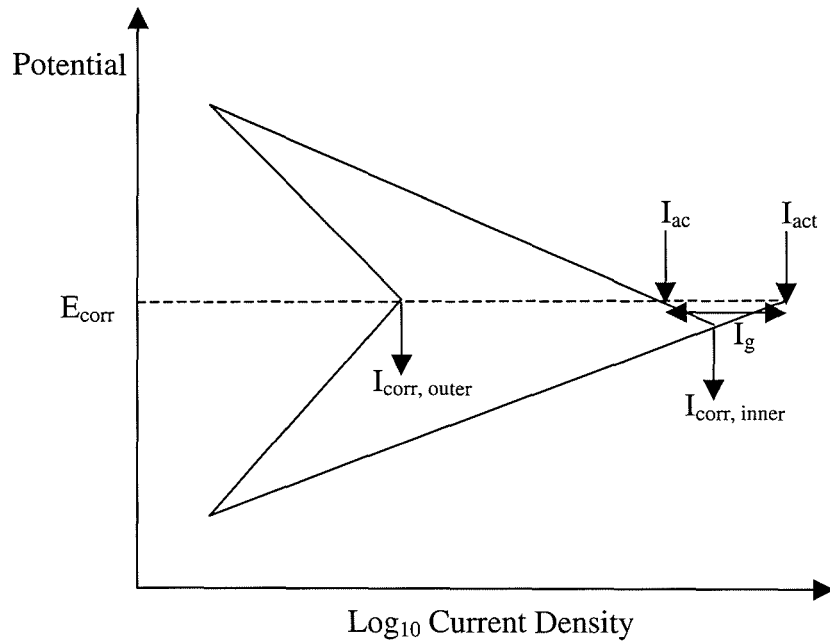


**Figure 8-3 Schematic diagram of the differing corrosion rates on a composite specimen**

Mansfield's discussion<sup>104</sup> of galvanic interactions focused on the more general situation of galvanic corrosion involving two different materials in the same environment. An expansion of this idea leads to the present situation of galvanic interaction between two areas of the same material exposed to different environments.

The results (Figure 7-39) demonstrate that both the anodic and cathodic reactions undergo less severe polarisation on the central specimen than on the outer specimen. Translating these findings to a composite specimen, Figure 8-3 shows a schematic diagram of a corroding composite specimen. Figure 8-3 illustrates schematically the increase in overall corrosion rate of the central region from  $I_{\text{corr, inner}}$  to  $I_{\text{act}}$  due to the substantial galvanic interaction;  $I_g$  represents the magnitude of galvanic current (obtained from the coupling experiments with separate specimens). Figure 8-3 further shows that the magnitude of the self-corrosion rate,  $I_{\text{ac}}$ , on the central region is indicated by the residual cathodic current on the central area<sup>104</sup>. It is evident that at low potential shifts from the free corrosion potential, the residual cathodic current,  $I_{\text{ac}}$ , on the inner part of the specimen, will be approximately equal to  $I_{\text{corr}}$  and hence, the actual dissolution rate of the inner part of the specimen,  $I_{\text{act}} = I_{\text{corr}} + I_g$ . In fact the potential shifts in this work were

rather high thus  $I_{\text{act}} = I_{\text{corr}} + I_g$  is not valid. However, as further consideration of Figure 8-3 for larger potential shifts shows, the overall corrosion rate of the central region is substantially increased by the galvanic interactions in this system.

In effect, the corrosion rate focused in the area under the impinging jet could actually be more than twice the corrosion rate measured over the surface of a composite specimen and also substantially greater than an uncoupled directly impinged specimen. Hence, the 'C' component in equation 3.16 and the 'S'' component in equation 3.15 are more complicated than originally thought. Not only do they include an increase in the corrosion rate due to erosion, but in a system such as this study, the components also include galvanic currents. The extent of these galvanic currents will also be influenced by the area ratio of the outer and impinged area. Where, as in this situation, a small anode exists and confines the galvanic attack and the depth of corrosion increases.

Taking into consideration the observations from this study, it is obvious that calculation of the 'C' component as a percentage of the total weight loss is complex and corrosion processes could be more severe in the region under a liquid-solid impinging jet than previously estimated.

The galvanic currents described and discussed above are associated with potential differences between the outer and inner specimens and are also attainable with coupling to another material. This instance may arise in a practical situation where a component, such as a stainless steel pump, is partially coated and only the coated part of the pump is under attack from liquid-solid impingement. The more noble stainless steel will anodically polarise the coated part (perhaps substantially) and lead to an increase in coating deterioration from the impingement at the free corrosion potential (Table 7-8). This situation was simulated in the experiments involving an anodic potential where not only was an increase in the material loss in central wear scar area noted, but also in the outer regions where there was substantial hard-phase removal occurred (Figure 7-46). Accompanied with the increased material loss were large anodic currents indicative of faster metal dissolution. This is in agreement with the findings of

significant increased anodic currents during galvanic coupling of the inner and outer parts of the coating. These initial increasing and subsequent levelling off of anodic currents mirror the pattern of currents found when cathodic protection is applied (Figure 6-18). The increasing cathodic current with increasing solid content and time adds to the hypothesis that increasing erosion conditions increases the corrosion rate.

Yet another feature indicating the gross complexities of erosion-corrosion were the patterns formed on the surface of the test specimen (Figure 7-44) and are as a result of complex hydrodynamic effects on the surface of the specimen. As explained earlier, the corrosion rate is dependant on mass transfer coefficients and these vary depending on the jet to plate distance and the radial position on the plate<sup>106</sup>. The 'intermediate zone' around the central wear scar, noticeable on specimens after free erosion-corrosion conditions could be as a result of the complex hydrodynamic effects varying the mass transfer of oxygen to the surface of the specimen. As the intermediate zone is accentuated after erosion-corrosion at anodic potentials, varying mass transfer coefficients cannot be the only reason.

Further complexities associated with corrosion and hydrodynamic effects are encountered when the impingement angle is reduced. Although no significant differences in the corrosion rates at the differing impact angles were observed, the photographs of the specimen indicate more erosion-corrosion effects on areas below the wear scar i.e. regions of higher turbulence.

Many of the issues raised here highlight the many, as yet unresolved, complexities within the erosion-corrosion mechanisms under an impinging jet.

### **8.3.2 Pure Erosive Effects under Liquid-Solid Erosion**

The pure erosion effects are determined by experiments conducted while cathodic protection is applied. While these tests were conducted over a four-hour period, which is a relatively short exposure time, the main aim of the results was to give an indication of how the coating deteriorated mainly in terms of

mechanisms, and partly as a function of time. As with the corrosion rate, the *erosion rate* (Table 8-1) increases with increasing solid content. At the lower sand loadings, the weight losses are too small to yield a dependable trend. However, at the higher sand loadings, the erosion rate appears constant, at least in the first few hours or exposure. This trend is in some agreement with Bjordal et al<sup>87</sup> who found an initial decrease in erosion rate with time followed by a steady state on other cermet coatings rotating in liquid-solid slurry. It might be thought that, under cathodic protection, the erosion rate should remain constant, as the material removal is solely dependant on the impacting sand particles. In the closed loop system, the velocity and concentration of sand particles remain constant and hence a constant erosion rate would be expected. But also as the sand particles impact the surface, the surface becomes rougher leaving, hard phase particles, singularly or in clusters easier to remove, so an increase in *erosion rate*, might not be unexpected.

	Solid Content (mg/l)		
Exposure Time	500	650	1500 (90°)
1 hour	<i>0.1</i>	<i>0.16</i>	<i>0.2</i>
4 hours	<i>0.05</i>	<i>0.1</i>	<i>0.225</i>

**Table 8-1 Average erosion rates in mg/hr under a solid-liquid impinging jet at 12 ms<sup>-1</sup>, 90° impingement and 18°C with the application of CP**

#### *Erosion mechanisms*

As stated earlier, the effect of corrosion on this coating is to dissolve the matrix leading to removal of the hard phase particles. This is also part of the mechanism of material removal in erosion-corrosion conditions as shown by spikes indicating hard phase removal at the lower solid content cases. However, in the absence of corrosion, these hard phase particles are still removed indicating that erosion can also remove these particles but a reduction in spike depths are noted (Table 6-7).

At the higher solid contents the spikes merge and show areas of high material loss (Figure 7-6). These areas of high material loss are craters where solid

particles have impacted the coating and removed a 'chunk' of matrix and hard phase. The 'chunks' are not associated with any specific microstructural aspect since the splat sizes range from 50-to100 $\mu\text{m}$  but could be a cluster of splats. The severity of removing 'chunks' decreases with the distance away from the central point of the wear scar. This is not unexpected since although the nominal impingement angle is  $90^\circ$ , an array of impingement angles exist<sup>69</sup>. The reduction in the size of chunks removed is related to the impacting energy ( $1/2 mv^2$ ) of the solid particles. At angles less than  $90^\circ$ , the perpendicular velocity vector will be reduced and hence a reduction in material loss in areas further from the central point of the wear scar is not unexpected.

Maximum erosion at nominally  $90^\circ$  impingement is also found in dry erosion conditions and indicates that material has a brittle nature<sup>54</sup>. It is difficult to easily transfer the same conclusion into aqueous erosion conditions, as there are additional complexities associated with the material deterioration. Furthermore, the different erosion mechanism at reduced angles, i.e. ploughing action by the solid particles (Figure 7-23) and the combination of material (typically brittle hard phase and ductile matrix in dry erosion) within the coating is difficult to define as one or the other.

Similar erosion attack manifesting as craters on the surface at  $90^\circ$  impingement was observed on a Ni-Cr-Si-B cermet coating<sup>52</sup> and on another multiphase surface<sup>51</sup> (cast iron) under liquid-solid impingement. The authors postulated that the hard phase removal on the cermet coating causes micro-pits and induces increased turbulence which promotes the drilling of the solid particles into the surface. This postulation is possibly confirmed by the surface profiles showing larger spikes with increasing solid content (Figures 7-2 to 7-6) and eventual consolidation of the spikes. The initial large spikes are where hard phases have been removed and when the solid particles continually impact these sites due to local turbulent conditions, more of the coating is removed. So the initial long, thin spikes are expanded and eventually merge with neighbouring spikes and cause areas of high material loss.

At other nominal impingement angles, i.e. 30° and 45°, the mechanism of material removal by erosion changes from that at 90°. At 45°, where the total weight loss is less than at 90°, the solid particles have a more ploughing action on the surface gouging out the material (Figure 7-24) still removing the hard phase particles but to a lesser extent than at 90° impingement (Figure 6-39). A further decrease in weight loss with a nominal impingement angle of 30° is again attributed to the less severe erosion mechanisms. Here the solid particles in some areas of the wear scar has only roughened the surface of the specimen, while the largest part of material loss concentrated in a small area of the wear scar where craters have appeared (Figure 7-21). Thus the reduction in weight loss with decreasing angle (Figure 7-12) is associated with the reduced energy at which the particles impact the surface as the distance away from the jet increases and since some particles follow streamlines which flow across the surface of the specimen causing no impacts.

Using the model formulated by Oka<sup>64</sup> described in Section 3.5.4, the experimental and model results for the pure erosion component at the various impact angles are shown Figure 8-4. The general trend of decreasing material loss with both the experimental and model results are in agreement. However, the model shows a higher material loss at each impact angle. The discrepancy could arise due to the fact that the model involves the hardness of the material and, as the coating is a combination of matrix and carbide with differing hardnesses, a true hardness value is difficult to obtain. Furthermore, as the model was developed for dry erosion conditions, and the experimental results are obtained in slurry conditions discrepancies are not surprising. The reduced velocity, and reduced kinetic energy, of particles in slurry conditions could account for the reduction in material loss.

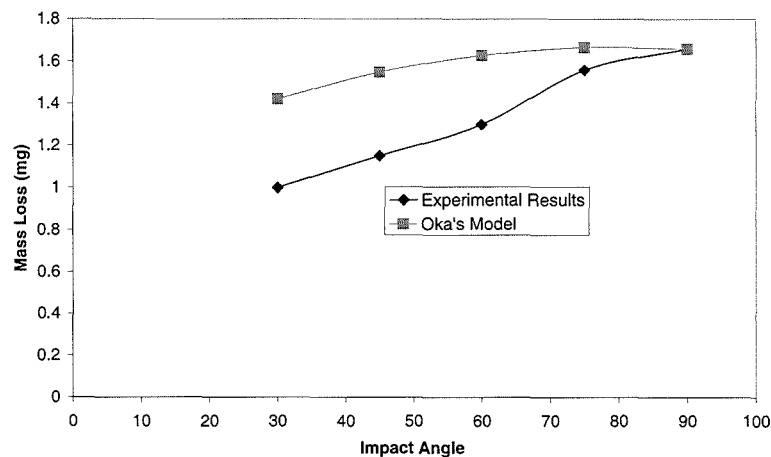


**Figure 8-4 Comparison of experimental results with modelled results**

### 8.3.3 Erosion-Corrosion and Synergy

Effects from the deleterious mechanical actions of the entrained solid particles within the aqueous liquid jet are twofold. The pure mechanical effects of erosion, E, can be assessed by experiments employing cathodic protection, and accounts for, in general, 50% of the total material loss. When the effects of corrosion and erosion are combined, the material loss increases. However, these separate components do not add up to the total weight loss. A third component, synergy, is introduced which arises from the effects of corrosion enhancing the erosion.

Synergism has been found on other cermet coatings<sup>52</sup>, carbon and stainless steels<sup>40</sup>. On passive alloys the synergism can be attributed to the penetration of the passive films by solid particles increasing corrosion and wear of the underlying material. However, on multiphase and possibly passive material, such as these cermet coatings, the mechanisms for erosion-corrosion and synergy become more complex.

This synergistic effect has been found to be in excess of 40% of the total weight loss, decreasing with decreasing solid content. This however, is a considerable amount of material loss and signifies that the interaction of the erosion and corrosion mechanisms are very important in the identifying the cause of material

wear. The proposed mechanisms for the degradation of a WC-Co-Cr coating under a liquid solid impinging jet are as follows. In less severe erosion-corrosion conditions (<1250 mg/l solids) corrosive effects remove hard phase particles leaving long thin spikes extending into the coating (Figure 8-5). These spikes or micro pits cause increased local turbulence which promotes the repeated impacts from solid particles in that area. The repeated impacts remove larger 'chunks' of the coating.

The matrix within the central area dissolves rapidly leaving exposed hard phase particles more vulnerable to be removed by the passing slurry. This increase in material loss would account for the third component, synergy, during erosion-corrosion. As the erosion-corrosion conditions become more severe, either due to increased time or solid content (Figure 8-6), the micro pits merge causing regions of high material loss. The turbulence again increases due to effects within the wear scar (on a macro scale) and increases the corrosion rate within the wear scar and a bigger driving force for the galvanic corrosion component.

#### **8.4 Practical Relevance of Work**

It is evident from this, and other<sup>52</sup>, work that in static saline conditions, these HVOF thermally sprayed cermet coatings although they will decrease the rate of deterioration when applied to a low-grade carbon steel substrate, do not improve the corrosion resistance when applied to a high-grade metallic material. Although these coatings are primarily used for tribo-corrosion applications, the coated component may intermittently be in static corrosion conditions. As has been clearly demonstrated, corrosion processes, both direct and indirect, represent a substantial proportion of the total weight loss in erosion-corrosion conditions and as such, an improvement in the corrosion resistance of these coatings is of much importance. Although passive coatings, such as the Ni-Cr-Si-C coating<sup>52</sup> have been obtained, in liquid-solid erosion-corrosion conditions the coating becomes rapidly active but has shown to have better resistance to wear than stainless steel.

Evidently corrosion, both direct and indirect is very detrimental to these coatings and one preventative measure is cathodic protection. Cathodic protection substantially reduces total weight loss and on a finer scale, reduces spike depths and more retained hard phase in the coating. Cathodic protection can increase the lifespan of the coated components and this may be a useful tactic to consider were component lives are extremely short in erosion-corrosion environments, e.g., on drill bits used for drilling for oil.

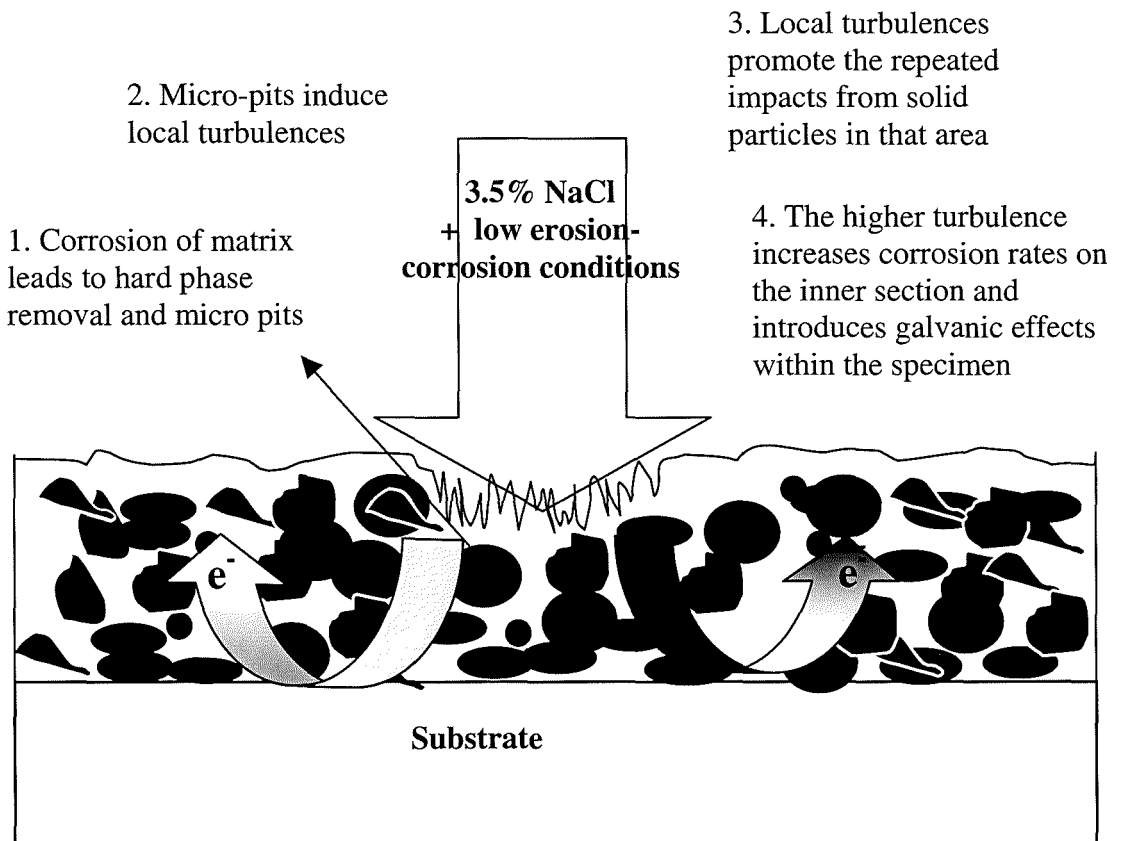


**Figure 8-5 Schematic diagram of erosion-corrosion mechanisms under a liquid-solid impinging jet I**

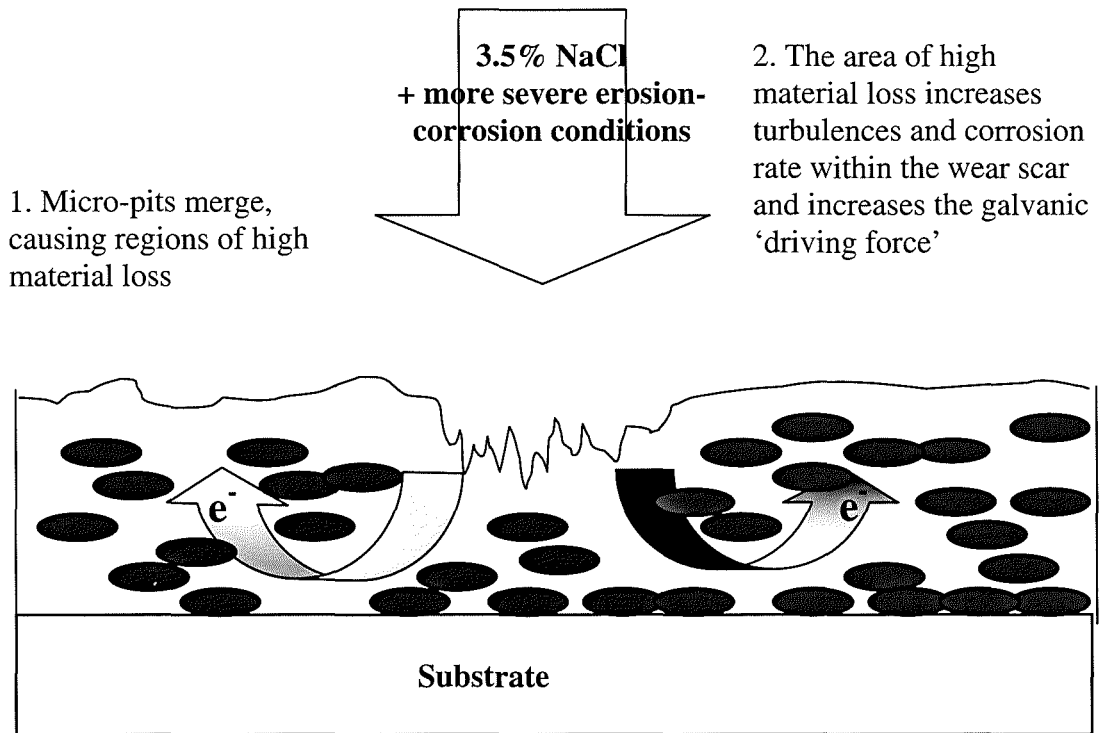


**Figure 8-6 Schematic diagram of erosion and corrosion mechanisms under a liquid-solid impinging jet II**

## Chapter 9

### Conclusions and Further Work

#### 9.1 Conclusions

- ❖ The addition of chromium to a cobalt matrix increases the corrosion resistance of a WC-based HVOF sprayed cermet coating.
- ❖ The use of an Atomic Force Microscope can aid the determination of corrosion mechanisms on a micro-scale.
- ❖ While the WC-Co coating suffers from localised attack, at 18°C in static conditions, accentuated at matrix/hard phase interface, the WC-CoCr has more uniform corrosion but leads to hard phase removal.
- ❖ An increase in temperature results in extensive dissolution of the cobalt matrix while on the Co-Cr matrix the attack in localised regions is not associated with specific microstructural features. It appears more like random localised attack on the matrix and the joining of the voids left by the carbides.
- ❖ Not only is the corrosion resistance lower at 50°C, but also has a deleterious time dependency.
- ❖ A liquid impinging jet increases the corrosion rate compared with that in static conditions and is further increased with increased temperature.
- ❖ The increased corrosion rate is as a result of faster anodic and cathodic reaction rates.
- ❖ In liquid-solid erosion-corrosion maximum material loss occurs within the area directly under the impinging jet.
- ❖ Pure erosion accounts for generally 50% of the overall weight loss in erosion-corrosion conditions.
- ❖ The presence of solids up to 170 mg/l even up to 4 hours impingement, does not affect the corrosion rate but after impingement with 500 mg/l solids after 1 hour, the corrosion rate increases.
- ❖ Increased temperature increases the corrosion rate in erosion-corrosion conditions dramatically.

- ❖ Interactions between erosion and corrosion produce complexities associated with the coating deterioration.
- ❖ Corrosion enhances the erosion process through synergism and can account for up to 40% of the total weight loss.
- ❖ The result of the liquid-solid impinging jet being focused on only the central part of the specimen introduces higher corrosion rates within the central region including accelerated corrosion due galvanic effects between the inner and outer sections of the specimen.
- ❖ Calculation of the corrosion rate on a composite specimen underestimates the actual damage due to corrosion in the region directly under the impinging jet.
- ❖ The damage mechanisms under a liquid-solid impinging jet are very complex. However the process is thought to be one where corrosion dissolves the matrix, erosion mechanisms involve the solid particles drilling into the coating and synergy is due to the solid particles removing the hard phase particles which are undermined by corrosive effects.

## **9.2 Recommendations For Further Work**

- ❖ To better identify the interactions between the matrix and hard phase materials, a study could incorporate spraying larger hard phase particles spaced further apart in the matrix would assist identification of the phases present, the actual effects from micro-galvanic effects and solve the issue of whether the matrix has passive corrosion properties using novel localised scanning techniques.
- ❖ Development of the chemistry of the coatings is greatly needed to increase the corrosion resistance of the matrix and to reduce any galvanic effects between the hard phase and matrix.
- ❖ It would be of great interest to expand on the findings of galvanic interactions between the inner and outer regions of specimens by a more detailed study of the behaviour of the concentric type specimens.
- ❖ To reflect the different corrosion rates, and indeed erosion rates, occurring over the composite specimen, further tests are required to fully

quantify the extent of their contribution on the separate regions of the specimens.

## Appendix 1

### Replicate results of polarisation curves

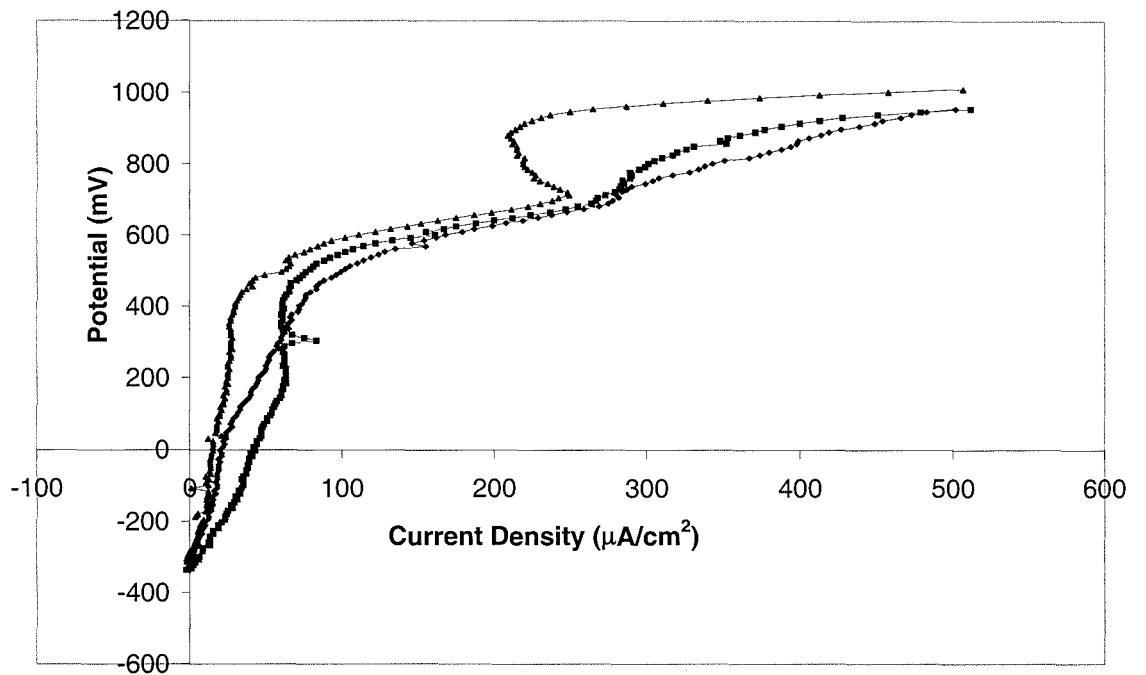


Figure A-1 Anodic Polarisation curves of coating 1 after one hour immersion at 18°C

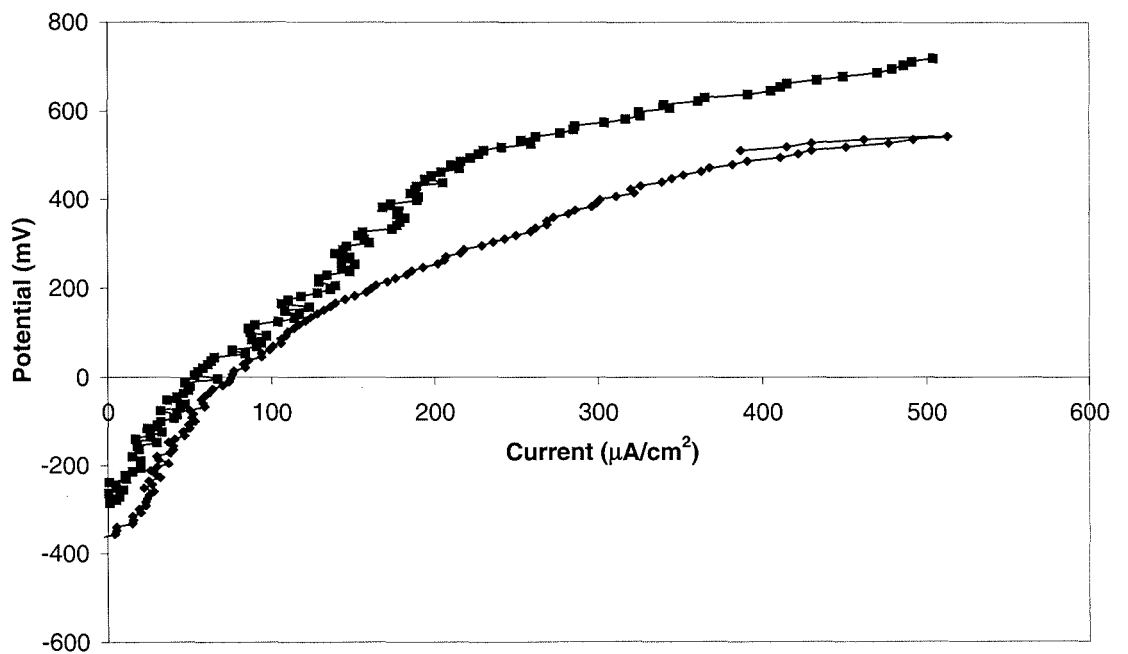


Figure A-2 Anodic Polarisation curves of coating 2 after one hour immersion at 50°C

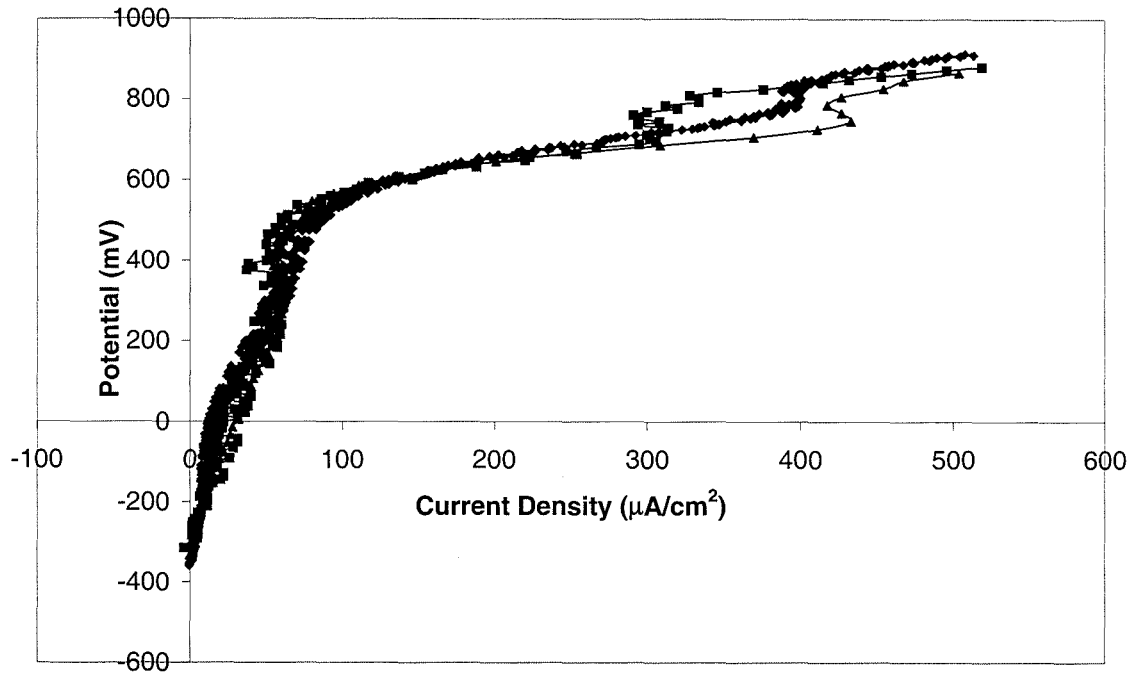


Figure A-3 Anodic Polarisation of coating 2 after one hour immersion at 18°C

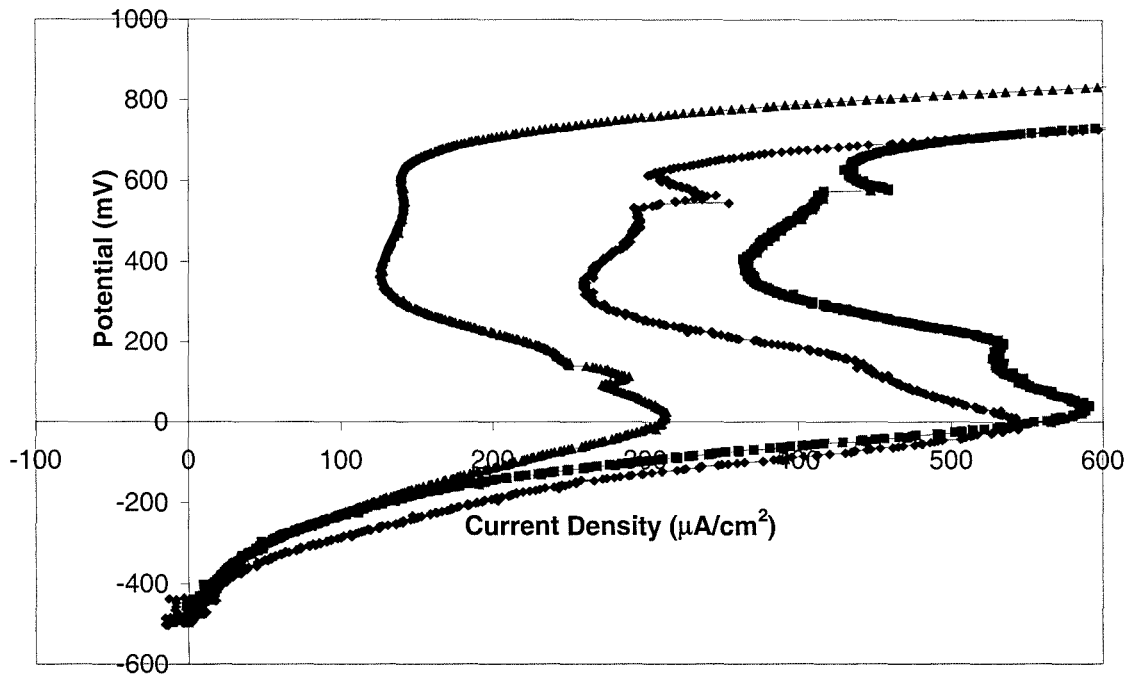


Figure A-4 Anodic polarisation curves of coating 3 after one hour immersion at 18°C

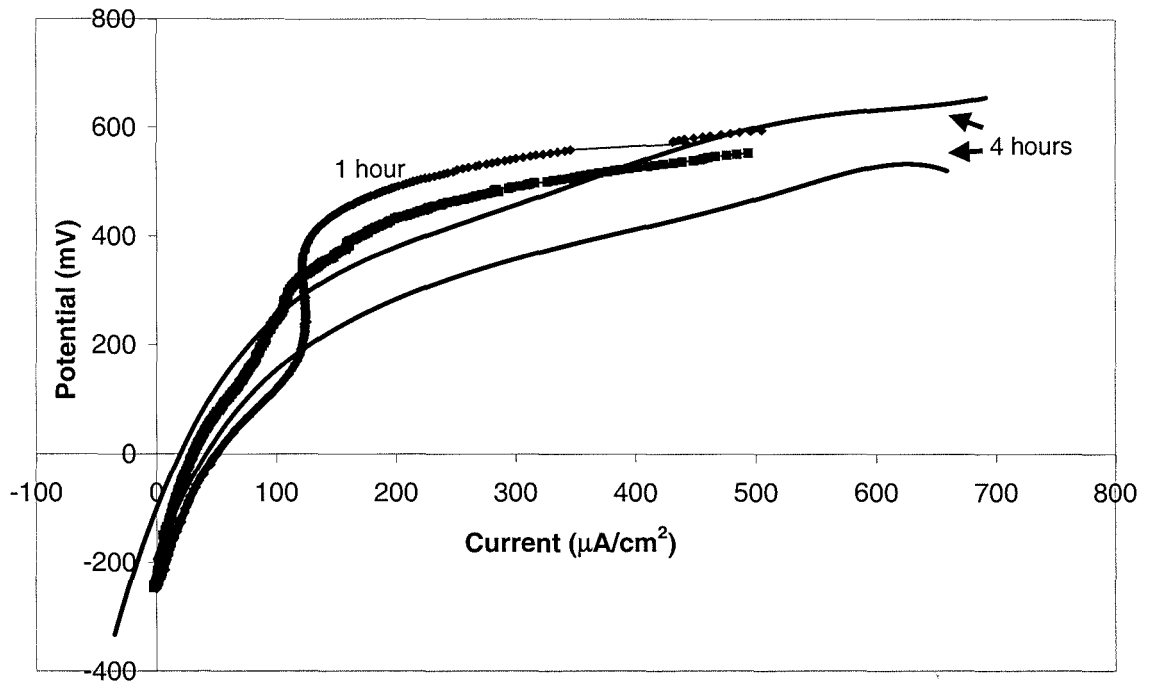


Figure A-5 Polarisation curves under liquid conditions after 1 and 4 hours at 18°C

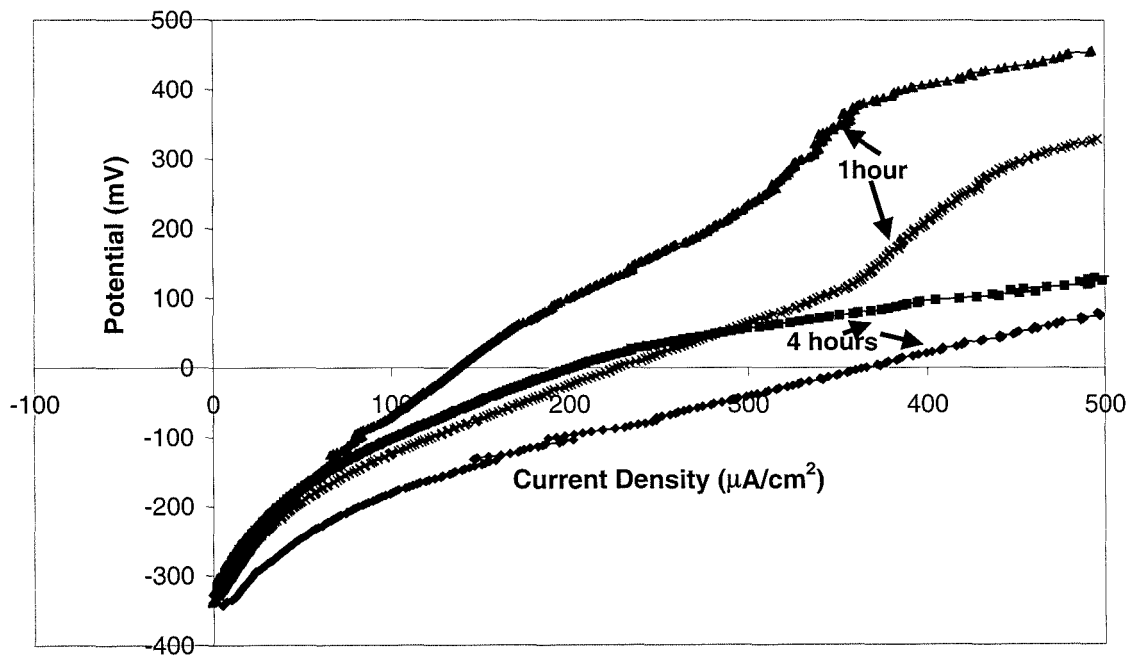


Figure A-6 Anodic Polarisation under liquid conditions at 50°C

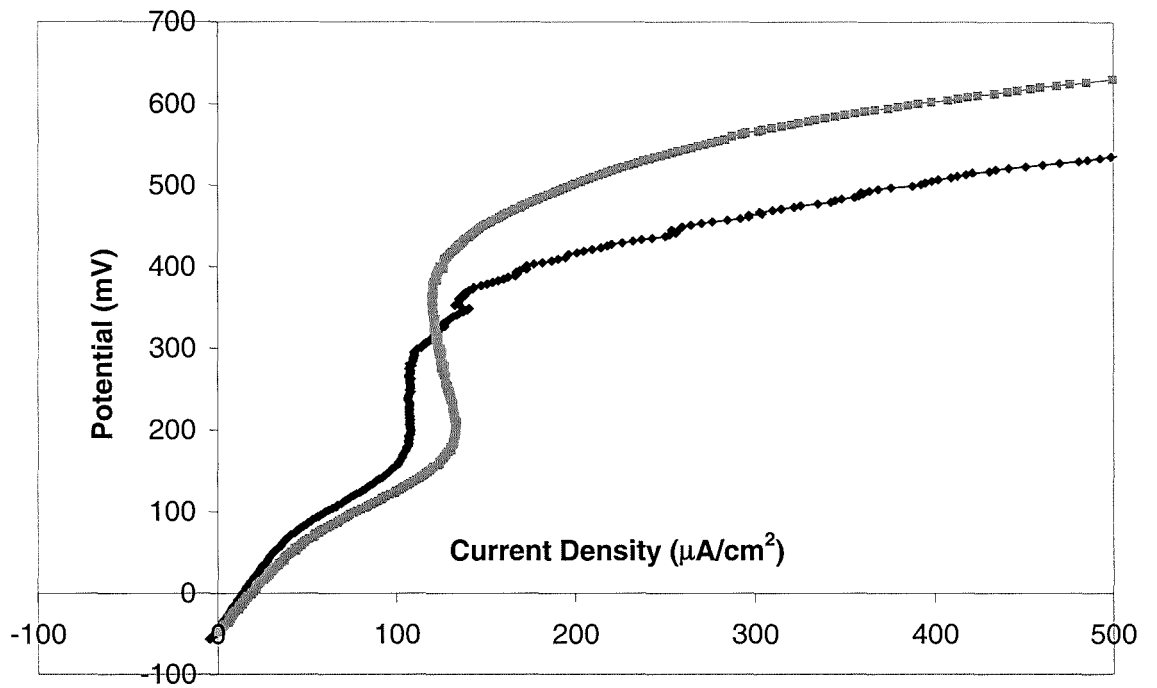


Figure A-7 Replicate polarisation curve after 4 hours impingement with 170 mg/l solids

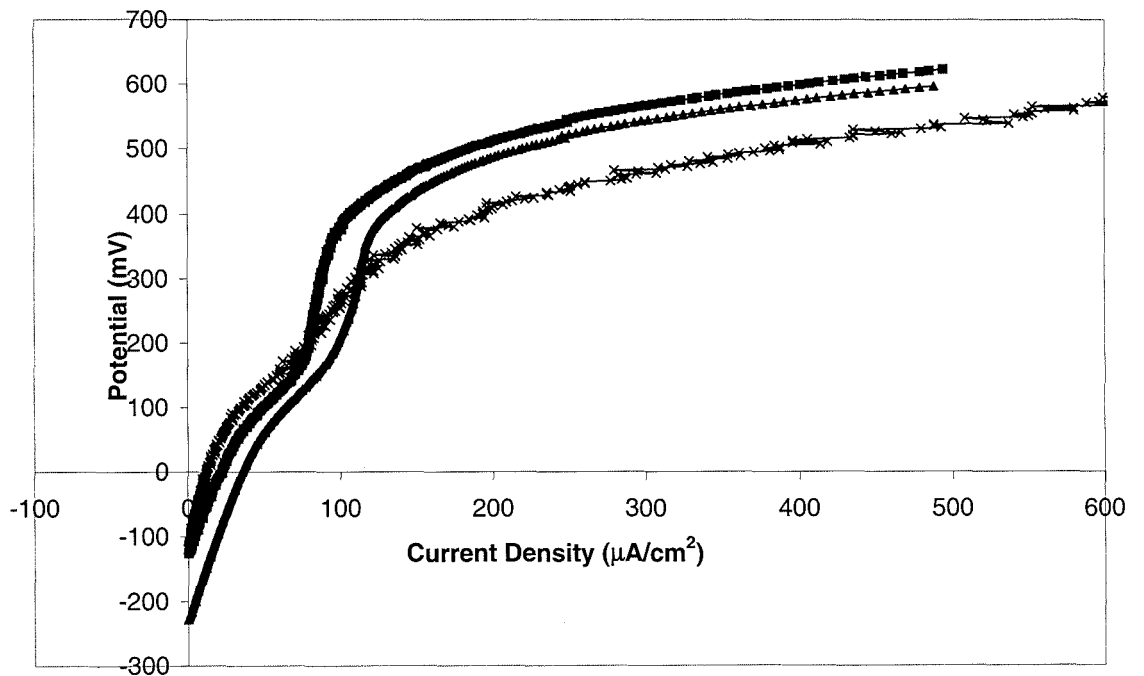


Figure A-8 Anodic Polarisation after 4 hours impingement 500mg/l 18°C

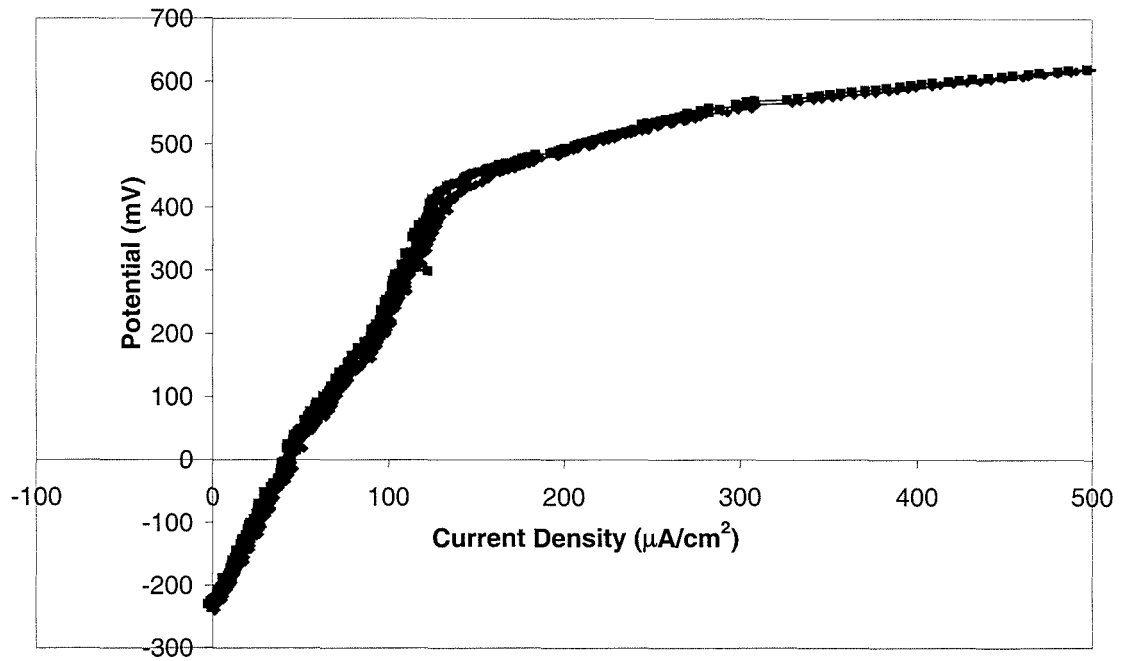


Figure A-9 Replicate polarisation curves under liquid-solid impingement for 1 hour with 650 mg/l solids

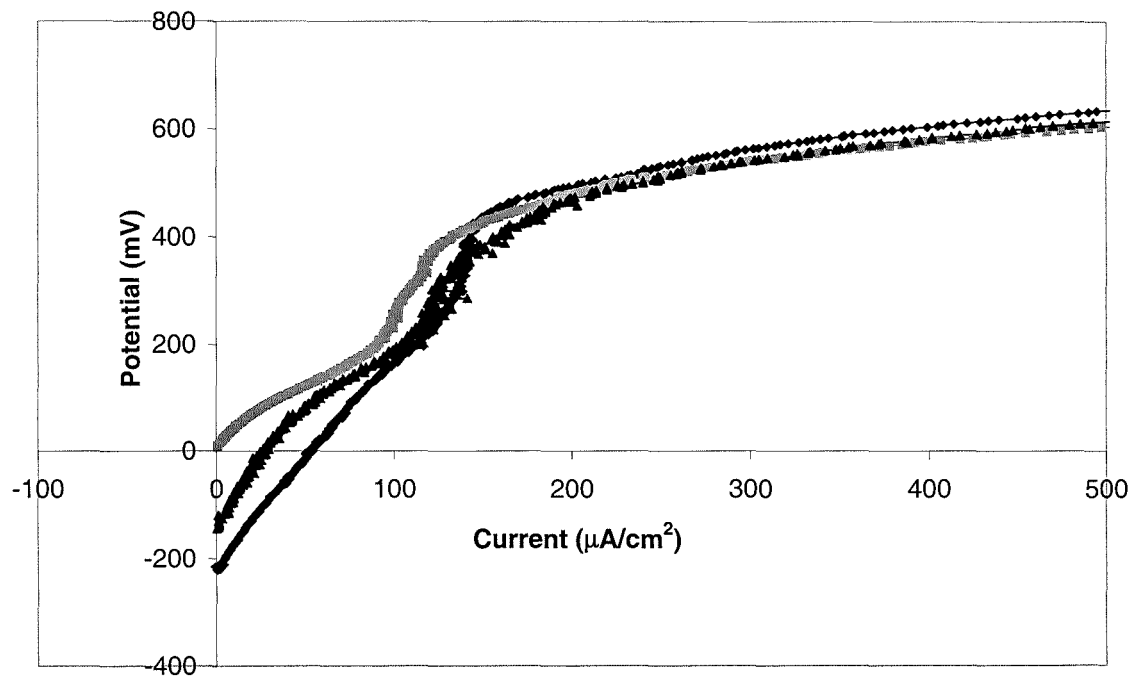


Figure A-10 Replicate anodic polarisation curves for 4 hours impingement with 650 mg/l solids

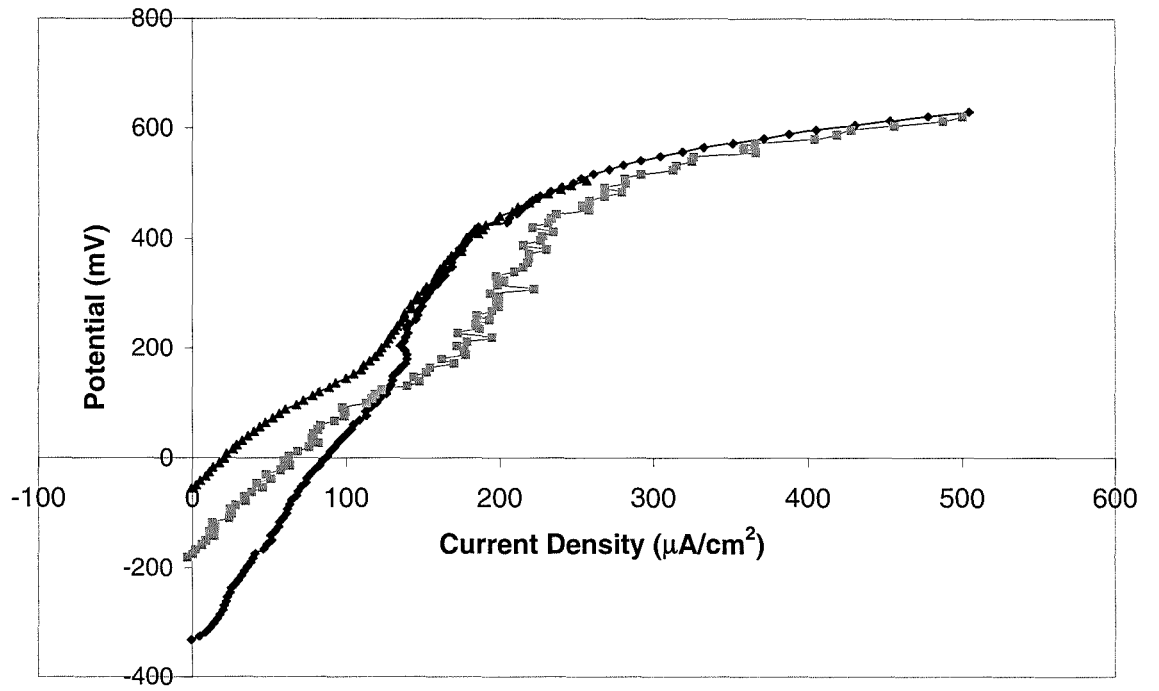


Figure A-11 Replicate polarisation curves after 4 hours impingement with 1500 mg/l solids at 45°

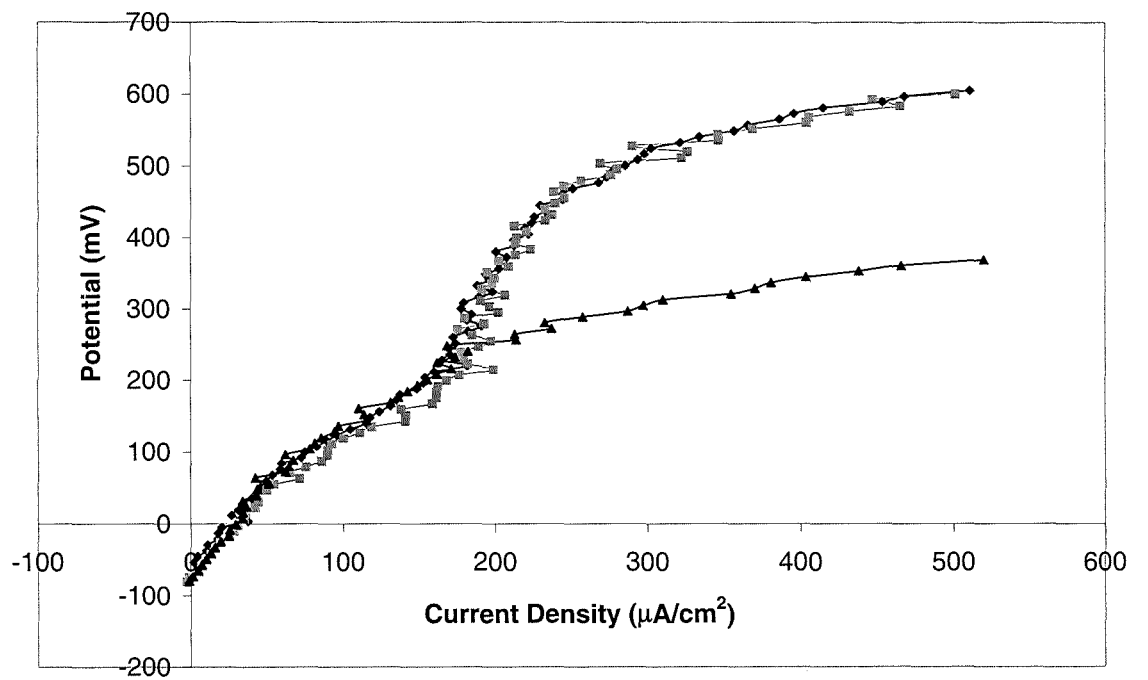


Figure A-12 Replicate polarisation curves after 4 hours impingement with 1500 mg/l solids at 90°

### “Corrected” Anodic Polarisation Curves

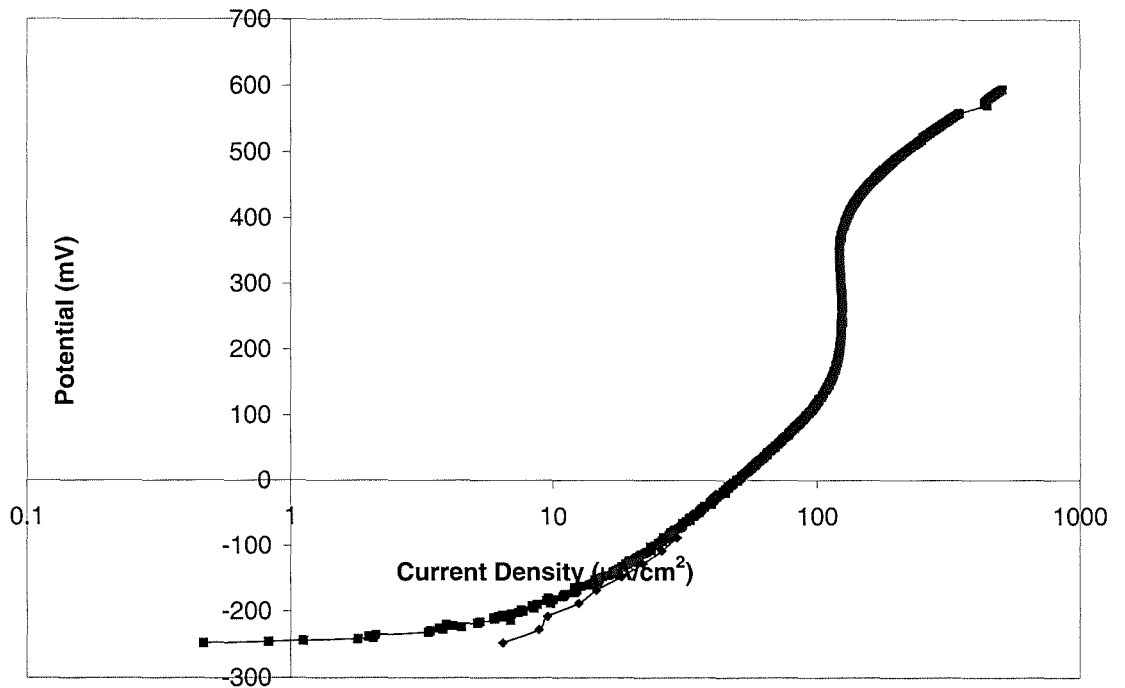


Figure A-13 Liquid-impingement after 1 hour at 18°C

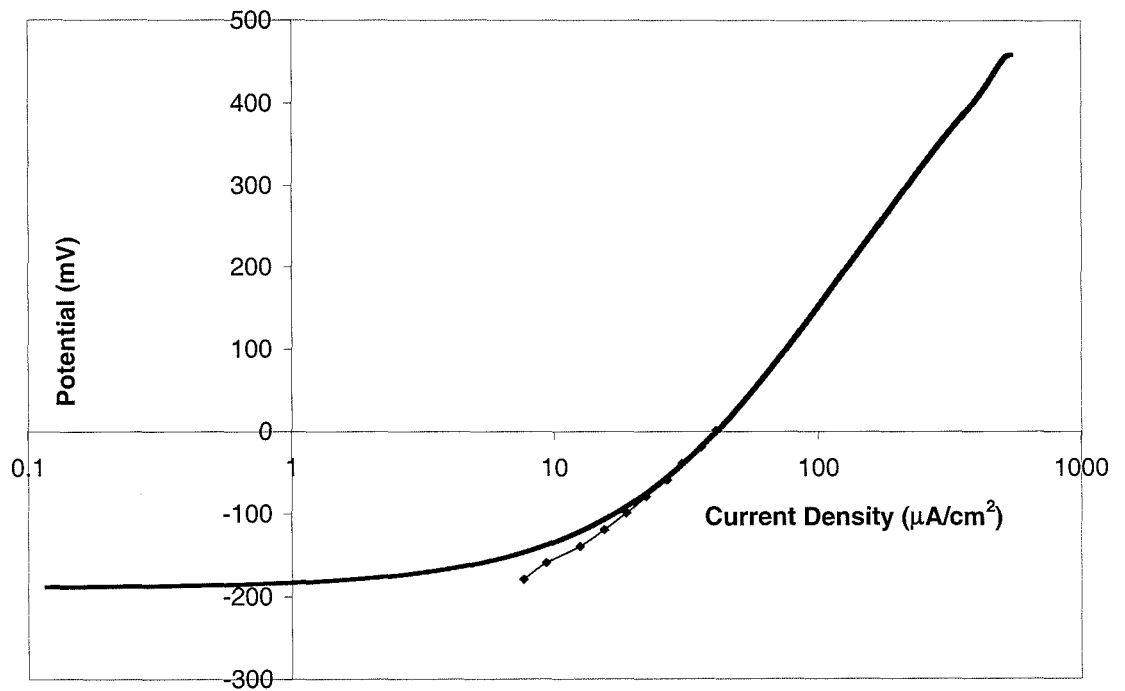


Figure A-14 Liquid Impingement after 4 hours impingement at 18°C

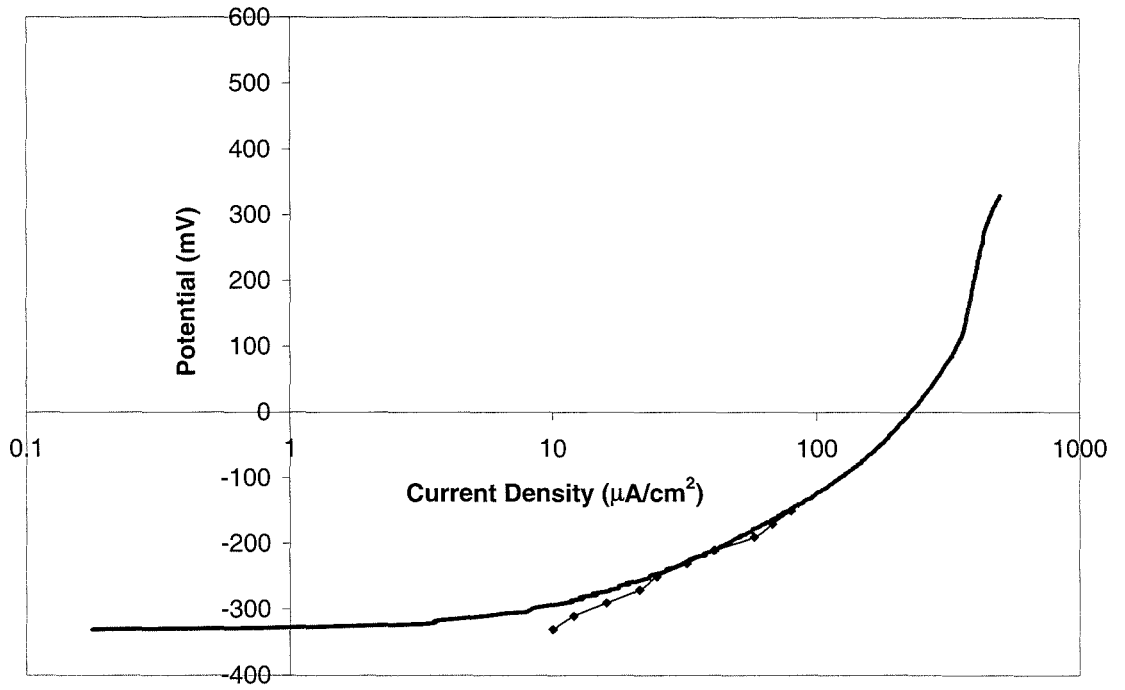


Figure A-15 Liquid impingement after 1 hour at  $50^\circ\text{C}$

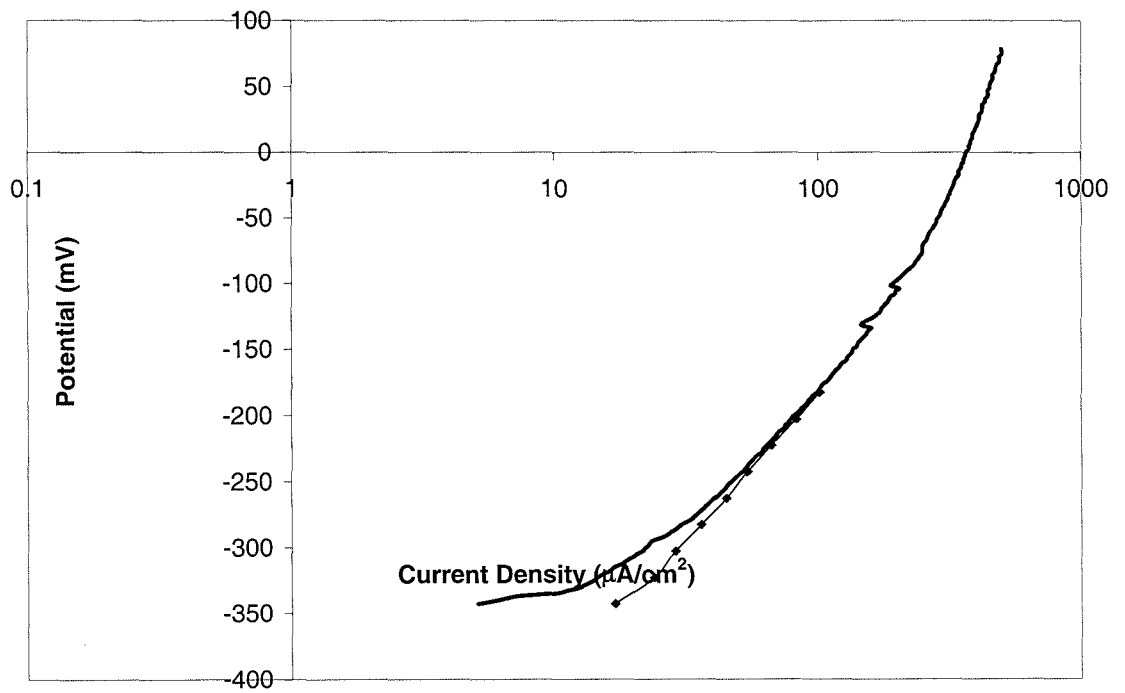


Figure A-16 Liquid impingement after 4 hours at  $50^\circ\text{C}$

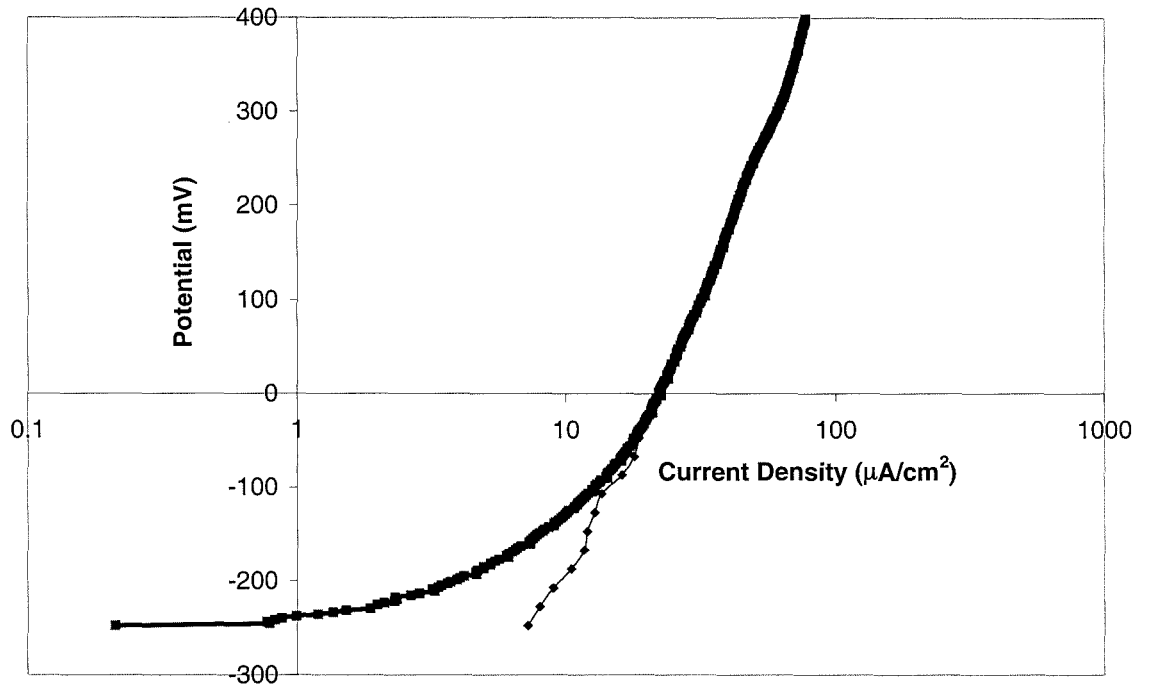


Figure A-17 170mg/l solid-liquid impingement after 1hour at 18°C

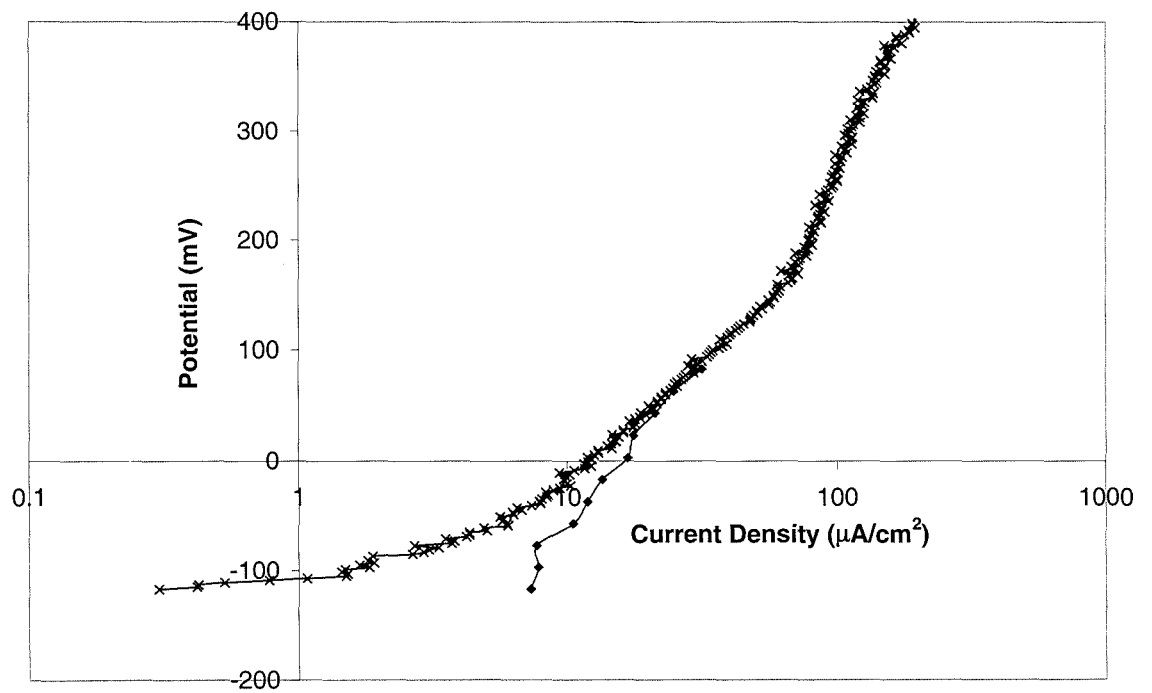


Figure A-18 170 mg/l solid-liquid impingement after 4 hours at 18°C

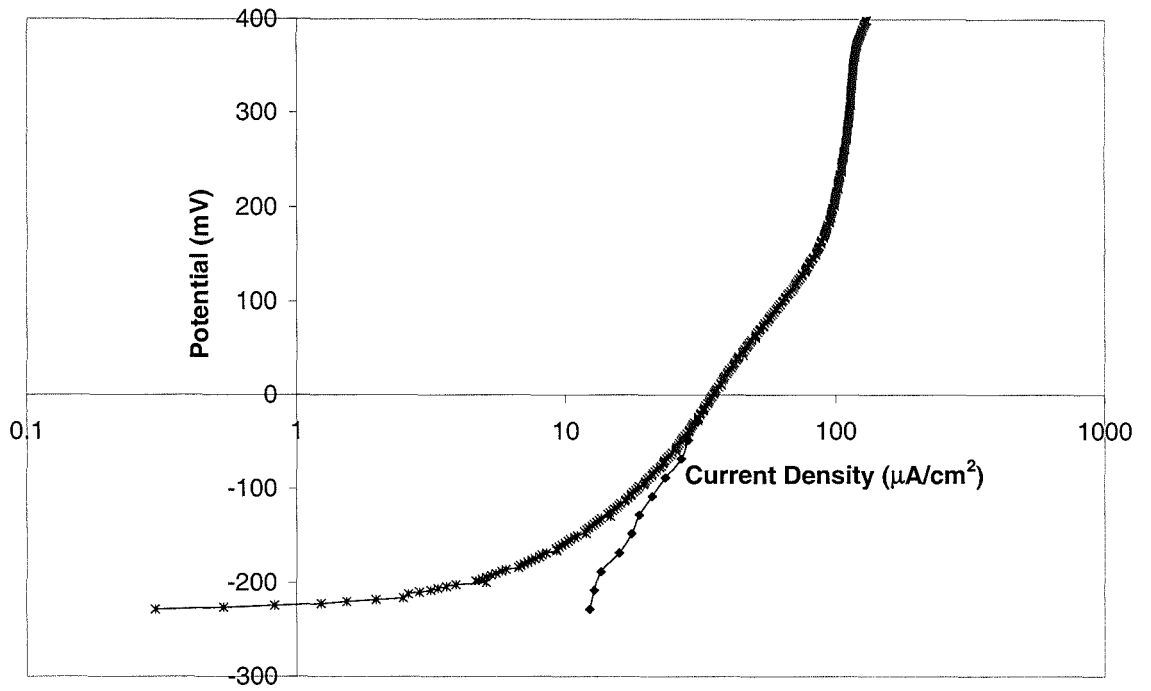


Figure A-19 500 mg/l solid-liquid impingement after 1 hour at 18°C

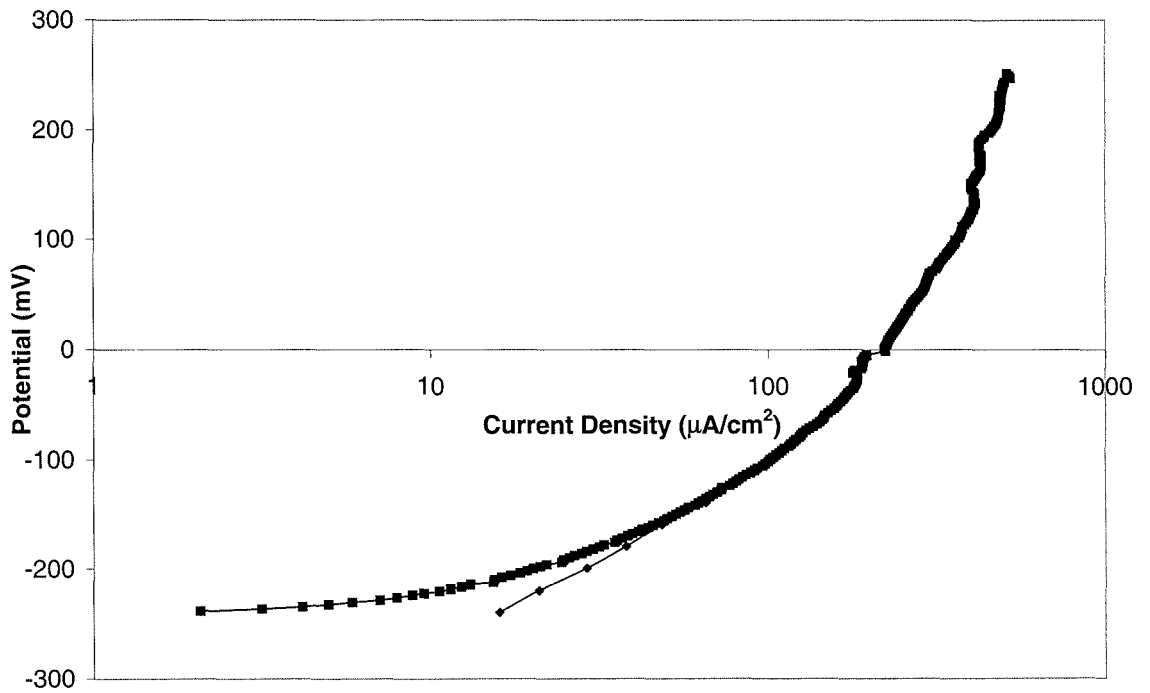


Figure A-20 500 mg/l solid-liquid impingement after 1 hours at 50°C

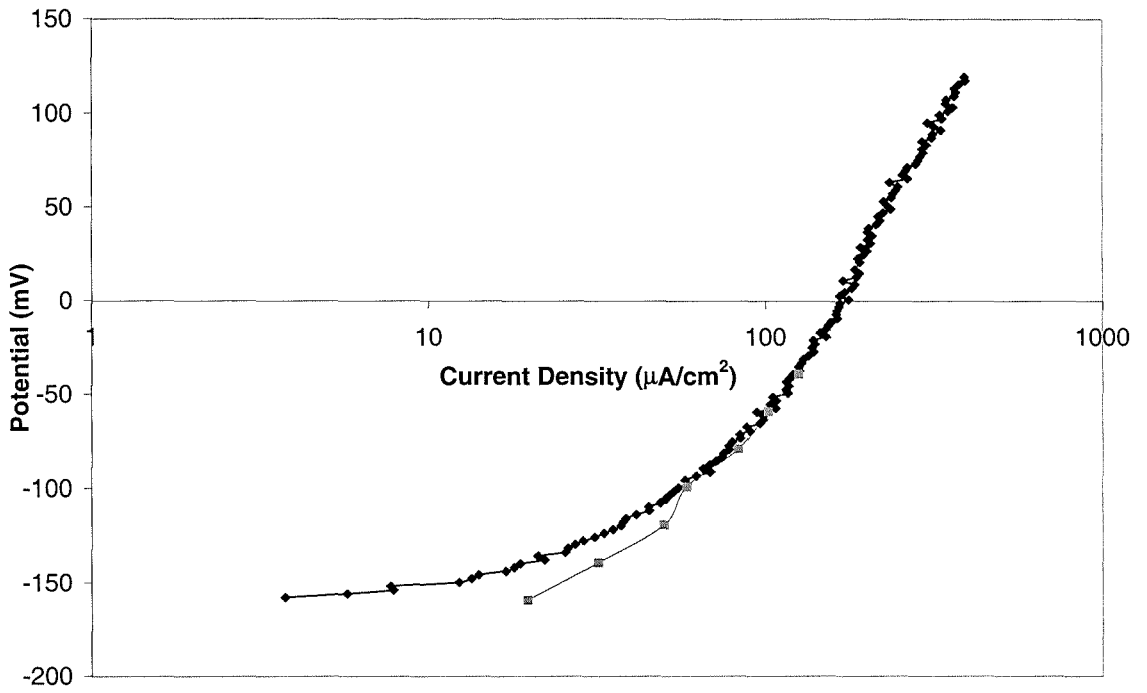


Figure A-21 500 mg/l solid-liquid impingement after 4hours at 50°C

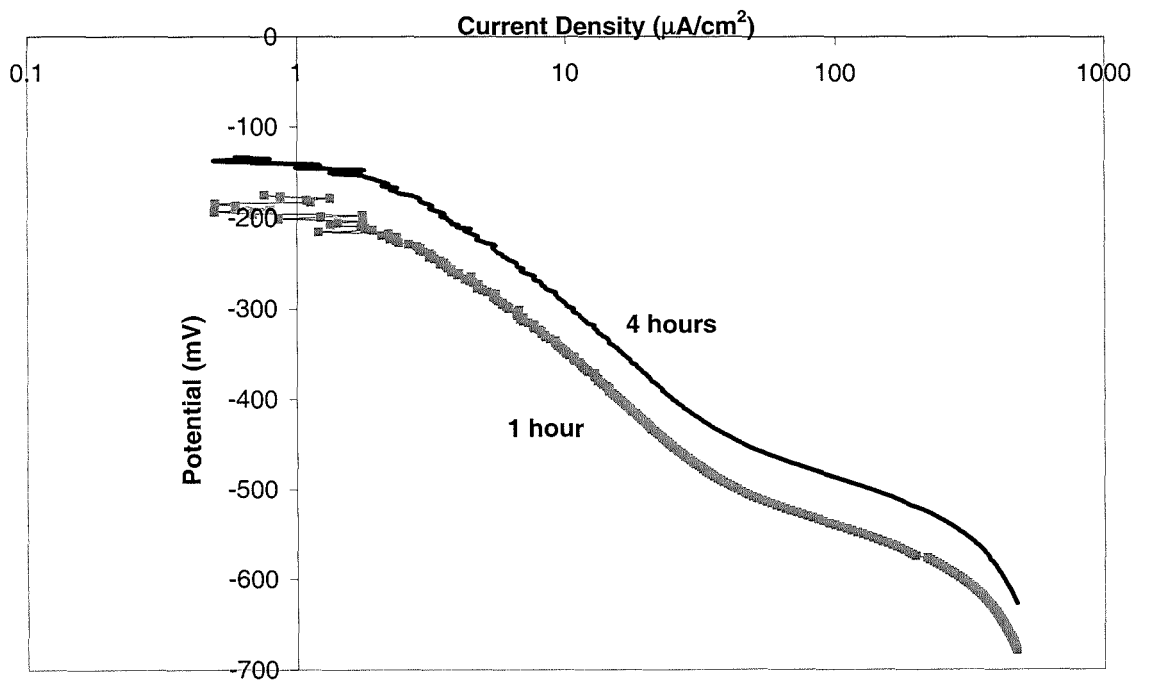


Figure A-22 Cathodic polarisation after 1 and 4 hours with 650 mg/l solids

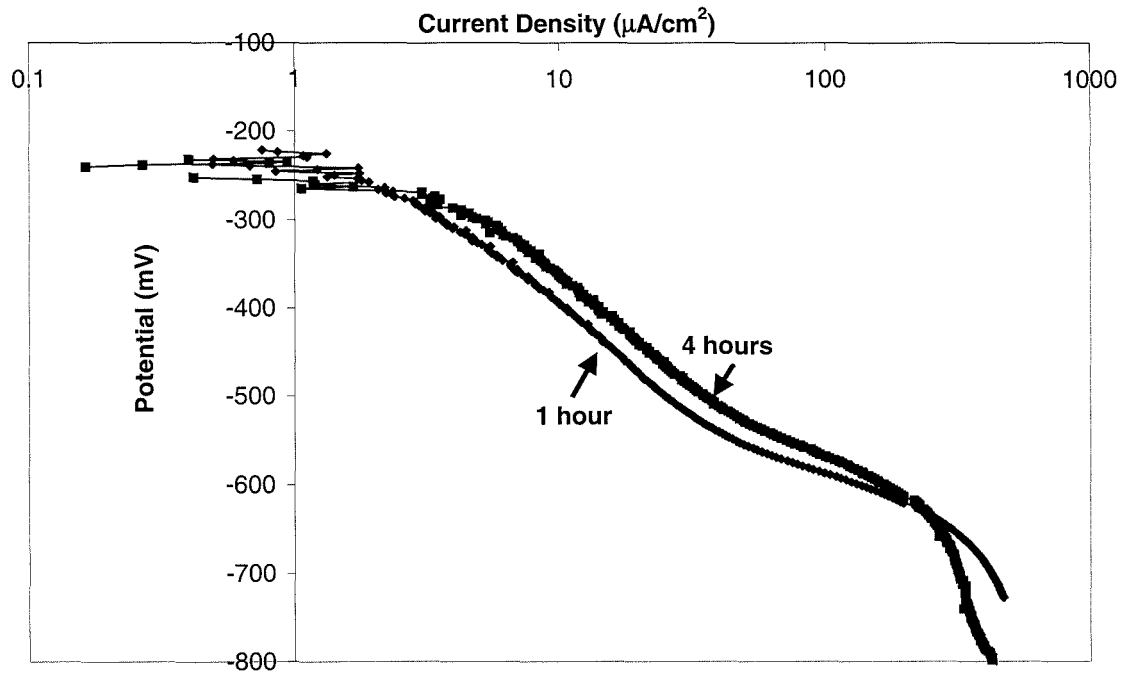


Figure A-23 Cathodic polarisation after 1 and 4 hours impingement with 1500 mg/l solids

**PAGE  
MISSING  
IN  
ORIGINAL**

## References

- 
- <sup>1</sup> P. Blazdell, S. Kuroda, "Thermal spraying in the new millennium," *Materials World*, April 1999 pp 205-207.
- <sup>2</sup> S.Y. Tsai, H.C. Shih, "The use of thermal-spray coatings for preventing wet H<sub>2</sub>S cracking in HSLA steel plates," *Corrosion Prevention and Control*, Vol. 44 (2) (1997) pp 42-48
- <sup>3</sup> R.J. Duncan, C.B. Thompson, "A guide to weld and thermal spray hardfacing in the pulp and paper industry; Part1: Process and consumable selection," *Materials and Design*, Oct 1991 pp 55-58.
- <sup>4</sup> R.J. Duncan, C.B. Thompson, "A guide to weld and thermal spray hardfacing in the pulp and paper industry; Part 2: Applications," *Materials and Design*, (Nov 1991) pp 71-75.
- <sup>5</sup> C.B. Thompson, A. Garner "Identification and control of wear in the pulp and paper industry," *Pulp and Paper Canada*, Vol. 87 No.3 (1986) pp 53-56
- <sup>6</sup> L. Pejryd, J. Wigren, D.J. Greving, J.R. Shadley, E.F. Rybicki, "Residual stresses as a factor in the selection of tungsten carbide coatings for a jet engine application," *Journal of Thermal Spray Technology*, Vol. 4 No.3 (1995) pp 268-274.
- <sup>7</sup> J. D. Haman, A.A. Boulware, L.C. Lucas and D.E. Crawmer, "High-Velocity Oxyfuel Thermal Spray Coatings for Biomedical Applications" *Journal of Thermal Spray Technology*, Vol. 4 No. 2 (1995) pp 179-184
- <sup>8</sup> D.S. Parker, "Case Study: application of HVOF sprayed coatings for replacement of chrome plating on navy P-3 aircraft hydraulic components and

---

landing gear.” Proc. 15<sup>th</sup> International Thermal Spray Conference, Nice, 1998 pp 243-247

<sup>9</sup> M.C. Nestler, G. Prenzel, T. Seitz, “ HVOF-spraying vs hard chrome plating-coating characteristics and aircraft applications” Proc. 15<sup>th</sup> International Thermal spray Conference, Nice 1998 pp 1073-1078.

<sup>10</sup> L. Poawlowski “The science and Engineering of thermal spray coatings,” John Wiley and Sons 1994

<sup>11</sup> H.D. Steffens, M. Gramlich, K. Nassentein “Thermal Spraying”, Materials Science Forum, Vol. 163-165 (1995) pp. 559-572.

<sup>12</sup> B. Irving, R. Knight, W. Smith, “The HVOF Process-The Hottest Topic in the Thermal Spray Industry,” Welding Journal, (July 1993) pp 25-30.

<sup>13</sup> S.J. Matthews, M.M. Hyland, “Statistical optimisation of HVAF sprayed Cr<sub>3</sub>C<sub>2</sub>-NiCr coatings for minimising decarburisation” Proc. International Thermal Spray Conference, Montreal, Canada, 2000 pp 543-550

<sup>14</sup> E.J. Kubert Jr “Powders dictate thermal spray coatings properties”, Advanced Materials and Processes, Vol. 12 1990 pp 24-32.

<sup>15</sup> C. Terry, J. Morris “ Macrocrystalline thermit process revealed,” Metal Powder Report, Vol. 54 (12) 1999 pp 22- 27.

<sup>16</sup> J. Nertz, B. Kushner, A. Rotolico, “Microstructural Evaluation of Tungsten Carbide-Cobalt Coatings,” Journal of Thermal Spray Technology Vol. 1 No.2 (1992) pp 147-152.

<sup>17</sup> Cj Li, A. Ohmori and Y. Harada “Formation of an Amorphous phase in thermally sprayed WC-Co-Cr,” Journal of Thermal Spray Technology, Vol. 5 No.1 (1996) pp 69-73.

- 
- <sup>18</sup> X. Provot, H. Burlet, M. Vardavoulias, D. Manese, C. Richard, J. Lu, "Comparative Studies of Microstructures Residual Stress Distributions and Wear Properties for HVOF and APS WC-Co Coatings of Ti6Al4V," Proceedings of the 1993 National Thermal Spray Conference, Anaheim, pp 159-166.
- <sup>19</sup> W. Coulson, S.J. Harris, "The Microstructure of WC-Co Coatings by HVOF Spraying with liquid fuel," Trans IMF, Vol.75 No.3 (1997) pp108-113.
- <sup>20</sup> M.S.A. Khan, T.W. Clyne, A.J. Sturgoen "Microstructure and Abrasion Resistance of WC-Co Coatings Produced by High Velocity Oxy-Fuel Spraying" Proceedings. International Thermal Spray Conference, 1997 pp 681-690.
- <sup>21</sup> M.D.F. Harvey, A.J. Sturgeon, F.J. Blunt, S.B. Dunkerton "Investigation into the relationship between fuel gas selection, wear performance and microstructure of HVOF sprayed WC-Co coatings," Proceedings of International thermal spray conference, Kobe, May 1995 pp 471-476.
- <sup>22</sup> J.M. Guilemany, J. Nutting, J.R. Miguel, Z. Dong "Microstructural Formation of HVOF Sprayed WC-Ni Coatings Deposited on Low Alloy Steel," Materials and Manufacturing Processes, 1997 Vol. 12 No. 5 pp 901-909.
- <sup>23</sup> L. Jacobs, MM Hyland, M De Bonte "Comparative Study of WC-cermet coatings sprayed via the HVOF and HVOF process," Journal of Thermal Spray Technology, Vol. 7 No.2 (1998) pp 313-218.
- <sup>24</sup> W.J. Jarosinski, M.F. Gruninger, C.H. Londry "Characterisation of Tungsten Carbide Cobalt Powders and HVOF coatings," Proceedings of 1993 National Thermal Spray Conference, Anaheim pp 153-157.
- <sup>25</sup> A.A. Ashary, R.C. Tucker " Electrochemical corrosion studies of alloys plasma sprayed with Cr<sub>2</sub>O<sub>3</sub>" Surface and Coatings Technology, Vol. 39/40 (1989) pp 701-709.

- 
- <sup>26</sup> A.A. Ashary and R.C. Tucker, "Electrochemical and longterm corrosion studies of several alloys in bare condition and plasma sprayed with Cr<sub>2</sub>O<sub>3</sub>" Surface and Coatings Technology, Vol. 43/44 (1990) pp 567-576.
- <sup>27</sup> A.A. Ashary and R.C. Tucker, "Corrosion characteristics of selected thermal spray coatings" Corrosion, 1993 NACE, Paper No 24.
- <sup>28</sup> R. Hoffman, M.P.W. Vreijling, G. M. Ferrari and J.H.W. de Wit, "Electrochemical Methods for Characterisation of Thermal Spray Corrosion resistant Stainless Steel Coatings" Materials Science Forum, Vols. 289-292 (1998) pp 641-654
- <sup>29</sup> A. Neville and T. Hodgkiess, "Corrosion behaviour and microstructure of two thermal sprayed coatings," Surface Engineering, 1996 Vol.12 No.4 pp 303-312.
- <sup>30</sup> T. Hodgkiess and A. Neville, "An analysis of environmental factors affecting corrosion behaviour of thermal spray cermet coatings." Proc. 15<sup>th</sup> International Spray Conference, Nice, May 1998.
- <sup>31</sup> A. Neville and T.Hodgkiess, " The Corrosion Behaviour of a cermet coating applied by HVOF Spraying," Proc. Thermal Spray 1997 pp 161-166.
- <sup>32</sup> A. Neville and T. Hodgkiess "An electrochemical study of the localised corrosion of vacuum furnace fused cermet coatings" Journal of American Ceramic Society.
- <sup>33</sup> T. Hodgkiess and A. Neville, " An Assessment of Galvanic Effects in thermal sprayed coating systems," Proc. Thermal Spray Indianapolis, 1997 pp 167-173
- <sup>34</sup> E. Lugscheider, P. Jokiel, V. Messerschmidt and G. Beckschulte, " Subsequent Sealing of Thermally Sprayed Coatings to Increase Corrosion Resistance." Surface Engineering

- 
- <sup>35</sup> S. Shrestha, A. Neville and T. Hodgkiess “ The Effect of Post Treatment of a HVOF Ni-Cr-Si-B Coating Part I: Microstructure/ Corrosion Behaviour Relationships” accepted for publication in Journal of Thermal Spray Technology.
- <sup>36</sup> I. Kretschmer, P. Heimgartner, R. Polak and P.A. Kammer “New fusible Alloys with Enhanced Corrosion Resistance” Proc Thermal Spray Conference, Ohio, USA, 1997 pp 199-202.
- <sup>37</sup> M.D.F. Harvey, A.J. Sturgeon, F.J. Blunt and S.B Dunkerton, “The Influence of Microstructure on the Aqueous Corrosion Behaviour of Alloy 625 Coatings Prepared by HVOF Spraying” Proceedings of the International Thermal Spray Conference, Kobe, May 1995 pp 531-535
- <sup>38</sup> J.M Guilemany, J. Fernandez, J.M. de Paco and J. Sanchez, “ Corrosion Resistance of HVOF WC-Co and TiC/Ni-Ti coatings sprayed on Commercial Steel,” Surface Engineering, Vol.14 No.2 (1998) pp133-135.
- <sup>39</sup> J.M. Guilemany, J.M. de Paco, J.R. Miguel, J. Sanchez, P. Smith, “ Corrosion Resistance HVOF Coatings Based Upon TiC+NiTi and (TiW)C+Ni,” Proceedings of the 15<sup>th</sup> International Thermal Spray Conference, Nice, France, May 1998.
- <sup>40</sup> A. Neville, T. Hodgkiess, J.T. Dallas, “A study of the erosion-corrosion behaviour of engineering steels for marine pumping applications” Wear, Vol. 186-187 (1995) pp 497-507
- <sup>41</sup> E. Heitz, “ Chemo-Mechanical Effects of Flow on Corrosion,” Corrosion, Vol.47 No.2 pp 135-145
- <sup>42</sup> S. Nesic and J. Postlethwaite, “Hydrodynamics of Disturbed flow and erosion-corrosion. Part 1 – Single-phase flow study” The Canadian Journal of Chemical Engineering, Vol 69 (1991) pp 698-703.

---

<sup>43</sup> B. Poulson, "Complexities in predicting erosion corrosion" *Wear* Vol. 233-235 (1999) pp 497-504.

<sup>44</sup> N. Rajartnam "Turbulent Jets" American Elsevier Publishing Company, New York 1976. ISBN 0-444-41373-3

<sup>45</sup> F. Giralt and O.Trass, "Mass Transfer from Crystalline Surfaces in a Turbulent Impinging Jet Part 2" *The Canadian Journal of Chemical Engineering*, Vol. 54 (1976) pp 148-155

<sup>46</sup> K.D. Efrid, E.J. Wright, J.A. Boros and T.G. Hailey, "Correlation of steel corrosion in pipe flow with jet impingement and rotating cylinder tests" *Corrosion* Vol. 49 No. 12 (1993) pp 991-1002

<sup>47</sup> B. Poulson, "Advances in understanding hydrodynamic effects on corrosion," *Corrosion Science*, Vol.35 No. 1- 4 (1993) pp 655-665.

<sup>48</sup> B. Poulson, "Mass Transfer from Rough Surfaces" *Corrosion Science*, Vol. 30 No.67 (1990) pp 743-746

<sup>49</sup> J. Weber, "Flow induced corrosion: 25 years of industrial research," *British Corrosion Journal*, Vol. 27 No.3 (1992) pp 193-199

<sup>50</sup> A. Neville and T. Hodgkiess, "An assessment of the corrosion behaviour of high-grade alloys in seawater at elevated temperature and under a high velocity impinging flow" *Corrosion Science*, Vol. 38 (1996)No. 6 pp 927-956

<sup>51</sup> A. Neville, T. Hodgkiess and H. XU, "An electrochemical and microstructural assessment of erosion-corrosion of cast iron" *Wear*, 233-235 (1999) pp 523-534

<sup>52</sup> T. Hodgkiess, A. Neville and S. Shrestha, "Electrochemical and mechanical interactions during erosion-corrosion of a high velocity oxy-fuel coating and a stainless steel," *Wear*, 233-235 (1999) pp 623-634

- 
- <sup>53</sup> P.A. Lush, S.P. Hutton, J.C. Rowlands and B. Angell, "The relation between impingement corrosion and fluid turbulence intensity" Proc 6<sup>th</sup> European Congress on Metallic Corrosion, 1977 pp 137-146
- <sup>54</sup> I. Finnie "Erosion of surfaces by solid particles" Wear, Vol. 3 (1960) pp 87-103
- <sup>55</sup> G.L. Sheldon and I. Finnie, "On the ductile behaviour of nominally brittle materials during erosive cutting" Trans. ASME 88B (1966) pp 387-392
- <sup>56</sup> I. M. Hutchings, Tribology: Friction and Wear of Engineering Materials, Edward Arnold 1992 ISBN 0-340-56184-X
- <sup>57</sup> G. Sundararajan, "The depth of plastic deformation beneath eroded surfaces: the influence of impact angle and velocity, particle shape and material properties," Wear, Vol. 149 (1991) pp 129-153
- <sup>58</sup> M.M. Stack, N. Corlett, S. Zhou, "Impact angles on the transition boundaries of the aqueous erosion-corrosion map" Wear, Vol. 225-229 (1999) pp 190-198
- <sup>59</sup> I. Finnie, "Some reflections on the past and future of erosion," Wear, Vol. 186-187 (1995) pp 1-10.
- <sup>60</sup> M. Liebhard and A. Levy, "The effect of erodent particle characteristics on the erosion of metals" Wear, Vol. 151 (1991) pp 381-390
- <sup>61</sup> A.V. Levy and P. Crook, "The erosion properties of alloys for the chemical processing industries" Wear, Vol. 151 1991 pp 337-350
- <sup>62</sup> A. J. Ninham and A. V. Levy, " The erosion of carbide-metal composites" Wear, Vol. 121 (1988) pp 347-360

- 
- <sup>63</sup> H.M. Hawthorne, M. Arsenault, J.P. Immarigoen, J.G. Legoux, V.R. Parameswaran, "Comparisaon of slurry and dry erosion behaviour of some HVOF thermal spray coatings," *Wear*, Vol. 225-229 (1999) pp 825-834
- <sup>64</sup> Y. I. Oka, H. Ohnogi, T. Hosokawa, M. Matsumura, "The impact dependence of erosion damage caused by solid particle impact" *Wear*, 203-204 (1997) pp 573- 579
- <sup>65</sup> K.T. Kembaiyan and K. Keshavan, " Combating severe fluid erosion and corrosion of drill bits using thermal spay coatings" *Wear*, Vol. 186-187 (1995) pp 487-492
- <sup>66</sup> B. Wang " Erosion-corrosion of thermal sprayed coatings in FBC boilers" *Wear*, Vol.199 (1996) p 24-32
- <sup>67</sup> L. Swadzba, B. Formanek, H.M. Gabriel, P. Liberski and P. Podolski, "Erosion-and-corrosion-resistant coatings for aircraft compressor blades" *Surface and Coatings Technology*, Vol. 62 (1993) pp 486-492.
- <sup>68</sup> H. M<sup>c</sup>I. Clark "The influence of the flow field in slurry erosion," *Wear*, Vol. 152 (1992) pp 223-240
- <sup>69</sup> M.T. Benchaita, P. Griffith and E. Rabinowicz, "Erosion of metallic plate by solid particles entrained in a liquid jet" *J. Eng. Ind.*, Vol. 105 (1983) p 215-222
- <sup>70</sup> R. S. Lynn, K.K. Wong, H M<sup>c</sup>I Clark, " On the particle size effect in slurries" *Wear*, Vol. 149 (1991) pp55-71
- <sup>71</sup> S. Turenne, M. Fiset and J. Masounave, " The effect of sand concentration on the erosion of materials by a slurry jet" *Wear*, Vol. 133 (1989) pp 95-106

- 
- <sup>72</sup> H.X. Zhoa, M. Yamamoto, M. Matsumura, "Slurry erosion properties of ceramic coatings and functionally gradient materials" *Wear*, Vol. 186-187 (1995) pp 473-478
- <sup>73</sup> A. Karimi, Ch. Verdon, J.L. Martin, R.K. Schmid, "Slurry erosion behaviour of thermally sprayed WC-M coatings" *Wear* Vol. 186-187 (1995) pp 480-486
- <sup>74</sup> R.J.K. Wood, B.G. Mellor and M.L. Binfield, "Sand erosion performance of detonation gun applied tungsten carbide/cobalt-chromium coatings" *Wear* Vol. 211 (1997) pp 70-83.
- <sup>75</sup> ASTM Standard Guide for Determining Synergism Between Wear and Corrosion G199-93
- <sup>76</sup> R.J.K. Wood and S.P. Hutton "The synergistic effect of erosion and corrosion; trends in published results" *Wear*, Vol.140 (1990) pp 387-394
- <sup>77</sup> B. W. Madsen "Measurement of Erosion-Corrosion synergism with a slurry wear test apparatus" *Wear*, Vol. 123 (1988) p127-142
- <sup>78</sup> S. Zhou, M.M. Stack, R.C. Newman, "Characterisation of Synergistic Effects between Erosion and Corrosion in an Aqueous Environment Using Electrochemical Techniques" *Corrosion Science*, Vol. 52 No. 12 (1996) pp 935-946
- <sup>79</sup> H. Abd-El-Kader and S.M. El Raghy "Wear-corrosion mechanism of stainless steel in chloride media" *Corrosion Science*, Vol. 26 No.8 (1986) pp 647-653
- <sup>80</sup> H.W. Wang and M.M. Stack "The erosive wear of PVD and CrN coatings" *Tribology Letters*, Vol. 6 (1999) pp 23-36
- <sup>81</sup> N.J. Laycock and R.C. Newman, "Localised dissolution kinetics, salt films and pitting potentials" *Corrosion Science*, Vol. 39 (1997) pp 1771-1790

---

<sup>82</sup> G.T. Burstein and K. Sasaki, “ The birth of corrosion pits as stimulated by slurry erosion” Corrosion Science, Vol. 42 (2000) pp 841-860

<sup>83</sup> M.C. Wang, S.Z. Ren, X.B. Wang and S.Z. Li “A study of sand slurry erosion of W-alloy cast irons” Wear, Vol. 160 (1993) pp 259-264

<sup>84</sup> M. Bjordal, E. Bardal, T. Rogne and TG Eggen “ Erosion and corrosion properties of WC-coatings and duplex stainless steel in sand containing seawater” Wear, Vol. 186-187 (1995) pp 508-514

<sup>85</sup> J. Berget, E. Bardal, T. Rogne, “Influence of WC Particle size and Matrix Composition on the Behaviour of WC-Co-Cr Coatings Sprayed by the HVOF Process” Proc. International Thermal Spray Conference Ohio, USA, 1997 pp783-789

<sup>86</sup> T. Rogne T. Solem and J. Berget “Effect of composition and corrosion properties of the metallic matrix on the erosion-corrosion behaviour of HVOF sprayed WC-coatings” Corrosion 98, paper no 495

<sup>87</sup> M. Bjordal, E. Bardal, T Rogne and T. G. Eggen, “Combined erosion and corrosion of thermal sprayed WC and CrC coatings” Surface and Coatings Technology, Vol. 70 (1995) pp 215-220

<sup>88</sup> E. Bardal, T. G. Eggen, T. Rogne and T. Solem “ The erosion and corrosion properties of thermal spray and other coatings” Proc. International thermal spray conference, 1995 pp 645-650

<sup>89</sup> T. Rogne, M. Bjordal, T. Solem, E. Bardal “The importance of corrosion on the erosion-corrosion performance of thermal spray ceramic-metallic coatings” Proc. International Thermal Spray Conference, Ohio, USA 1996 pp 207-215

- 
- <sup>90</sup> E. J. Wentzel and C. Allen “ Erosion-corrosion resistance of tungsten carbide hard metals with different binder compositions “ *Wear*, Vol. 181-183 (1995) pp 63-69
- <sup>91</sup> M.M. Stack, J. Chacon-Nava, F.H. Stott, “Relationship between the effects of velocity and alloy corrosion resistance in erosion-corrosion environments at elevated temperatures” *Wear*, Vol. 180 (1995) pp 91-99
- <sup>92</sup> M.M. Stack, S. Zhou, R.C. Newman, “Identification of transitions in erosion-corrosion regimes in aqueous environments” *Wear*, Vol. 186-187 (1995) pp 523-532
- <sup>93</sup> M.M. Stack, S. Zhou and R.C. Newman “Effects of particle velocity and applied potential on erosion of mild steel an carbonate/bicarbonate slurry” *Materials Science and Technology*, Vol. 12 pp 261-268
- <sup>94</sup> M.M. Stack, N. Corlett and S. Zhou, “A methodology for the construction of the erosion-corrosion map in aqueous environments” *Wear*, Vol.203-204 (1997) pp 474-48
- <sup>95</sup> M.M. Stack, N. Corlett and S. Zhou “Some thoughtd on the elastic rebounds on the boundaries of the aqueous erosion-corrosion map” *Wear*, Vol. 214 (1998) pp 175-185
- <sup>96</sup> M.M. Stack, N. Pungwiwat “A note on the construction of materials performance maps for resistance to erosion in aqueous slurries” *Wear*, Vol. 215 (1998) pp 67-76
- <sup>97</sup> H.M. Hawthorne, B. Arsenault, J.P. Immarigeon, J.G. Legoux and V.R. Parameswaran, “Comparison of slurry and dry erosion behaviour of some HVOF thermal sprayed coatings” *Wear* Vol. 225-229 (1999) pp 825-834.

---

<sup>98</sup> H. McI Clark, H. M Hawthorne and Y.Xie, "Wear rates and specific energies of some ceramic, cermet and metallic coatings determined in the Coriolis erosion tester" *Wear* Vol. 233-235 (1999) pp 319-327.

<sup>99</sup> B. Arsenault, J.G. Legoux and H. Hawthorne, "Slurry Erosion of High Velocity Oxy Fuel Thermal spray Coatings" *ASM Proceedings UTSC* 1997.

<sup>100</sup> J.M. Perry, A.Neville, T.Hodgkiess and V. Wilson "Assessment of the corrosion rates and mechanisms of a WC-Co-Cr HVOF coating in static and liquid-solid impingement saline environment" Accepted for publication in *Surface and Coatings Technology*, Sept 2000.

<sup>101</sup> J.D Voorhies, "Electrochemical and Chemical Corrosion of Tungsten Carbide (WC)" *Journal of Electrochemical Society: electrochemical science and technology*, Vol. 119 No 2 (1972) pp 219-222

<sup>102</sup> S. Srestha, A. Neville, T. Hodgkiess "The effect of post-treatment of a HVOF Ni-Cr-Mo-Si-B coating Part II: Erosion-Corrosion Behaviour, accepted for publication in *The Journal of Thermal Spray Technology*

<sup>103</sup> J.Berget PhD Thesis, Norwegian University of Science and Technology, Trondheim, Norway. 1997

<sup>104</sup> F. Mansfield, "The relationship between galvanic current and dissolution rates" *Corrosion*, Vol.29 (1973) No 10 pp 403-405

<sup>105</sup> T. Hodgkiess, A. Maciver, P.Y. Chong, "Galvanic studies related to the use in desalination plant of corrosion-resistant materials" *Desalination*, Vol. 66 (1987) pp 147-170

<sup>106</sup> B.Poulson, "Electrochemical measurements in flowing solutions" *Corrosion Science* Vol.23 No. 4 (1983) pp 391-430.

---

<sup>107</sup> M. Stern and A.L. Geary "A theoretical analysis of the shape of polarisation curves" *Journal of The Electrochemical Society* (1957) pp 56-63